Novel Electrocatalysts for Ammonia Synthesis and Hydrogen Evolution



Tim Sudmeier

Inorganic Chemistry Laboratory

Department of Chemistry

St Hugh's College

A thesis submitted for the degree of Doctor of Philosophy

Trinity Term 2019

Acknowledgments

Firstly, I would like to thank my supervisor Prof Edman Tsang for giving me the opportunity to work in his lab over the past four years, and the freedom he provided me with in approaching my project. Further, I would like to express my deepest gratitude to Dr Ian McPherson for teaching me electrochemistry, his continued guidance and support, as well as making the ammonia group a fun place to work at.

I would also like to thank Siemens UK and the Engineering and Physical Science Research Council for providing funding for this project which otherwise would not have been possible. Here, I would also like to thank my industrial supervisor Dr Ian Wilkinson for interesting discussions on energy storage from an industrial viewpoint. Further, I would like to express my gratitude to the Royal Commission of Exhibition of 1851 for their Industrial Fellowship which afforded me countless opportunities to improve my project and meet other scientist around the world.

Special thanks goes to Joshua Fellowes for extensive discussions about ammonia, as well as support and friendship in and out of the lab.

Dr Chen Huang is thanked for acquiring beautiful high-resolution STEM images and interesting discussions about electron microscopy. I would further like to thank Dr Diego Gianolio and Dr Matteo Aramini of Diamond Light Source for the fruitful collaboration on DFT-based XANES modelling. Dr Rosa Arrigo is thanked for providing me with her in-situ XAS electrochemistry cell. I would also like to thank Dr Phil Holdway and Dr Ashley Shepherd for their help in acquiring XPS data and discussions on molybdenum spectra.

Furthermore, I would like to thank Dr Lizze Raine for acquiring TEM data and Ting Chen for all his help with in-situ IR spectroelectrochemistry measurements. Additionally, I would like to thank Simson Wu for introducing me to XAS data analysis and wavelet transforms. I would also like to thank Chris Harrison for help with GO and SAC synthesis.

I would like to thank all members of the Tsang group for support, discussions and Great Bake Offs throughout the last four years. Particularly, I would like thank Dr Tugce Ayavali, Simson Wu, Iris Mo, Kirsty Purchase, Lizzie Raine and Jiri Kulhavy for their friendship.

Outside the lab, I would first like to thank my parents for their unwavering support and believe in me. I would also like to thank Serban Ilca, Joshua Fellowes and Hamish Lemmey for their friendship and support during the writing of this thesis. Also, thank you to my friends across the pond Robert Schittko, Aaron Krahn and Julian Kates-Harbeck for the awesome trips around the world that always managed to reenergize me. A huge shout out further goes to Biruk Terrefe and Ali Bargu for more than seven years of continued friendship and for making my time in Oxford such a great one.

Abstract

Novel Electrocatalysts for Ammonia Synthesis and Hydrogen Evolution

A thesis submitted for the degree of Doctor of Philosophy

Tim Sudmeier, St Hugh's College, Trinity 2019

This thesis explores the activity of single atom metal catalysts on graphene-like support (SACs) and metal nitrides for the nitrogen reduction reaction (NRR). Furthermore, extensive analysis of HER activity and in-situ characterisation are carried out to derive a structure-activity relationship of SACs in the hydrogen evolution reaction (HER).

To that end, a library of single atom transition metals on nitrogen-doped graphene (M-NGs) with comparable compositions is synthesised by a carbon backbone method. Their HER activity is assessed showing Ru-NG and Co-NG to be highly active. The data is correlated with the φ factor, a computationally suggested descriptor for electron density on the metal site constituting the first experimental substantiation of this design principle. Additionally it is found that HER activity on cobalt-containing SACs can be further tuned by changing the coordination environment of the metal via the inclusion of oxygen into the first coordination shell. In in-situ XANES and IR spectroelectrochemical thiocyanate poisoning experiments three distinct active sites are observed and it is suggested that distortion from the square planar Co-N_4 environment caused by axial oxygen ligands leads to decreased HER activity.

In the second part of this thesis Co_3Mo_3N was identified as a potential electrocatalyst for the direct reduction of N_2 to N^{3-} in molten chloride eutectics. Based on experimental evidence and previous literature reports, a Mars van Krevelen-type mechanism is suggested for the reaction in which Li^+ ions facilitate the activation of dinitrogen, as well as enable participation of the lattice nitrogen of Co_3Mo_3N.

List of Abbreviations

A	Absorbance
ALD	Atomic layer deposition
ATR	Attenuated total reflectance
CE	Counter electrode
CV	Cyclic voltammetry
DFT	Density Functional Theory
ECSA	Electrochemically active surface are
EXAFS	Extended X-ray absorption fine structure
FWHM	Full width half maximum
GCE	Glassy carbon electrode
HAADF	High-angle annular dark field
HER	Hydrogen evolution reaction
HR-TEM	High-resolution transmission microscopy
LSV	Linear scanning voltammetry
M-NGs	Atomically dispersed transition metals on nitrogen-doped graphene
NG	Nitrogen-doped graphene

NRR	Nitrogen reduction reaction
OCP	Open-circuit potential
OER	Oxygen evolution reaction
ORR	Oxygen reduction reaction
PEEK	polyether ether ketone
PEM	Polymer exchange membrane
PGM	Platinum group metal
Pt/C	Platinum catalyst supported on carbon black
RE	Reference electrode
RHE	Reversible hydrogen electrode
SACs	Single atom catalysts
SCE	Saturated calomel electrode
STEM	Scanning transmission electron microscopy
TEM	Transmission electron microscopy
TOF	Turnover frequency
TPD	Temperature programmed desorption
TPR	Temperature programmed reduction

WE	Working electrode
XANES	X-ray near edge structure
XAS	X-ray absorption spectroscopy
XPS	X-ray photoelectron spectroscopy
XRD	X-ray diffraction

List of Publications

1) McPherson, I. J.; Sudmeier, T.; Fellowes, J. P.; Wilkinson, I.; Hughes, T.; Tsang, E. S. C. The Feasibility of Electrochemical Ammonia Synthesis in Molten LiCl-KCl Eutectics. Angewandte Chemie International Edition 0 (ja).

2) McPherson, I.J.; Sudmeier, T.; Fellowes, J.; Edman Tsang, S. C. Materials for Electrochemical Ammonia Synthesis. Dalton Transactions 2019, 48 (5), 1562–1568.

3) Zheng, J.; Liao, F.; Wu, S.; Jones, G.; Chen, T.; Fellowes, J.; Sudmeier, T.; McPherson, I.J.; Wilkinson, I.; Tsang, E. S. C. Efficient Non-Dissociative Activation of Dinitrogen to Ammonia over Li Promoted Ru Nanoparticles at Low Pressure. Angewandte Chemie International Edition 0 (ja).

4) Sudmeier, T.; McPherson, I. J.; Huang, C.; Raine, E.M.; Harrison, C.; Fellowes, J. P.; Tsang, E. S. C. Understanding the Hydrogen Evolution Activity of Single Metal Atoms on Nitrogen-doped Graphene. *In preparation.*

5) Sudmeier, T.; Gianolio, D.; Aramini, M.; McPherson, I. J.; Huang, C.; Chen, T.; Arrigo, R; Raine, E.M.; Fellowes, J. P.; Tsang, E. S. C. Investigation of the Metal Centre Environment in Cobalt–containing Single-atom Catalysts. *In preparation.*

6) Sudmeier, T.; McPherson, I. J.; Fellowes, J. P.; Tsang, E. S. C. Cobalt Molybdenum Nitride as a Nitrogen Reduction Catalyst in Molten Salts. *In preparation.*

List of Figures

1 Introduction 1

Figure 1: *Volcano plot of hydrogen evolution reaction according to Trasatti*[11] *formed by plotting the exchange current density of HER over different metals versus the bond strenght of M-H. Reproduced with from reference under a Creative Commons license* [8]. 4

Figure 2: *Simplified depiction of reduction (A) and oxidation (B) of species A at an electrode. Reproduced from reference*[5] *with permission from John Wiley and Sons. The HOMO and LUMO roughly correspond to* E^0 *of the* A/A^- *and* A^+/A *couple, respectively.* 7

Figure 3: *Depiction of the Grahame model of the electrical double layer with anions (grey) specifically adsorbing to the negatively charged metal surface forming together with adsorbed solvents (empty circles) the inner Helmholtz plane (IHP) and solvated cations forming the outer Helmholtz plane (OHP). Figure was reproduced from reference*[5] *with permission from John Wiley and Sons.* 9

Figure 4: *HER activity of two theoretical catalysts in the same electrolyte illustrating the importance of using overpotential and Tafel slopes in conjunction in the assessment of electrocatalysts. (A) shows linear scanning voltammograms for HER whereas (B) shows the corresponding Tafel plots of the two catalysts. Reprinted with permission from reference* [14]. *Copy right 2014 American Chemical Society.* 15

Figure 5: *Hydrogen evolution activity as a function of hydrogen adsorption free energy. (A) Shows the experimentally obtained volcano relation between* ΔG_{H^*} *and the exchange current density showing Pt with a slightly negative* ΔG_{H^*} *to be most active. (B) shows the corresponding theoretically obtained volcano curve with a maximum at* $\Delta G_{H^*}=0$.[30] *Reprinted with permission from reference* [14]. *Copy right 2014 American Chemical Society.* 17

Figure 6: *Comparison of non-PGM based materials activity towards the acidic HER. Active Pt catalysts usually require an overpotential of around 25mV to reach 10mA* cm^{-2}. *Metal free systems include mostly carbon-based materials such as doped graphene-like systems. Republished with permission of the Royal Society of Chemistry from reference* [38]. 18

Figure 7: *Overview of cell types reported for electrochemical ammonia synthesis. Gibbs energies were calculated using FactSage, in B experimental values were used.* $E^0(O_2+H_2O/OH^-)$ *stems from another study.* E^0_{theory} *was calculated using* $E^0_{theory}=-\Delta_rG/nF$, *with n referring to the number of electrons and F is Faraday's constant. Republished with permission of the Royal Society of Chemistry from reference*[57]. 23

Figure 8: *Overview of rates and current efficiencies for electrochemical ammonia synthesis cells. Ammonia synthesis rate and its current density equivalent are plotted as a function of temperature. Colours represent the current efficiency (here abbreviated as CE) with colder colours indicating higher CE. If no current efficiency was reported circles were coloured grey Republished with permission of the Royal Society of Chemistry from reference*[57]. 24

Figure 9: *Overview of rates and current efficiencies of electrocatalysts for the aqueous nitrogen reduction reaction. Rate is plotted against current efficiency. Labelled data points a), b), c), d),*

e), and f) are referred to in the text. Colour code: Mo (cyan), Ru (green), Au (red), B (grey), Co (blue), C (dark blue), Pd (light red), Ag (dark grey), Cr (orange), Rh (ochre), Nb (light purple), CN (carbon nitride, brown), Ti (purple),V (pink), Fe (dark green), Ni (light brown), and Pt (green-grey). Republished with permission of the Royal Society of Chemistry from reference[57]. 26

Figure 10: *Comparison of HER and NRR limiting –potential (U_L) volcanos for metal (111) facets. HER (blue) and NRR potential (black) are plotted versus the nitrogen binding free energy (ΔG_N) of the respective metal. Reproduced with permission from John Wiley and Sons from reference*[94]. 29

Figure 11: *Schematic depiction of increase in surface free energy and specific activity upon moving towards lower coordination environments. Reprinted with permission from reference*[115]. *Copyright 2013 American Chemical Society.* 31

2 Analytical Techniques 47

Figure 1: *Simplified illustration of destructive interference of X-rays scattered from crystal planes. Reproduced with permission from the Royal Society of Chemistry from reference* [5]. 50

Figure 2: *Graphical illustration of formation and subsequent relaxation of an electron core hole in XPS. Reproduced from reference* [8] *from John Wiley and Sons.* 53

Figure 3: *Basic set-up for XAS measurement in fluorescence mode. Reproduced from reference* [13] *with permission of Cambridge University Press through PLSclear.* 56

Figure 4: Typical X-ray absorption spectrum showing the XANES and EXAFS regions. Reprinted from reference [12] with permission from Elsevier. 57

Figure 5: *Images showing aperture placement for bright field (left) and dark field (right) imaging in TEM mode. Reprinted from reference* [14] *by permission of Springer Nature.* 61

3 Experimental Methods 69

Figure 1: *Custom-made 3D printed dual compartment cell for electrochemical nitrogen reduction experiments. Cell shown assembled and in operation.* 74

Figure 2: *Graphical depiction of second iteration of NRR testing set up (A) and picture of laminated carbon paper electrode used as working electrode (B)* 75

Figure 3: *Graphical depiction of in-situ electrochemical XAFS cell designed for use at Diamond beamline B18, front view (A) and cross-section (B). Figure taken from supplementary information of reference*[3]. *The rights of these images belong to Diamond Light Source Limited. Diamond is a not for-profit limited company funded as a joint venture by the UK Government through the Science & Technology Facilities Council (STFC) in partnership with the Wellcome Trust.* 80

Figure 4: *Pictorial representation of molten salt reactor consisting of a stainless steel vessel (a), split furnace (b), thermocouple in alumina sheath (c), Ag/AgCl reference electrode in closed Pyrex tube(d), working gas electrode (e), counter gas electrode (f), Ar purge and salt addition tube (g), pressure gauge (h), vacuum pump (i), paraffin bubbler (j), acid trap bubbler*

(k), alumina crucible (l), and airtight flask for salt addition (m). Reproduced from reference[10] *with permission from John Wiley and Sons.* 83

Figure 5: *Picture of complete laboratory bench setup.* 84

4 Understanding the Electrocatalytic Activity of Single Metal Atoms on Nitrogen-doped Graphene Support 88

Figure 1: *Pictorial illustration of Co-NG synthesis from Co/GO suspension via freeze-drying and annealing under ammonia flow*..... 91

Figure 2: *X-ray diffraction patterns for atomically dispersed metals on N-graphene and precursors, graphite and graphene oxide. Colour code: Mn-NG (orange), Ru-NG (purple), Cu-NG (cyan), Fe-NG (yellow), Mo-NG (blue),Ni-NG (brown), Co-NG (red), NG (black), graphene oxide (olive) and graphite (grey).* 93

Figure 3: *High-resolution C1s spectra of NG (A), Co-NG (B), Fe-NG (C), Ni-NG (D), Mn-NG (E), Cu-NG (F), Ru-NG (G), and Mo-NG (H). The C1s spectrum of Mn-NG was recorded on a lower resolution machine explaining the lower signal strength. The black line, purple line and empty black circles, respectively represent the overall fit, background, and data points. Colour code: Carbon double bond (red), ether or imine moiety (blue), keto or nitrile moiety (yellow), and* π-π^* *satellite (green).*..... 96

Figure 4: *High-resolution N1s spectra of NG (A), Co-NG (B), Fe-NG (C), Ni-NG (D), Mn-NG (E), Cu-NG (F), Ru-NG (G), and Mo-NG (H). The N1s spectrum of Mn-NG (E) was recorded on a lower resolution machine explaining the lower signal strength. The N1s spectrum of Mo-NG contains contributions from the overlapping Mo3p region. The black line, purple line and empty black circles, respectively represent the overall fit, background, and data points. Colour code: pyridinic N (red), pyrrolic N (blue), quaternary N (yellow), N-oxide (green), and* $Mo3p_{3/2}$ *(grey).*..... 98

Figure 5: *XPS spectra of the metal p or d region of all M-NGs. Cu2p region of Cu-NG (A), Ni2p region of Ni-NG (B), Ru3p region of Ru-NG (C), Mo3d region of Mo-NG (D), Fe2p region of Fe-NG (E), Co2p region of Co-NG (F), and Mn2p of Mn-NG (G). Mn-NG spectrum was recorded on a lower resolution machine explaining the higher noise levels and lower signal strength in its Mn2p spectrum. The black line, purple line and empty black circles, respectively represent the overall fit, background, and data points. Strongly coloured traces represent respective* $p_{3/2}$ *or* $d_{5/2}$ *peaks, whereas faint coloured traces represent corresponding* $p_{1/2}$ *or* $d_{3/2}$ *peaks.* 101

Figure 6: *Bright-field TEM images of Mo-NG (A) and Ru-NG (B). Black lines represent ridges of wrinkles in the N-graphene support whereas dark grey areas represent basal planes of N-graphene.*..... 102

Figure 7: *HAADF-STEM images of Mn-NG (A), Mo-NG (B), Ni-NG (C) and Ru-NG (D) obtained on JEOL ARM200F at magnifications of 10MX (A, B), 25MX (C) and 30MX (D). Bright spots correspond to single metal atoms, grey areas correspond to several layers of N-graphene, darker area represent few layers and black areas show vacuum.* 104

Figure 8: *Cyclic voltammograms of Co-NG upon first immersion into Ar-sparged 0.5M H_2SO_4 measured at 150mV s^{-1} showcasing the activation of the catalyst. The catalyst was cycled from 1V to -0.5V vs RHE. Colour code: Scan 1 (dark blue), following scans going from cyan to light brown.* 106

Figure 9: *Linear scanning voltammograms of M-NGs, NG and Pt/C in Ar sparged 0.5M H_2SO_4 at a scan rate of 5mV s^{-1}. Colour code: Pt/C (grey), Co-NG (red), Ru-NG (purple), Fe-NG (yellow), Ni-NG (brown), Mn-NG (orange), Mo-NG (blue), Cu-NG (cyan), and NG (black).*. 108

Figure 10: *Linear scanning voltammograms of Co-NG in Ar sparged 0.5M H_2SO_4 at a scan rate of 5mV s^{1}. Colour code: Co-NG batch 1 (red) and Co-NG batch 2 (light red).* 109

Figure 11: *Tafel plots of the LSVs of M-NG, NG and Pt/C in Ar sparged 0.5M H_2SO_4 at a scan rate of 5mV s^{-1} showing the overpotential versus the logarithm of the magnitude of the current density (J). Colour code: Pt/C (grey), Co-NG (red), Ru-NG (purple), Fe-NG (yellow), Ni-NG (brown), Mn-NG (orange), Mo-NG (blue), Cu-NG (cyan), and NG (black).* 110

Figure 12: *Extended Tafel plots of the LSVs of M-NG, NG and Pt/C in Ar sparged 0.5M H_2SO_4 at a scan rate of 5mV s^{-1} showing the overpotential versus the logarithm of the magnitude of the current density (J). Colour code: Pt/C (grey), Co-NG (red), Ru-NG (purple), Fe-NG (yellow), Ni-NG (brown), Mn-NG (orange), Mo-NG (blue), Cu-NG (cyan), and NG (black).* 111

Figure 13: *Turn over frequency of M-NG catalysts plotted against overpotential. Colour code: Pt/C (grey dotted line), Co-NG (red), Ru-NG (purple), Fe-NG (yellow), Ni-NG (brown), Mn-NG (orange), Mo-NG (blue), Cu-NG (cyan), and NG (black).* 113

Figure 14: Chronoamperometry of Co-NG in Ar-sparged 0.5M H_2SO_4 at 10mA cm^{-2} (corresponding to 707µA) for 10h. 115

Figure 15: *Scatter plot of overpotential at 10mA cm^{-2} of M-NG catalysts vs phi factor* 117

Figure 16: *Bar chart summarising the initial screening of M-NG catalysts for electrochemical ammonia synthesis in setup one in 0.1M HCl bubbled with N_2 without Nafion in the system. Measurements were carried out for around 1h. Grey dashed horizontal lines indicates rate corresponding to measuring 0.05ppm and black dashed horizontal line indicates rate for the highest measured blank (no catalyst present and no potential applied). Error bars show standard deviation of ammonia quantification using triplicate measurements. Colour code: Dark coloured bars correspond to measurements at -0.25V vs RHE and dashed faint coloured bars correspond to measurements at -0.5V vs RHE.* 120

Figure 17: *Bar chart of Fe-NG catalyst NRR testing including Ar blanks in setup 1 in 0.1M HCl bubbled with N_2 without Nafion in the system. Measurements were carried out for around 1h. Black dashed horizontal line indicates rate for the highest measured blank (no catalyst present and no potential applied). Error bars show standard deviation of ammonia quantification using triplicate measurements. Colour code: Dark coloured bars correspond to measurements at -0.25V vs RHE and faint coloured bars correspond to measurements at -0.5V vs RHE.* 121

5 Active Site Engineering – Tailoring and Probing of Metal Centre Environments in Cobalt-containing Single Atom Catalysts 128

Figure 1: *X-ray diffraction patterns for Co-containing single-atom catalysts and precursors. Colour code: Co-G (olive), Co-NG/N (blue), Co-NG (red), NG (black), graphene oxide (golden), and graphite (brown).* 132

Figure 2: *High-resolution spectra of the Co2p region of Co-NG (A), Co-NG/N (B) and Co-G (C). Colour code: $Co2p_{3/2}$ (red), $Co2p_{3/2}$ satellite (blue), $Co2p_{1/2}$ (yellow), $Co2p_{1/2}$ satellite (green), total fit (black), and measured data (black circles).* 135

Figure 3: *High-resolution C1s spectra of NG (A), Co-NG (B), Co-NG/N (C) and Co-G (D). Colour code: Carbon double bond (red), ether or imine moiety (blue), keto or nitrile moiety (yellow), and π-π^* satellite (green).* 136

Figure 4: *High-resolution spectra of the N1s region of NG (A), Co-NG (B), Co-NG/N (C) and Co-G (D). Colour code: pyridinic N (red), pyrrolic N (blue), quaternary N (yellow), N-oxide (green), nitro moiety (orange), and nitrooxy moiety (pink).* 137

Figure 5: *High-resolution spectra of N1s region of Co-NG before (A) and after acid leaching (B). Colour code: pyridinic N (red), pyrrolic N (blue), quaternary N (yellow), and N-oxide (green). A smaller peak for pyridinic N is observed in comparison to other nitrogen species post acid leaching.* 139

Figure 6: *High-resolution spectra of the Co2p region of Co-NG (A), Co-NG before acid leaching (B), Co-G (C), and Co-G before acid leaching. Colour code: $Co2p_{3/2}$ (red), $Co2p_{3/2}$ satellite (blue), $Co2p_{1/2}$ (yellow), $Co2p_{1/2}$ satellite (green), total fit (black), and measured data (black circles).* 141

Figure 6: *Bright-field TEM image of Co-NG (A) and Co-NG/N (B)* 142

Figure 7: *HAADF images of Co-NG (A), Co-NG/N (B) and Co-G (C) obtained on a JEOL ARM200F* 145

Figure 8: *Bright-field images of Co-NG at a magnification of 10M (A) and 10M (B and C) showing the honeycomb lattice of N-graphene and its layered structure obtained on a JEOL ARM300F* 147

Figure 9: *Higher magnification HAADF images of Co-NG (A, B) obtained after beam showering on JEOL ARM300F* 148

Figure 10: *LSVs of cobalt-containing single-atom catalysts Co-NG, Co-NG/N and Co-G in Ar-sparged 0.5M H_2SO_4 recorded at 5mV s^{-1} normalised to geometric surface area of the working electrode* 150

Figure 11: *Tafel plot of cobalt-containing single-atom catalysts Co-NG, Co-NG/N and Co-G* 151

Figure 12: *Extended Tafel plot of cobalt-containing single-atom catalysts Co-NG, Co-NG/N and Co-G* 152

Figure 13: *ECSA measurement: CVs of Co-NG between -0.2 and -0.1 V vs SCE at different scan rates in Ar-sparged 0.5M H_2SO_4 (A) and the resulting geometrically normalised current densities of positive and negative scans plotted vs scan rate yielding the electrochemical double-layer capacitance as slope (B)* 153

Figure 14: *LSVs of cobalt-containing single-atom catalysts Co-NG, Co-NG/N and Co-G in Ar-sparged 0.5M H_2SO_4 recorded at 5mV s^{-1} normalised to electrochemically active surface area of the electrocatalysts*.....155

Figure 15: *Turn over frequency of Co-containing single-atom catalysts plotted against overpotential* 156

Figure 16: *Poisoning of Co SACs with potassium thiocyante. Dotted lines indicate presence of 27mM KSCN in 0.5M H_2SO_4.*.....158

Figure 17: *Difference spectrum of Co-NG at OCP in the presence of 0.265µM of KSCN* 160

Figure 18: *Overlay of spectra of the C-N stretch region for SCN-poisoned Co-NG, Co-NG/N, Co-G and free KSCN solution*.....161

Figure 19: *Potential dependence of peak height of C-N stretch of SCN^- on Co-NG (red squares), Co-NG/N (blue traces), and Co-G (olive traces) in 0.5M H_2SO_4. The time stamp for the OCP measurements indicate the time when the IR spectra collection was started in relation to the injection of KSCN solution.*.....162

Figure 20: *Fitted difference spectra of CN-stretch of SCN^- on Co-NG (A), Co-NG/N (B), and Co-G (C) at different potentials in 0.5M H_2SO_4. A baseline was fitted using asymmetric least squares smoothing and subtracted from the data. A Voigt profile was used to fit the peaks.*...164

Figure 21: *Change in position of peak maximum of CN-stretch versus potential for SCN^- on Co-NG (A), Co-NG/N (B) and Co-G (C).* 165

Figure 22: *Turn over frequencies of Co SACs normalised by C-N stretching peak area measured during SCN poisoning plotted against overpotential (A) and Overpotential at TOF of 0.1s^{-1} plotted vs peak maximum of CN stretch of adsorbed SCN^- (B). Dotted black line represents a linear fit for the three points and is provided to guide the eye.* 167

Figure 23: *Graphical representation of bound state transitions in first row transition metals. Left side shows energy levels in the ground state. The graphic in the middle illustrates the energy levels after 1s → 4p transition including the core hole. The right graphic illustrates a shakedown feature where an electron is transferred from a ligand orbital to the 3d of the metal. Reprinted from reference [47] with permission from Elsevier.*.....169

Figure 24: *Normalised Co K edge XANES spectra of Co-NG (red), Co-NG/N (blue) and Co-G (olive) in air measured in fluorescence mode.*.....173

Figure 25: *Normalised Co K edge XANES spectra of Co-NG (red), Co-NG/N (blue) and Co-G (olive) in 0.5M H_2SO_4 measured in fluorescence mode. Colour code: Stronger colour indicates more negative potential.*.....174

Figure 26: *Δµ-spectra of Co-NG (red), Co-NG/N (blue) and Co-G (green) obtained by subtracting XANES spectrum at OCP from the XANES spectrum of the dry catalyst.* 175

Figure 27: *Δµ-spectra of Co-NG (A), Co-NG/N (B) and Co-G (C) obtained in Ar-sparged 0.5M H_2SO_4 calculated by subtracting the XANES spectrum at OCP from the spectra outlined in the*

graphs. Colour code, all potentials vs RHE: 0.7V (red), 0.4V (blue), 0.1V (yellow), -0.2V (green), and -0.5V (purple). 177

Figure 28: *Wavelet transform of EXAFS of Co metal foil (A), Co-NG (B), Co-NG/N (C), and Co-G (D), all measured in air. White dashed lines indicate k value for which intensity maxima is reached. The R axis is not phase corrected. Colour code: Warmer colours indicate higher intensity. All Co SACs exhibit only one maximum around 3.3Å^{-1} indicating Co is coordinated to C/N/O and no Co-Co interactions (6.3 Å^{-1}) are present. All wavelets were calculated from 0 to 3Å using k^2 weighting and Morlet parameters of κ=3 and σ=1.* 179

Figure 29: *Overview of wavelet transform of EXAFS of Co SACs in air and at -0.5V vs RHE in 0.5MH_2SO_4. Co-NG in air (A), Co-NG/N in air (B), Co-G in air (C), Co-NG at -0.5V (D), Co-NG/N at -0.5V (E), and Co-G at -0.5V (F).White dashed lines indicate k value for which intensity maxima is reached. The R axis is not phase corrected. Colour code: Warmer colours indicate higher intensity. No Co-Co interactions (6.3 Å^{-1}) are observed for any catalysts. All wavelets were calculated from 0 to 3Å using k^2 weighting and Morlet parameters of κ=3 and σ=1.* 180

Figure 30: *Overview of geometry-optimised DFT structures based on the CoX_4C_{10} active site (X=N, O, C). Co-N_4 (A), Co-C_4 (B), Co-O_4 (C), Co-N_2O_2 across (D), Co-C_2N_2 across(E), Co-C_2O_2 (F), Co-C_2O_2 across (F), Co-N_2O_2 cis-connected via 2 carbons (G), Co-N_3O (H), and Co-N_2O_2 cis-connected via 3 carbons (I). Colour code: CPK with carbon (black), cobalt (pink), nitrogen (blue) and oxygen (red). Hydrogens terminating the 16 outwards facing carbons are not shown.* 182

Figure 31: *Selected Co-X_4C_{10} sites (X=N, O, C) with doubly bonded oxygen axially attached to the cobalt. Co-N_4=O (A), Co-O_4=O (B), Co-C_2N_2=O across (C), Co-N_2O_2=O across (D). Colour code: CPK with carbon (black), cobalt (pink), nitrogen (blue) and oxygen (red). Hydrogens terminating the 16 outward facing carbons are not shown.* 184

Figure 32: *Simulated polarised XANES spectra for Co-N_4-H. Dotted lines show five main features observed in the experimental XANES spectra of Co SACs. Feature d and e were slightly upshifted by 3eV. Colour code: z-polarisation (red) and xy-polarisation (blue).* 185

Figure 33: *Influence of coordination geometry on the 1s → 4p_z + LMCT (feature b). Dotted lines show five main features observed in the experimental XANES spectra of Co SACs. Feature b was slightly upshifted by 2eV. Colour code: Co-N_4 (dark blue), Co-N_4-O_2 (light blue), and Co-N_4-2O_2 (green).* 187

Figure 34: *Influence of oxygen in the first coordination shell on the XANES spectra of square planar Co-X_4C_{10} model active sites. Dotted lines show five main features observed in the experimental XANES spectra of Co SACs. Feature b was slightly upshifted by 2eV. Colour code: Co-N_4 (dark blue), Co-N_3O_1 (light blue), Co-N_2O_2 (light red), and Co-O_4.* 188

Figure 35: *Experimental XANES spectrum of Co-NG catalyst (red) and simulated XANES spectrum of Co-N_4C_{10} model active site (black dots). Vertical dotted lines show four of the five main features observed in the experimental XANES spectra of Co SACs.* 189

Figure 36: *Experimental XANES spectrum of Co-NG/N (blue) and Co-G (olive), as well as simulated XANES spectrum of Co-N_2C_2=O (black dotted) and Co-N_4=O (grey dash-dotted) model active sites. Vertical dotted lines show four of the five main features observed in the experimental XANES spectra of Co SACs.* 190

6 Cobalt Molybdenum Nitride for Electrochemical Nitrogen Reduction in Molten Salts ... 198

Figure 1: *Overview of steps in the synthesis of cobalt molybdenum nitride.* 200

Figure 2: *XRD patterns of Co_3Mo_3N and precursors. Colour code: dried $CoMoO_x$ phase (black), calcined $CoMoO_4$ (grey), and Co_3Mo_3N (red).* 202

Figure 3: *Temperature programmed reduction of Co_3Mo_3N. (A) shows XRD pattern of catalyst before (black) and after (red) TPR under H_2 flow up to 800°C. (B) plots the TCD signal (black) and temperature (blue) vs time for Co_3Mo_3N. Dashed lines indicate onset of signal in TCD.* . 204

Figure 4: *High-resolution Co2p spectra of Co_3Mo_3N before (A) and after removal of top oxide layer with Ar sputtering (B). Colour code: metallic $Co2p_{3/2}$ (red), +II $Co2p_{3/2}$ (blue), +III $Co2p_{3/2}$ (yellow),+II $Co2p_{3/2}$ satellite (green). The black line, purple line and empty black circles, respectively represent the overall fit, background, and data points. Faint coloured traces represent corresponding $Co2p_{1/2}$ peaks.* 206

Figure 5: *High-resolution Mo3d spectra of Co_3Mo_3N before (A) and after removal of top oxide layer with Ar sputtering (B). Colour code: metallic $Mo3d_{5/2}$ (red), +IV $Mo3d_{5/2}$ (blue), +V $Mo3d_{5/2}$ (yellow),+VI $Mo3d_{5/2}$ (green). The black line, purple line and empty black circles, respectively represent the overall fit, background, and data points. Faint coloured traces represent corresponding $Mo3d_{3/2}$ peaks.* 208

Figure 6: *High-resolution Mo3p/N1s spectra of Co_3Mo_3N before (A) and after removal of top oxide layer with Ar sputtering (B). Colour code: metallic $Mo3p_{3/2}$ (red), +V $Mo3p_{3/2}$ (blue), and N1s (yellow). The black line, purple line and empty black circles, respectively represent the overall fit, background, and data points. Faint coloured traces represent corresponding $Mo3p_{1/2}$ peaks.* 209

Figure 7: *High-resolution O1s spectra of Co_3Mo_3N before (A) and after removal of top oxide layer with Ar sputtering (B). The black line, purple line and empty black circles, respectively represent the overall fit, background, and data points. Colour code: metal oxide (red) and C-O/metal hydroxide (blue).* 211

Figure 8: *Bright-field TEM micrograph of Co_3Mo_3N powder at 40000X magnification.* 213

Figure 9: *Pictorial overview of electrochemical testing of Co_3Mo_3N in Li-K-Cl eutectic at 450°C. A carbon rod was used as counter electrode while a Ag/AgCl electrode consisting of a silver wire in a closed Pyrex tube containing 0.05mol% AgCl in Li-K-Cl eutectic was employed as the reference electrode. The working electrode was prepared by fixing a Co_3Mo_3N pellet between sheets of carbon felt connected to the potentiostat by a nickel wire. Argon or dinitrogen were flown over the working electrode at 20mL min^{-1}.* 216

Figure 10: *XPS spectra of Co2p region of Co_3Mo_3N as-prepared (A), at OCP (B), at 0.35V vs Li^+/Li under Ar flow (C), and at 0.35V vs Li^+/Li under N_2 flow (D). Colour code: +II $Co2p_{3/2}$*

(red), and +II $Co2p_{3/2}$ satellite (blue). The black line, purple line and empty black circles, respectively represent the overall fit, background, and data points. Faint coloured traces represent corresponding $Co2p_{1/2}$ peaks. 218

Figure 11: *XPS spectra of Mo3d region of Co_3Mo_3N as-prepared (A), at OCP (B), at 0.35V vs Li^+/Li under Ar flow (C), and at 0.35V vs Li^+/Li under N_2 flow (D). Colour code: metallic $Mo3d_{5/2}$ (red), and +V $Mo3d_{5/2}$ (blue). The black line, purple line and empty black circles, respectively represent the overall fit, background, and data points. Faint coloured traces represent corresponding $Mo3d_{3/2}$ peaks.* 219

Figure 12: *XRD patterns of Co_3Mo_3N pellets before and after exposure to Li-K-Cl melt under different conditions. Colour code: as-prepared Co_3Mo_3N (red), Co_3Mo_3N after melt at OCP and Ar flow (blue), Co_3Mo_3N after melt at 0.35 vs Li^+/Li and Ar flow (yellow), and Co_3Mo_3N after melt at 0.35 vs Li^+/Li and N_2 flow (green). Reflections of the Co_3Mo_3N phase (•), as well as impurities/ reaction products including Mo_2N (▼), Mo (*), Co (◊), and Li-K-Cl (•) are labelled using symbols.* 221

Figure 13: *Bar chart of total amounts of ammonia detected during experiments in molten Li-K-Cl at 450°C. Striped bars indicate application of 0.35V vs Li^+/Li to the working electrode during the experiment. Number of moles detected in post-reactor acid trap and in the melt were combined, a total of three measurements, to obtain the total amount of ammonia. Error bars correspond to a typical measurement error of 0.05ppm in each of the three ammonia measurements.* 224

Figure 14: Current densities recorded for CF (black trace) and Co_3Mo_3N with CF (green) at 0.35V vs Li^+/Li under N_2 flow in molten Li-K-Cl eutectic at 450°C. 225

Figure 15: *Simplified reaction scheme for Eley-Rideal/Mars-van Krevelen type associative mechanism. Reaction starting point is marked with an asterisk. Reproduced from reference [7] – published by the Royal Society of Chemistry.* 229

7 Conclusions and Outlook 235

8 Appendix 241

Figure A1: *Wavelet transform of EXAFS of Fe metal foil (A), and Fe-NG (B) all measured in air. The R axis is not phase corrected. Colour code: Warmer colours indicate higher intensity. Only one energy maximum is found for Fe-NG(B) at around 3-4 k and 1.4R which is significantly lower than the maximum observed for Fe metal conclusively showing that no iron-iron interactions are present in Fe-NG and as such Fe is atomically dispersed.* 241

Figure A2: *Comparison of calibration curves for ammonia detection with the salicylate method using a well-plate (A) and using cuvettes (B).* 242

List of Tables

1 Introduction 1

2 Analytical Techniques 47

3 Experimental Methods 69

4 Understanding the Electrocatalytic Activity of Single Metal Atoms on Nitrogen-doped Graphene Support 88

Table 1: *Overview of elemental compositions of NG and M-NG catalysts. *0.64at% of Cl were detected as well. ** N1s region of Mo-NG contains small contributions from Mo3p.* 101

5 Active Site Engineering – Tailoring and Probing of Metal Centre Environments in Cobalt-containing Single Atom Catalysts 128

Table 1: *Overview of synthesis conditions used to prepare Co-NG, Co-NG/N and Co-G* 131

Table 2: *Summary of composition of acid leached Co SACs in atomic % as determined by XPS* 133

Table 3: *Total nitrogen content and distribution of nitrogen species in Co-NG before and after acid leaching* 139

Table 4: *Cobalt content determined by XPS in Co-NG and Co-G before and after acid leaching step* 141

Table 4: *Summary of electrochemical double-layer capacitance and ECSA for Co-NG, Co-NG/N and Co-G measured in 0.5M H_2SO_4* 153

Table 5: *Features observed in XANES of cobalt-containing single atom catalysts, assignment based on reference[50]. LMCT is short for ligand-to-metal charge transfer.* 173

6 Cobalt Molybdenum Nitride for Electrochemical Nitrogen Reduction in Molten Salts 198

Table 1: *Overview of elemental composition of Co_3Mo_3N powder and Co_xMo_yN/CF deduced from XPS survey scans. Nitrogen content not shown due to the overlap of the N1s and Mo3p region prohibiting its unambiguous quantification using XPS survey scans.* 212

Table 2: *Comparison of ammonia synthesis rate of Co_3Mo_3N catalysts from this work and literature reports.* 214

Table 3: *Overview of electrochemical conditions used to test stability and NRR activity of Co_3Mo_3N at 450°C. Gases were flown at 20mL min^{-1} over the working electrode while 350mL min^{-1} Ar were supplied via the purge line.* 217

Table 4: *Overview of cobalt to molybdenum ratio of Co_3Mo_3N under different conditions.* 220

7 Conclusions and Outlook 235

8 Appendix 241

Table of contents

Acknowledgments i

Abstract iii

List of Abbreviations iv

List of Publications vii

List of Figures viii

List of Tables xvii

Table of contents xviii

1 Introduction 1

1.1 Electrocatalysis 2

1.1.1 Background 2

1.1.2 Mass Transport 3

1.1.3 Adsorption and Chemical Reactions 3

1.1.4 Charge Transfer 5

1.2 Hydrogen Evolution Reaction 10

1.2.1 Hydrogen - A Feedstock Chemical and Energy Vector 10

1.2.2 Reaction Mechanism 12

1.2.3 Activity Parameters 13

1.2.4 Descriptors 15

1.2.5 Catalyst Development 17

1.3 Electrochemical Ammonia Synthesis 19

1.3.1 Ammonia – An important Chemical and potential Energy Vector 19

1.3.2 Nitrogen Reduction Reaction 21

1.4 Electrocatalysts 29

1.4.1 Single-atom Catalysts 29

1.4.2 Metal Nitrides 33

1.5 Aims and Objectives 35

1.6 Thesis Overview 36

1.7 References 37

2 Analytical Techniques 47

2.1 Introduction 48
2.2 X-ray Diffraction 49
2.3 X-ray Photoelectron Spectroscopy 52
2.4 X-ray Absorption Spectroscopy 55
2.5 Transmission Electron Microscopy 59
2.6 Infrared Spectroscopy 62
2.7 Electrochemical Techniques 65
2.8 References 67
3 Experimental Methods 69
3.1 Characterisation 70
3.1.1 XRD 70
3.1.2 XPS 70
3.1.3 TEM 71
3.1.4 STEM 71
3.2 Catalyst Testing in Aqueous Media 71
3.2.1 HER Activity Testing 71
3.2.2 NRR Activity Screening 73
3.2.3 Ammonia Detection 75
3.2.4 In-situ IR Spectroelectrochemistry 77
3.2.5 In-situ XAS Spectroelectrochemistry 79
3.3 Experiments in Molten Salts 81
3.3.1 Experimental Setup 81
3.3.2 Salt Preparation 84
3.3.3 Electrochemistry in Molten Salts 85
3.3.4 Ammonia Detection 86
3.4 References 86
4 Understanding the Electrocatalytic Activity of Single Metal Atoms on Nitrogen-doped Graphene Support 88
4.1 Background and Objectives 89
4.2 Synthesis 89
4.2.1 Graphene Oxide 89

4.2.2 Single Metal Atoms on Nitrogen-doped Graphene 90
4.3 Characterisation 92
4.3.1 XRD 92
4.3.2 XPS 93
4.3.3 TEM 102
4.3.4 STEM 102
4.4 Hydrogen Evolution Reaction 105
4.4.1 Experimental Methods 105
4.4.2 Results and Discussion 105
4.4.3 Correlation with Theory 115
4.5 Electrochemical Ammonia Synthesis 118
4.5.1 Experimental Methods 118
4.5.2 Ammonia Detection 118
4.5.3 Results and Discussion 119
4.6 Conclusions 122
4.7 References 124
5 Active Site Engineering – Tailoring and Probing of Metal Centre Environments in Cobalt-containing Single Atom Catalysts 128
5.1 Background and Objectives 129
5.2 Synthesis 130
5.3 Characterisation 131
5.3.1 XRD 131
5.3.2 XPS 132
5.3.3 TEM 142
5.3.4 STEM 142
5.4 Hydrogen Evolution Reaction 149
5.4.1 Experimental Methods 149
5.4.2 Results and Discussion 149
5.5 In-situ Infrared Spectroelectrochemistry 156
5.5.1 Background 156
5.5.2 Experimental Methods 158
5.5.3 Results and Discussion 159

5.6 In-situ X-ray Absorption Spectroscopy 168
5.6.1 Background 168
5.6.2 Experimental Methods 170
5.6.3 Results and Discussion 171
5.7 XANES Modelling 181
5.7.1 Geometry Optimisation with Dmol3 181
5.7.2 Confirmation of Peak Assignment using FEFF9 184
5.7.3 The Effect of Coordination Sphere Composition and Geometry on XANES spectra assessed using CASTEP 186
5.8 Conclusions 191
5.9 References 193
6 Cobalt Molybdenum Nitride for Electrochemical Nitrogen Reduction in Molten Salts 198
6.1 Background and Objectives 199
6.2 Synthesis 200
6.2.1 Powder 200
6.3 Characterisation 201
6.3.1 XRD 201
6.3.2 TPR 202
6.3.3 XPS 205
6.3.4 TEM 212
6.4 Thermal Ammonia Synthesis 213
6.4.1 Experimental Methods 213
6.4.2 Results and Discussion 213
6.5 Nitrogen Reduction Reaction Testing 214
6.5.1 Experimental Methods 214
6.5.2 Results and Discussion 217
6.6 Conclusions 229
6.7 References 231
7 Conclusions and Outlook 235
7.1 Conclusions 236
7.2 Outlook 238

7.3 References 240
8 Appendix 241
8.1 References 247

1 Introduction

1 Introduction 1
1.1 Electrocatalysis 2
1.1.1 Background 2
1.1.2 Mass Transport 3
1.1.3 Adsorption and Chemical Reactions 3
1.1.4 Charge Transfer 5
1.1.4.1 The Electrochemical Potential 5
1.1.4.2 Capacitance and the Electrical Double Layer 7
1.1.4.3 Electrode Kinetics 9
1.2 Hydrogen Evolution Reaction 10
1.2.1 Hydrogen - A Feedstock Chemical and Energy Vector 10
1.2.2 Reaction Mechanism 12
1.2.3 Activity Parameters 13
1.2.4 Descriptors 15
1.2.5 Catalyst Development 17
1.3 Electrochemical Ammonia Synthesis 19
1.3.1 Ammonia – An important Chemical and potential Energy Vector 19
1.3.2 Nitrogen Reduction Reaction 21
1.3.2.1 Aqueous and low temperature NRR 24
1.3.2.2 NRR in Molten Salts 26
1.3.2.3 Challenges 28
1.4 Electrocatalysts 29
1.4.1 Single-atom Catalysts 29
1.4.1.1 Background 29
1.4.1.2 Synthesis 31
1.4.2 Metal Nitrides 33
1.4.2.1 Background 33
1.4.2.2 Synthesis 35
1.5 Aims and Objectives 35
1.6 Thesis Overview 36
1.7 References 37

1.1 Electrocatalysis

1.1.1 Background

Human made climate change caused by the excessive emission of carbon dioxide and other greenhouse gases is threatening the livelihood of the majority of humankind and is viewed as the defining challenge of the 21st century.[1] In order to limit global warming to 2°C or lower as per the Paris Agreement, CO_2 emissions must be lowered by a significant amount quickly and eventually will have to reach net zero.[1] Combustion of fossil fuels, in energy provision, transport and the chemical industry, is the main source of anthropogenic CO_2.[2] Alternatively, renewable energy sources such as wind and solar, can provide carbon-free energy in the form of electricity but do require efficient short- and long-term energy storage due to their intermittent nature. Furthermore, currently many processes in the chemical industry require energy input in the form of heat or chemical feedstocks (often hydrogen).[3] To replace fossil fuels with renewable power sources in the mentioned sectors, novel ways to store electrons and to transform electrical energy into fuels and chemical commodities are desperately needed.[3,4] At the forefront of the search for such technologies lays the field of electrocatalysis.

Electrocatalysis refers to processes that interconvert chemical and electrical energy using homogenous or heterogeneous catalysts. In such systems a reduction reaction is coupled with an oxidation reaction requiring two different surfaces, i.e. electrodes, connected electrically by e.g. a metal wire and via an ionically conductive medium, i.e. the electrolyte often based on solutions containing dissolved ions or solids allowing ion conduction.[5] In this thesis we will focus on heterogeneous electrocatalysis and as such will be concerned with catalytic processes at the electrode/ electrolyte interface. The rate

of such an electrochemical reaction is affected by several different steps including mass transport, adsorption and chemical reaction, as well as charge transfer.

1.1.2 Mass Transport

Mass transport describes the movement of species within a medium, here a solution. It occurs via three main mechanisms: migration, diffusion, and convection.[5] Migration refers to the displacement of charged species due to a gradient of electrical potential across the solution whereas diffusion relates to the statistical movement of species due to a difference in chemical potential, i.e. concentration gradient.[5] Convection can be separated into natural, occurring due to a density gradient, and forced, i.e. stirring, pumping etc.[6] Usually, in electrocatalytic testing the effect of mass transport is minimised to prevent it from being rate-limiting so that reactions at the electrode surface can be probed. Different hydrodynamic techniques are available to ensure sufficient transfer of reactants to as well as transporting products away from the electrode including amongst others rotating disk electrodes, wall jet electrodes and gas electrodes. Furthermore, reactants are often present in the electrolyte in high concentrations, such as protons in acidic electrolytes for the hydrogen evolution reaction (HER), providing ample amounts of reactant at any time to prevent mass transport limitations.

1.1.3 Adsorption and Chemical Reactions

In contrast to mass transport, adsorption phenomena and other surface based chemical reactions often exhibit a strong sensitivity to the electronic structure of the surface.[5] Adsorption and desorption, here understood as the formation/breaking of covalent bonds of the reactants/products with the electrode surface, are often critical for electrocatalytic reactions.[5] Figure 1 illustrates this for the hydrogen evolution reaction plotting the logarithm of the exchange current density, an indicator of the rate, of different metals

against the bond strength of M-H of the respective metal. A maximum is observed at around 60kcal mol^{-1} with platinum sitting atop the curve. This is effectively a demonstration of the Sabatier principle which states that the interaction between surface and reactants should not be too weak since otherwise no binding and hence no reactions occur but also not too strong since otherwise products will not desorb and the catalyst surface will be poisoned.[7] For metals with M-H bond strength below 60kcal mol^{-1} hydrogen binding is too weak whereas for the other metals the surface gets covered in H_{ad} largely preventing efficient H_2 evolution. Similar relations are found for many other electrocatalytic processes.[8–10]

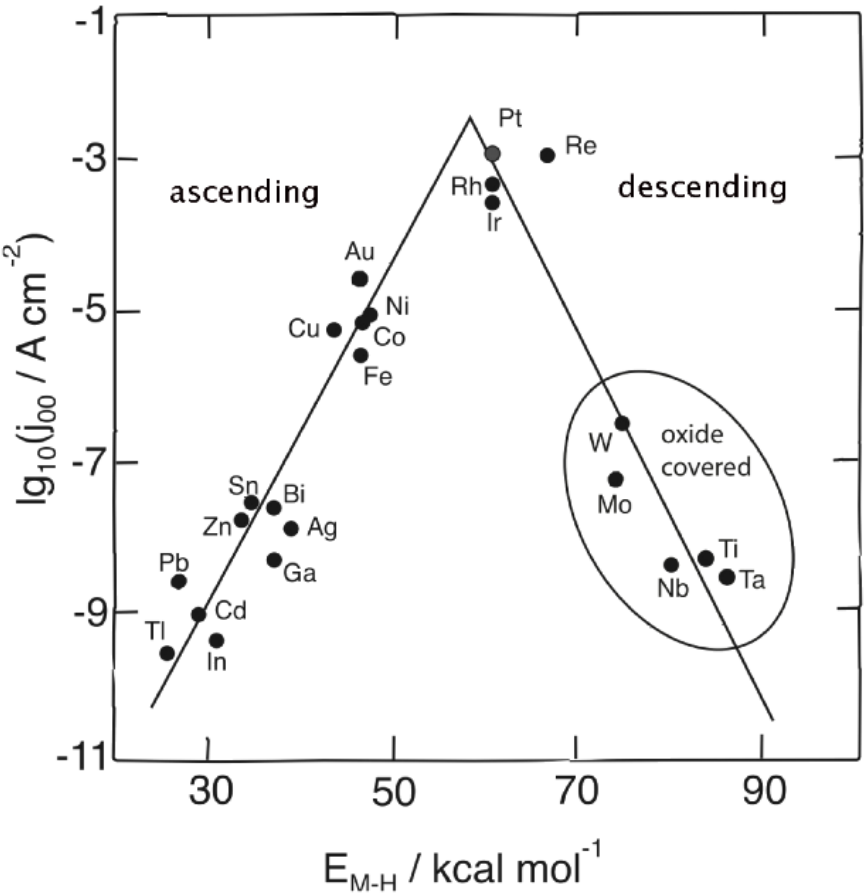


Figure 1: *Volcano plot of hydrogen evolution reaction according to Trasatti*[11] *formed by plotting the exchange current density of HER over different metals versus the bond strenght of M-H. Reproduced with from reference under a Creative Commons license* [8].

1.1.4 Charge Transfer

1.1.4.1 The Electrochemical Potential

The charge transfer between electrocatalyst and adsorbed reactant is governed by the electrochemical potential. In contrast to thermal catalysis where heat is utilised here the electrochemical potential provides the driving force to overcome the activation energy barrier.

The electrochemical potential ($\tilde{\mu}_B$) is defined as the partial molar Gibbs energy of a substance (B) in a specified phase (α) at a specified potential.[12] It can be calculated by adding the term $z_B F\Phi^\alpha$ to the chemical potential (Eq. 1), where z_B is the charge of species B, F is the Faraday constant, μ_B is the chemical potential of species B in α and Φ^α is the inner potential, defined as the work needed to bring a charge from infinity into phase α.

$$\tilde{\mu}_B^\alpha = \mu_B^\alpha + z_B F \Phi^\alpha \qquad \text{(Eq.1)}$$

By expressing the chemical potential of phases α and β in terms of the standard chemical potential the condition for chemical equilibrium between phases α and β can be defined (Eq.2).

$$\tilde{\mu}_B^\alpha - \tilde{\mu}_B^\beta = \mu_B^{\alpha 0} - \mu_B^{\alpha 0} + RT ln\left(\frac{a_B^\alpha}{a_B^\beta}\right) + z_B F(\Phi^\alpha - \Phi^\beta) \stackrel{\text{def}}{=} 0 \qquad \text{(Eq.2)}$$

Equation 2 can then be simplified by defining the difference of inner potentials as E and the difference of standard chemical potentials as the standard electrode potential E^0 yielding the Nernst equation (Eq.3).

$$E = E^0 + \frac{RT}{z_B F} ln\left(\frac{a_B^\alpha}{a_B^\beta}\right) \qquad \text{(Eq.3)}$$

The Nernst equation relates the difference in electrical potential to the activity of its components and can be expressed in more general terms substituting the activity for concentration (c) and stoichiometric numbers (v) and using the formal potential ($E^{0'}$) which is a slight function of the components of the electrolyte (Eq.4).

$$E = E^{0\prime} + \frac{RT}{z_B F} \sum_i v_i \, ln\left(\frac{c_i}{c^0}\right) \qquad \text{(Eq.4)}$$

Using the Nernst equation, the equilibrium potential (i.e. open-circuit potential) of an electrode can be determined given that the concentrations of both redox species of the potential setting couple are known.

Figure 2 provides a simplified depiction of the effect of changing the energy level of electrons in an electrode (i.e. Fermi level) by applying an external electrical potential. If a reducing potential is applied the energy level of electrons is increased and reaching levels high enough electrons are donated into vacant orbitals in solution (Fig.2.A). When an oxidising potential is applied the electron energy level is lowered and if it falls below occupied solution states electron transfer to the electrode can occur (Fig.2.B). The potential at which the reduction or oxidation occurs is related to the standard potential (E^0) of the specific substance in solution.[5] As such when all concentrations are known the Nernst equation can be used to calculate the thermodynamic potential required to induce a reduction or oxidation reaction at an electrode.[5,6] The simple picture in Figure 2 is a good description of fast (i.e. reversible) systems. Slow (i.e. irreversible) reactions often require a significant overpotential (η) with no electron transfer occurring at the thermodynamic potential.[6] The overpotential is defined as the applied potential needed to achieve a certain amount of charge transfer minus the thermodynamic potential (E-

E_{eq}).[6] The relationship between overpotential and current density is further explored in the Section 1.4.3.

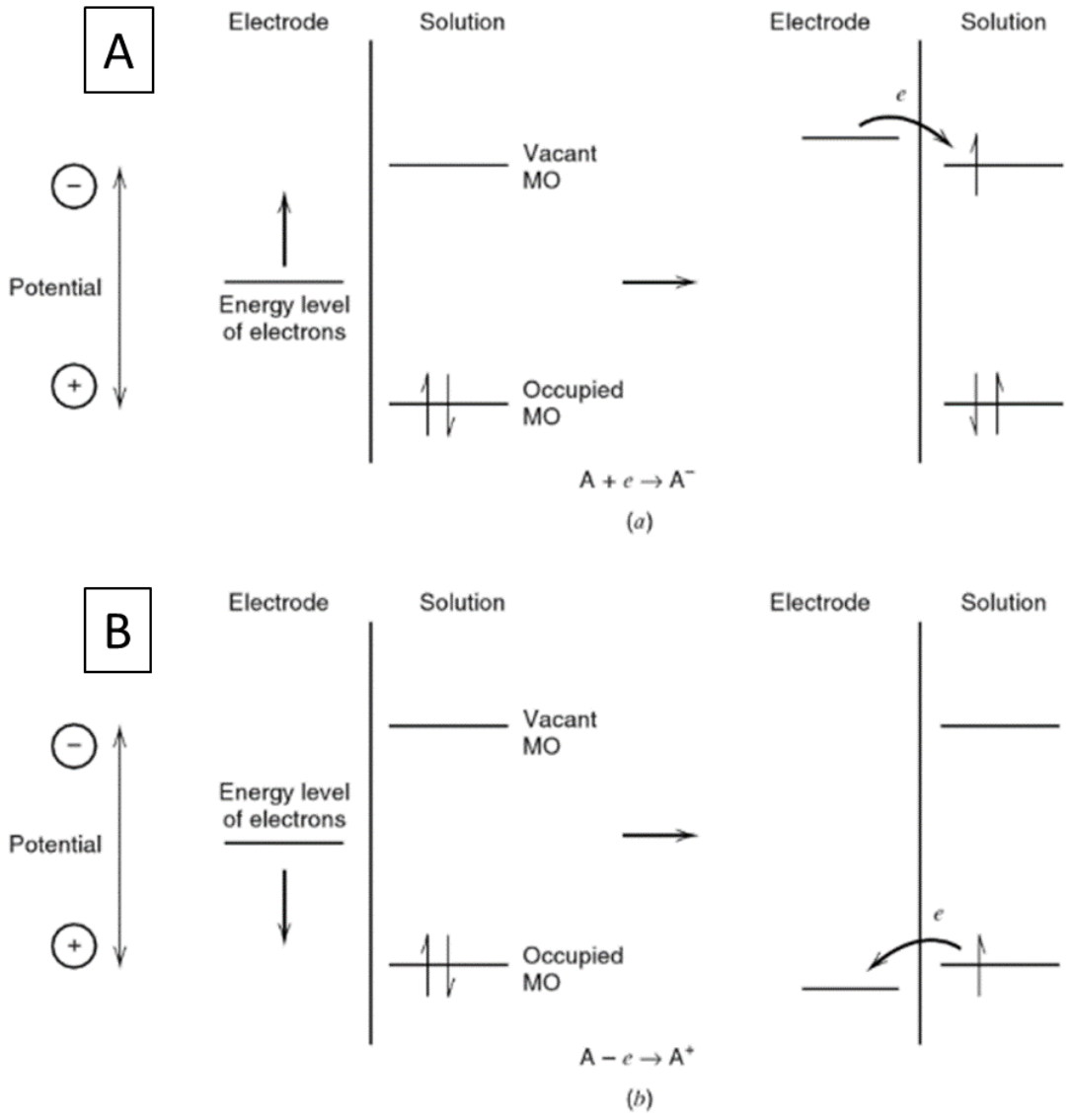


Figure 2: *Simplified depiction of reduction (A) and oxidation (B) of species A at an electrode. Reproduced from reference*[5] *with permission from John Wiley and Sons. The HOMO and LUMO roughly correspond to* E^0 *of the* A/A^- *and* A^+/A *couple, respectively.*

1.1.4.2 Capacitance and the Electrical Double Layer

Generally, surfaces in electrolytes are slightly charged due to charge separation events at the surface.[5] This leads to the reorientation of solvent molecules and ionic species at the

surface effectively storing electrical potential energy without charge transfer and is known as capacitance.[5] This behaviour is illustrated in Figure 3 for a negatively charged electrode surface. The first layer of adsorbates is believed to consist of solvent molecules, as well as specifically adsorbing anions and defined as the inner Helmholtz plane (IHP). The second layer is formed by solvated cations and referred to as the outer Helmholtz plane (OHP). The Stern model only considers a layer of solvent as the inner Helmholtz plane and describes the potential as dropping linearly from the electrode surface to the outer Helmholtz layer.[5] In reality some anions can lose their solvation shell and become specifically adsorbed to the electrode surface leading to significant disturbance of the potential resulting in highly nonlinear behaviour.[5] Specific adsorption is generally believed to be limited to anions due to their weaker solvation resulting from their larger size.[5] The double layer capacitance scales with the surface area of the electrode exposed to the electrolyte and is often used to experimentally determine the so called electrochemically active surface area (ECSA) which is sometimes used as a measure of active site density of an electrocatalyst.[5,13,14]

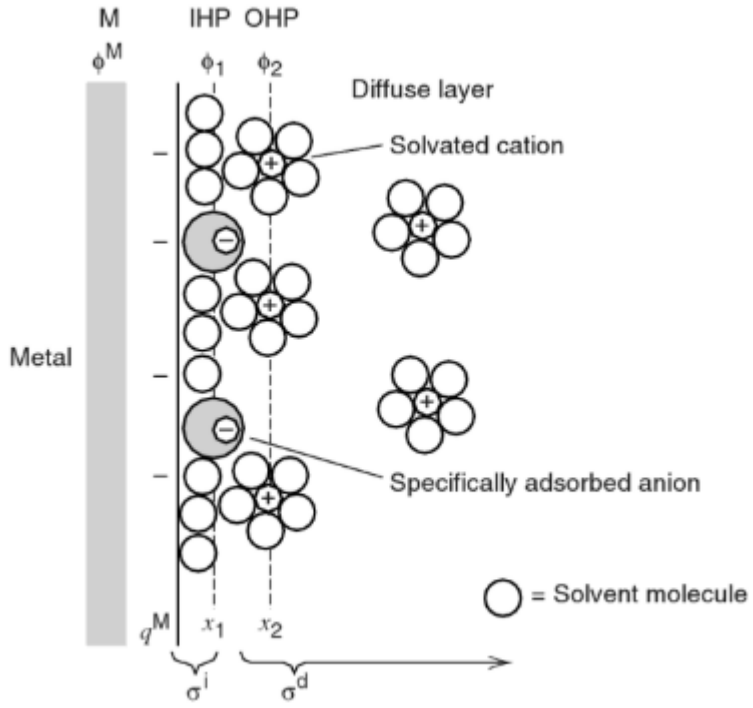


Figure 3: *Depiction of the Grahame model of the electrical double layer with anions (grey) specifically adsorbing to the negatively charged metal surface forming together with adsorbed solvents (empty circles) the inner Helmholtz plane (IHP) and solvated cations forming the outer Helmholtz plane (OHP). Figure was reproduced from reference*[5] *with permission from John Wiley and Sons.*

1.1.4.3 Electrode Kinetics

The dependence of the current on the electrical potential is given by the Butler-Volmer equation (Eq.5).

$$j = j_0 \cdot \left\{ \exp\left[\frac{\alpha_a z F \eta}{RT}\right] - \exp\left[-\frac{\alpha_c z F \eta}{RT}\right] \right\} \qquad \text{(Eq.5)}$$

Where j is the current density, j_0 is the exchange current density which is the magnitude of the anodic and cathodic current densities at the equilibrium which have opposite signs, α_a is the anodic transfer coefficient, α_c is the cathodic transfer coefficient, z is the number of electrons involved, F is the Faraday constant, R is the universal gas constant and η is the overpotential. The transfer coefficients α_a and α_c can be determined experimentally

and are usually found to be close to 0.5.[5,6] This equation strictly only holds for one-electron transfer reactions where α_a plus α_c equals one.[6]

For large overpotentials the Butler-Volmer equation simplifies to the Tafel equation, here shown for a cathodic reaction (Eq.6):

$$\eta = \frac{2.3RT}{\alpha_c nF} log j_0 + \frac{2.3RT}{\alpha_c nF} log j \qquad \text{(Eq.6)}$$

This relationship was first found empirically before its theoretical underpinnings were shown.[6] It can be used to obtain the exchange current density and the Tafel slope from linear scanning voltammograms. This is done by plotting the overpotential versus the logarithm of the magnitude of the current density and fitting an equation of the type shown in Equation 7 to the linear parts of the asymptotes, where b is the Tafel slope and a can be used to extract the exchange current density.

$$\eta = a + b \, log \, j \qquad \text{(Eq.7)}$$

The Tafel slope is an important parameter to compare activities of catalyst for the HER and other reactions, further discussed in Section 2.3.[14]

1.2 Hydrogen Evolution Reaction

1.2.1 Hydrogen - A Feedstock Chemical and Energy Vector

H_2 is an important feedstock chemical and a crucial reactant in many large-scale industrial processes such as the production of ammonia and methanol.[4,15] It has also been suggested as one of only few carbon-free energy carriers with the potential to decarbonise the energy and chemical industries, as well as the transport sector.[15–17] Hydrogen can be used as fuel for fuel cells converting its chemical energy into electricity at high efficiencies of above

40%. Technologies and products based on this are already commercially available today, such as fuel cell powered cars, although usually not at equivalent cost to fossil fuel based systems.[15]

Globally around 65 million tons of H_2 are produced annually with the majority stemming from steam methane reforming (SMR). In this process methane from natural gas and water are converted to dihydrogen and carbon monoxide at temperatures and pressures of up to 800°C and 25bar.[18] Via the water-gas shift reaction, carbon monoxide is reacted to further dihydrogen and carbon dioxide.[19] As such, present H_2 production contributes significantly to anthropogenic CO_2 emissions.

Water electrolysis presents another way of producing dihydrogen by electrochemically splitting water into H_2 and O_2. If powered by renewable energies this provides an attractive way to produce H_2 without carbon emissions, as well as presenting an opportunity to store and commodify intermittent renewable power sources, such as wind and solar. To date, water electrolysis only accounts for around 4% of total hydrogen production, largely due to the relatively low price of natural gas and the high capital expenditure costs (CAPEX) for electrolysers.[20,21] The main cost points in alkaline electrolysers is the hydrogen evolution electrocatalyst material, whereas in polymer electrolyte membrane electrolysers (PEM) this is less pronounced.[22] The hydrogen evolution catalysts are usually based on platinum due to its superior activity although its high cost and low natural abundance require the development of novel earth-abundant electrocatalysts for HER to further bring down the costs of electrolysers and enable large-scale deployment. Sections 2.2-5 discuss the reaction mechanism, activity parameters, descriptors, as well as ongoing advancements in the discovery of non-platinum group metal (non-PGM) hydrogen evolution electrocatalysts.

1.2.2 Reaction Mechanism

The hydrogen evolution reaction is one of the most studied reactions in electrochemistry and involves the transfer of two electrons to reduce two protons forming dihydrogen (Eq.8).

$$2H^+ + 2e^- \rightarrow H_2 \quad \text{(Eq.8)}$$

It is thought to operate via two of three possible reaction steps (Eq.9-11).

$$H^+ + e^- \rightarrow H_{ad} \quad \text{(Eq.9)}$$

$$H_{ad} + H^+ + e^- \rightarrow H_2 \quad \text{(Eq.10)}$$

$$H_{ad} + H_{ad} \rightarrow H_2 \quad \text{(Eq.11)}$$

The initial electron-coupled proton adsorption (Eq.9) is known as the Volmer step and has to occur for all catalysts. The formation and subsequent desorption of H_2 can proceed via two different mechanisms: the Heyrovsky step (Eq.10) or the Tafel step (Eq.11). In the Heyrovsky mechanism a previously formed adsorbed hydrogen atom reacts with a proton from the electrolyte to form H_2 in an electron transfer-coupled step. Counter to that, the Volmer step describes the chemical recombination of two adjacent previously formed adsorbed hydrogen atoms releasing H_2. Hence, HER can occur either via a Volmer-Heyrovksy or Volmer-Tafel mechanism. Several theoretical reports have linked the magnitude of the Tafel slope, obtained by plotting the overpotential η versus the logarithm of the magnitude of the current density, to the rate limiting step in hydrogen evolution and other electrocatalytic reactions. HER Tafel slopes of around 30mV dec^{-1}, 40mV dec^{-1} and 120mV dec^{-1} have been suggested to be evidence for the Tafel, Heyrovsky or Volmer step, respectively, to be rate limiting.[23] As such, Tafel analysis

provides a tool to gain initial insight into the reaction mechanisms at play. Although, it has to be noted that there is significant disagreement in the field about the applicability of Tafel analysis to reaction mechanisms and the exact meaning of the magnitude of Tafel slopes.[23–26] In order to be able to make strong claims it is advised to conduct additional kinetic studies and theoretical modelling.[14,25–27]

1.2.3 Activity Parameters

In literature, HER activity is assessed in many different ways quoting various figures of merit which can make comparison among catalysts difficult.[14] One of the most popular techniques in HER testing is linear scanning voltammetry (LSV) which, when performed at slow enough scan rates, provides an approximation of steady-state currents at various potentials (Fig.4.A). Normalisation to geometric surface area to obtain current densities is important in such measurements to enable a comparison to other in literature reported electrodes. One often used metric which can also be extracted form a LSV curve is the overpotential needed to reach a current density of 10mA cm^{-2}. A current density of 10mA cm^{-2} was chosen because it corresponds to the calculated current density of a solar-to-hydrogen device with an efficiency of 12.3%.[10,14,28] A device of such efficiency is suggested to be cost competitive with other hydrogen production methods.[14,29]

Overpotential at 10mA cm^{-2} alone is not a sufficient parameter to describe HER activity over a wide range of potential as shown in Figure 4. Two theoretical catalysts are shown with the same overpotential at 10mA cm^{-2} with largely varying characteristics (Fig.4.A). The first catalysts (blue trace) exhibits an early onset of catalytic current but performs badly at more negative potentials. In contrast, the second catalyst (red trace) shows a delayed onset of hydrogen evolution but exhibits higher current densities at more reducing potentials. Use of the Tafel slopes (Fig.4.B) can help to describe this behaviour,

with low slopes indicating that after HER onset activity increases quickly whereas large slopes indicate sluggish behaviour after the onset of hydrogen evolution.

Both Tafel slope and overpotential at specific geometric current densities measure the total activity meaning the number of active sites and their intrinsic activities are entangled. Using estimates for the number of active sites per electrode area the intrinsic activity of an active site can be determined, usually given as the turn over frequency (TOF). The TOF is expressed in s^{-1} and describes the number of product molecules produced per active site per second. Comparison of TOF values across catalysts is pivotal to gain a deeper understanding of the factors governing HER activity and to rationally design novel electrocatalysts. The determination of active sites and their density can be highly challenging and is further discussed in Chapter 4 Section 5.2 and Chapter 5 Section 5.2-6.

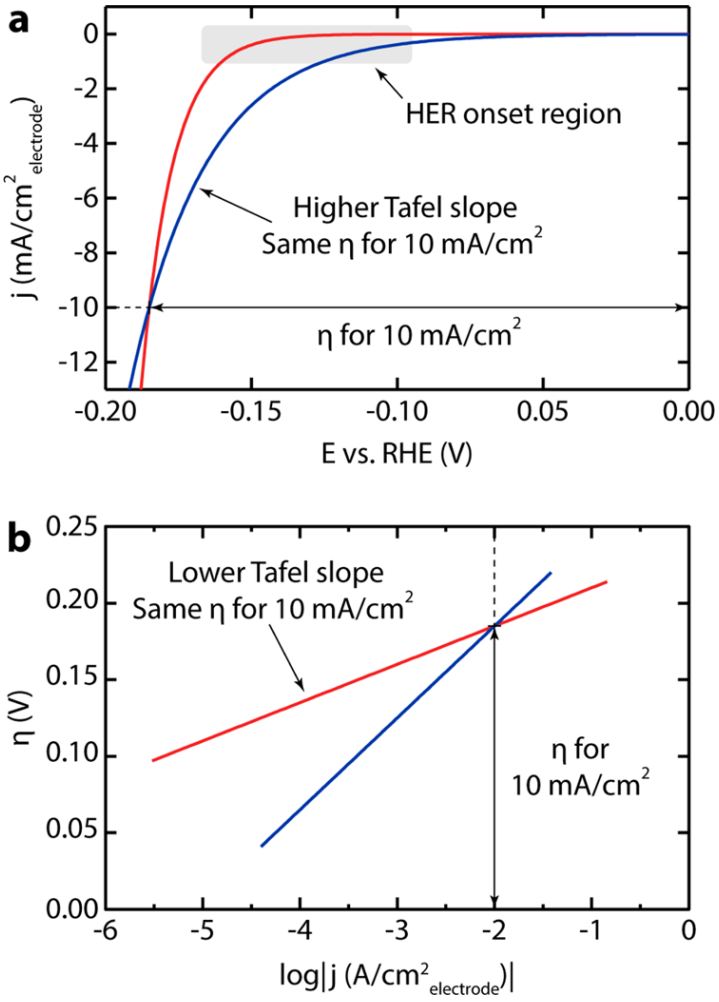


Figure 4: *HER activity of two theoretical catalysts in the same electrolyte illustrating the importance of using overpotential and Tafel slopes in conjunction in the assessment of electrocatalysts. (A) shows linear scanning voltammograms for HER whereas (B) shows the corresponding Tafel plots of the two catalysts. Reprinted with permission from reference* [14]*. Copy right 2014 American Chemical Society.*

In this thesis the overpotential at 10mA cm^{-2} and the Tafel slope will be used in conjunction to assess the HER activity of electrocatalysts. Additionally, turn over frequencies are calculated based on active site density estimations to investigate the intrinsic activity of different active sites.

1.2.4 Descriptors

As shown in section 2.2, both the initial adsorption of the reactant (protons) (Eq.9), as well the desorption of the product (H_2) (Eq.10-11) depend on the interaction between the

electrocatalyst and a hydrogen species and are as such dependent on the electrode-hydrogen bond strength as illustrated in Figure 1. This leads to a volcano type relation between HER activity and M-H strength which can be explained by the Sabatier principle (Fig.1). Instead of hydrogen bond strength the free energy of hydrogen adsorption (ΔG_{H*}) is often used as an effective descriptor of activity (Fig.5.A). If ΔG_{H*} is strongly negative hydrogen adsorbs too strongly to the surfaces and as such poisons it whereas if ΔG_{H*} is strongly positive hydrogen only binds weakly and no reaction can proceed since reactant coverage is too low. As such, theoretically an ideal HER catalyst should have a ΔG_{H*} of zero[28–30] (Fig.5.B). In experiments, Pt electrocatalysts were shown to be the most active heterogeneous materials with a ΔG_{H*} value slightly below zero.[14] Unsurprisingly, the free energy of hydrogen adsorption of nitrogenase and hydrogenase enzymes is even closer to zero explaining their superior TOFs for HER.[31,32]

Due to the difficulty of measuring ΔG_{H*} for individual active sites it is usually obtained from calculations. In order to screen large computational libraries of materials for their activity towards the HER descriptors based on more fundamental properties of the materials are highly sought after[10,33–36] to more quickly identify catalysts to be tested experimentally. One of such descriptors, the φ factor[37], will be discussed for single-atom catalysts in Chapter 4 Section 5.3.

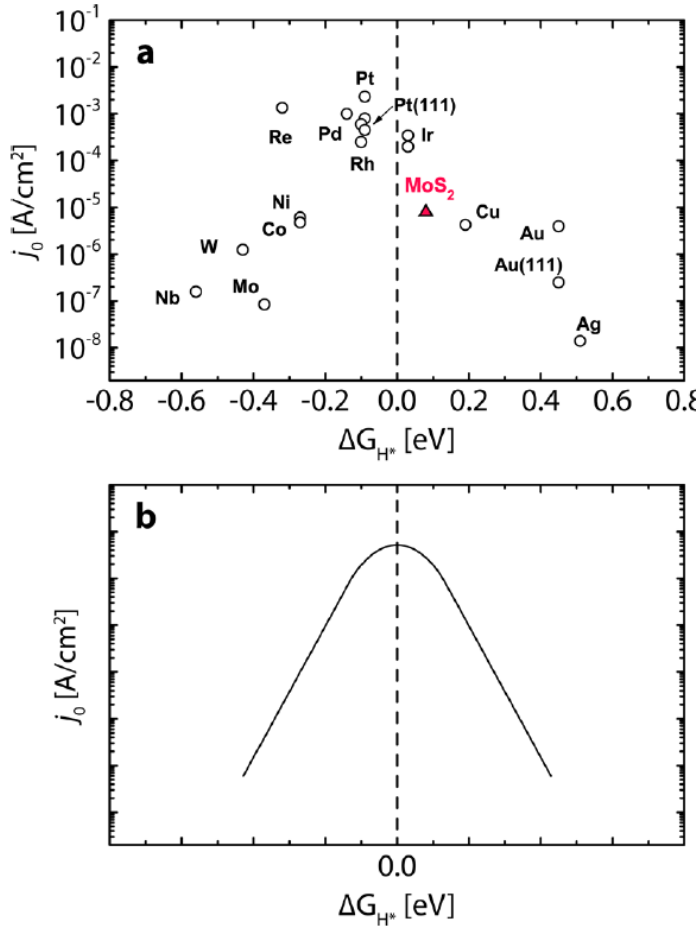


Figure 5: *Hydrogen evolution activity as a function of hydrogen adsorption free energy. (A) Shows the experimentally obtained volcano relation between ΔG_{H^*} and the exchange current density showing Pt with a slightly negative ΔG_{H^*} to be most active. (B) shows the corresponding theoretically obtained volcano curve with a maximum at $\Delta G_{H^*}=0$.*[30] *Reprinted with permission from reference* [14]*. Copy right 2014 American Chemical Society.*

1.2.5 Catalyst Development

Hydrogen evolution has been demonstrated in a wide range of pH. In this thesis hydrogen evolution in acidic media is investigated in further detail with a specific focus on heterogeneous catalyst materials.

Noble metals, platinum in particular, have for a long time been the only relevant catalyst for HER and most PEM electrolysers today still exclusively contain Pt cathodes.[38,39] Recently, significant progress in the search for non-PGM alternatives has been made with

the advent of transition metal dichalcogenide, nitride, carbide, and phosphide catalysts with activities closer to those of Pt-based materials illustrated (Fig.6).[38,39]

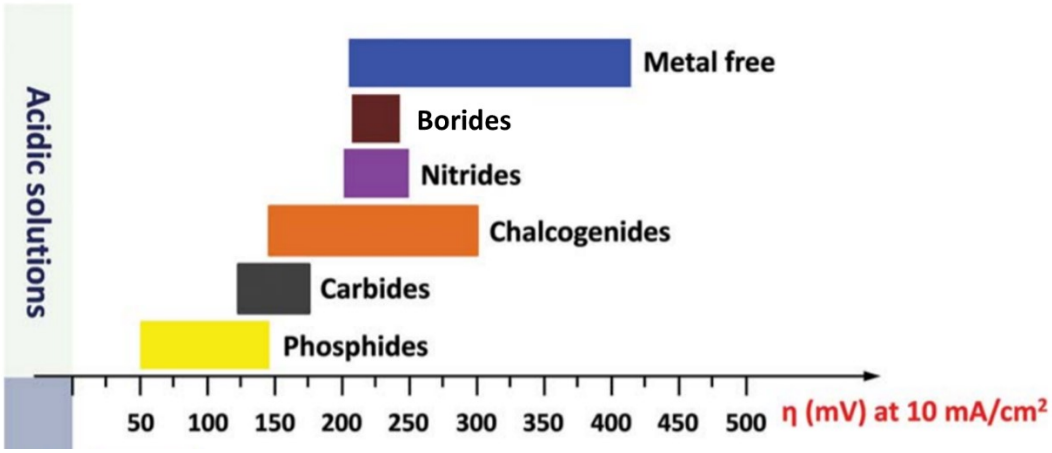


Figure 6: *Comparison of non-PGM based materials activity towards the acidic HER. Active Pt catalysts usually require an overpotential of around 25mV to reach 10mA cm^{-2}. Metal free systems include mostly carbon-based materials such as doped graphene-like systems. Republished with permission of the Royal Society of Chemistry from reference* **[38]**.

Strikingly, recent reports also show low overpotentials for HER over metal free carbon-based materials.[34,38,40] Even lower overpotentials are observed when defective carbon materials are doped with transition metals leading to the formation of single-atom catalysts (SACs).[40–42] In such systems atomically dispersed metal species are stabilised by nitrogen, carbon or oxygen moieties of the carbon support and exhibit vastly higher HER activities than their bulk counterparts.[38,41,43] Atomically dispersed Fe, Mo, W, Ni and Co catalysts have been shown to be active HER catalysts, with Co- and Ni-based SACs usually showing the lowest overpotentials.[40,43] A Ni SAC catalyst was shown to only need an overpotential of around 34mV to reach a current density of 10mA cm^{-2} with a Tafel slope of 41mV dec^{-1}. High atomic utilisation and activities close to those of Pt make SACs an exciting candidate for cathode materials in future cost-effective water electrolysis.

1.3 Electrochemical Ammonia Synthesis

1.3.1 Ammonia – An important Chemical and potential Energy Vector

Ammonia is one of the most produced chemicals in the world with around 150 million tons produced in 2017 alone.[44] Most ammonia is used in the production of fertilisers but it is also an important feedstock chemical in the production of plastics, synthetic fibres, resins, nitric acid, explosives and pharmaceuticals.[44,45] Currently, ammonia is produced via the Haber-Bosch process converting N_2 and H_2 into NH_3 over an iron catalyst at temperatures and pressures of up to 500°C and 200 atmospheres.[45] Such high pressure requirements drive up the CAPEX of ammonia plants due to the need for specialised equipment which, together with some constraints of the iron catalyst, are the reason why ammonia plants tend to be extremely large.[16,46] Dihydrogen used in the production is usually obtained from steam reformation of fossil fuels such as gas or coal leading to the emission of multiple tons of CO_2 per ton of ammonia.[46] Overall ammonia production is estimated to contribute around 1% to global anthropogenic carbon dioxide emissions.[16]

Furthermore, ammonia has recently been suggested as a potential carbon-free energy vector for renewable power sources.[4] It has a high energy density, comparable to methanol, and established storage and shipping protocols potentially enabling efficient long-term storage, as well as commodification and as such presents a way to export renewable energy globally.[16,46–48] Compared to hydrogen, it is significantly easier to store since it liquefies at around 8 bar leading to potentially higher round trip storage efficiencies. Ammonia can be burned in slightly adapted natural gas turbines or used in direct ammonia fuel cells to release stored electricity.[16,47–49] Additionally, it can be

cracked into N_2 and H_2 and as such has the potential to play a pivotal part in a future hydrogen economy.[17,50,51]

De-carbonising the chemical industry generally and ammonia production specifically requires coupling with renewable energy sources such as wind or solar.[17,51] As such conversion of electrical to chemical energy is needed. The first generation of green ammonia production is expected to involve producing H_2 from water electrolysis powered by a renewable power source.[46] This is then coupled with a small-scale Haber-Bosch-type ammonia synthesis reactor (eHB). In order to be useful as an energy storage system for distributed and intermittent energy sources small systems with low CAPEX are desired. Ammonia synthesis from H_2 and N_2 is an exothermic process at room temperature but the breaking of the dinitrogen triple bond requires the use of high temperature to supply sufficient activation energy which in turn requires the use of high pressure to shift the equilibrium back. In order to build small agile systems easily coupled to intermittent renewables novel catalysts working at low temperatures and pressures need to be developed. Recently, there has been progress in this area, especially with ruthenium and metal nitride based catalysts.[52–56]

An alternative to this approach is the direct electrochemical synthesis of ammonia. Here the activation energy is provided in the form of applied potential which relaxes the pressure requirement and theoretically enables ammonia production at atmospheric pressure and temperature.[57] In such systems the electrochemical nitrogen reduction reaction (NRR) at the cathode is coupled to an oxidation reaction such as the oxygen evolution reaction (OER).[57] Recently, NRR has gained more attention and a brief review of the current literature is presented in the next sections.

1.3.2 Nitrogen Reduction Reaction

Several different cells for producing ammonia electrochemically have been reported in literature with temperatures varying from more than 600°C to room temperature.[57] Generally, all reported cells adopted one of four geometries summarised in Figure 7. By far the most common cell geometry reduces dinitrogen to ammonia at the cathode in the presence of protons supplied by an aqueous or polymeric electrolyte (Fig.7.A). Said protons are formed in the corresponding anodic oxidation of water or less commonly hydrogen. The theoretical cell potential for this reaction scheme (-1.173V) is slightly lower than that of water splitting (-1.23V)[5] meaning in theory a small potential window in which NRR is favoured over HER exists. The second reaction scheme was observed in molten chloride eutectics which allow the direct reduction of dinitrogen to the nitride ion (N^{3-}) at the cathode coupled with an oxidation in the presence of H_2 (Fig.7.B). In contrast to N_2/H_2O, the reaction of N_2 and H_2 is exothermic at room temperature and only becomes slightly unfavourable at elevated temperatures meaning that theoretically only a low cell potential is needed to drive the reaction in Fig.7.B.[58,59] Recently, a third approach towards NRR was reported producing metallic lithium at the cathode (Fig.7.C) while oxidising water at the anode.[60] Li is then reacted with N_2 ex-situ to form Li_3N which in a separate step reacts spontaneously with H_2O to form ammonia. The formation of a more reduced intermediate species, i.e. Li, introduces a large energy penalty leading to a high theoretical cell potential of -2.87V. A fourth reaction scheme was developed in molten hydroxide systems using dispersed iron-based nanoparticles at slightly elevated temperatures coupling nitrogen reduction to alkaline water oxidation (Fig.7.D).[61,62] High rates at elevated current efficiencies were observed although the exact mechanism of such systems is not well understood yet.[57]

The two important figures of merit in NRR are the rate of electrochemically produced ammonia, in this thesis given in mol cm^{-2} s^{-1}, and the current efficiency, defined as the percentage of current used to reduce nitrogen. Figure 8 provides an overview of cells reporting rates for electrochemical ammonia synthesis versus their operating temperature. Interestingly, no general relationship between temperature and rate was observed across cells. When investigated within a single system a temperature dependence was indeed observed.[63,64] Due to the reversible exothermic nature of ammonia synthesis, NH_3 decomposition is favoured above a certain temperature leading to an upper limit.[57,63] The U.S. Department of Energy suggested a target rate of 9.3 x 10^{-7}mol cm^{-2} s^{-1} for a viable device. As is evident from Figure 8 all contemporary systems exhibit rates at least one to two orders of magnitude below that target clearly indicating further fundamental research into cell geometries and catalyst materials is needed.[57]Additionally, the majority of electrochemical ammonia synthesis systems exhibit current efficiencies of below 10% highlighting the need for strategies to increase selectivity and to limit the competing HER. Further discussion on this is provided in Section 3.2.3.

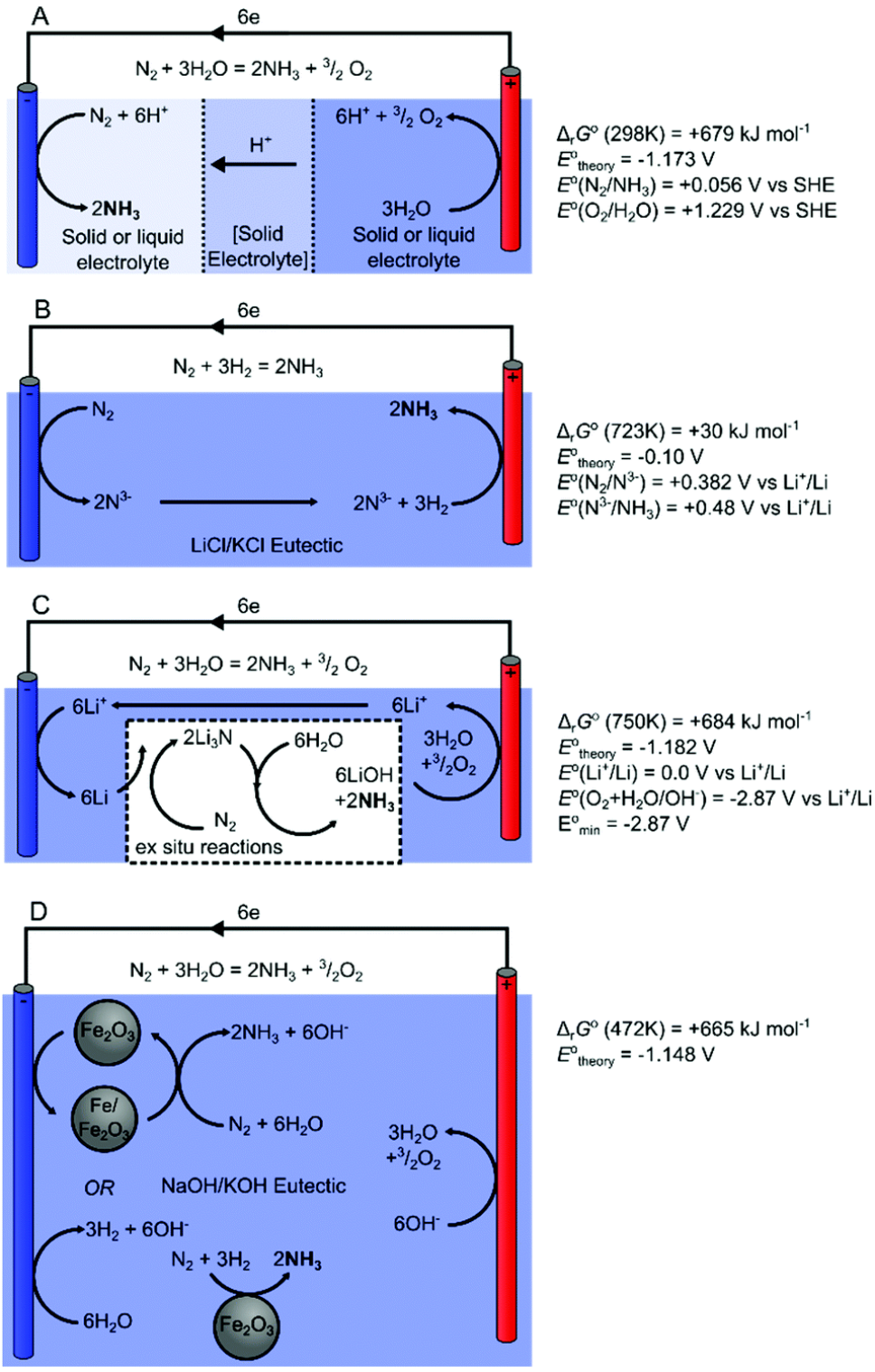


Figure 7: *Overview of cell types reported for electrochemical ammonia synthesis. Gibbs energies were calculated using FactSage, in B experimental values were used. $E^0(O_2+H_2O/OH^-)$ stems from another study. E^0_{theory} was calculated using $E^0_{theory}=-\Delta_rG/nF$, with n referring to the number of electrons and F is Faraday's constant. Republished with permission of the Royal Society of Chemistry from reference*[57].

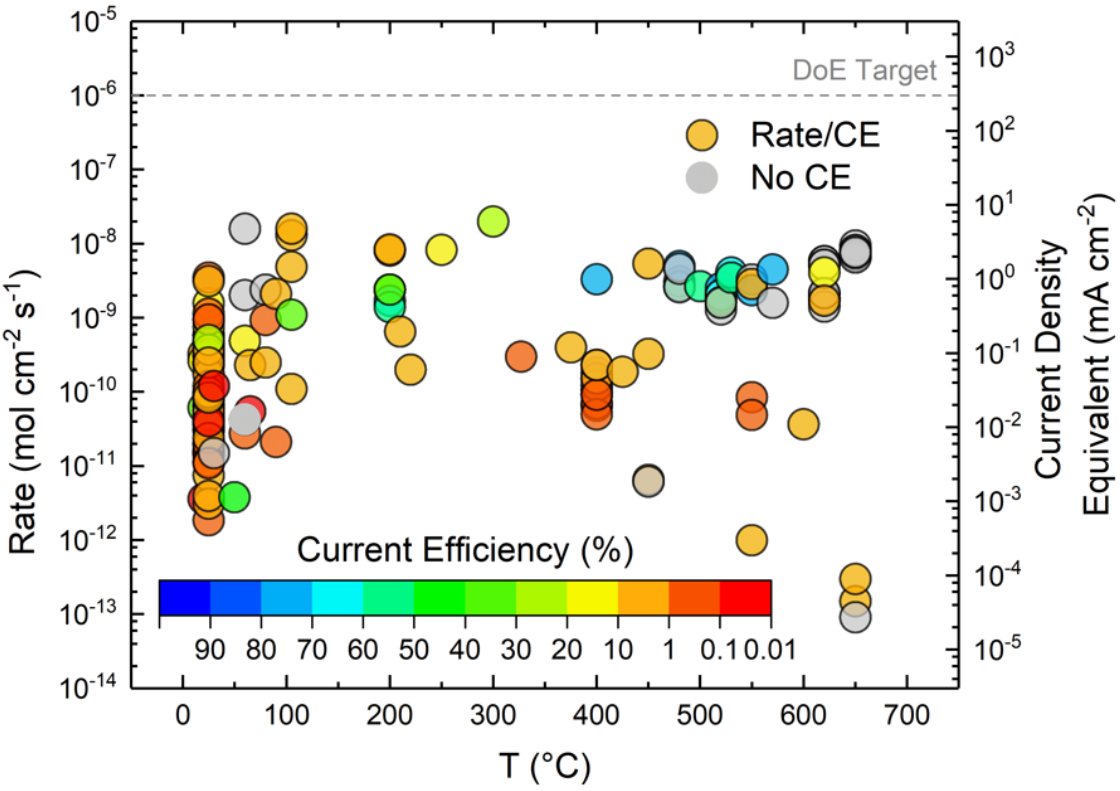


Figure 8: *Overview of rates and current efficiencies for electrochemical ammonia synthesis cells. Ammonia synthesis rate and its current density equivalent are plotted as a function of temperature. Colours represent the current efficiency (here abbreviated as CE) with colder colours indicating higher CE. If no current efficiency was reported circles were coloured grey Republished with permission of the Royal Society of Chemistry from reference*[57].

This thesis further investigates the nitrogen reduction reaction in aqueous electrolytes and in molten salts providing a brief discussion on recent developments in these areas in Sections 3.2.1 and 3.2.2.

1.3.2.1 Aqueous and low temperature NRR

Generally, two types of cells are reported for low temperature NRR those using liquid, often aqueous based, electrolytes, and those using solid polymeric conductors such as Nafion. High rates of up to 10^{-8}mol cm^{-2} s^{-1} have been reported for Nafion membrane-based systems using N_2/H_2[65] although several recent literature reports have found Nafion to be a source of nonelectrochemical ammonia, deeming Nafion as inappropriate for use

in electrochemical ammonia synthesis research.[66–68] Figure 9 summarises the NRR rates for aqueous systems plotting them against current efficiency. Note that many reports qualified as aqueous ammonia synthesis cells still contained Nafion membranes to separate catholyte and anolyte. Largely, rates are found to be below $1x10^{-9}$mol cm^{-2} s^{-1} with current efficiencies below 10%. Unsurprisingly, good HER catalysts such as Pt-based materials exhibit low current efficiencies of below 3% although reporting elevated rates above $1x10^{-9}$mol cm^{-2} s^{-1} (Fig.9.a).[69] In contrast to platinum, systems based on gold, a metal with rather poor activity towards HER, generally exhibit higher current efficiencies albeit at an order of magnitude lower rates (Fig.9.d). Additionally, size and crystal structure effects are examined for Au catalysts reporting sub-nanometre cluster to be more active than 6-30nm particles[70], as well as amorphous systems to be more active than crystalline ones[71].[57] It has been suggested that NRR on gold occurs via an associative mechanism, i.e. hydrogenation occurring before N-N bond dissociation, with in-situ IR studies observing N-N and H-N-H vibrations under nitrogen reduction conditions[72], as well as the detection of hydrazine (N_2H_2) during NRR experiments using high-index nanorods[73]. Interestingly, metal-free carbon and nitrogen-doped carbon based materials have also been reported to show activity for NRR (Fig.9.b-c).[57] Recently, single-atom catalysts (SACs), specifically atomically dispersed metals on nitrogen-doped carbon (M-N-C)[74–78] and carbon nitride (M/C_3N_4) (Fig.9.f),[79] have also been reported for electrochemical ammonia synthesis, after being suggested by theory[80–82] with single atom Ru on N-C reaching rates of $5.04x10^{-10}$mol cm^{-2} s^{-1} at a high current efficiency of 29.2%[74] (Fig.9.e).[57]

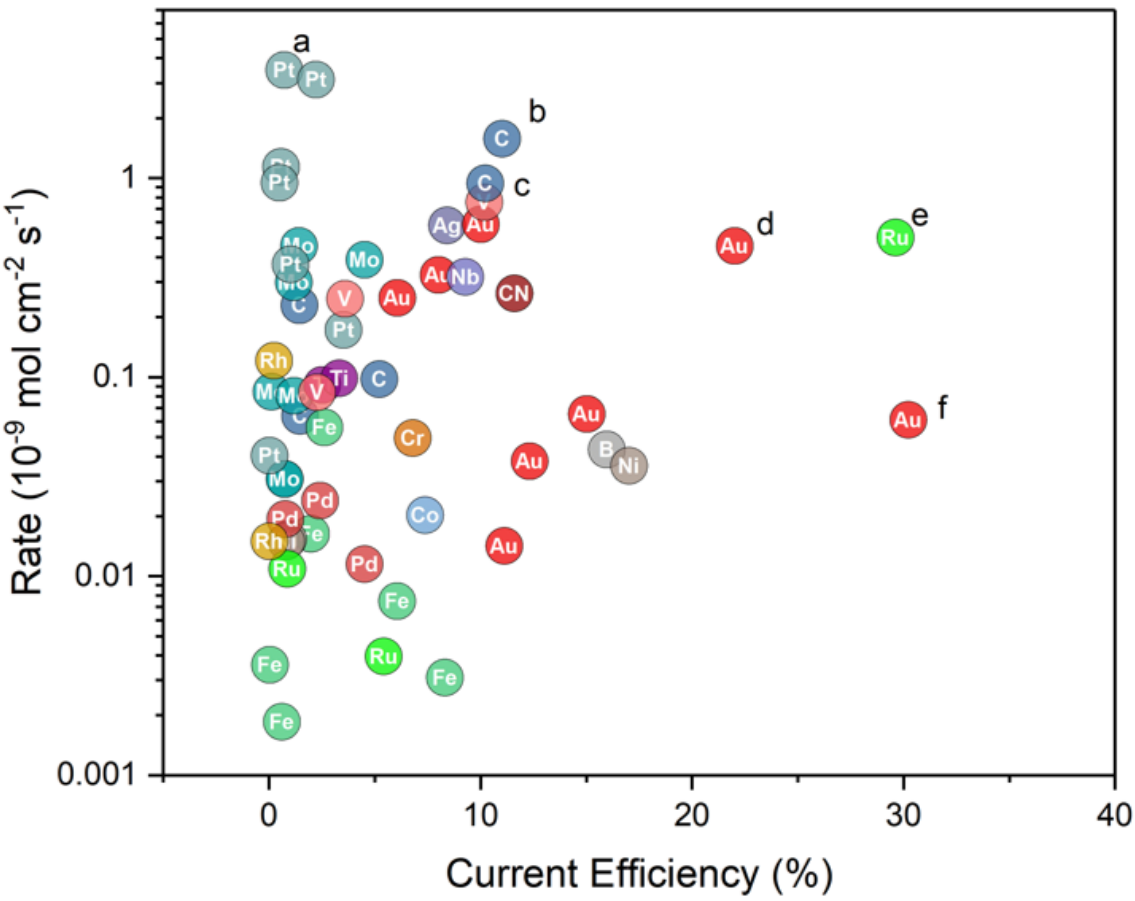


Figure 9: *Overview of rates and current efficiencies of electrocatalysts for the aqueous nitrogen reduction reaction. Rate is plotted against current efficiency. Labelled data points a), b), c), d), e), and f) are referred to in the text. Colour code: Mo (cyan), Ru (green), Au (red), B (grey), Co (blue), C (dark blue), Pd (light red), Ag (dark grey), Cr (orange), Rh (ochre), Nb (light purple), CN (carbon nitride, brown), Ti (purple),V (pink), Fe (dark green), Ni (light brown), and Pt (green-grey). Republished with permission of the Royal Society of Chemistry from reference*[57].

1.3.2.2 NRR in Molten Salts

In contrast to the aqueous and low temperature processes, molten salt-based ammonia synthesis cells operate at higher temperatures of up to 450°C and in some cases use dihydrogen as a proton source. While long-term a low temperature process is desired, to date molten salt systems exhibit the highest NRR rates, and are as such most relevant to industry.[57] Three different cell geometries are reported in molten eutectics (Fig.7.C-D). McEnany et al. used molten hydroxide/chloride electrolytes to electroplate metallic

lithium from LiOH which ex-situ was first transformed to Li_3N and then reacted with water to NH_3 (Fig.7.C) at a current efficiency of 88.5%.[60] A large overpotential was used and no rate was reported due to the batch nature of the approach.[57,60] In another approach nanoparticulate iron catalysts dispersed in molten hydroxides were reported to produce ammonia directly from N_2 and H_2O at a peak rate of 2.4 x 10^{-9}mol cm^{-2} s^{-1} and a current efficiency of 35%.[61,62] The exact mechanism remains unclear but it is hypothesised that the reaction occurs via a reduced iron intermediate.[83]

Finally, molten chloride eutectics have been suggested as electrolyte for direct electrochemical reduction of N_2 to N^{3-} (Fig.7.B) by Murakami et al.[58] In their system Li_3N was added to molten Li-K-Cs-Cl eutectics and H_2 and other hydrogen sources were supplied to form ammonia at rates of up to 2 x 10^{-8}mol cm^{-2} s^{-1}.[84–87] Recently, we were able to show in Li-K-Cl systems that N^{3-} indeed reacts chemically in the melt with H_2 to form NH_x species and H^- and eventually release NH_3 without applying potential showing that previously reported rates from molten chloride melts stem from a chemical reaction of added pre-reduced nitrogen rather than from actual electrochemical nitrogen reduction.[59] Using insights about the nitrogen redox chemistry in the melt obtained by cyclic voltammetry studies, we devised a new approach using dissolved LiH instead of Li_3N to electrochemically reduce dinitrogen to the nitride ion on a nickel foam cathode coupled with hydride oxidation at the anode.[59] Ammonia was evolved from a chemical reaction with dihydrogen and confirmed to be from nitrogen reduction using isotope labelling. A peak rate of 2.4 x 10^{-8}mol cm^{-2} s^{-1} and a maximum current efficiency of 4.2% were obtained.[59] It has to be noted that steady state was not reached due to changing melt conditions inhibiting the spontaneous evolution of ammonia from the melt.[59] Further research into the redox chemistry of the melt is as such required. Overall it is interesting

to mention that only few metals have been tested under NRR conditions in molten chlorides[88] with reported electrochemical ammonia synthesis rates only being available for Ni[59] and iron based nanoparticles[89]. This is potentially due to the propensity of some transition metals to form bulk nitrides rather than catalytically reducing dinitrogen.[90–93]

1.3.2.3 Challenges

The main challenge in NRR research is the competing HER which in most cell geometries significantly depresses the rate and current efficiency. This is illustrated for (111) transition metal surfaces in Figure 10 showing the calculated limiting potential of NRR to always be more negative than that of HER meaning for all presented surfaces HER is expected to dominate.[94] Similar relations have been found computationally for other classes of materials including metal nitrides[95–97] and metal sulfides[98,99] although here few materials were suggested to potentially have characteristics favourable for NRR.

Different strategies to limit HER have been proposed, generally by either limiting proton availability through use of aprotic or bulky proton donor electrolytes and electrode coatings or by limiting the electron accessibility.[100]

Another challenge in the field, especially for systems with low rates such as many of the aqueous cells, is the reliable quantification of ammonia stemming from electrochemical nitrogen reduction.[66–68] Lab environments contain many possible sources of extraneous ammonia and N-containing species interfering with common ammonia detection methods including cleaning products, amines, iron species, and even human breath.[66,68,101] In a rigorous recent study attempts to reproduce activity for many previously reported aqueous electrocatalysts failed highlighting the importance of control measurements.[66]

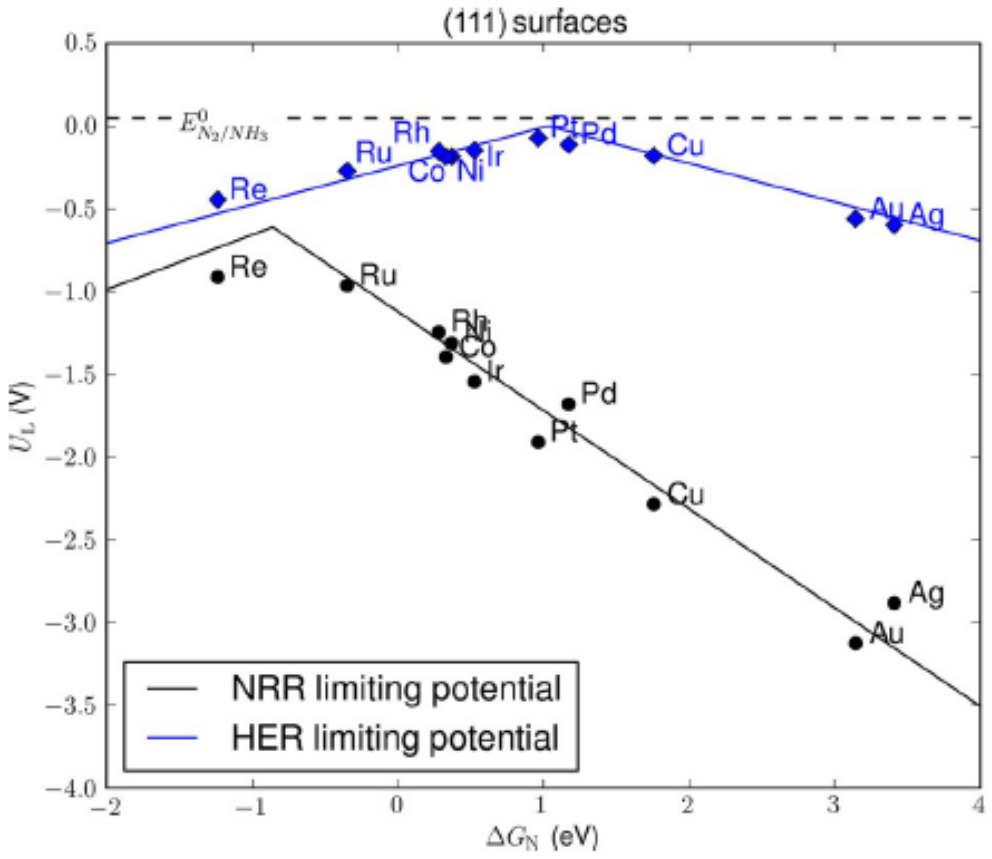


Figure 10: *Comparison of HER and NRR limiting –potential (U_L) volcanos for metal (111) facets. HER (blue) and NRR potential (black) are plotted versus the nitrogen binding free energy (ΔG_N) of the respective metal. Reproduced with permission from John Wiley and Sons from reference*[94].

1.4 Electrocatalysts

Two types of electrocatalysts are explored, namely: single-atom catalysts on graphene-like supports (SACs) and interstitial metal nitrides. A short background and an overview of available synthesis methods for both systems are given in the next sections.

1.4.1 Single-atom Catalysts

1.4.1.1 Background

Atomically dispersed metal species on various supports have recently received wide-ranging attention due to their expansive applications in catalysis and significant advances

in high-resolution electron microscopy, as well as synchrotron-based X-ray techniques helping with their characterisation.[102] They are often described as the bridge between homogenous and heterogeneous catalysis combining the high activity and atom utilisation of homogenous catalysts with the stability and facile recovery from product streams of heterogeneous systems. Indeed parallels in selectivity and activity of SACs and homogenous catalysts have been reported for applications in catalysis[103], as well as electrocatalysis[104,105]. Atomically dispersed metals, especially iron, on nitrogen doped carbons (M-N-Cs) have been shown to exhibit excellent activity towards the oxygen reduction reaction (ORR) approaching that of the Pt benchmark catalyst.[106–108] Interestingly, the first M-N-Cs were synthesised by heat treatment of iron and cobalt porphyrin and phthalocyanine complexes on carbon black support.[104,109] Such systems were shown to have similar activities to their homogeneous precursors[104,110–112], as well as exhibit similar signatures in XANES indicating that some of the structure of the metal coordination environment was retained.[113] Modern Fe-N-C systems synthesised via pyrolysis of e.g. MOFs are also found to contain structural motives similar to those of such early homogeneous systems[114] highlighting the connection between homogeneous and single-atom catalysis.

Generally, SACs represent the last step of minimising metal cluster size and as such theoretically enable 100% atom utilisation (Fig.11). Although in such systems the metal is atomically dispersed it is still interacting with the support usually in the form of covalent bonds which is why sometimes the term heterogeneous single-metal-site catalysts is used to describe SACs.[103] In another parallel to homogeneous catalysis the interaction with the support, i.e. ligand, can have large impact on the activity. For SACs these interactions are often only poorly understood due to active site heterogeneity in

many catalyst systems, as well as limited techniques to investigate the active site at high enough spatial and elemental resolution.

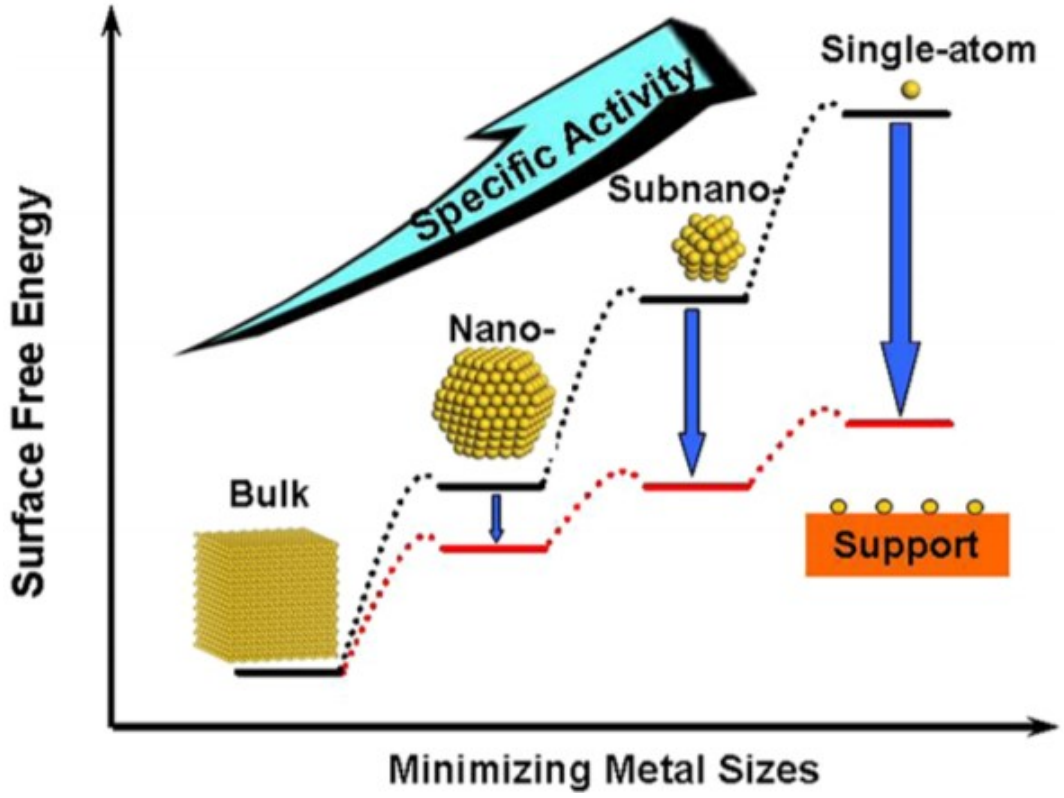


Figure 11: *Schematic depiction of increase in surface free energy and specific activity upon moving towards lower coordination environments. Reprinted with permission from reference*[115]*. Copyright 2013 American Chemical Society.*

This thesis focuses on SACs on graphene-like carbon supports for which a short review of currently available synthesis methods is given in the next section.

1.4.1.2 Synthesis

SACs on defective carbon supports have been at the forefront of single-atom catalysis research due to their relatively facile synthesis, stability and the conductivity of the support enabling them to be used in electrocatalysis. A large variety of synthesis methods has been developed in recent years which can roughly be classified into five categories:

pyrolysis, ball milling, electron/ion irradiation, atomic layer deposition (ALD), impregnation and carbon backbone methods.

Pyrolysis methods are the most ubiquitous in literature and usually work by heating a metal, carbon and nitrogen precursor in an unreactive atmosphere to temperatures above 700°C. Precursors can include molecular systems such as transition metal macrocycles, e.g. phthalocyanines, as well as polymeric precursors such as polyaniline or carbon nitride amongst others.[43,102,103] Recently, metal organic frameworks (MOFs) have also been shown to work as precursors for SACs with the nodes acting as metal precursor and the linkers forming the (nitrogen-doped) carbon support.[43,103]

Ball milling was also shown to produce atomically dispersed metal species on carbon supports when using metal phthalocyanine precursors, analogously to pyrolysis methods.[43,104]

The electron/ion irradiation technique works by introducing defects into graphene by bombardment with high energy electrons or ions, which are then used to trap atomic metal species. This provides exciting opportunities for in-situ electron imaging and very well defined catalysts but is likely not relevant for industrial applications.[43]

ALD has also been applied to synthesise SACs by first oxidising graphene and then depositing metal species on it. Metal loading can be controlled precisely using ALD but cost and scalability issues remain a problem.[43]

Another exciting new method for SAC synthesis uses defective carbon materials to trap reduced single metal atoms from low temperature ice structures or solutions. Low temperatures of around -60°C are used here to kinetically inhibit nucleation of metal

clusters.[43,103] This synthesis method is particularly interesting since it can provide reduced single-atoms but has only been demonstrated for a few metals.[43]

The carbon backbone method uses graphene oxide (GO) as a carbon precursor and thermal annealing of it in the presence of a metal precursor leads to the formation of a SAC.[41–43] Additional nitrogen-doping can be introduced by annealing in ammonia or adding other nitrogen precursors.[41] The reduction of GO does not require any catalysing by metals to obtain a reduced carbon support meaning SACs with similar morphologies and compositions can be formed independent of the metal precursor. One drawback of this method is that generally only low loadings of metal can be achieved since increased metal precursor concentrations lead to aggregation and nanoparticle formation.[41]

In this thesis the carbon backbone method is applied to synthesise a wide range of atomically dispersed metal species on nitrogen-doped graphene (M-NGs) in a potentially scalable way while minimising morphology and active site variations.

1.4.2 Metal Nitrides

1.4.2.1 Background

Transition metal nitrides have recently garnered significant amounts of interest due to their various applications ranging from industrial tools to catalysis.

Generally, nitrides can be categorised into three sub-classes: covalent, ionic and interstitial nitrides. Interstitial nitrides represent a structural class where the N^{3-} occupies the interstitial sites of close packed metal lattices. [116,117]Many non-stoichiometric phases are observed for this class of nitrides which often exhibit metal-like properties such as hardness, lustre, and electrical conductivity. [117] Ionic nitrides are usually formed by alkali and alkaline earth metals but some of the nitrides of the transition metals of group VIII

to X are also classified as ionic (e.g. Cu_3N).[117] This is largely due to the decrease in atomic size of the metal disallowing the N^{3-} ion to be fitted into interstitial sites (Hägg's rule).[116,118] Covalent nitrides are mostly formed by elements of group XIII and higher, such as carbon and sulphur, dominated by covalent interactions.

Interstitial metal nitrides have received most of the attention as catalyst materials for various reactions. For example, several computational and experimental reports have suggested transition metal nitrides to potentially be effective catalysts for the nitrogen reduction reaction in aqueous electrolytes.[57,95,97] Another example of special importance is the high activity of the η-6 phase of cobalt molybdenum nitride (Co_3Mo_3N) towards thermal ammonia synthesis.[55,119] A cobalt molybdenum alloy had been predicted to balance the adsorption free energy of nitrogen of cobalt and molybdenum and to sit on top of the volcano curve.[120] As such this interpolation approach explains the activity of Co_3Mo_3N simply as an alloy effect of cobalt and molybdenum.[120] Doubt has been cast on this explanation by recent experimental work showing the structural carbide analogues of cobalt molybdenum nitride, Co_3Mo_3C and Co_6Mo_6C, to be transformed to a nitride before showing activity or to not exhibit any activity in ammonia synthesis at all, respectively.[121,122] Combined theory and experimental studies further suggest that the lattice nitrogen of Co_3Mo_3N is mobile and allows ammonia synthesis to operate via a Mars-van Krevelen-type mechanism, where the lattice anion participates in the reaction.[118,121] This indicates that nitrogen plays a special role in the electronic structure of metal nitrides and is pivotal to their catalytic activity. Co_3Mo_3N has also been used as an electrocatalyst for ammonia synthesis in a solid electrolyte cell.[123]

As such we determined Co_3Mo_3N to be of interest as an electrocatalyst for the nitrogen reduction reaction in molten chlorides due to the mobility of its lattice nitrogen at above

400°C and its electrical conductivity. In the next section a brief overview of various synthesis techniques to obtain cobalt molybdenum nitride is provided.

1.4.2.2 Synthesis

Three different synthesis methods have been reported for Co_3Mo_3N and other molybdenum-containing nitrides, namely NH_3 temperature programmed reduction (TPR), N_2/H_2 temperature programmed reduction and thermal decomposition of metal-amine complexes. In the TPR based methods mixed metal oxide precursors, usually prepared from aqueous solutions[55,119] or grinding of individual oxide phases of the constituting metals[124], are treated in ammonia or in a 3:1 H_2/N_2 mixture at different temperatures usually around 700°C. The heating regime, especially the rate of heating has been shown to have a significant effect on the surface area and catalytic activity for Mo-containing metal nitrides.[125–129] In the third approach an amine such as hexamethylenetetramine (HMT) is added to an aqueous solution of the constituent metals which is hypothesised to lead to the formation of metal-amine complexes upon evaporation of the solvent. The resulting mixture is annealed at temperatures of 650°C in Ar flow reportedly leading to the formation of the ternary Co_3Mo_3N phase.[130]

1.5 Aims and Objectives

As discussed in the previous sections, both the hydrogen evolution reaction and the nitrogen reduction reaction have the potential to play a crucial role in the move towards an electrified chemical industry and decarbonisation of the energy sector. In this thesis novel catalysts are tested for these reactions and investigations into their structure-activity relationships are launched.

As illustrated previously, the main challenge in electrochemical ammonia synthesis is the competing hydrogen evolution reaction depressing rates and current efficiencies. We undertook a detailed investigation into the structural factors determining HER activity of atomically dispersed metals on graphene-like supports to gain a deeper understanding of their structure-activity relationship and apply these findings towards the search for effective HER but also NRR catalysts in aqueous solutions.

Molten chloride eutectics provide a way to reduce nitrogen in the absence of hydrogen species by stabilising the nitride ion, N^{3-}, as such potentially eliminating HER as a side reaction. We suggest cobalt molybdenum nitride as a novel electrocatalysts material in this system due to its lattice nitrogen mobility and inherent ability to activate dinitrogen in the absence of hydrogen. Its stability and nitrogen reduction activity are tested at 450°C in molten Li-K-Cl eutectic.

1.6 Thesis Overview

This thesis contains seven chapters with Chapters 4 to 6 detailing the experimental and computational work carried out over the course of my DPhil degree.

Chapter 1 introduces some basic concepts of electrocatalysis and offers brief introductions of the two target reactions, hydrogen evolution and nitrogen reduction, and outlines recent progress in catalyst development for these reactions. Additionally, a background description and a review of synthetic methods is provided for single-atom catalysts and metal nitrides as they are the two classes of catalysts used in the experimental chapters.

Chapter 2 provides an overview and brief theoretical discussion of the operational principles of the analytical techniques used in this thesis.

Chapter 3 details the experimental protocols followed during characterisation and activity testing of catalysts reported in the following experimental chapters.

Chapter 4 outlines the synthesis and characterisation of a library of atomically dispersed metals on nitrogen-doped graphene and explores their metal-activity relationship for the hydrogen evolution reaction. Furthermore, attempts are made to apply this insight to the search for effective electrochemical nitrogen reduction reaction (NRR) catalysts.

Chapter 5 details the synthesis and characterisation of three cobalt-containing single atom catalysts and investigates the effect of elemental composition and spatial arrangement of the first coordination shell of cobalt on its HER activity. Two different in-situ techniques are applied to monitor the catalysts during turn over.

Chapter 6 outlines the synthesis and characterisation of a cobalt molybdenum nitride catalyst and assesses its potential as a nitrogen reduction electrocatalyst in molten chloride eutectics.

Chapter 7 summarises the findings of the previous chapters and provides a brief discussion on future directions.

1.7 References

(1) The Paris Agreement | UNFCCC https://unfccc.int/process-and-meetings/the-paris-agreement/the-paris-agreement (accessed Oct 5, 2019).
(2) Global Energy and CO2 Status Report 2018. *Energy Demand* **2018**, 29.
(3) Schiffer, Z. J.; Manthiram, K. Electrification and Decarbonization of the Chemical Industry. *Joule* **2017**, *1* (1), 10–14. https://doi.org/10.1016/j.joule.2017.07.008.
(4) Technology Roadmap - Energy Storage https://webstore.iea.org/technology-roadmap-energy-storage (accessed Dec 26, 2019).
(5) Bard, A. J. *Electrochemical Methods: Fundamentals and Applications*, Second edition.; Wiley: New York ; Chichester, 2001.
(6) Crow, D. R. *Principles and Applications of Electrochemistry, 4th Edition [Electronic Resource]*, 4th ed.; Routledge, 2017.

(7) Medford, A. J.; Vojvodic, A.; Hummelshøj, J. S.; Voss, J.; Abild-Pedersen, F.; Studt, F.; Bligaard, T.; Nilsson, A.; Nørskov, J. K. From the Sabatier Principle to a Predictive Theory of Transition-Metal Heterogeneous Catalysis. *J. Catal.* **2015**, *328*, 36–42. https://doi.org/10.1016/j.jcat.2014.12.033.
(8) Quaino, P.; Juarez, F.; Santos, E.; Schmickler, W. Volcano Plots in Hydrogen Electrocatalysis – Uses and Abuses. *Beilstein J. Nanotechnol.* **2014**, *5*, 846–854. https://doi.org/10.3762/bjnano.5.96.
(9) Stamenkovic, V. R.; Mun, B. S.; Arenz, M.; Mayrhofer, K. J. J.; Lucas, C. A.; Wang, G.; Ross, P. N.; Markovic, N. M. Trends in Electrocatalysis on Extended and Nanoscale Pt-Bimetallic Alloy Surfaces. *Nat. Mater.* **2007**, *6* (3), 241–247. https://doi.org/10.1038/nmat1840.
(10) Seh, Z. W.; Kibsgaard, J.; Dickens, C. F.; Chorkendorff, I.; Nørskov, J. K.; Jaramillo, T. F. Combining Theory and Experiment in Electrocatalysis: Insights into Materials Design. *Science* **2017**, *355* (6321), eaad4998. https://doi.org/10.1126/science.aad4998.
(11) Trasatti, S. Work Function, Electronegativity, and Electrochemical Behaviour of Metals: III. Electrolytic Hydrogen Evolution in Acid Solutions. *J. Electroanal. Chem. Interfacial Electrochem.* **1972**, *39* (1), 163–184. https://doi.org/10.1016/S0022-0728(72)80485-6.
(12) *Quantities, Units, and Symbols in Physical Chemistry*, 2nd ed.; Mills, I., International Union of Pure and Applied Chemistry, International Union of Pure and Applied Chemistry, Eds.; Blackwell Scientific Publications ; CRC Press [distributor]: Oxford ; Boston : Boca Raton, Fla, 1993.
(13) Henze, G. Analytical Voltammetry and Polarography. In *Handbook of Analytical Techniques*; John Wiley & Sons, Ltd, 2008; pp 785–825. https://doi.org/10.1002/9783527618323.ch25.
(14) Benck, J. D.; Hellstern, T. R.; Kibsgaard, J.; Chakthranont, P.; Jaramillo, T. F. Catalyzing the Hydrogen Evolution Reaction (HER) with Molybdenum Sulfide Nanomaterials. *ACS Catal.* **2014**, *4* (11), 3957–3971. https://doi.org/10.1021/cs500923c.
(15) Technology Roadmap - Hydrogen and Fuel Cells https://webstore.iea.org/technology-roadmap-hydrogen-and-fuel-cells (accessed Jan 18, 2020).
(16) Ye, L.; Nayak-Luke, R.; Bañares-Alcántara, R.; Tsang, E. Reaction: "Green" Ammonia Production. *Chem* **2017**, *3* (5), 712–714. https://doi.org/10.1016/j.chempr.2017.10.016.
(17) IEA webstore. The Future of Hydrogen https://webstore.iea.org/the-future-of-hydrogen (accessed Jan 18, 2020).
(18) Simpson, A. P.; Lutz, A. E. Exergy Analysis of Hydrogen Production via Steam Methane Reforming. *Int. J. Hydrog. Energy* **2007**, *32* (18), 4811–4820. https://doi.org/10.1016/j.ijhydene.2007.08.025.
(19) Rhodes, C.; Hutchings, G. J.; Ward, A. M. Water-Gas Shift Reaction: Finding the Mechanistic Boundary. *Catal. Today* **1995**, *23* (1), 43–58. https://doi.org/10.1016/0920-5861(94)00135-O.
(20) IEA Energy Technology Essentials: Hydrogen Production & Distribution https://webstore.iea.org/iea-energy-technology-essentials-hydrogen-production-distribution (accessed Jan 18, 2020).
(21) Hydrogen Production and Storage https://webstore.iea.org/hydrogen-production-and-storage (accessed Jan 18, 2020).
(22) FCH JU Book - Fuel cell and hydrogen technology: Europe's journey to a greener world | www.fch.europa.eu https://www.fch.europa.eu/publications/fch-ju-book-fuel-cell-and-hydrogen-technology-europes-journey-greener-world (accessed Oct 8, 2019).
(23) Shinagawa, T.; Garcia-Esparza, A. T.; Takanabe, K. Insight on Tafel Slopes from a Microkinetic Analysis of Aqueous Electrocatalysis for Energy Conversion. *Sci. Rep.* **2015**, *5* (1), 13801. https://doi.org/10.1038/srep13801.

(24) Durst, J.; Siebel, A.; Simon, C.; Hasché, F.; Herranz, J.; Gasteiger, H. A. New Insights into the Electrochemical Hydrogen Oxidation and Evolution Reaction Mechanism. *Energy Env. Sci* **2014**, *7* (7), 2255–2260. https://doi.org/10.1039/C4EE00440J.
(25) Marković, N. M.; Grgur, B. N.; Ross, P. N. Temperature-Dependent Hydrogen Electrochemistry on Platinum Low-Index Single-Crystal Surfaces in Acid Solutions. *J. Phys. Chem. B* **1997**, *101* (27), 5405–5413. https://doi.org/10.1021/jp970930d.
(26) Sheng, W.; Gasteiger, H. A.; Shao-Horn, Y. Hydrogen Oxidation and Evolution Reaction Kinetics on Platinum: Acid vs Alkaline Electrolytes. *J. Electrochem. Soc.* **2010**, *157* (11), B1529. https://doi.org/10.1149/1.3483106.
(27) Kucernak, A. R.; Zalitis, C. General Models for the Electrochemical Hydrogen Oxidation and Hydrogen Evolution Reactions: Theoretical Derivation and Experimental Results under Near Mass-Transport Free Conditions. *J. Phys. Chem. C* **2016**, *120* (20), 10721–10745. https://doi.org/10.1021/acs.jpcc.6b00011.
(28) Walter, M. G.; Warren, E. L.; McKone, J. R.; Boettcher, S. W.; Mi, Q.; Santori, E. A.; Lewis, N. S. Solar Water Splitting Cells. *Chem. Rev.* **2010**, *110* (11), 6446–6473. https://doi.org/10.1021/cr1002326.
(29) Seitz, L. C.; Chen, Z.; Forman, A. J.; Pinaud, B. A.; Benck, J. D.; Jaramillo, T. F. Modeling Practical Performance Limits of Photoelectrochemical Water Splitting Based on the Current State of Materials Research. *ChemSusChem* **2014**, *7* (5), 1372–1385. https://doi.org/10.1002/cssc.201301030.
(30) Parsons, R. The Rate of Electrolytic Hydrogen Evolution and the Heat of Adsorption of Hydrogen. *Trans. Faraday Soc.* **1958**, *54*, 1053. https://doi.org/10.1039/tf9585401053.
(31) Hinnemann, B.; Moses, P. G.; Bonde, J.; Jørgensen, K. P.; Nielsen, J. H.; Horch, S.; Chorkendorff, I.; Nørskov, J. K. Biomimetic Hydrogen Evolution: MoS2 Nanoparticles as Catalyst for Hydrogen Evolution. *J. Am. Chem. Soc.* **2005**, *127* (15), 5308–5309. https://doi.org/10.1021/ja0504690.
(32) McPherson, I. J.; Vincent, K. A. Electrocatalysis by Hydrogenases: Lessons for Building Bio-Inspired Device. *J. Braz. Chem. Soc.* **2014**, *25* (3), 427–441. https://doi.org/10.5935/0103-5053.20140042.
(33) Zheng, Y.; Jiao, Y.; Jaroniec, M.; Qiao, S. Z. Advancing the Electrochemistry of the Hydrogen-Evolution Reaction through Combining Experiment and Theory. *Angew. Chem. Int. Ed.* **2015**, *54* (1), 52–65. https://doi.org/10.1002/anie.201407031.
(34) Xia, Z. Hydrogen Evolution: Guiding Principles. *Nat. Energy* **2016**, *1* (10), 1–2. https://doi.org/10.1038/nenergy.2016.155.
(35) Ling, C.; Shi, L.; Ouyang, Y.; Wang, J. Searching for Highly Active Catalysts for Hydrogen Evolution Reaction Based on O-Terminated MXenes through a Simple Descriptor. *Chem. Mater.* **2016**, *28* (24), 9026–9032. https://doi.org/10.1021/acs.chemmater.6b03972.
(36) Kibsgaard, J.; Tsai, C.; Chan, K.; D. Benck, J.; K. Nørskov, J.; Abild-Pedersen, F.; F. Jaramillo, T. Designing an Improved Transition Metal Phosphide Catalyst for Hydrogen Evolution Using Experimental and Theoretical Trends. *Energy Environ. Sci.* **2015**, *8* (10), 3022–3029. https://doi.org/10.1039/C5EE02179K.
(37) Xu, H.; Cheng, D.; Cao, D.; Zeng, X. C. A Universal Principle for a Rational Design of Single-Atom Electrocatalysts. *Nat. Catal.* **2018**. https://doi.org/10.1038/s41929-018-0063-z.
(38) Zeng, M.; Li, Y. Recent Advances in Heterogeneous Electrocatalysts for the Hydrogen Evolution Reaction. *J. Mater. Chem. A* **2015**, *3* (29), 14942–14962. https://doi.org/10.1039/C5TA02974K.
(39) Vesborg, P. C. K.; Seger, B.; Chorkendorff, I. Recent Development in Hydrogen Evolution Reaction Catalysts and Their Practical Implementation. *J. Phys. Chem. Lett.* **2015**, *6* (6), 951–957. https://doi.org/10.1021/acs.jpclett.5b00306.

(40) Liu, H.; Peng, X.; Liu, X. Single-Atom Catalysts for the Hydrogen Evolution Reaction. *ChemElectroChem* **2018**, *5* (20), 2963–2974. https://doi.org/10.1002/celc.201800507.
(41) Fei, H.; Dong, J.; Arellano-Jiménez, M. J.; Ye, G.; Dong Kim, N.; Samuel, E. L. G.; Peng, Z.; Zhu, Z.; Qin, F.; Bao, J.; et al. Atomic Cobalt on Nitrogen-Doped Graphene for Hydrogen Generation. *Nat. Commun.* **2015**, *6*, 8668. https://doi.org/10.1038/ncomms9668.
(42) Fei, H.; Dong, J.; Feng, Y.; Allen, C. S.; Wan, C.; Volosskiy, B.; Li, M.; Zhao, Z.; Wang, Y.; Sun, H.; et al. General Synthesis and Definitive Structural Identification of MN4C4 Single-Atom Catalysts with Tunable Electrocatalytic Activities. *Nat. Catal.* **2018**, *1* (1), 63–72. https://doi.org/10.1038/s41929-017-0008-y.
(43) Fei, H.; Dong, J.; Chen, D.; Hu, T.; Duan, X.; Shakir, I.; Huang, Y.; Duan, X. Single Atom Electrocatalysts Supported on Graphene or Graphene-like Carbons. *Chem. Soc. Rev.* **2019**. https://doi.org/10.1039/C9CS00422J.
(44) Nitrogen Statistics and Information https://www.usgs.gov/centers/nmic/nitrogen-statistics-and-information (accessed Oct 7, 2019).
(45) Appl, M. *Ammonia: Principles and Industrial Practice*; Wiley-VCH, 1999.
(46) Bañares-Alcántara, R.; Iii, G. D.; Fiaschetti, M.; Grünewald, P.; Lopez, J. M.; Tsang, E.; Yang, A.; Ye, L.; Zhao, S. Analysis of Islanded Ammonia-Based Energy Storage Systems. 158.
(47) Al-Zareer, M.; Dincer, I.; Rosen, M. A. Transient Thermodynamic Analysis of a Novel Integrated Ammonia Production, Storage and Hydrogen Production System. *Int. J. Hydrog. Energy* **2019**, *44* (33), 18214–18224. https://doi.org/10.1016/j.ijhydene.2019.04.085.
(48) Siddiqui, O.; Dincer, I. Design and Analysis of a Novel Solar-Wind Based Integrated Energy System Utilizing Ammonia for Energy Storage. *Energy Convers. Manag.* **2019**, *195*, 866–884. https://doi.org/10.1016/j.enconman.2019.05.001.
(49) Wijayanta, A. T.; Oda, T.; Purnomo, C. W.; Kashiwagi, T.; Aziz, M. Liquid Hydrogen, Methylcyclohexane, and Ammonia as Potential Hydrogen Storage: Comparison Review. *Int. J. Hydrog. Energy* **2019**, *44* (29), 15026–15044. https://doi.org/10.1016/j.ijhydene.2019.04.112.
(50) Avery, W. H. A Role for Ammonia in the Hydrogen Economy. *Int. J. Hydrog. Energy* **1988**, *13* (12), 761–773. https://doi.org/10.1016/0360-3199(88)90037-7.
(51) Potential Roles of Ammonia in a Hydrogen Economy https://www.energy.gov/eere/fuelcells/downloads/potential-roles-ammonia-hydrogen-economy (accessed Jan 18, 2020).
(52) Zheng, J.; Liao, F.; Wu, S.; Jones, G.; Chen, T.; Fellowes, J.; Sudmeier, T.; MacPherson, I.; Wilkinson, I.; Tsang, E. S. C. Efficient Non-Dissociative Activation of Dinitrogen to Ammonia over Li Promoted Ru Nanoparticles at Low Pressure. *Angew. Chem. Int. Ed. 0* (ja). https://doi.org/10.1002/anie.201907171.
(53) Kitano, M.; Inoue, Y.; Yamazaki, Y.; Hayashi, F.; Kanbara, S.; Matsuishi, S.; Yokoyama, T.; Kim, S.-W.; Hara, M.; Hosono, H. Ammonia Synthesis Using a Stable Electride as an Electron Donor and Reversible Hydrogen Store. *Nat. Chem.* **2012**, *4* (11), 934–940. https://doi.org/10.1038/nchem.1476.
(54) Kitano, M.; Kanbara, S.; Inoue, Y.; Kuganathan, N.; Sushko, P. V.; Yokoyama, T.; Hara, M.; Hosono, H. Electride Support Boosts Nitrogen Dissociation over Ruthenium Catalyst and Shifts the Bottleneck in Ammonia Synthesis. *Nat. Commun.* **2015**, *6* (1). https://doi.org/10.1038/ncomms7731.
(55) Kojima, R.; Aika, K. Cobalt Molybdenum Bimetallic Nitride Catalysts for Ammonia Synthesis. *Chem. Lett.* **2000**, No. 5, 514–515.

(56) Wang, P.; Chang, F.; Gao, W.; Guo, J.; Wu, G.; He, T.; Chen, P. Breaking Scaling Relations to Achieve Low-Temperature Ammonia Synthesis through LiH-Mediated Nitrogen Transfer and Hydrogenation. *Nat. Chem.* **2016**. https://doi.org/10.1038/nchem.2595.
(57) McPherson, I.J.; Sudmeier, T.; Fellowes, J.; Tsang, S. C. E. Materials for Electrochemical Ammonia Synthesis. *Dalton Trans.* **2019**, *48* (5), 1562–1568. https://doi.org/10.1039/C8DT04019B.
(58) Murakami, T.; Nishikiori, T.; Nohira, T.; Ito, Y. Electrolytic Synthesis of Ammonia in Molten Salts under Atmospheric Pressure. *J. Am. Chem. Soc.* **2003**, *125* (2), 334–335. https://doi.org/10.1021/ja028891t.
(59) McPherson, I. J.; Sudmeier, T.; Fellowes, J. P.; Wilkinson, I.; Hughes, T.; Tsang, S. C. E. The Feasibility of Electrochemical Ammonia Synthesis in Molten LiCl-KCl Eutectics. *Angew. Chem. Int. Ed.* **2019**. https://doi.org/10.1002/anie.201909831.
(60) McEnaney, J. M.; Singh, A. R.; Schwalbe, J. A.; Kibsgaard, J.; Lin, J.; Cargnello, M.; Jaramillo, T.; Norskov, J. K. Ammonia Synthesis from N_2 and H_2O Using a Lithium Cycling Electrification Strategy at Atmospheric Pressure. *Energy Env. Sci* **2017**. https://doi.org/10.1039/C7EE01126A.
(61) Licht, S.; Cui, B.; Wang, B.; Li, F.-F.; Lau, J.; Liu, S. Ammonia Synthesis by N2 and Steam Electrolysis in Molten Hydroxide Suspensions of Nanoscale Fe2O3. *Science* **2014**, *345* (6197), 637–640. https://doi.org/10.1126/science.1254234
(62) Cui, B.; Zhang, J.; Liu, S.; Liu, X.; Xiang, W.; Liu, L.; Xin, H.; Lefler, M. J.; Licht, S. Electrochemical Synthesis of Ammonia Directly from N_2 and Water over Iron-Based Catalysts Supported on Activated Carbon. *Green Chem* **2017**, *19* (1), 298–304. https://doi.org/10.1039/C6GC02386J.
(63) Vasileiou, E.; Kyriakou, V.; Garagounis, I.; Vourros, A.; Manerbino, A.; Coors, W. G.; Stoukides, M. Electrochemical Enhancement of Ammonia Synthesis in a BaZr0.7Ce0.2Y0.1O2.9 Solid Electrolyte Cell. *Solid State Ion.* **2016**, *288*, 357–362. https://doi.org/10.1016/j.ssi.2015.12.022.
(64) Mukherjee, S.; Cullen, D. A.; Karakalos, S.; Liu, K.; Zhang, H.; Zhao, S.; Xu, H.; More, K. L.; Wang, G.; Wu, G. Metal-Organic Framework-Derived Nitrogen-Doped Highly Disordered Carbon for Electrochemical Ammonia Synthesis Using N 2 and H 2 O in Alkaline Electrolytes. *Nano Energy* **2018**. https://doi.org/10.1016/j.nanoen.2018.03.059.
(65) Xu, G.; Liu, R. Sm1.5Sr0.5MO4 (M=Ni, Co, Fe) Cathode Catalysts for Ammonia Synthesis at Atmospheric Pressure and Low Temperature. *Chin. J. Chem.* **2009**, *27* (4), 677–680. https://doi.org/10.1002/cjoc.200990111.
(66) Andersen, S. Z.; Čolić, V.; Yang, S.; Schwalbe, J. A.; Nielander, A. C.; McEnaney, J. M.; Enemark-Rasmussen, K.; Baker, J. G.; Singh, A. R.; Rohr, B. A.; et al. A Rigorous Electrochemical Ammonia Synthesis Protocol with Quantitative Isotope Measurements. *Nature* **2019**. https://doi.org/10.1038/s41586-019-1260-x.
(67) Ren, Y.; Yu, C.; Tan, X.; Han, X.; Huang, H.; Huang, H.; Qiu, J. Is It Appropriate to Use the Nafion Membrane in Electrocatalytic N_2 Reduction? *Small Methods* **2019**, 1900474. https://doi.org/10.1002/smtd.201900474.
(68) Nielander, A. C.; McEnaney, J. M.; Schwalbe, J. A.; Baker, J. G.; Blair, S. J.; Wang, L.; Pelton, J. G.; Andersen, S. Z.; Enemark-Rasmussen, K.; Čolić, V.; et al. A Versatile Method for Ammonia Detection in a Range of Relevant Electrolytes via Direct Nuclear Magnetic Resonance Techniques. *ACS Catal.* **2019**, 5797–5802. https://doi.org/10.1021/acscatal.9b00358.
(69) Lan, R.; Irvine, J. T. S.; Tao, S. Synthesis of Ammonia Directly from Air and Water at Ambient Temperature and Pressure. *Sci. Rep.* **2013**, *3*. https://doi.org/10.1038/srep01145.

(70) Shi, M.-M.; Bao, D.; Wulan, B.-R.; Li, Y.-H.; Zhang, Y.-F.; Yan, J.-M.; Jiang, Q. Au Sub-Nanoclusters on TiO_2 toward Highly Efficient and Selective Electrocatalyst for N_2 Conversion to NH_3 at Ambient Conditions. *Adv. Mater.* **2017**, *29* (17), 1606550. https://doi.org/10.1002/adma.201606550.

(71) Li, S.-J.; Bao, D.; Shi, M.-M.; Wulan, B.-R.; Yan, J.-M.; Jiang, Q. Amorphizing of Au Nanoparticles by CeO_x-RGO Hybrid Support towards Highly Efficient Electrocatalyst for N_2 Reduction under Ambient Conditions. *Adv. Mater.* **2017**, *29* (33), 1700001. https://doi.org/10.1002/adma.201700001.

(72) Yao, Y.; Zhu, S.; Wang, H.; Li, H.; Shao, M. A Spectroscopic Study on the Nitrogen Electrochemical Reduction Reaction on Gold and Platinum Surfaces. *J. Am. Chem. Soc.* **2018**. https://doi.org/10.1021/jacs.7b12101.

(73) Bao, D.; Zhang, Q.; Meng, F.-L.; Zhong, H.-X.; Shi, M.-M.; Zhang, Y.; Yan, J.-M.; Jiang, Q.; Zhang, X.-B. Electrochemical Reduction of N_2 under Ambient Conditions for Artificial N_2 Fixation and Renewable Energy Storage Using N_2/NH_3 Cycle. *Adv. Mater.* **2017**, *29* (3), 1604799. https://doi.org/10.1002/adma.201604799.

(74) Geng, Z.; Liu, Y.; Kong, X.; Li, P.; Li, K.; Liu, Z.; Du, J.; Shu, M.; Si, R.; Zeng, J. Achieving a Record-High Yield Rate of 120.9 $MgNH_3$ Mgcat.−1 H−1 for N_2 Electrochemical Reduction over Ru Single-Atom Catalysts. *Adv. Mater.* **2018**, 1803498. https://doi.org/10.1002/adma.201803498.

(75) Lü, F.; Zhao, S.; Guo, R.; He, J.; Peng, X.; Bao, H.; Fu, J.; Han, L.; Qi, G.; Luo, J.; et al. Nitrogen-Coordinated Single Fe Sites for Efficient Electrocatalytic N2 Fixation in Neutral Media. *Nano Energy* **2019**, *61*, 420–427. https://doi.org/10.1016/j.nanoen.2019.04.092.

(76) Han, L.; Liu, X.; Chen, J.; Lin, R.; Liu, H.; Lu, F.; Bak, S.; Liang, Z.; Zhao, S.; Stavitski, E.; et al. Atomically Dispersed Mo Catalysts for High-Efficiency Ambient N2 Fixation. *Angew. Chem. Int. Ed.* **2018**. https://doi.org/10.1002/anie.201811728.

(77) Gao, Y.; Han, Z.; Hong, S.; Wu, T.; Li, X.; Qiu, J.; Sun, Z. ZIF-67 Derived Cobalt/Nitrogen-Doped Carbon Composites for Efficient Electrocatalytic N2 Reduction. *ACS Appl. Energy Mater.* **2019**, acsaem.9b01135. https://doi.org/10.1021/acsaem.9b01135.

(78) Qin, Q.; Heil, T.; Antonietti, M.; Oschatz, M. Single-Site Gold Catalysts on Hierarchical N-Doped Porous Noble Carbon for Enhanced Electrochemical Reduction of Nitrogen. *Small Methods* **2018**, 1800202. https://doi.org/10.1002/smtd.201800202.

(79) Wang, X.; Wang, W.; Qiao, M.; Wu, G.; Chen, W.; Yuan, T.; Xu, Q.; Chen, M.; Zhang, Y.; Wang, X.; et al. Atomically Dispersed Au 1 Catalyst towards Efficient Electrochemical Synthesis of Ammonia. *Sci. Bull.* **2018**. https://doi.org/10.1016/j.scib.2018.07.005.

(80) Guo, X.; Gu, J.; Hu, X.; Zhang, S.; Chen, Z.; Huang, S. Coordination Tailoring towards Efficient Single-Atom Catalysts for N2 Fixation: A Case Study of Iron-Nitrogen-Carbon (Fe@N-C) Systems. *Catal. Today* **2019**, S0920586119302925. https://doi.org/10.1016/j.cattod.2019.06.014.

(81) Ling, C.; Bai, X.; Ouyang, Y.; Du, A.; Wang, J. Single Molybdenum Atom Anchored on N-Doped Carbon as a Promising Electrocatalyst for Nitrogen Reduction into Ammonia at Ambient Conditions. *J. Phys. Chem. C* **2018**, *122* (29), 16842–16847. https://doi.org/10.1021/acs.jpcc.8b05257.

(82) Cao, Y.; Gao, Y.; Zhou, H.; Chen, X.; Hu, H.; Deng, S.; Zhong, X.; Zhuang, G.; Wang, J. Highly Efficient Ammonia Synthesis Electrocatalyst: Single Ru Atom on Naturally Nanoporous Carbon Materials. *Adv. Theory Simul.* **2018**, 1800018. https://doi.org/10.1002/adts.201800018.

(83) Li, F.-F.; Licht, S. Advances in Understanding the Mechanism and Improved Stability of the Synthesis of Ammonia from Air and Water in Hydroxide Suspensions of Nanoscale Fe_2O_3. *Inorg. Chem.* **2014**, *53* (19), 10042–10044. https://doi.org/10.1021/ic5020048.

(84) Murakami, T.; Nohira, T.; Goto, T.; Ogata, Y. H.; Ito, Y. Electrolytic Ammonia Synthesis from Water and Nitrogen Gas in Molten Salt under Atmospheric Pressure. *Electrochimica Acta* **2005**, *50* (27), 5423–5426. https://doi.org/10.1016/j.electacta.2005.03.023.
(85) Murakami, T.; Nishikiori, T.; Nohira, T.; Ito, Y. Investigation of Anodic Reaction of Electrolytic Ammonia Synthesis in Molten Salts Under Atmospheric Pressure. *J. Electrochem. Soc.* **2005**, *152* (5), D75. https://doi.org/10.1149/1.1874752.
(86) Murakami, T.; Nohira, T.; Ogata, Y. H.; Ito, Y. Electrolytic Ammonia Synthesis in Molten Salts under Atmospheric Pressure Using Methane as a Hydrogen Source. *Electrochem. Solid-State Lett.* **2005**, *8* (4), D12. https://doi.org/10.1149/1.1870633.
(87) Murakami, T.; Nohira, T.; Ogata, Y. H.; Ito, Y. Electrochemical Synthesis of Ammonia and Coproduction of Metal Sulfides from Hydrogen Sulfide and Nitrogen under Atmospheric Pressure. *J. Electrochem. Soc.* **2005**, *152* (6), D109. https://doi.org/10.1149/1.1904984.
(88) Kim, K.; Kim, J.-N.; Yoon, H. C.; Han, J.-I. Effect of Electrode Material on the Electrochemical Reduction of Nitrogen in a Molten LiCl–KCl–CsCl System. *Int. J. Hydrog. Energy* **2015**, *40* (16), 5578–5582. https://doi.org/10.1016/j.ijhydene.2015.02.130.
(89) Kim, K.; Yoo, C.-Y.; Kim, J.-N.; Yoon, H. C.; Han, J.-I. Electrochemical Synthesis of Ammonia from Water and Nitrogen Catalyzed by Nano-Fe2O3 and CoFe2O4 Suspended in a Molten LiCl-KCl-CsCl Electrolyte. *Korean J. Chem. Eng.* **2016**, *33* (6), 1777–1780. https://doi.org/10.1007/s11814-016-0086-6.
(90) Goto, T.; Ito, Y. Electrochemical Reduction of Nitrogen Gas in a Molten Chloride System. *Electrochimica Acta* **1998**, *43* (21), 3379–3384. https://doi.org/10.1016/S0013-4686(98)00010-3
(91) Tsujimura, H.; Goto, T.; Ito, Y. Electrochemical Formation and Control of Chromium Nitride Films in Molten LiCl–KCl–Li3N Systems. *Electrochimica Acta* **2002**, *47* (17), 2725–2731. https://doi.org/10.1016/S0013-4686(02)00137-8.
(92) Goto, T.; Iwaki, T.; Ito, Y. Electrochemical Formation of AlN in Molten LiCl–KCl–Li3N Systems. *Electrochimica Acta* **2005**, *50* (6), 1283–1288. https://doi.org/10.1016/j.electacta.2004.08.018.
(93) Tsujimura, H.; Goto, T.; Ito, Y. Electrochemical Surface Nitriding of Pure Iron by Molten Salt Electrochemical Process. *J. Alloys Compd.* **2004**, *376* (1), 246–250. https://doi.org/10.1016/j.jallcom.2003.12.042.
(94) Montoya, J. H.; Tsai, C.; Vojvodic, A.; Nørskov, J. K. The Challenge of Electrochemical Ammonia Synthesis: A New Perspective on the Role of Nitrogen Scaling Relations. *ChemSusChem* **2015**, *8* (13), 2180–2186. https://doi.org/10.1002/cssc.201500322.
(95) Abghoui, Y.; Skúlason, E. Electrochemical Synthesis of Ammonia via Mars-van Krevelen Mechanism on the (111) Facets of Group III–VII Transition Metal Mononitrides. *Catal. Today* **2016**. https://doi.org/10.1016/j.cattod.2016.06.009.
(96) Abghoui, Y.; Skúlason, E. Electrochemical Synthesis of Ammonia via Mars-van Krevelen Mechanism on the (111) Facets of Group III–VII Transition Metal Mononitrides. *Catal. Today* **2017**, *286*, 78–84. https://doi.org/10.1016/j.cattod.2016.06.009.
(97) Abghoui, Y.; Skúlasson, E. Transition Metal Nitride Catalysts for Electrochemical Reduction of Nitrogen to Ammonia at Ambient Conditions. *Procedia Comput. Sci.* **2015**, *51*, 1897–1906. https://doi.org/10.1016/j.procs.2015.05.433.
(98) Abghoui, Y.; Sigtryggsson, S. B.; Skúlason, E. Biomimetic Nitrogen Fixation Catalyzed by Transition Metal Sulfide Surfaces in an Electrolytic Cell. *ChemSusChem* **2019**, cssc.201901429. https://doi.org/10.1002/cssc.201901429.
(99) Li, F.; Chen, L.; Liu, H.; Wang, D.; Shi, C.; Pan, H. Enhanced N_2 -Fixation by Engineering the Edges of Two-Dimensional Transition Metal Disulfides. *J. Phys. Chem. C* **2019**, acs.jpcc.9b04730. https://doi.org/10.1021/acs.jpcc.9b04730.

(100) Singh, A. R.; Rohr, B. A.; Schwalbe, J. A.; Cargnello, M.; Chan, K.; Jaramillo, T. F.; Chorkendorff, I.; Nørskov, J. K. Electrochemical Ammonia Synthesis—The Selectivity Challenge. *ACS Catal.* **2017**, *7* (1), 706–709. https://doi.org/10.1021/acscatal.6b03035.
(101) Greenlee, L. F.; Renner, J. N.; Foster, S. L. The Use of Controls for Consistent and Accurate Measurements of Electrocatalytic Ammonia Synthesis from Dinitrogen. *ACS Catal.* **2018**. https://doi.org/10.1021/acscatal.8b02120.
(102) Wang, A.; Li, J.; Zhang, T. Heterogeneous Single-Atom Catalysis. *Nat. Rev. Chem.* **2018**, *2* (6), 65–81. https://doi.org/10.1038/s41570-018-0010-1.
(103) Cui, X.; Li, W.; Ryabchuk, P.; Junge, K.; Beller, M. Bridging Homogeneous and Heterogeneous Catalysis by Heterogeneous Single-Metal-Site Catalysts. *Nat. Catal.* **2018**, *1* (6), 385–397. https://doi.org/10.1038/s41929-018-0090-9.
(104) Alves, M. C. M.; Dodelet, J. P.; Guay, D.; Ladouceur, M.; Tourillon, G. Origin of the Electrocatalytic Properties for Oxygen Reduction of Some Heat-Treated Polyacrylonitrile and Phthalocyanine Cobalt Compounds Adsorbed on Carbon Black as Probed by Electrochemistry and x-Ray Absorption Spectroscopy. *J. Phys. Chem.* **1992**, *96* (26), 10898–10905. https://doi.org/10.1021/j100205a054.
(105) Jaouen, F.; Herranz, J.; Lefèvre, M.; Dodelet, J.-P.; Kramm, U. I.; Herrmann, I.; Bogdanoff, P.; Maruyama, J.; Nagaoka, T.; Garsuch, A.; et al. Cross-Laboratory Experimental Study of Non-Noble-Metal Electrocatalysts for the Oxygen Reduction Reaction. *ACS Appl. Mater. Interfaces* **2009**, *1* (8), 1623–1639. https://doi.org/10.1021/am900219g.
(106) Kramm, U. I. Non Precious Catalysts for Fuel Cells - A Short Review on Mößbauer Spectroscopy of Fe-N-C Catalysts for ORR. *ECS Trans.* **2013**, *58* (1), 119–127. https://doi.org/10.1149/05801.0119ecst.
(107) Kramm, U. I.; Herrmann-Geppert, I.; Behrends, J.; Lips, K.; Fiechter, S.; Bogdanoff, P. On an Easy Way To Prepare Metal–Nitrogen Doped Carbon with Exclusive Presence of MeN_4 -Type Sites Active for the ORR. *J. Am. Chem. Soc.* **2016**, *138* (2), 635–640. https://doi.org/10.1021/jacs.5b11015.
(108) Shen, H.; Thomas, T.; Rasaki, S. A.; Saad, A.; Hu, C.; Wang, J.; Yang, M. Oxygen Reduction Reactions of Fe-N-C Catalysts: Current Status and the Way Forward. *Electrochem. Energy Rev.* **2019**, *2* (2), 252–276. https://doi.org/10.1007/s41918-019-00030-w.
(109) Gojkovic, S. L.; Gupta, S.; Savinell, R. F. Heat-Treated Iron(III) Tetramethoxyphenyl Porphyrin Chloride Supported on High-Area Carbon as an Electrocatalyst for Oxygen Reduction Part II. Kinetics of Oxygen Reduction. *J. Electroanal. Chem.* **1999**, 10.
(110) Van Den Brink, F.; Visscher, W.; Barendrecht, E. Electrocatalysis of Cathodic Oxygen Reduction by Metal Phthalocyanines: Part II. Cobalt Phthalocyanine as Electrocatalyst: A Mechanism of Oxygen Reduction. *J. Electroanal. Chem. Interfacial Electrochem.* **1983**, *157* (2), 305–318. https://doi.org/10.1016/S0022-0728(83)80358-1.
(111) Alt, H.; Binder, H.; Sandstede, G. Mechanism of the Electrocatalytic Reduction of Oxygen on Metal Chelates. *J. Catal.* **1973**, *28* (1), 8–19. https://doi.org/10.1016/0021-9517(73)90173-5.
(112) Coutanceau, C.; Crouigneau, P.; Léger, J. M.; Lamy, C. Mechanism of Oxygen Electroreduction at Polypyrrole Electrodes Modified by Cobalt Phthalocyanine. *J. Electroanal. Chem.* **1994**, *379* (1), 389–397. https://doi.org/10.1016/0022-0728(94)87162-0.
(113) Melendres, C.; Tadjeddine, A.; North Atlantic Treaty Organization. Scientific Affairs Division; NATO Advanced Research Workshop on Synchrotron Techniques in Interfacial Electrochemistry Funchal, M. I. *Synchrotron Techniques in Interfacial Electrochemistry*;

NATO ASI series. Series C, Mathematical and physical sciences ; vol. 432; Kluwer Academic: Dordrecht ; London, 1994.
(114) Jia, Q.; Liu, E.; Jiao, L.; Pann, S.; Mukerjee, S. X-Ray Absorption Spectroscopy Characterizations on PGM-Free Electrocatalysts: Justification, Advantages, and Limitations. *Adv. Mater.* **2018**. https://doi.org/10.1002/adma.201805157.
(115) Yang, X.-F.; Wang, A.; Qiao, B.; Li, J.; Liu, J.; Zhang, T. Single-Atom Catalysts: A New Frontier in Heterogeneous Catalysis. *Acc. Chem. Res.* **2013**, *46* (8), 1740–1748. https://doi.org/10.1021/ar300361m.
(116) Oyama, S. T.; Congress of Pacific Rim Chemical Societies Honolulu, H. *The Chemistry of Transition Metal Carbides and Nitrides*; Blackie Academic & Professional: London, 1996.
(117) Gregory, D. H. Structural Families in Nitride Chemistry. *J. Chem. Soc. Dalton Trans.* **1999**, No. 3, 259–270. https://doi.org/10.1039/A807732K
(118) Alexander, A.-M.; Hargreaves, J. S. J. Alternative Catalytic Materials: Carbides, Nitrides, Phosphides and Amorphous Boron Alloys. *Chem. Soc. Rev.* **2010**, *39* (11), 4388. https://doi.org/10.1039/b916787k.
(119) Jacobsen, C. J. H. Novel Class of Ammonia Synthesis Catalysts. *Chem. Commun.* **2000**, No. 12, 1057–1058. https://doi.org/10.1039/b002930k.
(120) Jacobsen, C. J. H.; Dahl, S.; Clausen, B. S.; Bahn, S.; Logadottir, A.; Nørskov, J. K. Catalyst Design by Interpolation in the Periodic Table: Bimetallic Ammonia Synthesis Catalysts. *J. Am. Chem. Soc.* **2001**, *123* (34), 8404–8405. https://doi.org/10.1021/ja010963d.
(121) Zeinalipour-Yazdi, C. D.; Hargreaves, J.; Laassiri, S.; Catlow, R. C. A. The Integration of Experiment and Computational Modelling in Heterogeneously Catalysed Ammonia Synthesis over Metal Nitrides. *Phys. Chem. Chem. Phys.* **2018**. https://doi.org/10.1039/C8CP04216K.
(122) AlShibane, I.; Daisley, A.; Hargreaves, J. S. J.; Hector, A. L.; Laassiri, S.; Rico, J. L.; Smith, R. I. The Role of Composition for Cobalt Molybdenum Carbide in Ammonia Synthesis. *ACS Sustain. Chem. Eng.* **2017**, *5* (10), 9214–9222. https://doi.org/10.1021/acssuschemeng.7b02168.
(123) Díez-Ramírez, J.; Kyriakou, V.; Garagounis, I.; Vourros, A.; Vasileiou, E.; Sánchez, P.; Dorado, F.; Stoukides, M. Enhancement of Ammonia Synthesis on a Co_3Mo_3N-Ag Electrocatalyst in a K-BAl_2O_3 Solid Electrolyte Cell. *ACS Sustain. Chem. Eng.* **2017**, *5* (10), 8844–8851. https://doi.org/10.1021/acssuschemeng.7b01618.
(124) Prior, T. J.; Battle, P. D. Facile Synthesis of Interstitial Metal Nitrides with the Filled β-Manganese Structure. *J. Solid State Chem.* **2003**, *172* (1), 138–147. https://doi.org/10.1016/S0022-4596(02)00171-8.
(125) Volpe, L.; Boudart, M. Ammonia Synthesis on Molybdenum Nitride. *J. Phys. Chem.* **1986**, *90* (20), 4874–4877. https://doi.org/10.1021/j100411a031
(126) Volpe, L.; Boudart, M. Compounds of Molybdenum and Tungsten with High Specific Surface Area: I. Nitrides. *J. Solid State Chem.* **1985**, *59* (3), 332–347. https://doi.org/10.1016/0022-4596(85)90301-9.
(127) Roberts, K. L.; Markel, E. J. Generation of Mo2N Nanoparticles from Topotactic Mo2N Crystallites. *J. Phys. Chem.* **1994**, *98* (15), 4083–4086. https://doi.org/10.1021/j100066a029
(128) Hargreaves, J. S. J. Nitrides as Ammonia Synthesis Catalysts and as Potential Nitrogen Transfer Reagents. *Appl. Petrochem. Res.* **2014**, *4* (1), 3–10. https://doi.org/10.1007/s13203-014-0049-y.
(129) Hargreaves, J. S. J.; Mckay, D. A Comparison of the Reactivity of Lattice Nitrogen in Co3Mo3N and Ni2Mo3N Catalysts. *J. Mol. Catal. Chem.* **2009**, *305* (1–2), 125–129. https://doi.org/10.1016/j.molcata.2008.08.006.

(130) Wang, H.; Li, W.; Zhang, M. New Approach to the Synthesis of Bulk and Supported Bimetallic Molybdenum Nitrides. *Chem. Mater.* **2005**, *17* (12), 3262–3267. https://doi.org/10.1021/cm047735d.

2 Analytical Techniques

2.2 X-ray Diffraction 49
2.3 X-ray Photoelectron Spectroscopy 52
2.4 X-ray Absorption Spectroscopy 55
2.5 Transmission Electron Microscopy 59
2.6 Infrared Spectroscopy 62
2.7 Electrochemical Techniques 65
2.8 References 67

2.1 Introduction

Over the last century, scientists have developed a wide range of analytical techniques and characterisation methods exploiting an extensive spectrum of physical phenomena to investigate the electronic and structural properties of catalytic materials.[1] These techniques range from microscopy which images the structure and morphology of catalysts down to Angstrom level, to absorption techniques probing the electronic structure to diffraction which explores the crystal structure of materials.[1] Often a lot of different characterisation methods need to be used in conjunction to obtain a good understanding of a catalyst and obtain a structure-activity relationship which can guide the rational development of future catalytic materials. [2]

The last couple of decades have seen a massive increase in capabilities of characterisation techniques particularly in microscopy due to commercialisation of aberration correctors and in X-ray techniques due to the use of synchrotron radiation. These developments had an extensive impact on the research landscape. The advent of atomic resolution imaging with aberration corrected transmission electron microscopes in the early 2000s has, for example, led to an explosion of the research area of single-atom catalysts loosely defined as catalytic materials comprised of atomically dispersed transition metals on a heterogeneous support.[3] Most synthesis techniques and applications in that field have been known for decades but only after advances in electron microscopy did the research field gain in size, highlighting the importance of instrument development as a driver for research.[3]

Rapid progress has recently also been made in in-situ and operando techniques making it possible to observe catalysts in conditions more closely resembling real life settings. [2] Most analytical techniques investigate catalytic material ex-situ, often in special

conditions such as high vacuum widely different to the operational environment in reactors meaning that the material might look and behave significantly differently, especially at the active site.[2] Emerging techniques such as environmental transmission electron microscopy and X-ray photoelectron spectroscopy, as well as in-situ and operando X-ray absorption make it more and more possible to observe the active site during catalytic turnover and will hopefully translate into a new generation of rationally designed catalysts enabling novel and more renewable chemical transformations.

2.2 X-ray Diffraction

Powder X-ray powder diffraction (XRD) is a powerful technique to investigate the crystalline structure of heterogeneous catalyst materials.[4] More specifically, it is used as a fingerprint to identify the material, elucidate the lattice constants, unit cell parameters, the dominant phases and estimate crystallite sizes and strains.[4] X-ray radiation is composed of high-energy photons which when shone onto a sample are elastically scattered by the electron density around nuclei.[5] X-rays have a wavelength in the Angstrom range, similar to the interatomic spacing in crystalline materials. The ordered crystallographic planes act as a grating and hence the incident X-rays are subject to diffraction.[5] Due to the low interaction between X-rays, as well as with atoms of the material, they penetrate deeply into the material and hence XRD is considered a bulk characterisation technique. [5]

In most lab-based diffractometers X-rays are produced in cooled evacuated tubes by applying a voltage between a hot cathode and an anode.[5] The cathode emits high-energy electrons into the vacuum which crash into the anode, often made of copper, tungsten or molybdenum leading to the ejection of core electrons from these materials.[5] Electrons from higher energy orbitals drop down, resulting in the emission of X-ray radiation with

a wavelength specific to the source materials. These X-rays are passed through a collimator and a monochromator to produce a parallel beam of photons with a narrow wavelength distribution.[5] The material of interest is illuminated with this beam at different incident angles, usually by moving the X-ray source. If long-range crystalline order is present, the elastically scattered photons can constructively or destructively interfere depending on the incident angle, photon wavelength and the interlayer spacing (Fig.1), leading to a unique diffraction pattern which can be compared to reference data bases for material identification.

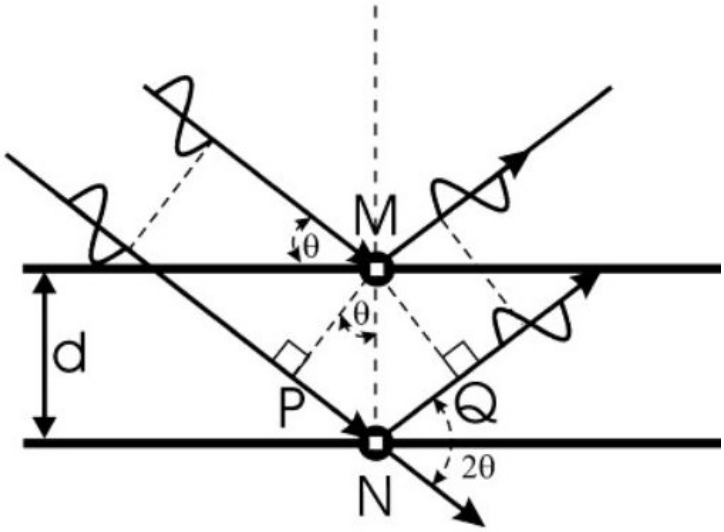


Figure 1: *Simplified illustration of destructive interference of X-rays scattered from crystal planes. Reproduced with permission from the Royal Society of Chemistry from reference* [5].

Bragg's law (Eq.1) is used to elucidate the interlayer spacing (d) from the experimentally determined diffraction angle (θ) and the known wavelength of the beam (λ).

$$n\lambda = 2\, d\, sin\theta \qquad \text{(Eq.1)}$$

Using the obtained interlayer spacing for the individual peaks it is possible to index the pattern, i.e. assign a crystallographic plane with Miller indices to a peak from which the

lattice type can be inferred. Furthermore, this information can be used to determine the lattice parameters as shown in Equation 2 for cubic systems where a is the lattice parameter and h, k and l are the Miller indices:

$$\frac{1}{d^2} = \frac{(h^2+k^2+l^2)}{a} \quad \text{(Eq.2)}$$

Compression or expansion of the lattice is observed by shifts in the diffraction angles and can be related to changes in the lattice due to alloying, intercalation or differences in interstitial site occupation.

Due to the long-range order of crystallographic systems, destructive interference occurs at all angles other than the diffraction angles leading to sharp well defined peaks. When the crystallite size is decreased, the interlayer spacing distribution is widened due to the increased influence of edges, as well as surfaces, and as such diffraction occurs at a wider range of angle leading to peak broadening. The Scherrer equation (Eq.3) can be used to estimate the crystallite size:

$$\tau = \frac{K\lambda}{\beta\, cos\theta} \quad \text{(Eq. 3)}$$

where τ is the crystallite size, K is a form factor (usually close to unity), λ is the wavelength of the incident photon, β is the peak broadening at full width half maximum (FWHM) of the peak of interest minus the instrumental line broadening and θ is the diffraction angle. Care should be taken when using crystallite size estimates obtained via the Scherrer equation due to uncertainties associated with this strategy, such as difficulties to accurately determine the background for particles in the nanometre range, overestimation of particle size due weighting by volume rather than by particle number,

etc. Additionally, factors other than crystallite size, such as strains, twinning and defects can also lead to peak broadening making it an imperative to use other characterisation techniques such as transmission electron microscopy (TEM) or dynamic light scattering (DLS) in conjunction with XRD to obtain an accurate estimate of particle size.

2.3 X-ray Photoelectron Spectroscopy

X-ray photoelectron spectroscopy (XPS) is a surface sensitive chemical characterisation technique which provides information about the elemental composition of a sample, as well as the oxidation states and bonding environments of the elements present.[4] As with XRD, in XPS the sample is illuminated with an X-ray beam but the source element usually is aluminium instead of copper, resulting in lower energy photons of around 1486.7 eV.[6] In contrast to XRD, XPS is not based on diffraction but the photoelectric effect wherein the incident photons are absorbed by core electrons of individual elements within the sample leading to subsequent ejection of photoelectrons. The quantity and energy of the photoelectrons is measured and used to determine the binding energy of the electron using the following equation deduced by Rutherford (Eq.4):

$$E_b = h\nu - E_{kin} - \Phi \qquad \text{(Eq. 4)}$$

where E_b is the binding energy of the excited electron, h is Planck's constant, E_{kin} is the measured kinetic energy of the ejected electron and Φ is the work function of the spectrometer. [7]

The emission of a photoelectron leads to the formation of a core hole which is relaxed by an electron from a higher energy orbital dropping down. The excess energy is released by the emission of X-ray radiation of element specific wavelength or can be transferred to a secondary electron which is subsequently emitted (Fig.2). These secondary electrons

are referred to as Auger electrons and are also detected during XPS measurements with their kinetic energy equalling the difference of the energy of the initial electronic transition and ionization energy of the orbital from which the Auger electron was emitted. Auger peaks in conjunction with photoelectron peaks can be helpful for the identification of chemical states.[6]

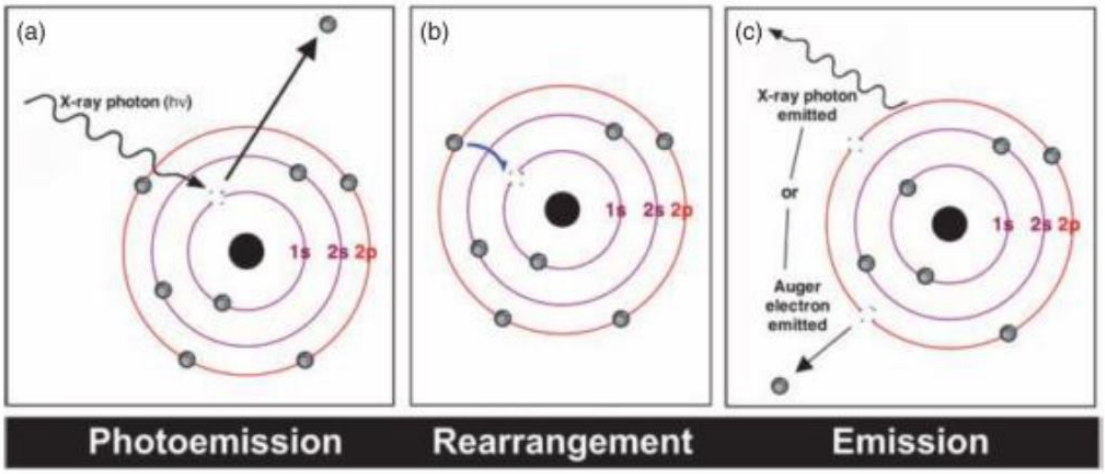


Figure 2: *Graphical illustration of formation and subsequent relaxation of an electron core hole in XPS. Reproduced from reference* [8] *from John Wiley and Sons.*

A standard laboratory spectrometer consists of an X-ray source, a monochromator, a stainless steel sample chamber under ultra-high vacuum and an electron detector. Recent detector developments and access to synchrotron X-ray sources have produced spectrometers which are able to measure in few mbar of atmosphere and even in the presence of liquids.[9]

The obtained binding energies of measured photoelectrons are characteristic for elements such that low resolution surveys taken from 0 to around 1400eV can be used to determine the overall relative composition of the sample.[7] In order to obtain accurate compositional data the relative sensitivity factors (RSF) of elements need to be taken into account. [7]

To investigate the oxidation states, chemical bonding environment and crystal structure acquiring higher resolution scans of element specific regions is necessary. Generally speaking, peaks shifting to higher binding energies indicates an oxidation of the element of interest and is generally on the order of few eV. Peaks for photoelectrons from p, d and f orbitals split into doublets due to spin-orbit coupling in the final state with the respective ratios of 2:1, 3:2 and 4:3 with the peak of lower total angular momentum quantum number occurring at higher binding energies.[6] The magnitude of the splitting is orbital element specific, increasing with atomic number and decreasing with distance to nucleus, which can be helpful in the analysis of materials containing elements with mixed oxidation states. [6]

The loss of electrons due to the photoelectric effect can lead to a charging of the surface which is especially problematic when the sample is non-conducting or not in good contact with the spectrometer. The accumulation of positive charge around the measurement area leads to a consistent upshift of binding energies. This problem can be tackled experimentally using a combination gun or obtained spectra can be charge corrected post experiment.[6] Post experimental charge correction is often done by fixing the 1s peak of sp^3 hybridised carbon to 284.8 eV and shifting all other spectra accordingly.[10] Most samples that were exposed to atmosphere at some point are surface contaminated with adventitious carbon, which typically contains a C-C component in its C1s region that can be used to do the charge correction, making this method widely applicable.[11] Depending on the surface of the sample 284.8eV might not always be a valid reference value and other charge referencing techniques, e.g. using the Fermi edge, should be used. [6,11]

The surface sensitivity of this technique stems from the fact that the emitted photoelectrons have to travel through the sample into the continuum to be detected. On

their way, photoelectrons can interact with the sample in several ways including recapture or trapping within excited states, inelastic collisions or recombination leading to attenuation of the signal from ejected electrons. This attenuation increases exponentially with sample depth leading to the majority of measured photoelectrons coming from the first 0-10nm of the sample.[7] Different techniques to investigate the change of chemical composition of the sample with depth have been developed including angle-resolved XPS where the sample is tilted, and depth profiling using ion sputtering. In depth profiling monatomic ion beams are used to etch away surface contamination and/or the top layers of the sample to measure the composition of the underlying surface, subsurface or bulk.[7] The amount of material removed per incident ion, often referred to as sputter yield, depends on the identity of the ions, energy of the ion beam, incident angle and the sample itself. Halogens are often used for ion sputtering applications with Ar^+ being the most common choice for XPS depth profiling.[7]

2.4 X-ray Absorption Spectroscopy

X-ray absorption spectroscopy (XAS) is another technique that utilises X-ray radiation to excite core electrons. It is used to determine the electronic state, chemical bonding environment and local geometry of matter. Usually, XAS measurements are conducted at synchrotrons due to the availability of high intensity and tunable X-rays, enabling the detection and analysis of very dilute samples. Since XAS does not require periodicity and can look at almost every element in the periodic table, it is a powerful method to analyse a wide range of materials in gaseous, liquid and solid state.[12] In contrast to XPS, X-rays are detected instead of electrons which interact far less strongly with the sample meaning XAS is considered a bulk characterisation technique.[12] Surface sensitivity can be

achieved by electron yield measurements, effectively detecting Auger electrons emitted from the sample due to X-ray absorption.[12]

XAS is measured in two geometries, namely transmission and fluorescence. In transmission mode the initial and final intensity of the beam are measured, with an ion chamber before and after the sample, using Beer-Lambert law to determine the absorption coefficient. This approach is limited to concentrated samples (>10mM) and is often used to measure standards of materials.[12] As previously mentioned, the initial absorption of X-ray radiation by a core electron leads to the ejection of a photoelectron leaving the element of interest in an excited state which is relaxed by an electron of a higher energy orbital dropping down. The excess energy is released either in form of an Auger electron or as X-ray radiation (fluorescence). In fluorescence measurements the X-ray detectors is placed at an angle, usually 90°, to the sample (Fig.3) and require some kind of energy resolution, usually in the form of a low pass filter, to distinguish fluorescent X-rays from background scattering of the initial beam.[12] This technique is able to measure X-ray absorption spectra for very dilute samples, making it particularly popular in the analysis of catalysts, biological and environmental samples.

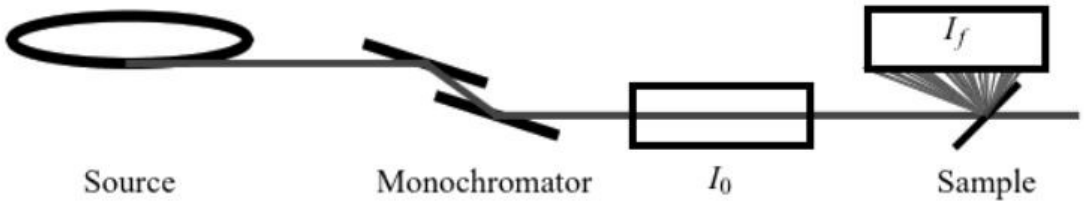


Figure 3: *Basic set-up for XAS measurement in fluorescence mode. Reproduced from reference* [13] *with permission of Cambridge University Press through PLSclear.*

XAS spectra are generally divided into two regions, so called X-ray Absorption Near-edge Structure (XANES) and Extended X-ray Absorption Fine Structure (EXAFS)

(Fig.4). The distinction is largely arbitrary since the governing physics of photoabsorption are the same but is of value since the data analysis and theoretical modelling vary significantly. The XANES portion of the spectrum describes the region around the white line intensity and is sensitive to the oxidation state and the geometry of the coordination environment of the absorbing atom.[12] Next to the edge energy, important features in the XANES include electric-dipole allowed transition from the core level to quasi-bound states (e.g. 1s → 4p for first row transition metals) in the rising edge, as well as dipole selection rule forbidden transitions (e.g. 1s →3d for first row transition metals) in the pre-edge. These can be used to probe the electronic structure of the absorber and its coordination geometry. A more in depth discussion of XANES is provided in Chapter 5 Section 6.

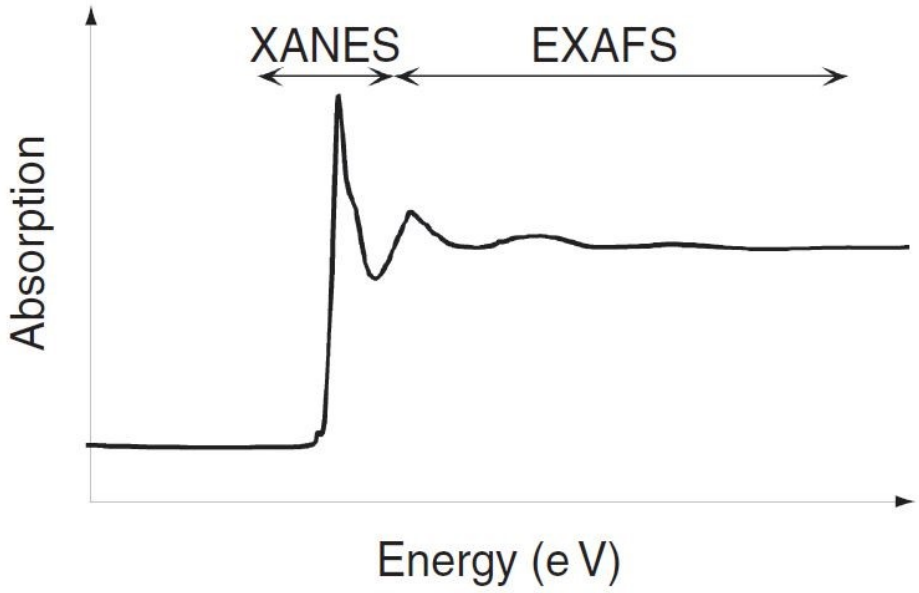


Figure 4: Typical X-ray absorption spectrum showing the XANES and EXAFS regions. Reprinted from reference [12] with permission from Elsevier.

The EXAFS region extends several hundred eV from the white line of the element and provides information of the coordination number of the absorber, distance to and identity

of the neighbouring atoms. The EXAFS is best understood as a scattering phenomenon of a photoelectron that either constructively or destructively interferes with a second photoelectron from the absorber leading to an oscillating behaviour of the spectrum.[12] This is possible due to the higher kinetic energy of the photoelectron in this region giving it a de Broglie wavelength on the scale of the atomic distance between the absorber and its closest neighbours.[12] Scattering is dependent on the atomic number of the neighbouring atoms meaning it is not only possible to infer the number of atoms in the first coordination sphere but also their identity. Classically, Fourier transform analysis is performed on EXAFS to obtain a pseudo-radial distribution. This provides an estimate of the distance between the absorber and the nearest neighbours from which, using reference materials, inferences about the identity of neighbours can be drawn. In systems with several potential scatters conclusive identification of the neighbouring elements using FT can be difficult due to the overlap of several scattering paths to form one peak. Obtaining radial as well as k-space resolution is necessary to separate contributions from different neighbours at roughly similar distances to the absorber. This can be realised using wavelet transform analysis. For application in this thesis, Morlet wavelets (Eq.5) will be used which essentially consist of a complex sine function confined by a Gaussian:

$$\psi(t) = \frac{1}{\sqrt{2\pi}\sigma}\left(\exp(i\kappa t) - \exp\left(-\frac{\kappa^2}{2}\right)\right)\exp\left(-\frac{t^2}{2\sigma^2}\right) \qquad \text{(Eq.5)}$$

Here κ and σ are the free Morlet parameters. σ stands for the half-width of the Gaussian envelope and κ signifies the number of oscillations under the Gaussian in case of σ=1. These parameters can be adjusted to obtain better resolution in either k- or R-space with

lower κ values yielding higher resolution in k-space. Further discussion of WT analysis for EXAFS is provided in Chapter 5 Section 6.3.2.

XAS is useful technique to observe catalysts during reactions under in-situ or operando conditions due to possibilities to easily measure in the gaseous, liquid and solid state over a wide range of temperatures. New developments in the measurement modes, such as "quick EXAFS" scanning, have also cut down the time needed to acquire good quality EXAFS, as well as XANES spectra, significantly increasing the time resolution.

2.5 Transmission Electron Microscopy

Since the advent of modern catalyst development there has been a large demand for accurate imaging of catalyst surfaces and visualisation of active sites at the atomic level. This is not possible with standard light microscopy due to the Abbe resolution limit of around 1μm set by the wavelength of visible light. The de Broglie wavelength of electrons is significantly smaller allowing electron microscopes to image materials with much better resolution. Transmission electron microscopy (TEM) is becoming one of the most important imaging techniques in field of catalysis due to it is superior resolution compared to SEM and large array of available additional detectors. Similarly to SEM, detectors for secondary electrons (SE), back-scattered electrons (BSE), Auger electrons (AE) and characteristic X-ray radiation (EDX) can also be fitted to TEMs allowing the simultaneous acquisition of data on elemental composition, electronic structure and topography.[1] Furthermore, there are several different imaging modes out of which bright field, dark field, as well as some scanning transmission electron microscopy techniques will be introduced here.

A standard TEM consists of an electron gun, usually composed of a heated tungsten or LaB6 cathode filament from which electrons can be ejected thermoionically and are accelerated towards an anode.[1] Newer instruments such as the JEOL ARM200F used in this thesis use cold field-emission guns where the tungsten emitter is kept at room temperature leading to a narrower energy distribution of the electron beam (~0.3eV) which is advantageous for spectroscopic applications. The resulting electron beam is focused using several electromagnetic condenser lenses, as well as apertures and shone onto a perpendicularly placed sample stage.[1] For TEM ultrathin samples are required (<200nm) which are usually mounted onto holey carbon copper or gold grids. Electrons of the beam are either passed through the sample without interacting (transmission), diffracted or inelastically scattered leading to secondary electrons, Auger electrons, X-ray emission. Transmitted and diffracted electrons are refocused using an objective lens.[1] Objective apertures are inserted in the back focal plane of the objective lens to select between diffracted and transmitted electrons (Fig.5). When the central beam, i.e. transmitted electrons, are let through the aperture the bright field image will be displayed showing high electron density as dark areas whereas when the aperture allows scattered electrons to pass the dark field image is shown where electron dense areas appear bright. Following this aperture, an intermediate and a projector lens magnify and project, respectively, the selected part of the electron beam onto a fluorescent screen or a charge-coupled device (CCD) camera.

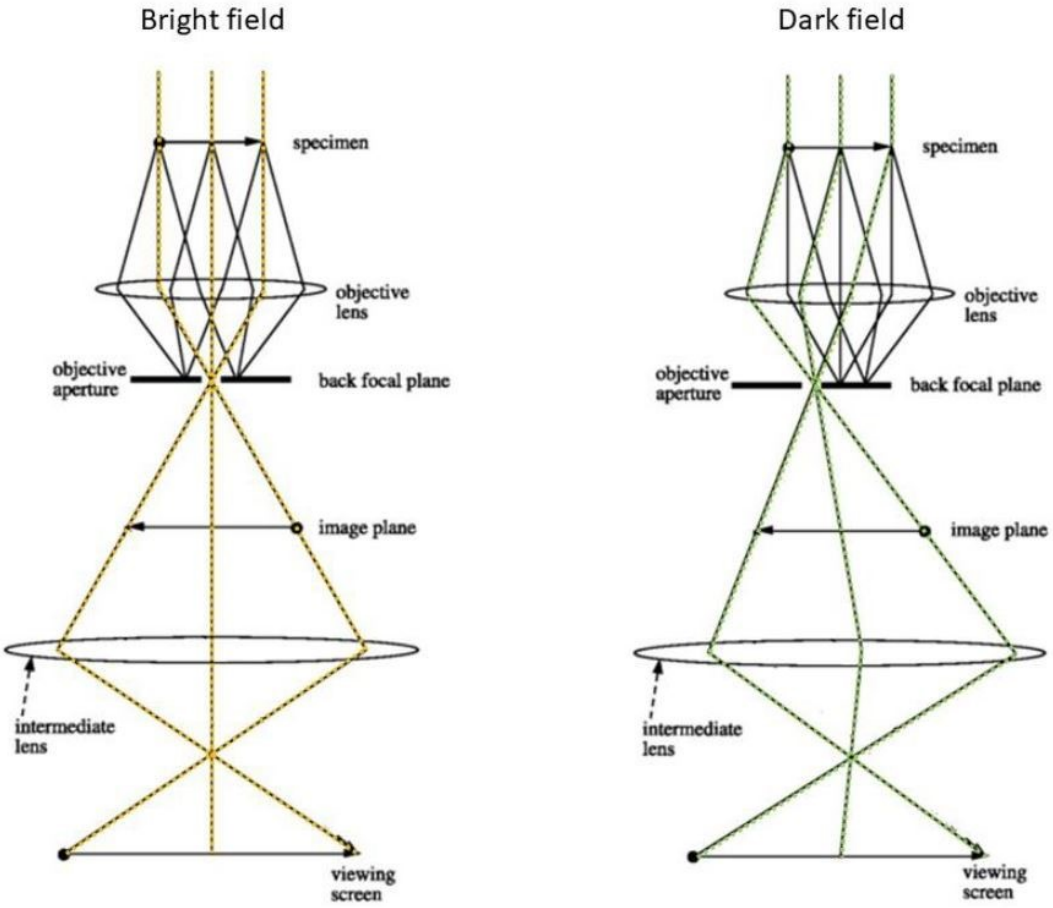


Figure 5: *Images showing aperture placement for bright field (left) and dark field (right) imaging in TEM mode. Reprinted from reference* **[14]** *by permission of Springer Nature.*

Resolution in such standard systems is limited by the de Broglie wavelength of the beam electrons and the quality of the objective lens. Increasing the acceleration voltage to shorten the wavelength of the electrons can increase resolution although it can also lead to the destruction of the sample through knock-on damage.[1] For some samples of interest, like graphene the acceleration voltage to cause knock-on damage is as low as 80keV which does not leave room for resolution improvement.[15] The main indicator of objective lens quality is spherical aberration coefficient (C_s) which describes smearing in the image caused by incorrectly focused high angle electron rays.[1] This limitation is more and more mitigated using nonround lenses with negative C_s values based on hexapoles or

quadrupole/octopole designs.[15] Chromatic aberrations, another source of resolution loss, can be alleviated using a monochromator.[16] The arrival of such aberration corrected TEM and STEM systems pushed down the resolution limit to below 0.5Å making the imaging of single-atoms possible and more widely available.[17]

Some transmission electron microscopes are fitted with additional equipment to allow for measurements in scanning transmission electron microscopy (STEM). Using scanning coils the electron beam is focused to a very fine spot (spot size 0.05 – 0.2nm) which is scanned across the sample in a raster fashion. Additional removable detectors are fitted including a bright field (BF) detector in the way of the beam measuring transmitted electrons. In contrast to conventional TEM, no objective aperture is used to isolate scattered electrons but an annular dark field (ADF) detector which surrounds the beam and hence excludes unscattered electrons. When placed at very high angles, they are often referred to as high-angle annular dark field (HAADF) detectors which measure incoherently scattered electrons.[1] HAADF-STEM is particularly sensitive to the atomic number (with contrast being roughly proportional to Z^2) making this a great technique to investigate dispersed heavy atoms on lighter support such as metal nanoparticles or even atomically dispersed metal species on a carbon support. A further advantage is that the linearly transmitted beam can also be analysed in particular using a characterisation method called electron energy loss spectroscopy (EELS).

2.6 Infrared Spectroscopy

In infrared spectroscopy (IR) samples are illuminated with photons of wavelength between 0.8 to 1000μm usually measuring absorption.[4] Typical IR spectra display the photon frequency in the unit wavenumber (cm^{-1}) on the x-axis and absorbance or transmittance on the y-axis. Absorption at characteristic frequencies corresponds to

vibrational states of intramolecular bonds making it possible to show the presence of a wide range of functional groups. As such, IR is an important technique in structure identification of organic and organometallic compounds. In heterogeneous catalysis, IR is more commonly used to study chemisorbed molecules, investigating the electronic and geometric properties of the surface, monitor reaction intermediates or investigate active site poisoning phenomena. [2,18]

Most modern IR spectrometers use a Michelson interferometer, a set-up of motorised mirrors, leading to the exposure of the sample with IR photons of several wavelengths at the same time, rapidly changing the composition of the beam. A computer collates the resulting spectra and uses Fourier transform (FT) to infer the absorption at individual wavelengths.[1] This approach has several advantages over classical scanning approaches where the sample is exposed to a beam of photons at single wavelength which is continually varied, resulting in higher signal-to-noise ratio.

Intramolecular vibrations can be thought of as two masses connected via a spring and as such can be approximated as a harmonic oscillator with the absorption frequency equalling the resonant frequency of the system. Hooke's law (Eq.6) describes such a simple harmonic oscillator:

$$\nu = \frac{1}{2\pi c}\sqrt{\frac{k(m_1+m_2)}{m_1 m_2}} \qquad \text{(Eq.6)}$$

where ν is the vibrational frequency in cm^{-1}, c is the speed of light, k is the force constant of the bond and m_1 and m_2 are the masses of the bonding forming atoms. This makes it possible to relate the absorption frequency to the bond strength and mass of atoms involved enabling functional group assignment, as well as probing the effect of isotopic

substitution. Molecules can vibrate in several ways including amongst others stretching, rocking, scissoring, twisting and wagging with nonlinear molecules having 3N-6 degrees of vibrational freedom.[1] In order for a vibrational mode to be IR active a change of dipole has to occur.

A standard IR spectrometer is composed of an IR source, an interferometer, a beam splitter, a reference and a sample chamber, a splitter alternating between the reference and sample beam to reach the detector which is connected to a data analysis system.[1] Samples are often measured diluted in a pellet of a matrix such as KBr or CsI. Heterogeneous catalyst materials or other parts of the reaction mixture often heavily absorb IR radiation or require measurements in-situ which are not possible in such a matrix approach. Attenuated total reflectance (ATR) is used to overcome this limitation. ATR uses the phenomenon of total internal reflection; where light passing through a high refractive index material is totally reflected at the interface with a lower refractive index material above certain angles. At the points of reflection an evanescent wave is created stretching into lower refractive index material.[19,20] Material at the interface can absorb energy from the wave and as such attenuate the IR beam in the energy range of the absorbing vibrational mode. An IR beam can be reflected several times inside the high refractive index material before passing onto the detector. Using FT a standard IR spectrum is produced. In order to guarantee total internal reflection ATR crystals are made of very high refractive index materials transparent to IR radiation such as germanium and zinc selenide.[19] In this configuration, liquid and solid samples can be measured without further preparation by direct deposition onto the crystal. Recently, ATR IR set-ups have also been used in electrochemical flow cells enabling in-situ

measurements of surface adsorbates. A more in-depth discussion on this topic is provided in Chapter 5 Section 5.

2.7 Electrochemical Techniques

Herein electrochemical characterisation methods using a three electrode set-up consisting of a working (WE), counter (CE) and reference electrode (RE) connected to a potentiostat are described. Commonly used reference electrodes in aqueous electrolytes include saturated calomel electrode (SCE), silver/silver chloride electrode (Ag/AgCl) or mercury/mercury oxide (Hg/HgO) which can be calibrated to the reversible hydrogen electrode potential to make measured potentials comparable across reference electrodes and pH.[21,22] Conversion of potential to the RHE scale can be achieved experimentally by measuring the potential difference between the reference electrode of interest and a RHE or by measuring the zero crossing potential of a Pt wire in the hydrogen-saturated electrolyte of interest.[21,22] Counter electrodes in aqueous electrolytes are often made of platinum and are separated from the catholyte using a frit to inhibit contamination with dissolving Pt species or oxidation/reduction products.[22] Glassy carbon electrodes (GCE) are standardly used as working electrodes due to their electrocatalytical inertness over a large potential window and good conductive properties.[22] In order to test its electrochemical properties, a known amount of electrocatalyst ink, often containing ion conducting polymers such as Nafion, is drop casted onto the GCE forming the WE.[22] The rate of an electrochemical reaction can be controlled by controlling the magnitude of the Faradaic current, i.e. the number of electrons transferred across the electrode-electrolyte interface from or to the electrode to achieve a reaction per time. The performance of an electrocatalysts can then be assessed by measuring the overpotential, i.e. the potential that is needed in addition to the thermodynamic potential to obtain a certain amount of

current or turnover which is effectively a proxy for the activation energy of the electrocatalytic process over the electrocatalyst at hand.[21]

A frequently used analysis method is voltammetry which measures current as a function of potential. The potential can be stepped or continuously changed. A special case of this is linearly scanning voltammetry (LSV) which changes the potential on a linear ramp.[21] LSV is a popular method to quickly evaluate the performance of electrocatalysts across a wide potential range because at very low scan rates (<5mV/s) capacitive contributions to the signal become minute[22] and the measured current can be approximated to be an estimate of the steady-state current at the given potential.

Another powerful technique is cyclic voltammetry (CV) where the potential is swept back in the opposite direction after the initial sweep.[21] This is done to assess the reversibility of redox processes occurring at the electrode surface and can further provide a breadth of information on species in solution, reaction kinetics, catalyst surface composition and area.[21] To determine whether a redox couple is reversible its Faradaic peak currents as well as peak potentials should be determined at varying scan rates. The relationship between peak currents and scan rate can provide information on the type of species involved and the peak separation contains information about the reversibility of the reaction. [22] In electrocatalysis, CVs are often used to clean the surface of the catalyst from adsorbates such as adventitious carbon by sweeping between reducing and oxidising potentials. Furthermore, cyclic voltammetry can be used to provide an estimate of the electrochemically active surface area (ECSA) by determining the double layer capacitance or by investigating surface specific adsorption phenomena such as the underpotential deposition of hydrogen onto platinum surfaces (H_{UPD}).[21]

Another subclass of electroanalytical techniques is chronoamperometry (CR) which measures the current as a function of time at a fixed potential.[21,22] CR is routinely used as an initial investigation into the long-term stability of electrocatalysts. The voltammetry equivalent to this is called chronovoltammetry where the potential is measured as a function of time while passing a fixed current. [21,22]

Further discussion on the theoretical underpinnings of voltammetry can be found in Chapter 1 Section 1.

2.8 References

(1) Günzler, H.; Williams, A. *Handbook of Analytical Techniques*; Wiley-VCH: Weinheim ; Chichester, 2001.

(2) Rodríguez, J. A.; Hanson, J. C.; Chupas, P. J. *In-Situ Characterization of Heterogeneous Catalysts*; Wiley: Hoboken, New Jersey, 2013.

(3) Yang, X.-F.; Wang, A.; Qiao, B.; Li, J.; Liu, J.; Zhang, T. Single-Atom Catalysts: A New Frontier in Heterogeneous Catalysis. *Accounts of Chemical Research* **2013**, *46* (8), 1740–1748. https://doi.org/10.1021/ar300361m.

(4) Atkins, P. W. *Shriver & Atkins' Inorganic Chemistry*; Oxford University Press: Oxford; New York, 2010.

(5) Dinnebier, R. E.; Billinge, S. J. L. *Powder Diffraction: Theory and Practice*; Royal Society of Chemistry: Cambridge, 2008.

(6) Briggs, D.; Grant, J. T.; SurfaceSpectra Limited. *Surface Analysis by Auger and X-Ray Photoelectron Spectroscopy*; IM Publications: Chichester, 2003.

(7) Van der Heide, P. *X-Ray Photoelectron Spectroscopy: An Introduction to Principles and Practices*; Wiley: Hoboken, N.J., 2012.

(8) Vickerman, J. C.; Gilmore, I. S. *Surface Analysis: The Principal Techniques*, 2nd ed.; John Wiley & Sons Ltd: Chichester, 2009.

(9) Fadley, C. S. X-Ray Photoelectron Spectroscopy: Progress and Perspectives. *Journal of Electron Spectroscopy and Related Phenomena* **2010**, *178–179*, 2–32. https://doi.org/10.1016/j.elspec.2010.01.006.

(10) Miller, D. J.; Biesinger, M. C.; McIntyre, N. S. Interactions of CO2 and CO at Fractional Atmosphere Pressures with Iron and Iron Oxide Surfaces: One Possible Mechanism for Surface Contamination? *Surface and Interface Analysis* **2002**, *33* (4), 299–305. https://doi.org/10.1002/sia.1188.

(11) Barr, T. L.; Seal, S. Nature of the Use of Adventitious Carbon as a Binding Energy Standard. *Journal of Vacuum Science & Technology A: Vacuum, Surfaces, and Films* **1995**, *13* (3), 1239–1246. https://doi.org/10.1116/1.579868.

(12) Penner-Hahn, J. E. 2.13 - X-Ray Absorption Spectroscopy. In *Comprehensive Coordination Chemistry II*; McCleverty, J. A., Meyer, T. J., Eds.; Pergamon: Oxford, 2003; pp 159–186. https://doi.org/10.1016/B0-08-043748-6/01063-X.

(13) Bunker, G. *Introduction to XAFS: A Practical Guide to X-Ray Absorption Fine Structure Spectroscopy*; Cambridge University Press: Cambridge, UNITED KINGDOM, 2010.
(14) Fultz, B. *Transmission Electron Microscopy and Diffractometry of Materials [Electronic Resource]*, 4th ed. 2013.; Graduate texts in physics; Springer Berlin Heidelberg: Berlin, Heidelberg, 2013.
(15) Rose, H. H.; Wan, W. Aberration Correction in Electron Microscopy. **2005**, 5.
(16) Hetherington, C. Aberration Correction for TEM. *Materials Today* **2004**, *7* (12), 50–55. https://doi.org/10.1016/S1369-7021(04)00571-1.
(17) Erni, R.; Rossell, M. D.; Kisielowski, C.; Dahmen, U. Atomic-Resolution Imaging with a Sub-50-Pm Electron Probe. *Phys. Rev. Lett.* **2009**, *102* (9), 096101. https://doi.org/10.1103/PhysRevLett.102.096101.
(18) Nakamoto, K. Infrared and Raman Spectra of Inorganic and Coordination Compounds. In *Handbook of Vibrational Spectroscopy*; American Cancer Society, 2006. https://doi.org/10.1002/0470027320.s4104.
(19) Gremlich, H.-U. Infrared and Raman Spectroscopy. In *Handbook of Analytical Techniques*; John Wiley & Sons, Ltd, 2008; pp 465–507. https://doi.org/10.1002/9783527618323.ch17.
(20) George, W. O. *Infrared Spectroscopy*; Analytical Chemistry by Open Learning (Series); Published on behalf of ACOL, London, by Wiley: Chichester [West Sussex] ; New York, 1987.
(21) Bard, A. J. *Electrochemical Methods: Fundamentals and Applications*, Second edition.; Wiley: New York ; Chichester, 2001.
(22) Brett, C. M. A. *Electrochemistry: Principles, Methods, and Applications*; Oxford science publications; University Press: Oxford, 1993.

3 Experimental Methods

3.1 Characterisation 70

3.1.1 XRD 70

3.1.2 XPS 70

3.1.3 TEM 71

3.1.4 STEM 71

3.2 Catalyst Testing in Aqueous Media 71

3.2.1 HER Activity Testing 71

3.2.2 NRR Activity Screening 73

3.2.3 Ammonia Detection 75

3.2.4 In-situ IR Spectroelectrochemistry 77

3.2.5 In-situ XAS Spectroelectrochemistry 79

3.3 Experiments in Molten Salts 81

3.3.1 Experimental Setup 81

3.3.2 Salt Preparation 84

3.3.3 Electrochemistry in Molten Salts 85

3.3.4 Ammonia Detection 86

3.4 References 86

3.1 Characterisation

3.1.1 XRD

Powder X-ray diffraction patterns were obtained using a PANalytical X'Pert Pro diffractometer with $Cu_{K\alpha}$ (λ=1.5406Å) operating at 40kV and 40mA. Samples were prepared on a fixed-depth well quartz slide by gently pressing the powder into position using a glass slide. XRD patterns were collected scanning from 5° to 90° with a step size of 0.008° and a step time of 25.4s.

3.1.2 XPS

X-ray photoelectron spectroscopy (XPS) was carried out on a Thermo Scientific K-Alpha XPS instrument equipped with a microfocussed monochromated Al X-ray source in the Materials department. The source was operated at 12 keV with a 400 micron spot size. The analyser was operated at a constant analyser energy (CAE) of 200 eV for survey scans and 50eV for in-depth scans. Charge neutralization was established using a combined low energy / ion flood source. Thermo Scientifics Avantage software was used to acquire and Casa XPS to analyse the data. The elemental composition was determined from the areas of the peaks detected on the survey scan post background subtraction and considering the relative sensitivity factors. Peak fitting for high-resolution spectra of element-specific regions was also carried out in CasaXPS generally following the procedure put forward in reference[1]. The background was determined on a case by case basis choosing between linear, Shirley and Tougaard backgrounds or spline versions thereof. Fitting was optimised according to the χ factor and then tested for physical relevance taking into consideration area ratios of $p_{3/2}$ to $p_{1/2}$ or $d_{5/2}$ to $d_{3/2}$ peaks, experimentally reported peak splitting factors, as well as previously reported line shapes

(especially important for metallic contributions), FWHM values and existence of satellite features sourced from different reference via the NIST database[2].

3.1.3 TEM

TEM was performed on a JEOL 3000F operated at 300kV in the Materials Department. Sample inks were prepared by dispersing around 1mg in 4mL of isopropanol and ultrasonicating the mixture for around 30min. A few drops of catalyst ink were then applied onto a holey carbon copper grid and left to dry.

3.1.4 STEM

High-resolution aberration corrected scanning transmission electron microscopy (STEM) and transmission electron microscopy (TEM) was carried out by Dr. Chen Huang on a JEOL ARM200F and a JEOL ARM300F at ePSIC centre, Diamond Light Source, Harwell. Sample inks were prepared by dispersing around 1mg of catalyst in 8mL of isopropanol and ultrasonicating the mixture for around 30min. A few drops of catalyst ink were then applied onto holey carbon grid copper or gold grids and left to dry under vacuum overnight. Imaging was executed in high-angle annular dark field (HAADF) and bright-field (BF) mode for STEM. All samples were beam showered before high-resolution imaging was carried out.

3.2 Catalyst Testing in Aqueous Media

3.2.1 HER Activity Testing

All electrochemical testing was carried out in a standard glass cell in a three electrode configuration using either a Compactstat (Ivium Technologies) or Vertex (Ivium Technologies) potentiostat. A standard calomel electrode (SCE, IJ Cambria Ltd) was used as the reference electrode, a Pt mesh (Fuel Cell Earth) separated from the catholyte by a

porous frit was used as the counter electrode and a glassy carbon electrode (3mm diameter, IJ Cambria Ltd) was used as working electrode. 0.5M H_2SO_4 was prepared as electrolyte and around 40mL were filled into the catholyte compartment and around 5mL into the anolyte compartment of the cell. Before testing, the electrolyte was sparged with Ar for at least 30min to remove dissolved dioxygen. The cell was kept under an Ar atmosphere during electrochemical testing. Electrochemical impedance spectroscopy (EIS) measurements were carried out at zero applied bias between 100kHz and 0.1Hz with a potential amplitude of 10mV to determine the uncompensated resistance (R_U) in the set up. R_U was then used to compensate for the iR drop in the cell.

The working electrode was prepared by dropcasting an ink of the catalyst of interest. The inks were prepared by ultrasonicating 2mg of sample in 500µL of isopropanol for 2h followed by the addition of 20µL of 10wt% Nafion in aqueous solution (Sigma-Aldrich, 31175-20-9) and further ultrasonication for 15 minutes. 5µL of the as-prepared ink was then dropped onto the glassy carbon working electrode and dried in air for 30 minutes yielding a catalyst loading of around 0.27 mg cm^{-2}.

The SCE reference electrode was calibrated against the reversible hydrogen electrode either by measuring the potential between the SCE and a RHE reference in the electrolyte or by sparging the electrolyte with hydrogen for at least 30min before recording the CV of a Pt wire working electrode at 1mV s^{-1}. The average of the zero-crossing potentials from the anodic and cathodic scan was taken as 0V vs RHE.

Before catalysts were tested for their activity, they were cycled between -0.5 and 1V vs RHE at 100mV s^{-1} for at least 10 cycles. Linear scan voltammetry was carried out to determine the HER activity usually scanning from 0.2V to -1.2V vs RHE at a scan rate

of 5mV s^{-1}. Chronoamperometry experiments to investigate the stability of catalysts were performed at a current density of 10mA cm^{-2} corresponding to a current of 707µA in this setup.

3.2.2 NRR Activity Screening

Initially, the testing of the as-prepared SACs for electrochemical ammonia synthesis was carried out in a custom 3D printed cell in a three electrode configuration using either an Compactstat (Ivium Technologies) or Vertex (Ivium Technologies) potentiostat (Fig. 1). A standard calomel electrode (SCE) was used as the reference electrode (IJ Cambria Ltd) and laminated carbon paper with 1cm^2 exposed area was used as working electrode. The counter electrode was prepared by dropping 50µL of 2mg mL^{-1} 20wt% Pt/C in 4:1 water/ethanol ink onto a 1cm^2 carbon paper electrode. All carbon paper electrodes were treated in 5M HCl before use to remove ammonia and metal impurities followed by several washing steps with MQ water and drying. To test the SACs inks were prepared by ultrasonicating 2mg of sample in 500µL of isopropanol for 2h followed by the addition of 20µL of 10wt% Nafion in aqueous solution (Sigma-Aldrich, 31175-20-9) and further ultrasonication for 15 minutes. 50µL of the as-prepared ink was then dropped onto the acid-leached carbon paper working electrode and dried in air for 30 minutes yielding a catalyst loading of around 0.19 mg cm^{-2}. Chronovoltammetry experiments at different potentials for up to 6h were carried out under N_2 flow, as well as Ar flow as blank experiments.

The 3D printed cell (3D Hubs, Amsterdam) made out of Formlabs Clear Resin consists of two compartments, each holding 7mL of electrolyte with the possibility to separate the cathode and anode chamber by a 1cm^2 117 Nafion (Sigma-Aldrich, 31175-20-9) membrane. 0.1M HCl was used as the electrolyte and freshly prepared before each

experiment. The cell was sparged with N_2 (B.O.C, 99.99%) or Ar (B.O.C, 99.99%) gas for 30min prior to experiments. The gas feed was directed through a bubbler filled with electrolyte before entering the cell to clean it from potential ammonia impurities and to prevent the cell from drying out.

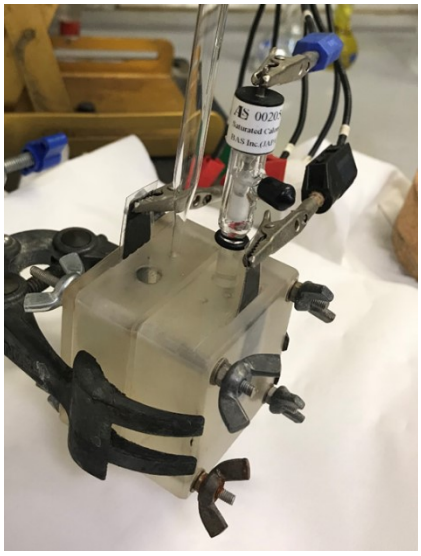


Figure 1: *Custom-made 3D printed dual compartment cell for electrochemical nitrogen reduction experiments. Cell shown assembled and in operation.*

Later iterations of electrochemical ammonia synthesis experiments used a closed glass vial containing 14mL of 0.1M HCl as cell with the gas feed setup but did not include any Nafion membrane or Nafion in the ink preparation (Fig.2.A). A three electrode configuration was employed using a SCE as reference electrode, acid –leached laminated carbon paper as working electrode (Fig.2.B) and a Pt mesh separated by a porous frit from the catholyte as counter electrode.

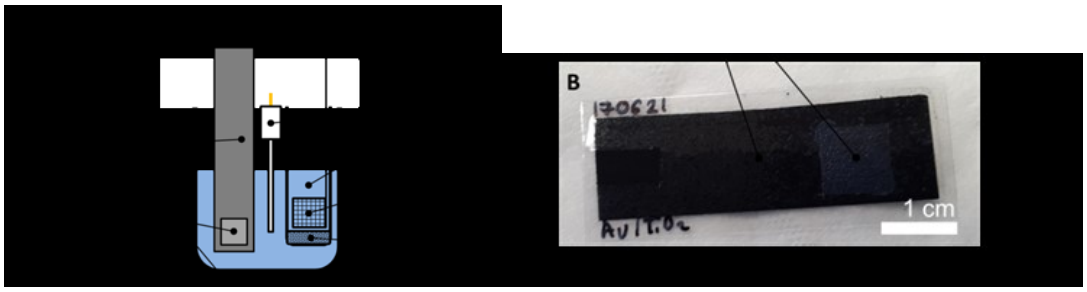


Figure 2: *Graphical depiction of second iteration of NRR testing set up (A) and picture of laminated carbon paper electrode used as working electrode (B)*

In a standard NRR experiment, the working electrode was held at -0.25V or -0.5V vs RHE for one to six hours while constantly bubbling N_2 gas. Two types of blank measurements were also carried out: first electrolyte was bubbled with N_2 in the cell without the catalyst present (referred to as blanks form here on) and secondly holding the catalyst at -0.25V or -0.5V vs RHE for one to six hours while constantly bubbling Ar gas (referred to as Ar blanks).

3.2.3 Ammonia Detection

Several different analytical techniques to quantify ammonia exist. We tested Nessler's method, an ion selective electrode (ISE) and the salicylate test, an adapted version of the Berthelot test.

Nessler's method uses a solution of HgI_4K_2 in KOH which turns deeper in yellow colour in the presence of ammonia allowing photometrical quantification. The use of Nessler's method is widely reported and sensitivities down to 0.02ppm have been reported. This method has two major drawbacks namely: the toxicity of the used mercury compound, as well as a limited range of analysis due to the formation of a brown precipitate at higher ammonia concentrations.

An ammonia ISE (Thermo Scientific Orion, No. 9512HPBNWP) connected to an ISE meter (Thermo Scientific Orion, Star A214 pH/ISE Benchtop Meter) was also used to quantify ammonia. ISEs detect by measuring a change of potential of a pH probe immersed in aqueous NH_3 solution which is separated from the analyte by a hydrophobic membrane. After adjusting the pH of the analyte to above 11 using small amounts of 10M NaOH the trapped ammonia in form of the ammonium ion is liberated and diffuses through the hydrophobic membrane. This leads to an increase in OH^- ions within the ISE compartment and as such to a change in pH which is measured as a change of potential of the pH probe. Advantages of this method include its large measurement range (0.01 to 17000ppm) and its general selectivity against ionic nitrogen contaminations although interference with organic amines is observed. We found the ISE to work well for ammonia concentrations above 0.05ppm below that threshold however long stabilization times increased the measurement error significantly.

A lot of the previous literature in aqueous NRR, as well as our results often yield ammonia concentrations below 0.05ppm which lead us to use the salicylate method to quantify ammonia for aqueous NRR testing. Three solutions are prepared for the salicylate test: Solution A made up of 4g of sodium hydroxide, 5g of sodium citrate and 5g of salicylic acid in 100mL MQ water, solution B made up of 8mL sodium hypochlorite solution in 100mL MQ water and solution C consisting of 0.1g sodium ferricyanide dihydrate in 10mL MQ water. Initially the analysis was carried out in a well plate to enable rapid screening, later on cuvettes were used. Equal amounts of the analyte and solution A were mixed (100µL each/1mL each) followed by the addition of 50% of the analyte volume of solution B (50 µL/500 µL). Finally, 10% of the analyte volume of solution C were added (10 µL/100 µL). Calibration solutions in the range from 0.01ppm

to 2ppm were prepared and treated in the same form. The resulting mixtures were left to react for around 6h over which the colour changed from yellow to shades of green if ammonia was present. The samples were analysed using UV-Vis spectrometer and quantified using the absorption at 650nm. The addition of solution A leads to formation of NH_3 from the trapped NH_4^+ state and its reaction with the hypochlorite ion to form monochloroamine. In the second step said monochloroamine reacts with salicylate to form 5-aminosalicylate which is accelerated in the presence of sodium nitroferricyanide. 5-aminosalicylate reacts with salicylate to form the salicylate analogue of indophenol which in the oxidised form exhibits a blue colour. Drawbacks of this method including interferences and extraneous sources of ammonia are discussed in Chapter 4 Section 4.5.

3.2.4 In-situ IR Spectroelectrochemistry

All experiments were carried out with the help of Ting Chen of the Vincent group. A Varian 680-IR spectrometer, operated using the Varian Resolutions software, was used to collect IR spectra. An Autolab potentiostat operated by the NOVA software was used to perform cyclic voltammetry and chronoamperomentry. The spectroelectrochemical cell used in the following experiments was designed by Dr. R. Hidalgo Gonzalez consisting of poly ether ketone (PEEK) fitted with a trapezoidal Si ATR element (8.39 x 5 x 1mm, Crystal GmbH) with a calculated penetration depth of 0.5μm in aqueous solution. The cell was designed to be operated under flow conditions using a peristaltic pump. Inside the cell, electrochemistry was performed in a three electrode set up with a leak-free miniature SCE reference electrode and Pt wire as the counter electrode. The working electrode was comprised of a carbon rod pressing onto carbon paper the size of the ATR element. The catalyst of interest was dropcasted directly onto the Si element and

put into electrical contact with the carbon rod via the carbon paper ensuring the catalyst acts as the working electrode. 0.5M H_2SO_4 was used as the electrolyte.

Catalyst inks were prepared by ultrasonicating 1mg of catalyst in 500μL isopropanol for 2h followed by the addition of 5μL of 10wt% Nafion in aqueous solution (Sigma-Aldrich, 31175-20-9) and further ultrasonicating for 15min. 5μL of the as-prepared ink were dropped evenly onto the ATR element and left to dry for 1h.

Prior to electrochemical operation, several background infrared spectra were collected including of the bare ATR element, 0.5M H_2SO_4 solution, 32mM KSCN in 0.5M H_2SO_4 solution, catalysts and the catalysts under 0.5M H_2SO_4 flow at OCP. All spectra obtained in this chapter were averaged from 258 scans.

For all experiments a total volume of 6mL of Ar-sparged 0.5M H_2SO_4 was used as electrolyte and flowed through the ATR cell at 13mL min^{-1}. Once a background IR spectrum of the catalyst at OCP in 0.5M H_2SO_4 was acquired, it was cycled between -0.5V and 1V vs RHE for ten cycles and another background spectrum was acquired. Following that, 144μL of 0.3M KSCN in 0.5M H_2SO_4 solution were added leading to a KSCN concentration of 7mM in the electrolyte solution. Several IR spectra were obtained until no further increase in peak height for the C-N stretch was observed. Subsequently, chronoamperometry at following potentials was carried out for at least 420s: 0.51V, 0.31V, 0.11V, -0.09V, -0.29V and -0.49V vs RHE. At each potential at least two IR spectra were recorded.

Data analysis was performed using the Varian Resolutions software. The background spectrum of the catalyst of interest at OCP under 0.5M H_2SO_4 was subtracted from the spectra acquired under poisoning conditions in order to magnify the changes occurring

upon binding of SCN^-. Furthermore, changing amounts of water vapour in the experiments were observed in the spectra, stemming either from diffusion of water through the sealing around the ATR element or changes in water vapour in the lab, generally. This required subtraction of a previously acquired spectrum of water vapour.

3.2.5 In-situ XAS Spectroelectrochemistry

The in-situ X-ray absorption studies of the Co SACs were carried out on the Core XAS beamline B18 at Diamond Light Source, Harwell, UK. Beamline scientist Dr. Diego Gionolio supported the experiments. A Si(111) monochromator was used as well as the 36-element solid state Ge detector. Measurement of samples were performed in fluorescence mode, whereas spectra of metal standards were obtained in transmission mode. In fluorescence mode the detector was placed at an angle to the sample around 7cm apart. XAFS spectra of the Co K edge (7709eV) were obtained from 200eV before to 750eV after the edge. The measuring time of a XAS scan was about 3mins and usually five scans of the same condition were collected consecutively.

All testing was carried out in a PTFE cell provided by Dr. Rosa Arrigo specially designed for use on B18[3] shown in Figure 3. A free-standing sheet of catalyst was used as working electrode (orange circle, Fig.3) fitted into a recess at the front of the cell held in place by a metal lid pressing on an O-ring. The metal lid is used as the current collector and is fitted with a circular Kapton window of $1cm^2$ to allow X-ray radiation to hit the catalyst. The other side of the catalyst is a compartment filled with 10mL of 0.5M H_2SO_4 solution, with circular area of exactly $1cm^2$ of catalyst being exposed to solution. A commercial micro Ag/AgCl reference electrode (MI-409F, thin grey rod) was fitted close to the working electrode. Pt wire (white, Fig.3.B) was used as the counter electrode. The cell

was constantly bubbled with argon via a gas inlet (brown cap, Fig.3.B). An Ivium Compactstat potentiostat was used to control the potential of the working electrode.

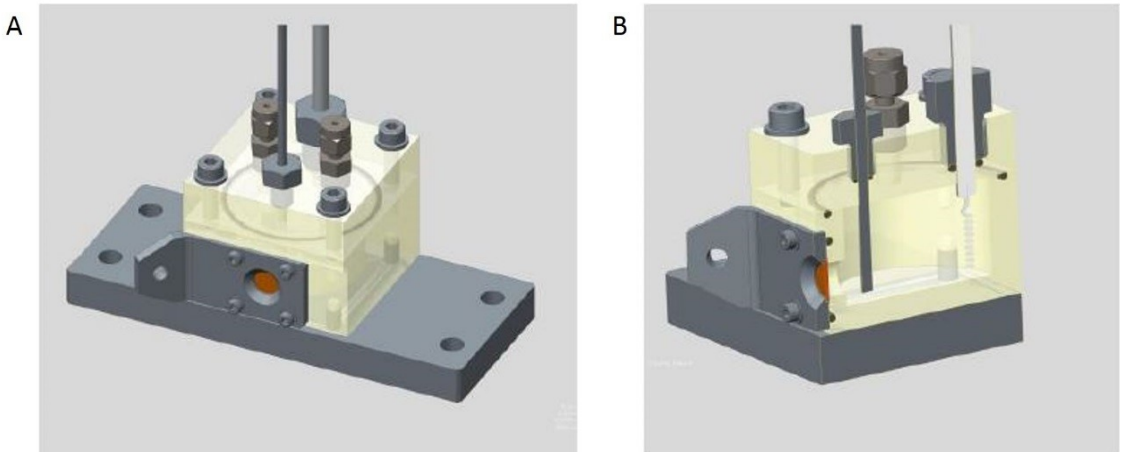


Figure 3: *Graphical depiction of in-situ electrochemical XAFS cell designed for use at Diamond beamline B18, front view (A) and cross-section (B). Figure taken from supplementary information of reference*[3]*. The rights of these images belong to Diamond Light Source Limited. Diamond is a not for-profit limited company funded as a joint venture by the UK Government through the Science & Technology Facilities Council (STFC) in partnership with the Wellcome Trust.*

Free-standing electrodes of our Co SAC materials were prepared by vacuum filtering the corresponding precursor solutions (Co/GO) onto a PTFE membrane. The resulting Co/GO sheets were peeled off the membrane and annealed under either Ar or NH_3 corresponding to the syntheses discussed in Chapter 4 Section 3.

Five scans of a sample in the dry state were collected before moving on to in-situ measurements. Afterwards the cell was filled with 10mL of 0.5M H_2SO_4 and bubbled with Ar for 20min. Following that five XAS scans were collected at OCP. Subsequently, the catalyst was cycled between -0.8V and 0.8V vs RHE for ten cycles. After electrochemical activation, chronoamperometry experiments were carried out while collecting further XAS scans. The catalyst was stepped from 0.7V to -0.5V vs RHE in

steps of 0.3V, holding the catalysts at each potential for 15min while collecting five XAS scans.

Data analysis was carried out with the Athena program of Demeter analysis suite. Usually five spectra measured under the same conditions were merged to increase the signal-to-noise ratio and then normalised. Linear pre- and post-edge backgrounds were subtracted. FT-EXAFS and XANES modelling were carried out with the FEFF9 code.[4,5] Further XANES modelling was performed in CASTEP.[6] Wavelet transform analysis was accomplished using the HAMA code.[7–9]

3.3 Experiments in Molten Salts

3.3.1 Experimental Setup

The molten salt reactor was designed by Dr. Ian McPherson and Robert Selway (Inspired Engineering Design Ltd.) and constructed in the Physical and Theoretical Chemistry Department's workshop. Figure 4 provides a graphical representation of the setup. The main reactor consists of a custom-made stainless steel vessel (a) fitted inside a split-furnace (Vecstar Ltd) (b). An assortment of tubes can be inserted into the stainless-steel via six ports of different size equipped with compression seals. In all experiments a thermocouple in a closed alumina sheath (c) and a custom-made Ag/AgCl reference electrode in a closed Pyrex tube (d) are fitted. The Ag/AgCl reference is prepared by adding around 6.4mg of AgCl (99.9%, Alfa Aesar) to 5g of Li-K-Cl eutectic mixture yielding an AgCl concentration of 0.05mol% in a Pyrex tube and immersing a Ag wire (0.25mm O.D., 99.9%, Alfa Aesar) in the mixture. Reference electrodes were prepared freshly before each experiment. Further gas electrodes can be inserted inside alumina tubes connected via Swagelock Ultra-Torr fittings to a gas manifold allowing the

electrodes to be flushed with Ar, N_2 or H_2 (e and f). An additional Ni wire electrode was fitted via an alumina tube capped with a rubber septum instead of a gas connection. The Ni wire electrode was used to determine the Li^+/Li potential, used as reference potential in the following sections, by measuring the zero-crossing potential in cyclic voltammograms after reductively plating lithium onto the electrode. Li-K-Cl eutectic salt mixtures were prepared in a glove box and added to the reactor in a gas tight flask (m) via a large alumina tube (g) which is further connected via a T-piece to the gas manifold and is used as Ar purge. The salt is held within an alumina crucible (k) suspended from the reactor lid on a stainless-steel holder. The pressure in measured with a pressure gauge (h) on the outgoing gas tube onto which a vacuum pump (i) is connected in order to evacuate the reactor during salt preparation. Under operation, gas leaves the reactor through a paraffin bubbler (j) to inhibit oxygen or moisture contamination, followed by an acid trap bubbler (k) filled with 10mM H_2SO_4 solution.

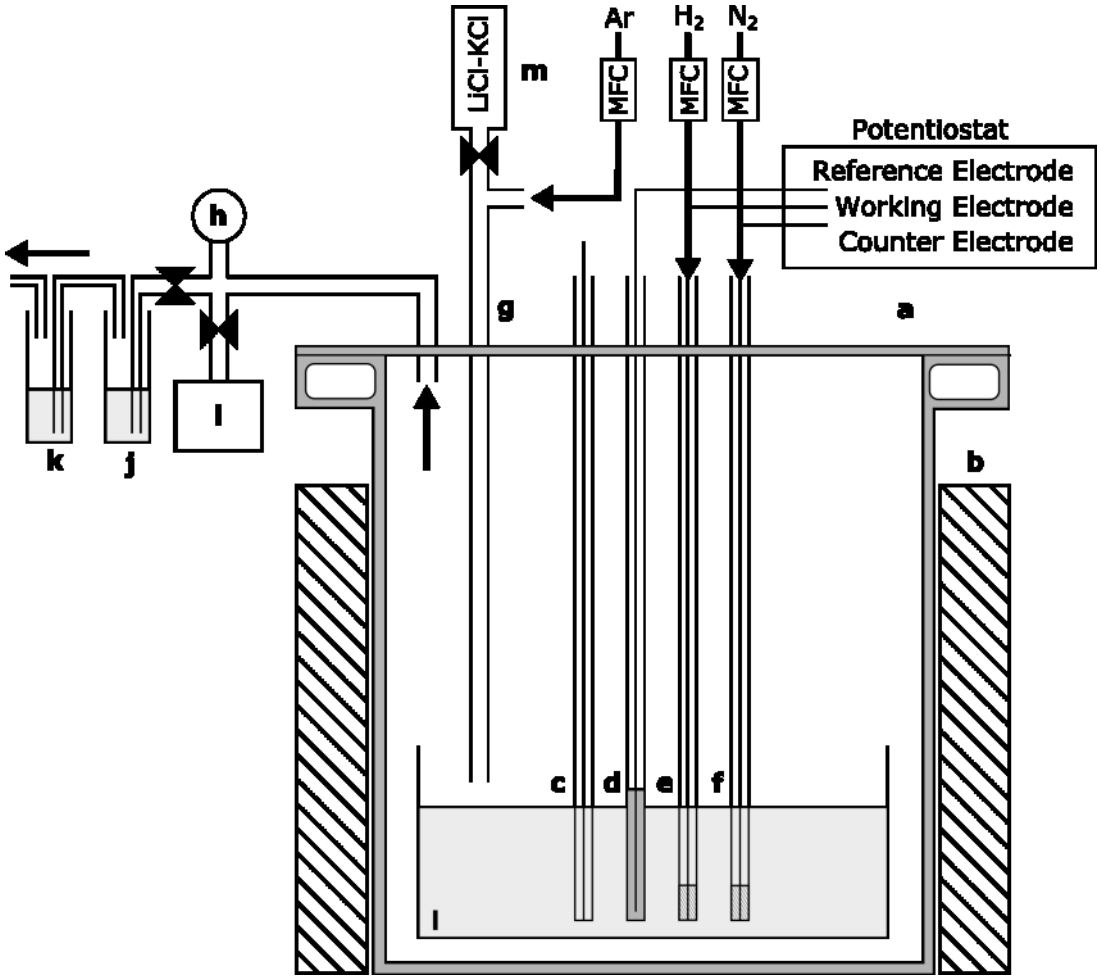


Figure 4: *Pictorial representation of molten salt reactor consisting of a stainless steel vessel (a), split furnace (b), thermocouple in alumina sheath (c), Ag/AgCl reference electrode in closed Pyrex tube(d), working gas electrode (e), counter gas electrode (f), Ar purge and salt addition tube (g), pressure gauge (h), vacuum pump (i), paraffin bubbler (j), acid trap bubbler (k), alumina crucible (l), and airtight flask for salt addition (m). Reproduced from reference*[10] *with permission from John Wiley and Sons.*

Figure 5 provides an overview of the laboratory bench setup including the previously described reactor-furnace arrangement (right side). Furthermore, mass flow controllers (MFCs) and control unit are shown enabling precise control of gas flow rates. The furnace is controlled using a PID control (Eurotherm 2216). In order to assure safe operation and prevent the pressure seals of the six ports from overheating the reactor lid is water-cooled to around 22°C with its temperature being monitored by a thermocouple. As a safety feature, the furnace automatically turns off in case the lid reaches temperatures above

30°C, water flow is disrupted, the temperature of the furnace surpasses a certain value or the split furnace is opened. All relevant reactor data including gas flow rates, furnace temperature, temperature inside the reactor and lid temperature, is further centrally monitored in a Labview program with the additional feature of monitoring partial hydrogen pressure inside the reactor.

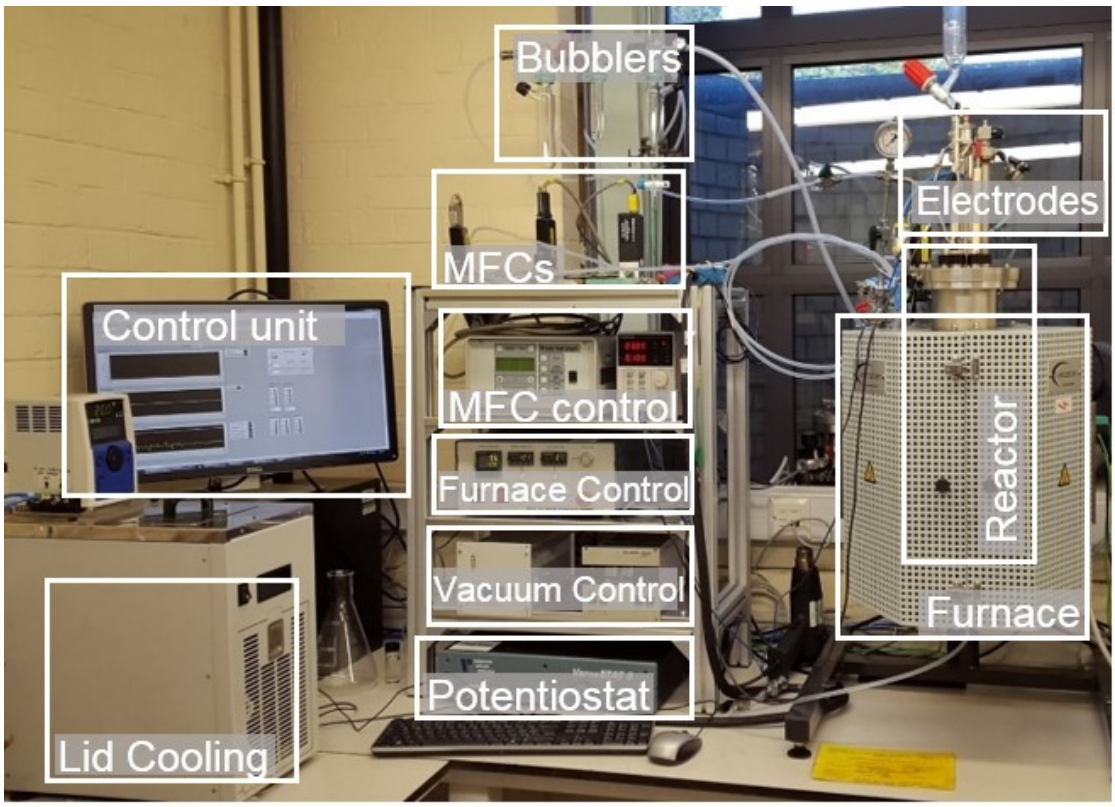


Figure 5: *Picture of complete laboratory bench setup.*

3.3.2 Salt Preparation

Potassium chloride and especially lithium chloride are very hygroscopic making it important to properly dry the salt before using it as electrolyte.[11–13] High water content in chloride eutectics otherwise leads to the formation of HCl upon melting forming a highly corrosive atmosphere, problematic for stainless steel parts in the reactor.[11–13] Furthermore, elevated concentrations of water prohibited collection of meaningful

voltammetry data due to excessive background signal caused by the hydrogen evolution and corrosion of metal electrodes.

Salts were stored in an Ar glovebox (<0.5ppm water content). For each experiment 50g of LiCl (99%, Alfa Aesar) and 61g of KCl (99%, Alfa Aesar) were weighed out, mixed inside the gas tight flask and connected to the reactor with gas tight Swagelock Ultra-Torr fittings. After a cycle of Ar purging and evacuation of the reactor, the salt was filled into the crucible inside the reactor under Ar flow. Subsequently, the reactor was evacuated to $1x10^{-1}$mbar and kept at 150°C for at least 24h. Following that, the reactor was filled with Ar and a previously fitted stainless steel rod cathode and a graphite rod anode were lowered into the salt mixture with a potential of 2.7V applied across. The potential was applied using a Vertex potentiostat (Ivium Technologies). The reactor was heated to 450°C and kept at that temperature until the preelectrolysis current consistently stayed below 1mA for more than 4h. After the pre-electrolysis step the reactor was cooled to room temperature under Ar flow.

3.3.3 Electrochemistry in Molten Salts

Electrochemical experiments were carried out in a three electrode set up with the previously described Ag/AgCl reference electrode, a graphite rod as counter electrode and different gas electrodes, metal nitride pellets or Ni wire as working electrode using either a Vertex or Compactstat potentiostat (Ivium Technologies). Using the purge tube, the reactor was constantly flooded with Ar at 350mL min^{-1}. N_2 or Ar were flown over the working electrode at 50mL min^{-1}. The Li^+/Li potential was determined by performing cyclic voltammetry at 100mV s^{-1} on a Ni wire sweeping to below the Li^+ reduction potential. The zero-crossing potential on the anodic scan was then set as 0 on the Li^+/Li scale (between -2.3 to -2.5V vs Ag/AgCl).

3.3.4 Ammonia Detection

Following electrochemical experiments, nitrogen reduction was quantified using an Ion Selective Electrode (ISE, ThermoFisher Scientific). For further information on the working principles of an ISE see section 2.3. Ammonia trapped in the acid bubbler was quantified directly but a significant amount of reduced nitrogen remained in the melt in form of Li_3N which was transformed into ammonia by dissolving known amounts of frozen melt in 10mM H_2SO_4 solution. Typically the ionic strength and pH of the analyte solutions was adjusted by an ionic strength adjustor (ThermoFisher Scientific) and ammonia was subsequently measured using the ISE. Calibrations of the ISE were performed for concentrations between 0.05 to 10ppm by serial dilution of a 1000ppm ammonia standard (Hach) in 10mM H_2SO_4. For quantification of nitride dissolved in the melt, ammonia concentration in the samples was additionally quantified using the salicylate method (see Section 2.3) yielding similar concentrations to rule out any effect of dissolved Li-K-Cl melt onto the ammonia readings.

3.4 References

(1) Peak Fitting in XPS http://www.casaxps.com/help_manual/manual_updates/peak_fitting_in_xps.pdf (accessed Jan 18, 2020).

(2) NIST XPS Database, Selected Element Search Result https://srdata.nist.gov/xps/EngElmSrchQuery.aspx?EType=PE&CSOpt=Retri_ex_dat&Elm=N (accessed Sep 10, 2019).

(3) Genovese, C.; Schuster, M. E.; Gibson, E. K.; Gianolio, D.; Posligua, V.; Grau-Crespo, R.; Cibin, G.; Wells, P. P.; Garai, D.; Solokha, V.; et al. Operando Spectroscopy Study of the Carbon Dioxide Electro-Reduction by Iron Species on Nitrogen-Doped Carbon. *Nat. Commun.* **2018**, *9* (1). https://doi.org/10.1038/s41467-018-03138-7.

(4) J. Rehr, J.; J. Kas, J.; D. Vila, F.; P. Prange, M.; Jorissen, K. Parameter-Free Calculations of X-Ray Spectra with FEFF9. *Phys. Chem. Chem. Phys.* **2010**, *12* (21), 5503–5513. https://doi.org/10.1039/B926434E.

(5) Rehr, J. J.; Kas, J. J.; Prange, M. P.; Sorini, A. P.; Takimoto, Y.; Vila, F. Ab Initio Theory and Calculations of X-Ray Spectra. *Comptes Rendus Phys.* **2009**, *10* (6), 548–559. https://doi.org/10.1016/j.crhy.2008.08.004.

(6) Clark, S. J.; Segall, M. D.; Pickard, C. J.; Hasnip, P. J.; Probert, M. I. J.; Refson, K.; Payne, M. C. First Principles Methods Using CASTEP. *Z. Für Krist. - Cryst. Mater.* **2005**, *220* (5/6). https://doi.org/10.1524/zkri.220.5.567.65075.

(7) Funke, H.; Chukalina, M. Wavelet Analysis of EXAFS Data - First Studies. *FZR Annu. Rep.* **2001**, 45.
(8) Funke, H.; Scheinost, A. C.; Chukalina, M. Wavelet Analysis of Extended X-Ray Absorption Fine Structure Data. *Phys. Rev. B* **2005**, *71* (9), 094110. https://doi.org/10.1103/PhysRevB.71.094110.
(9) Timoshenko, J.; Kuzmin, A. Wavelet Data Analysis of EXAFS Spectra. *Comput. Phys. Commun.* **2009**, *180* (6), 920–925. https://doi.org/10.1016/j.cpc.2008.12.020.
(10) McPherson, I. J.; Sudmeier, T.; Fellowes, J. P.; Wilkinson, I.; Hughes, T.; Tsang, E. S. C. The Feasibility of Electrochemical Ammonia Synthesis in Molten LiCl-KCl Eutectics. *Angew. Chem. Int. Ed.* **2019**. https://doi.org/10.1002/anie.201909831.
(11) Lovering, D. G. *Molten Salt Techniques*; Plenum Press, 1983.
(12) Janz, G. J. *Molten Salts Handbook*; Elsevier, 2013.
(13) Mamantov, G.; Marassi, R. *Molten Salt Chemistry: An Introduction and Selected Applications*; Springer Science & Business Media, 1987.

4 Understanding the Electrocatalytic Activity of Single Metal Atoms on Nitrogen-doped Graphene Support

4.1 Background and Objectives 89

4.2 Synthesis 89

4.2.1 Graphene Oxide 89

4.2.2 Single Metal Atoms on Nitrogen-doped Graphene 90

4.3 Characterisation 92

4.3.1 XRD 92

4.3.2 XPS 93

4.3.3 TEM 102

4.3.4 STEM 102

4.4 Hydrogen Evolution Reaction 105

4.4.1 Experimental Methods 105

4.4.2 Results and Discussion 105

4.4.3 Correlation with Theory 115

4.5 Electrochemical Ammonia Synthesis 118

4.5.1 Experimental Methods 118

4.5.2 Ammonia Detection 118

4.5.3 Results and Discussion 119

4.6 Conclusions 122

4.7 References 124

4.1 Background and Objectives

Single-atom catalysts (SACs) often display varying metal loading, nitrogen-doping, morphologies and active site environments often due to their synthesis conditions (see Chapter 1 Section 4.1.2). Additionally, few studies report the successful synthesis of a variety of metals following the same synthesis strategy. This complicates the comparison of SACs with different metals as active sites significantly and as such impedes the search for a structure-activity relationship.

The primary aim of this chapter is to synthesise a library of atomically dispersed transition metal catalysts to derive the metal-activity relationship in some key electrocatalytic test reactions. In contrast to other carbon supported single metal catalysts, the M-NG systems are synthesised using graphene oxide as a preformed backbone to minimise morphology variation between catalysts. A range of characterisation techniques, including XRD, XPS, TEM, and STEM are used to investigate the composition and morphology of the catalysts, as well as assess the dispersion of metals on the graphene support. Electrochemical activity is tested and correlated with the effective electron density at the metal centre, as determined by the factor φ, a metric recently proposed from computation.

Attempts are then made to apply this insight to the search for effective electrochemical nitrogen reduction reaction (NRR) catalysts.

4.2 Synthesis

4.2.1 Graphene Oxide

Graphene oxide was used as a carbon starting material and was synthesised using the improved Hummers' method. [1] 3.0g of natural graphite flakes (Sigma-Aldrich, 7782-42-5) and 18.0g of $KMnO_4$ (Alfa Aesar, 7722-64-7) were placed in a beaker and

dispersed in 400mL of a 9:1 mixture of concentrated H_2SO_4/H_3PO_4 (Sigma-Aldrich, 7664-93-9 and Alfa 13598-36-2). The resulting mixture was heated to 50°C and stirred for 16h. After that the reaction was allowed to cool to room temperature and subsequently poured onto 400mL of ice mixed with 5mL of 30wt% H_2O_2 solution (Sigma-Aldrich, 7722-84-1). The mixture was centrifuged for 30min at 5000rpm and the supernatant was decanted away followed by a dispersion of the remaining solid in MQ water using sonication. This procedure was repeated until a pH neutral supernatant was obtained at which point the solid was again dispersed in MQ water and sifted through a U.S. standard testing sieve (Cole-Parmer, 300μm). Following the same procedure, the solid was washed with concentrated HCl. Finally, the solid was washed twice with ethanol and dispersed in MQ water again using sonication. The water/GO suspension was freeze-dried to obtain a fluffy brown powder. To assess if the oxidation was successful XRD was used to analyse the product.

4.2.2 Single Metal Atoms on Nitrogen-doped Graphene

Metal on nitrogen-doped graphene (M-NG) with single-atom dispersion was synthesized by adapting a procedure published by Fei et al..[2] Figure 1 provides an overview of the steps involved in the synthesis.

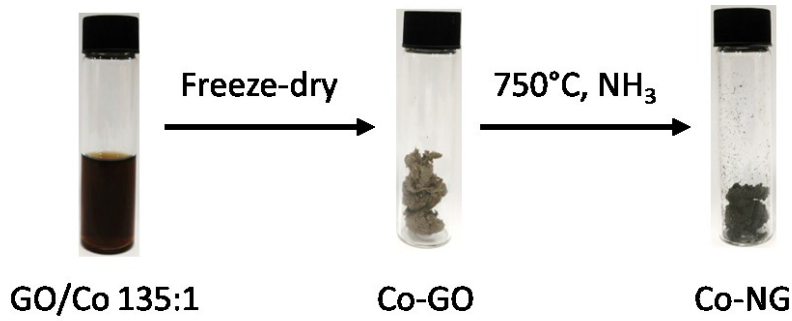


Figure 1: *Pictorial illustration of Co-NG synthesis from Co/GO suspension via freeze-drying and annealing under ammonia flow*

50mg of graphene oxide were dispersed in 25mL MQ water and sonicated for 2h. 1.5mg of $CoCl_2 \cdot 6H_2O$ (6.3 μM) dissolved in 0.5mL MQ water were added to the suspension and further sonicated for 30min. The resulting mixture was freeze-dried to obtain a dark brown solid which was placed into a tube furnace and heated to 750°C at 10°C min^{-1} while flowing NH_3 at 150mL min^{-1}. The furnace was kept at 750°C for 1h and then cooled down under N_2 flow to obtain a black powder. Blank NG, Ni-NG, Mo-NG, Mn-NG, Cu-NG, Fe-NG and Ru-NG were produced analogously from GO and $NiCl_2 \cdot 6H_2O$ (Sigma-Aldrich, 7791-20-0), $MoCl_3$ (Sigma-Aldrich, 13478-18-7), $MnCl_2$ (Sigma-Aldrich, 7773-01-5), $CuCl_2 \cdot 2H_2O$ (Sigma-Aldrich, 10125-13-0), $FeCl_2 \cdot 4H_2O$ (Sigma-Aldrich, 13478-10-9), and $RuCl_3$ (Sigma-Aldrich, 10049-08-8). The as-synthesized materials were boiled in concentrated HCl at 60°C for 3h and subsequently accumulated using vacuum filtration. The filtrate was washed with MQ water until neutral washings were obtained.

The obtained materials were analysed using XRD, XPS, TEM, STEM, EELS and electrochemical techniques.

4.3 Characterisation

Seven M-NG catalysts and undoped N-graphene (NG) were synthesised and characterised in this section. XRD, TEM and XPS were carried out to confirm the retention of a graphene-like structure, as well as establish the similarity in morphology and nitrogen doping across catalysts. Additionally high-resolution STEM was performed to verify atomic dispersion for all M-NG catalysts.

4.3.1 XRD

X-ray diffraction patterns of graphite, graphene oxide, NG and M-NGs were obtained (Fig.2). Figure 2 confirms the synthesis of graphene oxide (black trace) from graphite (brown trace) exhibiting a main reflection at around 11° indicating a large increase in interlayer spacing which is in line with exfoliation and oxidation of the individual graphene planes during the improved Hummer's method[1].

Figure 2 shows that for NG, as well as all M-NG phases only one broad main reflection can be observed at around 26.5° which can be identified as the (002) plane of N-graphene[3,4]. The main peak is at a similar position to the (002) reflection of graphite showing that for NG and M-NG the initial graphite interlayer spacing is restored by removal of oxygen functionalities and subsequent restacking of individual N-graphene layers post reduction. Some catalysts show minor reflections at around 15° which correspond to minor impurities of not fully reduced graphene oxide. No metal or metal oxide reflections were observed.

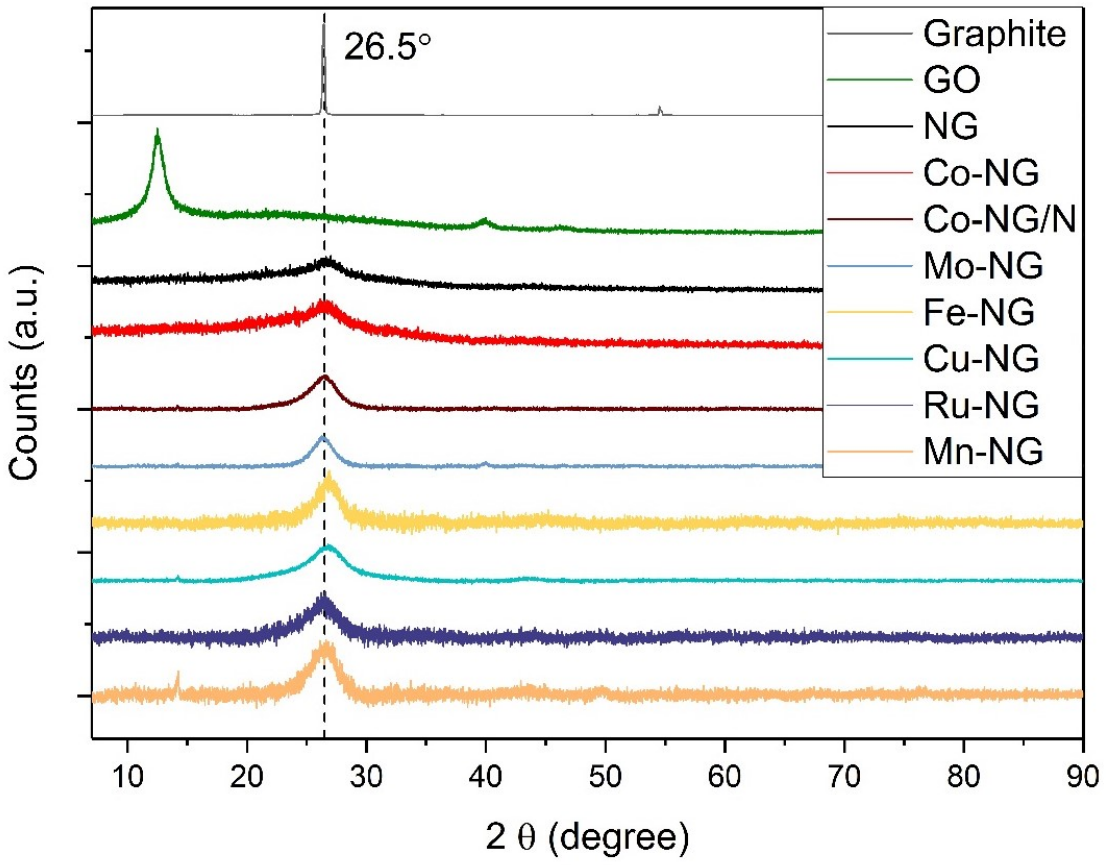


Figure 2: *X-ray diffraction patterns for atomically dispersed metals on N-graphene and precursors, graphite and graphene oxide. Colour code: Mn-NG (orange), Ru-NG (purple), Cu-NG (cyan), Fe-NG (yellow), Mo-NG (blue),Ni-NG (brown), Co-NG (red), NG (black), graphene oxide (olive) and graphite (grey).*

4.3.2 XPS

For details about the XPS acquisition procedure, refer to Chapter 3 Section 1.2.

XPS was used to establish the general elemental composition of the catalysts and confirm the reductive nitrogen doping. It was attempted to use ICP-MS as a complementary technique to determine the metal loading of the M-NG materials. Reaching complete dissolution of the material in concentrated acid proved difficult complicating the sample preparation. Additionally, large errors in ICP measurements of standards and samples of

other lab members using the same service led us to focus on XPS to determine the metal loading of the M-NG materials in this thesis.

After the nitridation the C1s spectra of NG and M-NG show all features typical for sp^2-hybridised carbon, as well as moieties characteristic for N-doped materials.[2,5,6] This is shown in Figure 3 by comparing the C1s of NG and M-NGs. Fig.3.A depicts the C1s region of NG containing fits for the characteristic feature of sp^2- hybridised carbon at around 284.6eV (red trace), as well as contributions from ether/ imine (blue trace) and keto/ nitrile moieties (yellow trace), all well-known constituents of nitrogen-doped carbon materials.[3,5,6] Furthermore, a π-π^* satellite feature is observed at around 292eV (green trace) characteristic for graphene-like materials. The same features are observed in the C1s spectrum of all M-NGs (Fig. 3.B-H). This clearly shows all materials were effectively reduced in the nitridation step forming graphene-like carbon support. The N1s spectra of NG and M-NGs are shown in Fig. 4.A and Fig.4.B-H, respectively, exhibiting contributions from pyridinic N (red trace), pyrrolic N (blue trace), quaternary N (yellow trace) and trace amounts of N-oxide (green trace), in similar proportions. Metal-nitrogen interactions are indistinguishable from pyridinic nitrogen contributions[2]. Most metal-doped materials seem to contain slightly increased amounts of pyrrolic nitrogen compared to NG which is likely due to the acid-washing step further discussed for Co-NG in Chapter 5 Section 3.2. All mentioned nitrogen and carbon moieties are commonly found in N-doped carbon materials and the fitted peak positions and shapes are all in accordance with literature values.[2,5–9] This confirms that all M-NG and NG were effectively doped with nitrogen during the annealing step in ammonia.

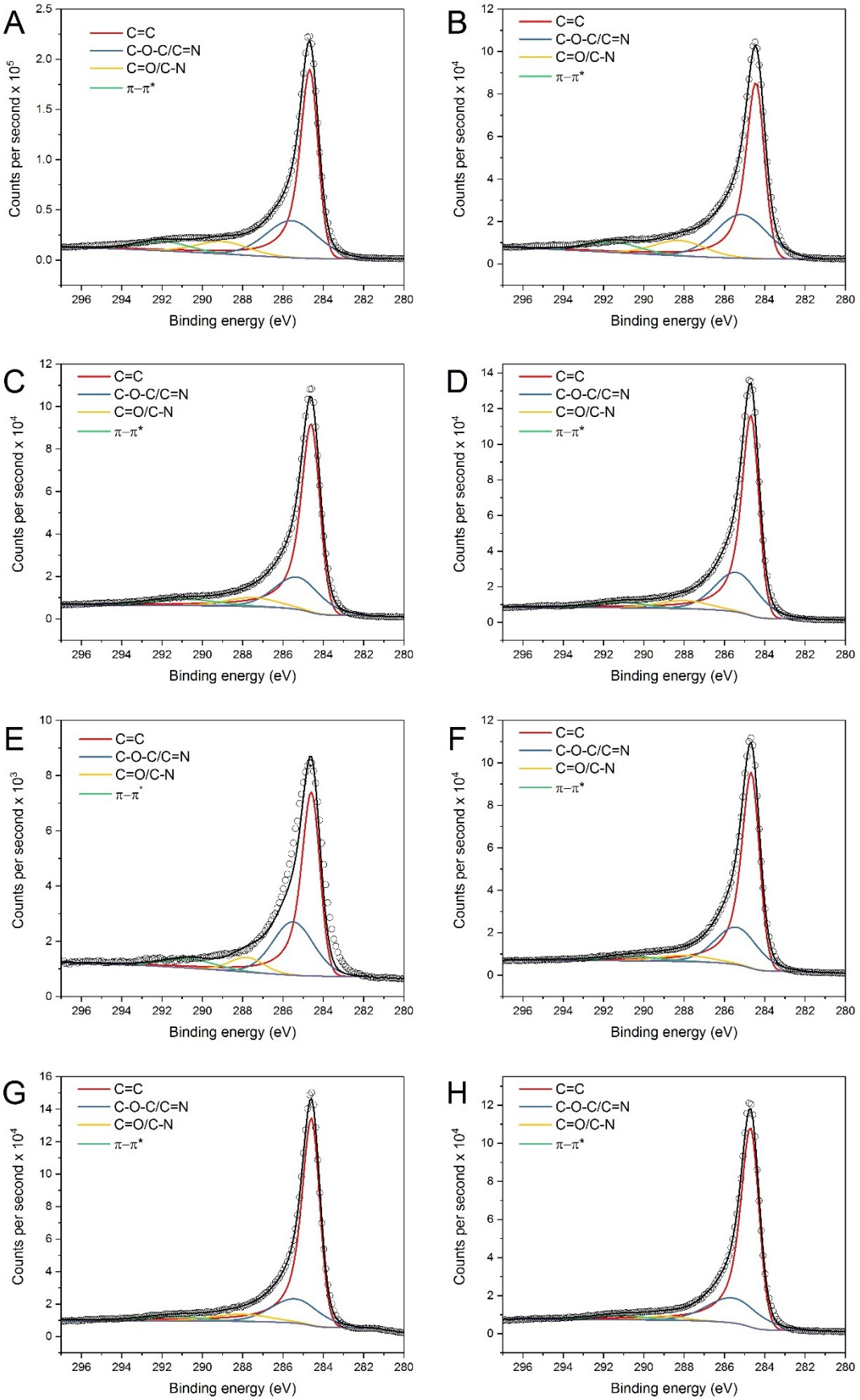

A
B
C
D
E
F
G
H
C=C
C-O-C/C=N
C=O/C-N
π–π*
Counts per second x 10^5
Counts per second x 10^4
Counts per second x 10^3
Binding energy (eV)
296
294
292
290
288
286
284
282
280

Figure 3: *High-resolution C1s spectra of NG (A), Co-NG (B), Fe-NG (C), Ni-NG (D), Mn-NG (E), Cu-NG (F), Ru-NG (G), and Mo-NG (H). The C1s spectrum of Mn-NG was recorded on a lower resolution machine explaining the lower signal strength. The black line, purple line and empty black circles, respectively represent the overall fit, background, and data points. Colour code: Carbon double bond (red), ether or imine moiety (blue), keto or nitrile moiety (yellow), and* π-π^* *satellite (green).*

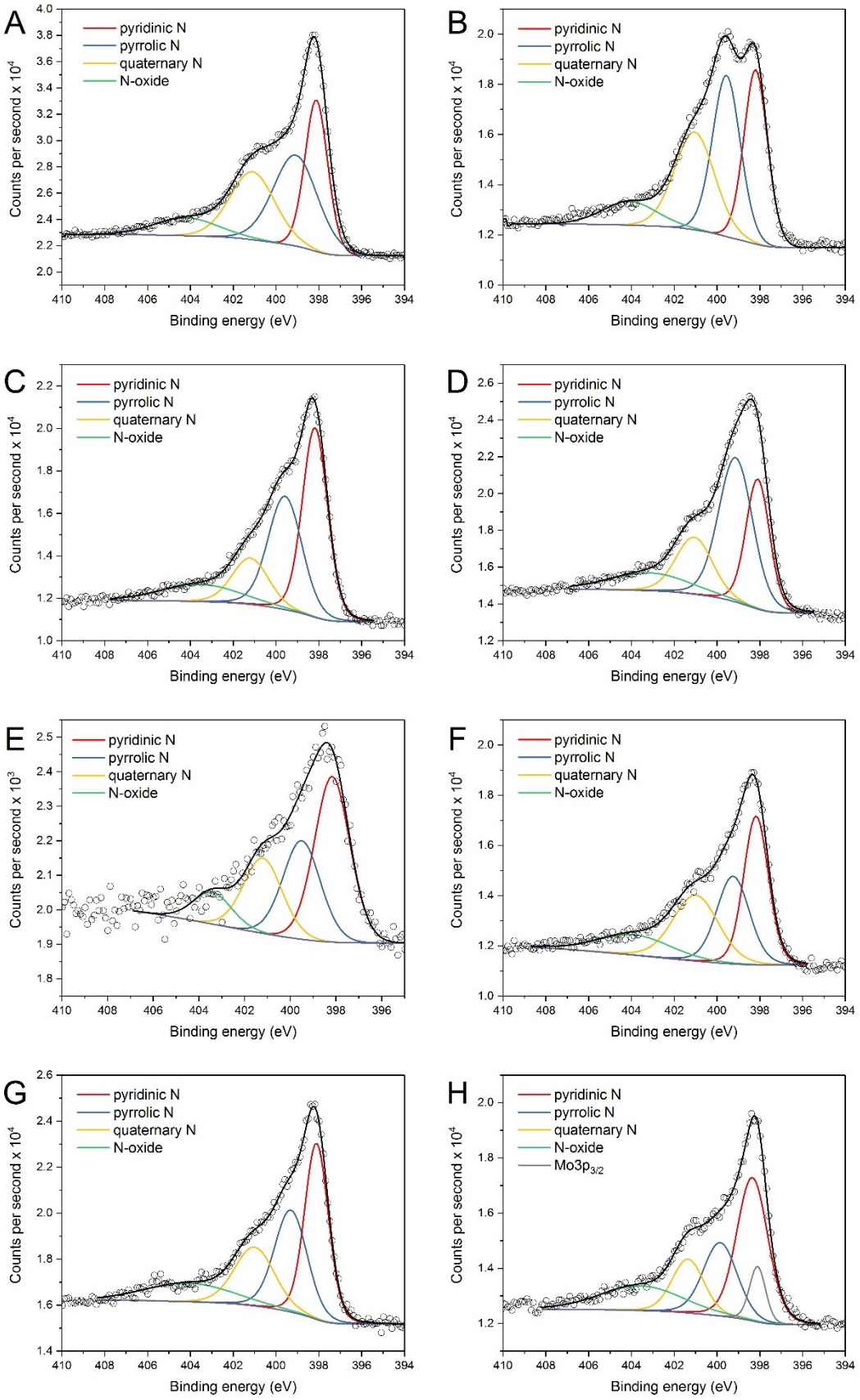

A
B
C
D
E
F
G
H
pyridinic N
pyrrolic N
quaternary N
N-oxide
Mo3p3/2
Counts per second x 10^4
Counts per second x 10^3
Binding energy (eV)

Figure 4: *High-resolution N1s spectra of NG (A), Co-NG (B), Fe-NG (C), Ni-NG (D), Mn-NG (E), Cu-NG (F), Ru-NG (G), and Mo-NG (H). The N1s spectrum of Mn-NG (E) was recorded on a lower resolution machine explaining the lower signal strength. The N1s spectrum of Mo-NG contains contributions from the overlapping Mo3p region. The black line, purple line and empty black circles, respectively represent the overall fit, background, and data points. Colour code: pyridinic N (red), pyrrolic N (blue), quaternary N (yellow), N-oxide (green), and Mo3p$_{3/2}$ (grey).*

All M-NG survey scans detect the metal species of interest but only at very low amounts of <0.25at% (Table1). The corresponding metals can be observed in the higher resolution scans of their respective 2p/3p/3d orbitals (Fig.5). Due to the low metal loading determination of the exact oxidation states of the metal centres is difficult. Especially for metals with lower relative sensitivity factors even high-resolution metal region scans were found to be quite noisy (Fig.5.E-G). The peak positions of $p_{3/2}$ or $d_{5/2}$, as well as the satellite peaks nevertheless show that all metal species in the M-NG systems are present in ionic form since no characteristic contributions of asymmetric metallic peaks at lower binding energies were detected for any of them.

For Cu-NG Cu2p$_{3/2}$ peaks at around ~932.5 and 934.7eV are observed (Fig.5.A) indicating the presence of Cu(I) and Cu(II) species.[10,11] In the Ni2p region of Ni-NG a 2p$_{3/2}$ peak at around 855.0eV (Fig.5.B) is detected implying Ni to be present in an oxidation state of +II or higher although the general peak shape and the presence of only a weak satellite feature at 861.01eV are unusual for oxidised nickel species.[12–14] Ru was found to be +III or +IV in Ru-NG with a 3p$_{3/2}$ peak at 463.2eV (Fig.5.C).[8,15] For Mo-NG two $d_{5/2}$ peaks were observed at 230.8 and 232.2eV (Fig.5.D) corresponding to Mo(IV) and Mo(V) species, respectively.[8,16,17] The peak positions of Fe2p$_{3/2}$ at around 711eV in Fe-NG shows the metal to be present in ionic form and indicates +III as prevalent oxidation state since metallic Fe and Fe(II) usually exhibit peaks at lower binding energies (706.6 and 708.4eV, respectively).[18] The presence of only minor satellite

features in the Co2p region of Co-NG (Fig.5.F) indicate that here the metal is present in a mixture of +II and +III. Further discussion of the Co2p region and the effect of acid leaching on metal content is provided in Section 4.4.2. The Mn2p region of Mn-NG was found to be quite noisy but the peak position of $p_{3/2}$ at around 642.4eV nevertheless indicates Mn(IV) to be the predominant species.[18,19]

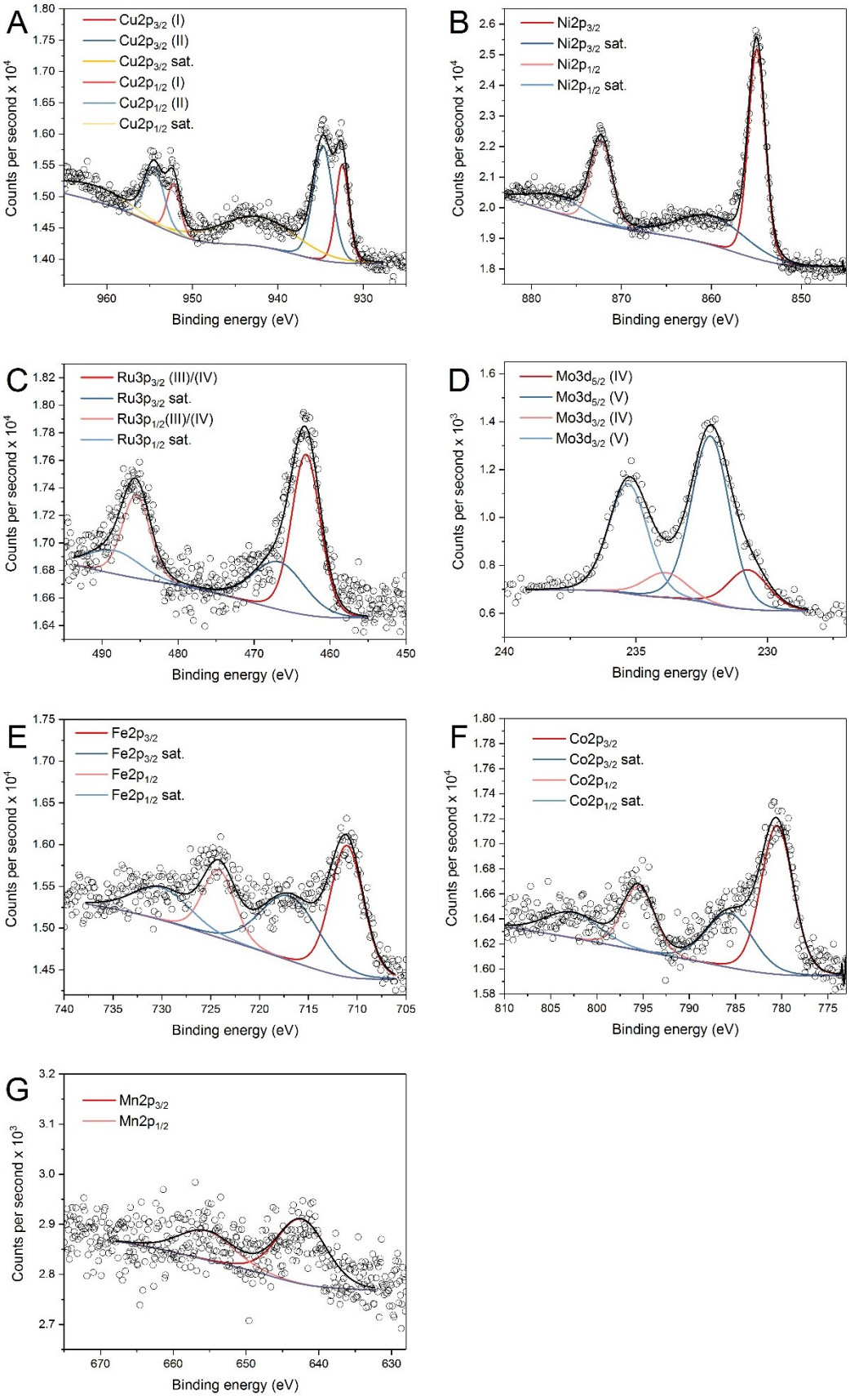

A
Cu2p3/2 (I)
Cu2p3/2 (II)
Cu2p3/2 sat.
Cu2p1/2 (I)
Cu2p1/2 (II)
Cu2p1/2 sat.
Counts per second x 10^4
Binding energy (eV)
B
Ni2p3/2
Ni2p3/2 sat.
Ni2p1/2
Ni2p1/2 sat.
Counts per second x 10^4
Binding energy (eV)
C
Ru3p3/2 (III)/(IV)
Ru3p3/2 sat.
Ru3p1/2(III)/(IV)
Ru3p1/2 sat.
Counts per second x 10^4
Binding energy (eV)
D
Mo3d5/2 (IV)
Mo3d5/2 (V)
Mo3d3/2 (IV)
Mo3d3/2 (V)
Counts per second x 10^3
Binding energy (eV)
E
Fe2p3/2
Fe2p3/2 sat.
Fe2p1/2
Fe2p1/2 sat.
Counts per second x 10^4
Binding energy (eV)
F
Co2p3/2
Co2p3/2 sat.
Co2p1/2
Co2p1/2 sat.
Counts per second x 10^4
Binding energy (eV)
G
Mn2p3/2
Mn2p1/2
Counts per second x 10^3
Binding energy (eV)

Figure 5: *XPS spectra of the metal p or d region of all M-NGs. Cu2p region of Cu-NG (A), Ni2p region of Ni-NG (B), Ru3p region of Ru-NG (C), Mo3d region of Mo-NG (D), Fe2p region of Fe-NG (E), Co2p region of Co-NG (F), and Mn2p of Mn-NG (G). Mn-NG spectrum was recorded on a lower resolution machine explaining the higher noise levels and lower signal strength in its Mn2p spectrum. The black line, purple line and empty black circles, respectively represent the overall fit, background, and data points. Strongly coloured traces represent respective $p_{3/2}$ or $d_{5/2}$ peaks, whereas faint coloured traces represent corresponding $p_{1/2}$ or $d_{3/2}$ peaks.*

Table 1: *Overview of elemental compositions of NG and M-NG catalysts. *0.64at% of Cl were detected as well. ** N1s region of Mo-NG contains small contributions from Mo3p.*

Sample	Carbon (at%)	Nitrogen (at%)	Oxygen (at%)	Metal (at%)
NG	91.52	6.43	2.04	-
Co-NG*	78.06	7.55	13.62	0.13
Fe-NG	87.45	7.42	4.98	0.14
Cu-NG	89.99	5.93	3.96	0.12
Ru-NG	88.92	5.62	4.11	0.21
Mo-NG	90.97	5.59**	3.32	0.11
Mn-NG	85.76	5.28	8.84	0.12
Ni-NG	88.10	8.33	3.36	0.21

Overall, the XPS studies show that all M-NG samples and NG were successfully doped with nitrogen (around 5-8at%, Table 1) via annealing in ammonia atmosphere. Furthermore, all catalysts were shown to contain carbon moieties characteristic for doped graphene-like structures. Successful metal doping (around 0.2at%, Table 1) was verified by XPS survey scans and high-resolution spectra of the metal p or d regions demonstrate that all metal species are present in oxidised form.

4.3.3 TEM

Transmission electron microscopy was performed to investigate the morphology of the catalysts and check for the presence of nanoparticles. Figure 6 shows typical bright-field TEM micrographs of M-NG catalysts.

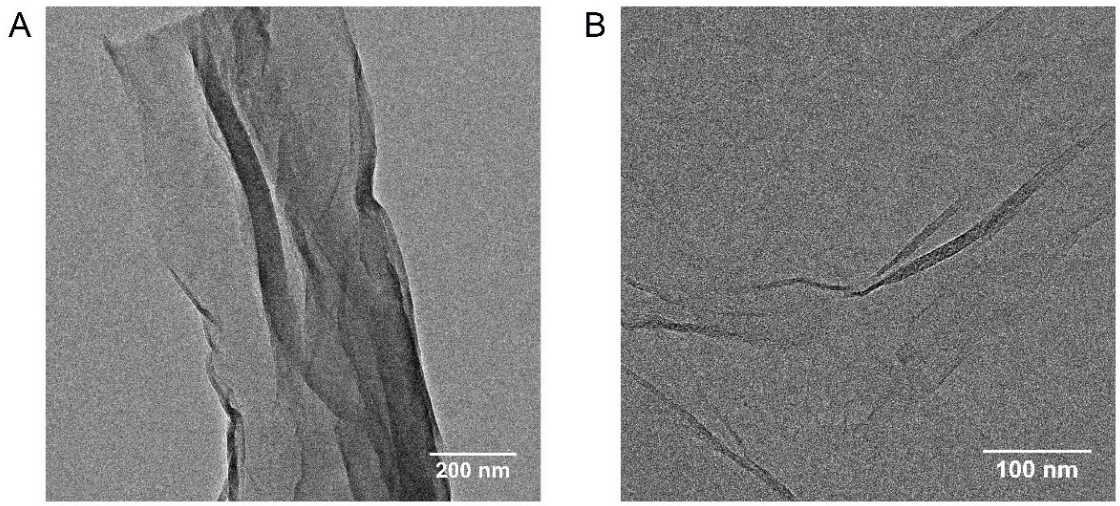


Figure 6: *Bright-field TEM images of Mo-NG (A) and Ru-NG (B). Black lines represent ridges of wrinkles in the N-graphene support whereas dark grey areas represent basal planes of N-graphene.*

As expected, M-NG catalysts exhibited a similar morphology to the un-doped NG sample; wrinkled graphene-like sheets with no detectable nanoparticles (Fig. 6). The N-graphene sheets were found to be roughly 50μm across. This aligns with literature reports on the morphology of N-graphene based materials obtained via thermal reduction in ammonia.[4–6]

4.3.4 STEM

To exclude the possibility of the formation of small metal clusters and confirm atomic dispersion of the metal onto the nitrogen doped graphene support, high resolution aberration corrected high-angle annular dark field scanning transmission electron microscopy (HAADF-STEM) was carried out for Co-NG, Mn-NG, Ni-NG, Ru-NG and

Mo-NG. The single-atom character of Fe-NG was shown by WT-EXAFS (Appendix Fig.A1). All samples were beam showered before high-resolution imaging was carried out.

Figure 7 shows HAADF-STEM micrographs of Mn-NG, Ni-NG, Mo-NG and Ru-NG. Micrographs of Co-NG and detailed discussion can be found in Chapter 5 Section 3.4. Single bright spots of a diameter of below 0.3nm were found to be homogeneously dispersed on large sheets clearly showing that the metals exist in single atom form (Fig.7). The sheets were found to have a honeycomb lattice and a thickness of around 0.6nm to 2nm. This corresponds to roughly two to five layers of N-graphene indicating that slight restacking occurs during the synthesis but that overall a high surface area is retained. No clusters or nanoparticles were found under normal imaging conditions. Consecutive excessive beam showering did occasionally lead to severe damage to the graphene support creating large holes and lead to the artificial formation of nanoparticles on the remaining carbon islands. This behaviour was especially prominent for the Ni-NG catalyst.

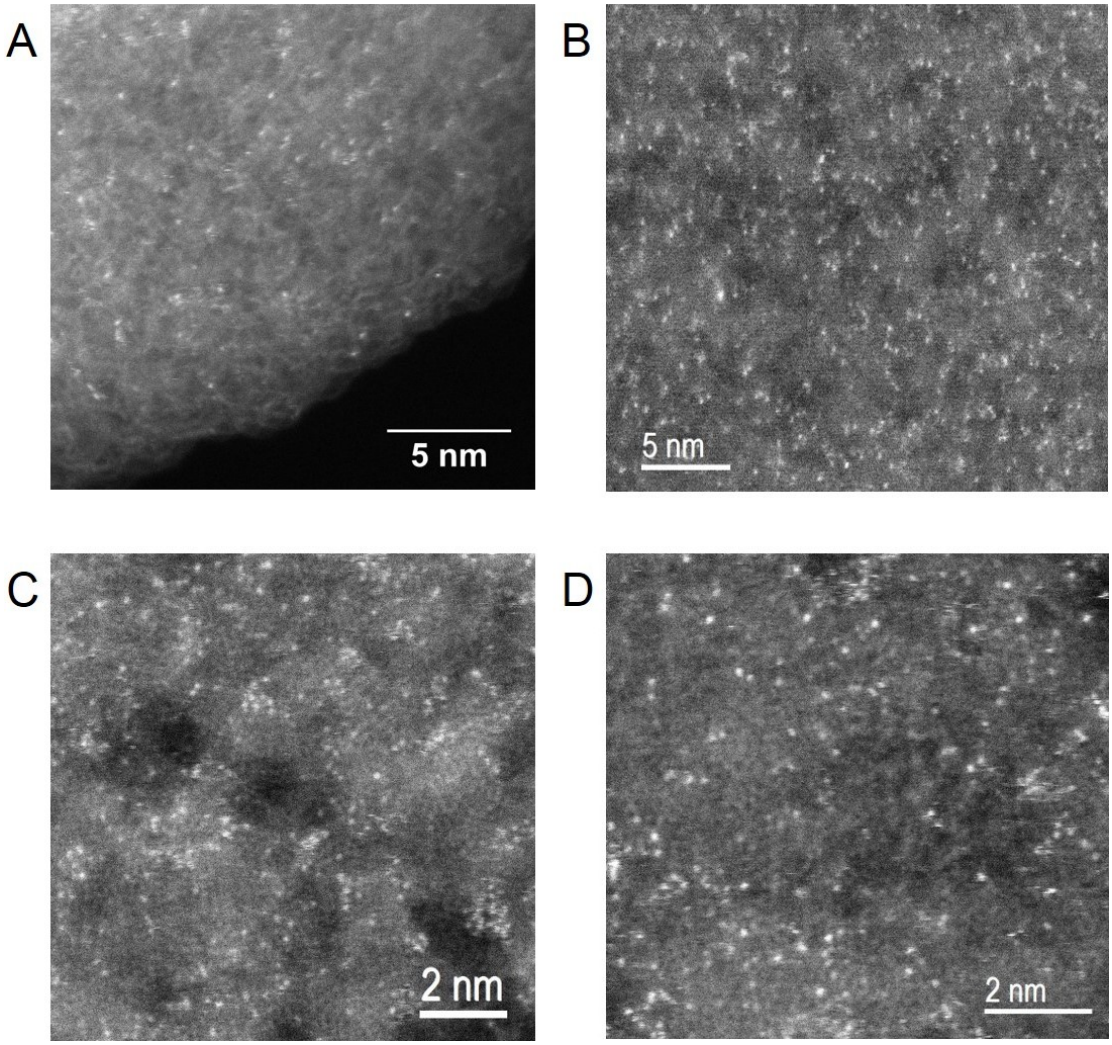


Figure 7: *HAADF-STEM images of Mn-NG (A), Mo-NG (B), Ni-NG (C) and Ru-NG (D) obtained on JEOL ARM200F at magnifications of 10MX (A, B), 25MX (C) and 30MX (D). Bright spots correspond to single metal atoms, grey areas correspond to several layers of N-graphene, darker area represent few layers and black areas show vacuum.*

Overall STEM imaging shows that atomic dispersion for M-NGs was achieved with the carbon support retaining its graphene-like structure after N-doping.

4.4 Hydrogen Evolution Reaction

4.4.1 Experimental Methods

For details on the experimental methods, see Chapter 3 Section 2.1.

In summary, all electrochemical testing was carried out in a standard glass cell in a three electrode configuration using 0.5M H_2SO_4 as electrolyte. Before testing, the electrolyte was sparged with Ar for at least 30min to remove dissolved oxygen. The working electrode was prepared by dropcasting an ink of the catalyst of interest onto the glassy carbon electrode yielding a loading of around 0.27 mg cm^{-2}.

Before catalysts were tested for their activity, they were cycled between -0.5 and 1V vs RHE at 100mV s^{-1} for at least 10 cycles. Linear scan voltammetry was carried out to determine the HER activity usually scanning from 0.2V to -1.2V vs RHE at a scan rate of 5mV s^{-1}. To investigate the stability of catalysts chronoamperometry experiments were performed at a current density of 10mA cm^{-2} corresponding to a current of 707µA in this setup. Testing of M-NG catalysts from different batches yielded similar results usually differing by only around 20mV in overpotential needed to reach a current density of 10mA cm^{-2}.

4.4.2 Results and Discussion

For all M-NG catalysts it was observed that after a couple of potential cycles the activity for the hydrogen evolution reaction increased dramatically, seen by an earlier (less negative) onset potential of the Faradaic current. As an example Figure 8 illustrates this behaviour for Co-NG. During the first scan the onset potential for HER seems to be more negative than -0.1V whereas in the following scan catalytic current can already be observed at -0.05V. Compared to the following scans, the first scan exhibits significantly

higher oxidative currents above 0.7V vs RHE which seem to be responsible for the activity increase. In line with that exposure to oxidative potentials of 0.8 to 1V vs RHE for short periods of time prior to CVs or LSVs also leads to similar increases in activity. It is hypothesised that the surface of the catalyst is cleaned from loosely adsorbed species, such as adventitious carbon, during these procedures leading to an increased exposure of active sites to the electrolyte. This type of behaviour is well documented for other electrocatalysts in acidic environments, such as platinum[20]. Additionally, broad oxidation/reduction peaks with a halfway potential of around 0.65V vs RHE were observed (Fig.8, c_1/a_1) and attributed to quinone/hydroquinone functionalities often found in carbon materials.[21,22]

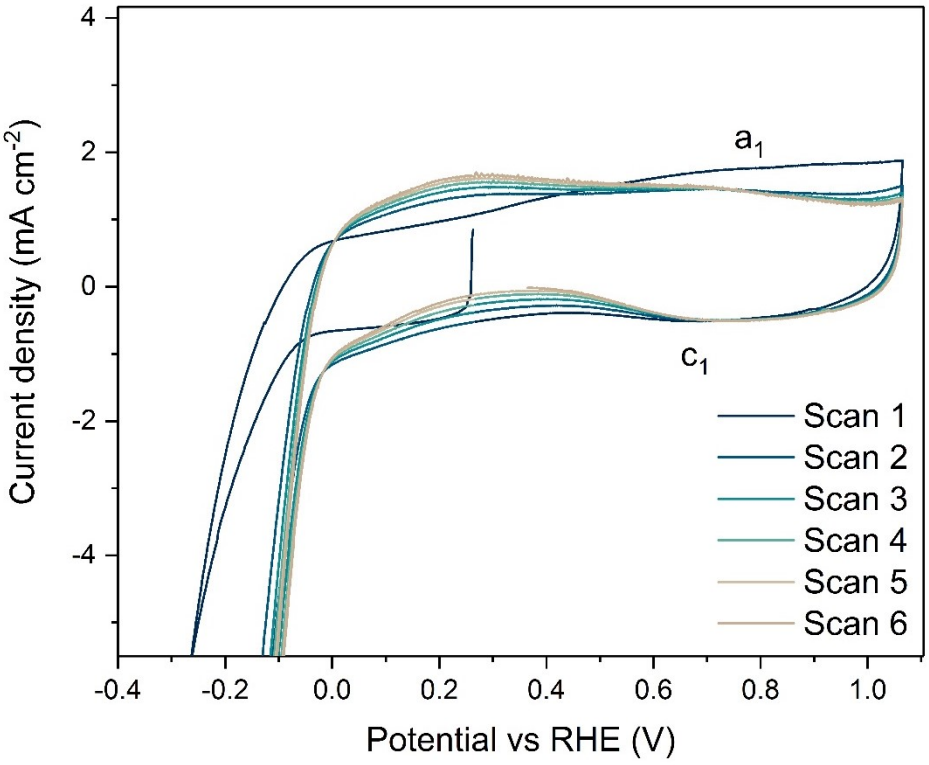


Figure 8: *Cyclic voltammograms of Co-NG upon first immersion into Ar-sparged 0.5M H_2SO_4 measured at 150mV s^{-1} showcasing the activation of the catalyst. The catalyst was cycled from 1V to -0.5V vs RHE. Colour code: Scan 1 (dark blue), following scans going from cyan to light brown.*

To compare the activity of the M-NG catalysts LSVs from 0.2V to -1.2V vs RHE were recorded at a scan rate of 5mV s^{-1} (Fig.9). All metal doped catalysts were found to be more active than the un-doped NG (black trace) exhibiting lower onset potentials, as well as lower potentials required to achieve a current density of 10mA cm^{-2}. The commercially used platinum on carbon catalyst (grey trace) appeared to be more active than all M-NG catalysts on the basis of current density (current normalised to the geometric area of the electrode). The shape of the LSVs was similar for all catalysts with a sharp increase in current due to the HER past the onset potential with the notable exception of Mo-NG. At an overpotential of around 100mV a linear increase of Faradaic current is observed for the Mo-NG catalyst but no gas bubbles seem to form on the electrode surface. A sharp non-linear increase in current is observed at overpotentials above 500mV and a large amount of gas bubbles is observed indicating the onset of HER. It is hypothesised that the current between 100mV and 500mV originates from slow H_2 evolution over a molybdenum oxo/oxide species which gets reduced at overpotentials larger than 500mV. Co-NG and Ru-NG were both found to be very active with overpotentials at 10mA cm^{-2} of 116mV and 189mV, respectively.

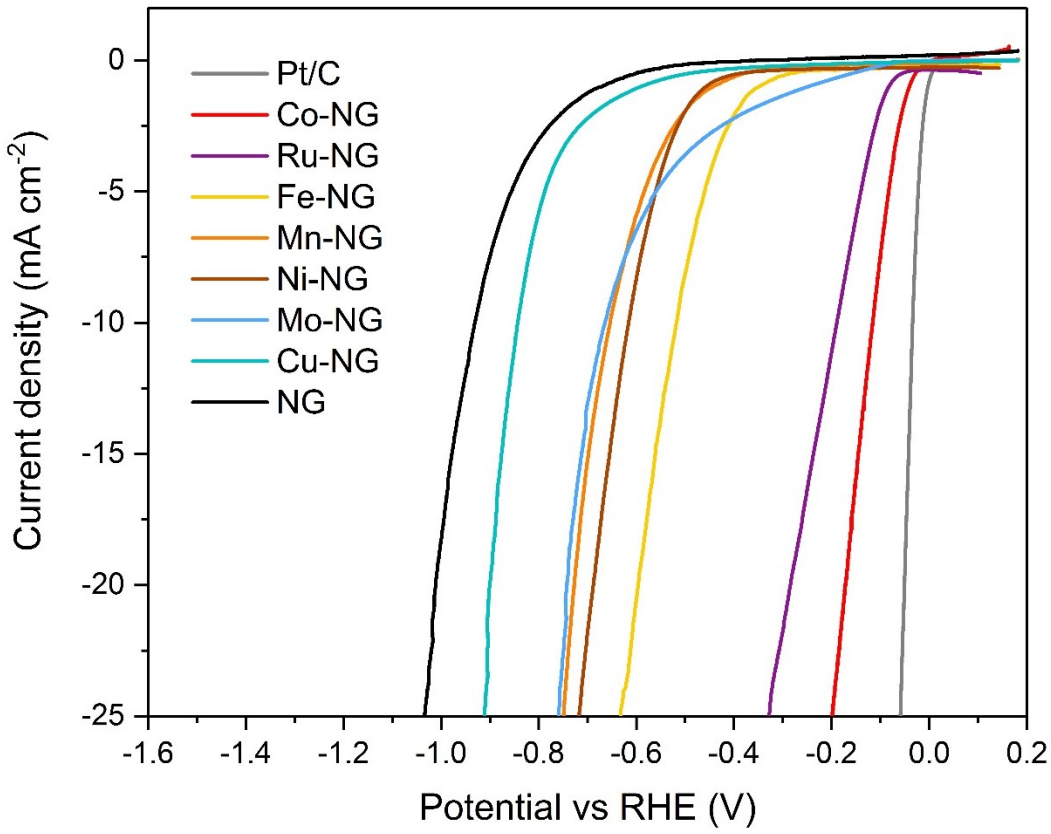


Figure 9: *Linear scanning voltammograms of M-NGs, NG and Pt/C in Ar sparged 0.5M H_2SO_4 at a scan rate of 5mV s^{-1}. Colour code: Pt/C (grey), Co-NG (red), Ru-NG (purple), Fe-NG (yellow), Ni-NG (brown), Mn-NG (orange), Mo-NG (blue), Cu-NG (cyan), and NG (black).*

Variation in electrocatalytic activity between batches was found to be small as shown in Figure 10 for Co-NG. Batch 1 and 2 were synthesised via the same procedure outlined in Section 2 several weeks apart. The difference in overpotential needed to reach a current density of 10mA cm^{-2} between the two batches was observed to be below 20mV.

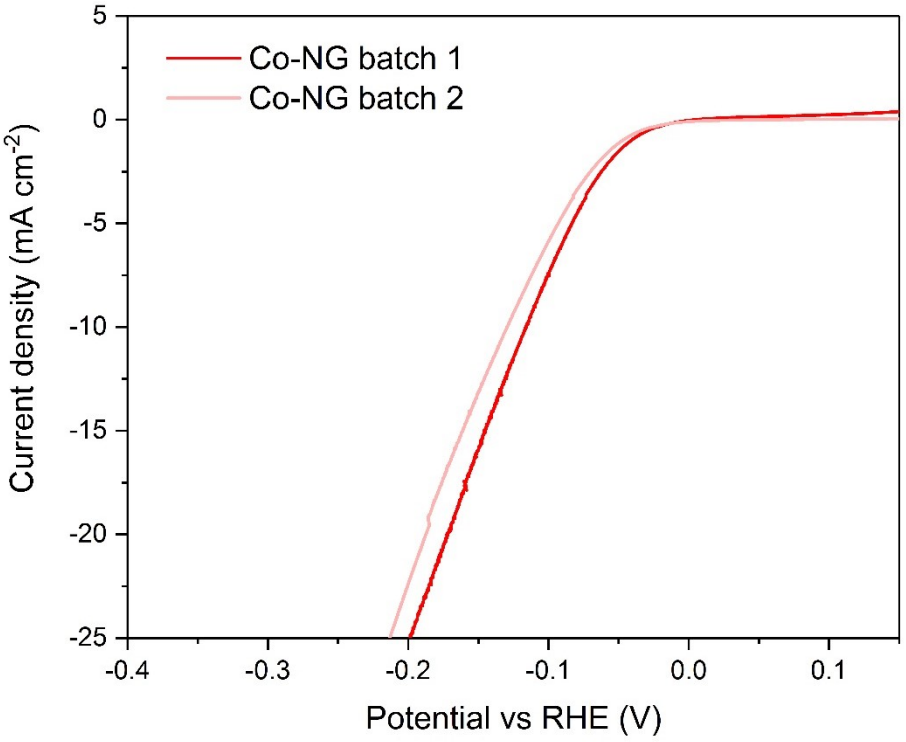


Figure 10: *Linear scanning voltammograms of Co-NG in Ar sparged 0.5M H_2SO_4 at a scan rate of 5mV s^{-1}. Colour code: Co-NG batch 1 (red) and Co-NG batch 2 (light red).*

Tafel analysis was carried out to determine Tafel slopes of all catalysts (Fig.11). Pt/C exhibits a Tafel slope of 31mV dec^{-1} which agrees well with previously reported literature values[20,23] and as discussed in Section 1.2.2 indicates that it operates via a Volmer-Tafel mechanism with the Tafel step being rate limiting[2,20,23] though this has been a source of contention[24]. Low Tafel slopes of 70mV dec^{-1} and 51mV dec^{-1} were found for Ru-NG and Co-NG, respectively. This is an indication for proton reduction to proceed via the Volmer step followed by the rate determining Heyrovsky step.[20] Interestingly, the Tafel slope for Co-NG is significantly lower than that of similar Co-based catalysts reported in literature.[2,25] Fei et al. report a Tafel slope of 82mV dec^{-1} for their atomically dispersed cobalt on N-graphene catalyst.[2] They did not employ an acid leaching step during their synthesis[2] giving rise to the possibility of other cobalt species, such as small clusters, cobalt nitride or cobalt carbide contributing to the HER activity of their catalyst or

blocking the atomically dispersed Co centres and as such masking the true Tafel slope of the Co-N_4 active sites.

All other M-NG and NG have Tafel slopes in excess of 120mV dec^{-1} implying the initial proton adsorption (Volmer step) to be rate limiting. Mo-NG (light blue trace) exhibited several linear regions in the Tafel plot with the first one being shown in Fig. 11. As discussed above, it is believed that for overpotentials up to 500mV H_2 is evolved on a less active form of Mo-NG meaning the displayed Tafel slope of 183mV dec^{-1} does not correspond to HER observed at higher overpotentials. Due to this process occurring between -0.2 to -0.5V vs RHE it was not possible to determine the Tafel slope for the HER on active Mo-NG.

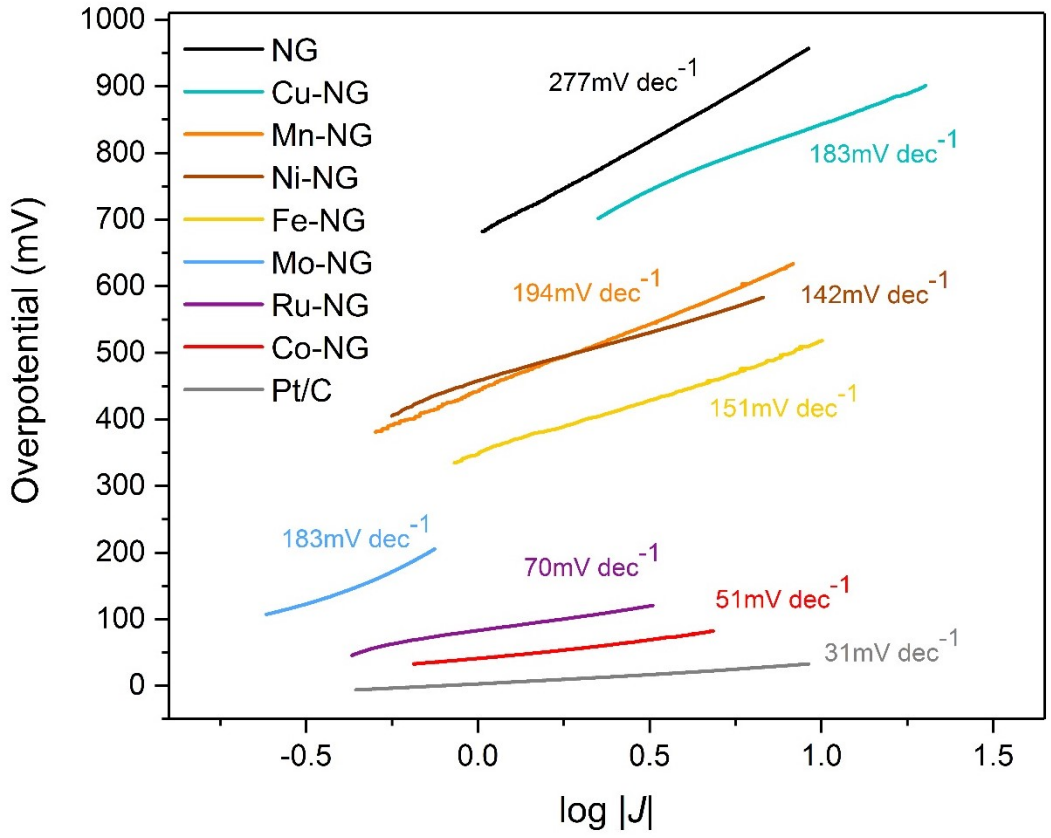


Figure 11: *Tafel plots of the LSVs of M-NG, NG and Pt/C in Ar sparged 0.5M H_2SO_4 at a scan rate of 5mV s^{-1} showing the overpotential versus the logarithm of the magnitude of the current density (J). Colour code:*

Pt/C (grey), Co-NG (red), Ru-NG (purple), Fe-NG (yellow), Ni-NG (brown), Mn-NG (orange), Mo-NG (blue), Cu-NG (cyan), and NG (black).

Figure 12 shows the Tafel slopes for all catalysts over an extended window including its Tafel slopes at 10mA cm^{-2} (equal to 1 on the logarithmic scale). Most SACs show only a small increase in slope. For Co-NG (red trace) and especially Ru-NG (purple trace) this increase is more pronounced. For Mo-NG (blue trace) the Tafel slope for HER around and above 500mV is shown which is found to vary between 300mV dec^{-1} to around 200mV dec^{-1}, respectively.

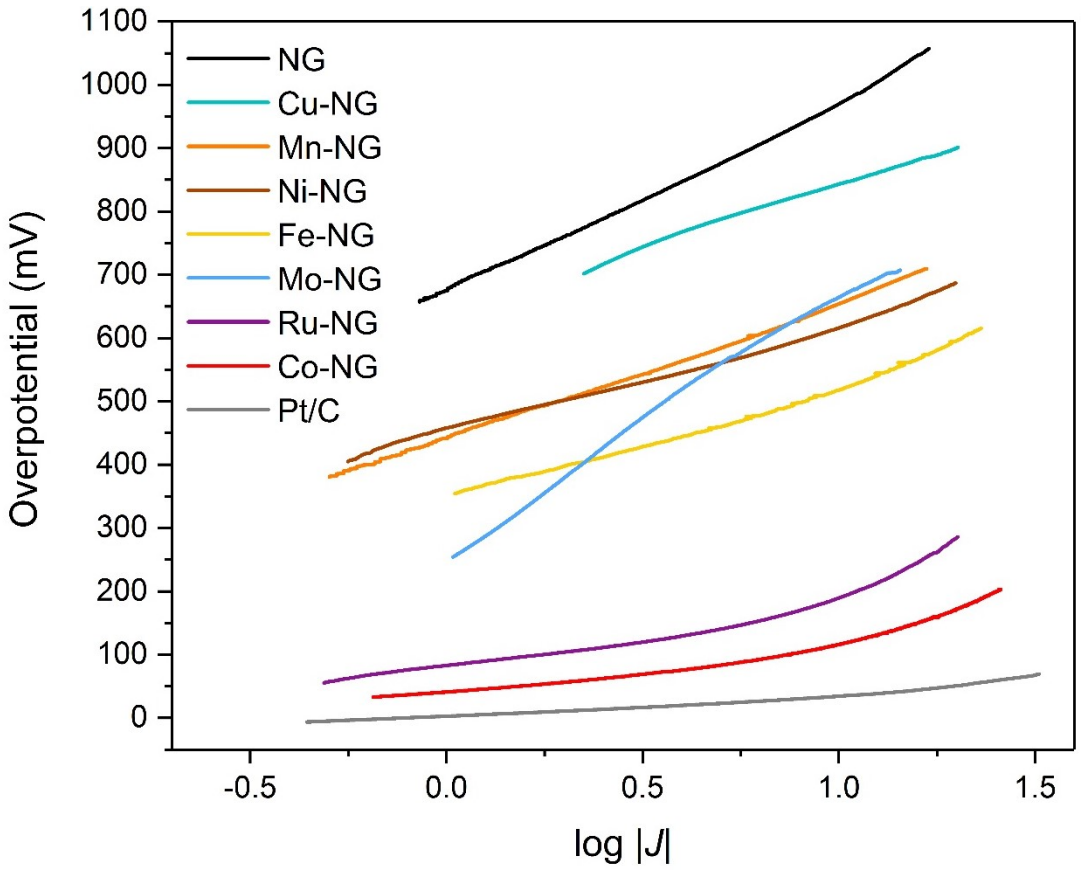


Figure 12: *Extended Tafel plots of the LSVs of M-NG, NG and Pt/C in Ar sparged 0.5M H_2SO_4 at a scan rate of 5mV s^{-1} showing the overpotential versus the logarithm of the magnitude of the current density (J). Colour code: Pt/C (grey), Co-NG (red), Ru-NG (purple), Fe-NG (yellow), Ni-NG (brown), Mn-NG (orange), Mo-NG (blue), Cu-NG (cyan), and NG (black).*

The turn over frequencies (TOFs) were determined to compare the activity of the M-NG catalysts on a per active site basis (Eq.1).

$$TOF = \frac{|I|}{\rho_{active\ sites} \times n_e \times F} \quad (1)$$

Where I is the current density in A cm^{-2}, F is Faraday's constant in C mol^{-1}, n_e is the number of electrons needed per number of products (here two) and $\rho_{active\ sites}$ is the active site density in mol cm^{-2}. The number of active sites per geometric surface area was estimated using XPS measurements in which the metal content in acid-leached samples was found to be below 0.21at%. This ultra-low loading of metal in the M-NG systems makes it hard to determine the exact loading of metal due to the measurement error of XPS of around 0.5at%. As such, an upper bound of 0.7at% loading of metal was used to calculate an active site density of around 1.5×10^{-7} mol cm^{-2}. Likely, the effective active site density is lower due to not all metal centres being exposed to the electrolyte and actual metal loading being lower than 0.7at%. Using the upper bound active site density a lower bound turn over frequency was calculated for all M-NG systems (Fig. 13).

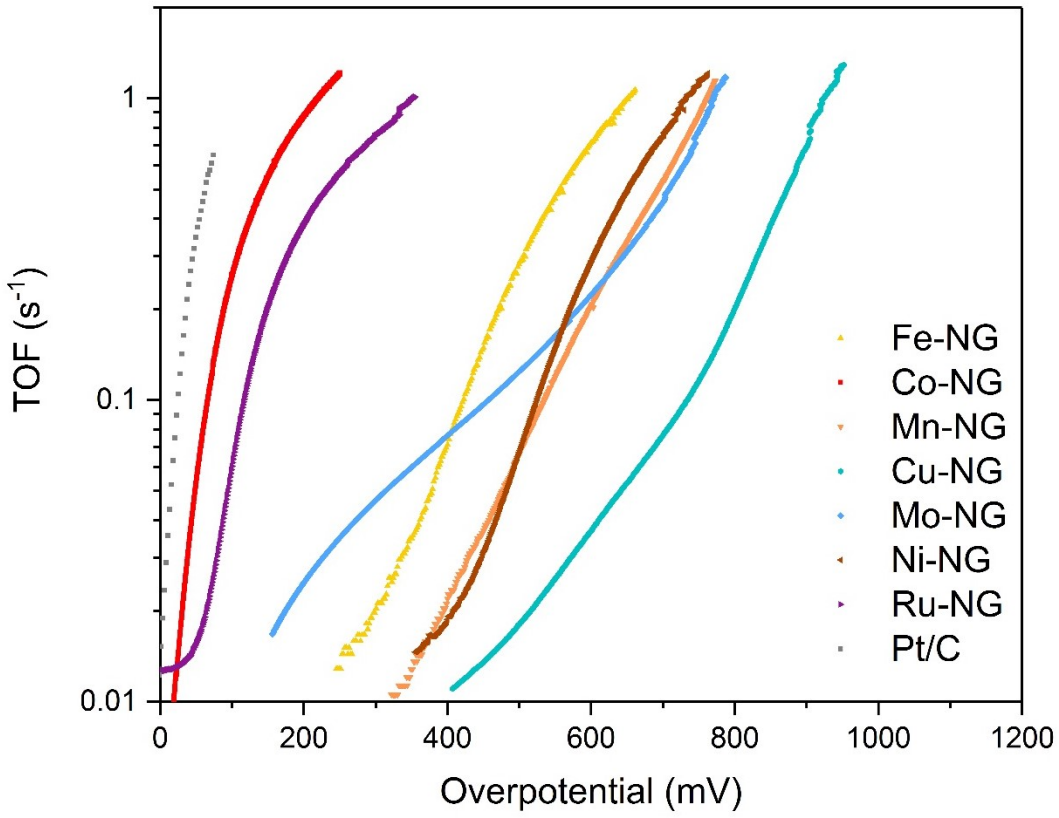


Figure 13: *Turn over frequency of M-NG catalysts plotted against overpotential. Colour code: Pt/C (grey dotted line), Co-NG (red), Ru-NG (purple), Fe-NG (yellow), Ni-NG (brown), Mn-NG (orange), Mo-NG (blue), Cu-NG (cyan), and NG (black).*

The active site density of the Pt/C catalyst was approximated to be equal to the total loading of Pt atoms (2.9 x 10^{-7} mol cm^{-2}). This is very likely an overestimation as well since most Pt atoms are present in the form of small nanoparticles (1-2nm) in the Pt/C catalyst and hence only a few of them are exposed to the electrolyte.

Overall Figure 13 shows that the TOFs of Ru-NG and especially Co-NG are getting close to the one of the commercial Pt/C catalyst. Co-NG and Ru-NG require overpotentials of around 74mV and 117mV respectively to achieve a TOF of 0.1 s^{-1} compared to 25mV required with the Pt/C catalyst.

Platinum is very expensive costing more than three times as much as ruthenium and can be up to 900 times the price of cobalt[26], meaning that even though Ru and Co centres are slightly less active for HER compared to Pt, Co or Ru SACs could be economically competitive by increasing the loading of metal to match the current densities of Pt/C. Increasing the metal loading in SAC systems while maintaining atomic dispersion of metal centres should as such be a major research focus in the area. Novel concepts towards this goal based on the pyrolysis of MOF[27–31], COF[32,33] and polymer[34,35] precursors, as well as ionothermal methods[36] have recently been reported in literature[37] and might provide a way forward for SAC systems as HER catalysts under acidic conditions. Next to considerations about the current prices of metal precursors, it is important to take their future availability into account. Global cobalt reserves are estimated to amount to around 6.9 million tons with global yearly production being 139000 tons in 2017 meaning at current production levels cobalt will be available over the next 40 years. Cobalt production is believed to increase significantly over the next years because of its use in cobalt oxide cathodes in lithium ion batteries deployed in electric vehicles which could drive up its price although it has to be considered that cobalt is mostly obtained as a byproduct from copper and nickel mining and as such its price is influenced by the demand for these metals as well.[26] Similarly, platinum is often produced as a byproduct from copper, nickel or cobalt production though some ores contain high enough concentrations to warrant solely Pt mining.[26] Proven reserves of Pt (~5700 tons) are estimated to last for a minimum of 40 years considering production levels from 2008 (~170 tons per annum).[26]

Another hurdle on the way to application in real life devices is the stability of the catalyst under continued operation.[37] An initial test was conducted for Co-NG running the catalyst

at 10mA cm^{-2} for almost 10h showing only a small drop in required overpotential (Fig.14).

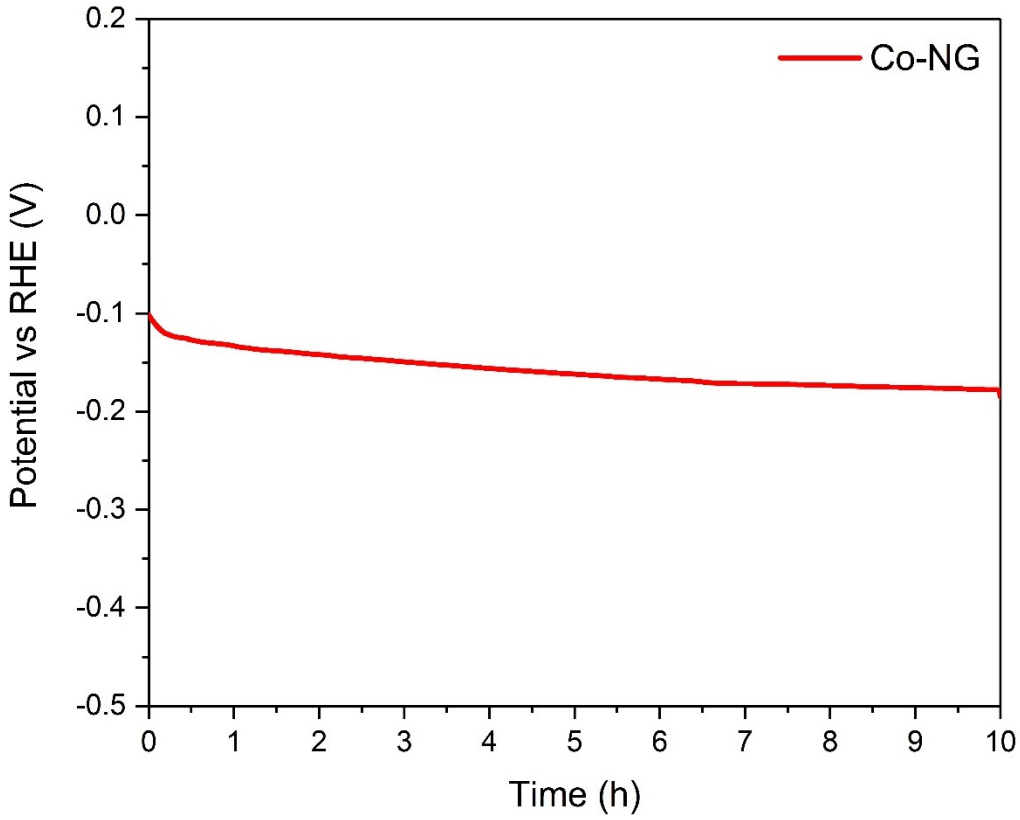


Figure 14: Chronoamperometry of Co-NG in Ar-sparged 0.5M H_2SO_4 at 10mA cm^{-2} (corresponding to 707μA) for 10h.

Further stability tests in aqueous conditions using accelerated stress tests, as well as stability tests in the gas phase as membrane electrode assembly (MEA) are needed to assess the potential of Co SAC based HER catalysts for PEM electrolysers.

4.4.3 Correlation with Theory

Recent computational investigation of atomically dispersed transition metal atoms on carbon materials by Xu et al. introduced factor φ as a predictor for the HER activity of SACs[38]. It was theoretically vetted by showing good correlation with calculated hydrogen binding energies (ΔG_{H*}) for 112 different geometry-optimised SAC configurations.[38]

ΔG_{H^*} is an established activity indicator and should be 0 for the ideal HER catalyst.[20,38-41] The φ factor is calculated using Equation 2.

$$\varphi = \theta_d \times \frac{E_M + \alpha \times (n_N \times E_N + n_C \times E_C)}{E_{O/H}} \quad (2)$$

Where θ_d signifies the number of d electrons of a single transition metal atom in the metallic state (oxidation state 0), E_M the electron negativity of the metal, n_N and E_N the number and electronegativity, respectively, of nitrogen ligands, n_C and E_C the number and electronegativity, respectively, of carbon ligands in the first coordination shell of the metal centre, E_H stands for the electronegativity of the reactant, hydrogen, and α is a correction factor[38]. The φ factor can be understood as a proxy for electron density on the metal centre. A M-N_4 active site with pyridinic nitrogen as ligands was assumed, based on previous literature reports[2,7,30,42] and XANES (see section 5.6.3), to calculate φ factors for the as-prepared M-NG systems. Hence n_N equalled four and n_C equalled zero. The correction factor α which was introduced by the authors to account for a difference in ring size between pyridine and pyrrole based active sites is unity in this instance.[38]

Figure 15 shows that our data correlates with φ forming a volcano relationship with Co being at the top with a φ factor of 44.67. This is in line with the maximum of the calculated volcano of around 42 (for Pt in a single vacancy with C_2N_1 coordination) reported by Xu et al.[38].

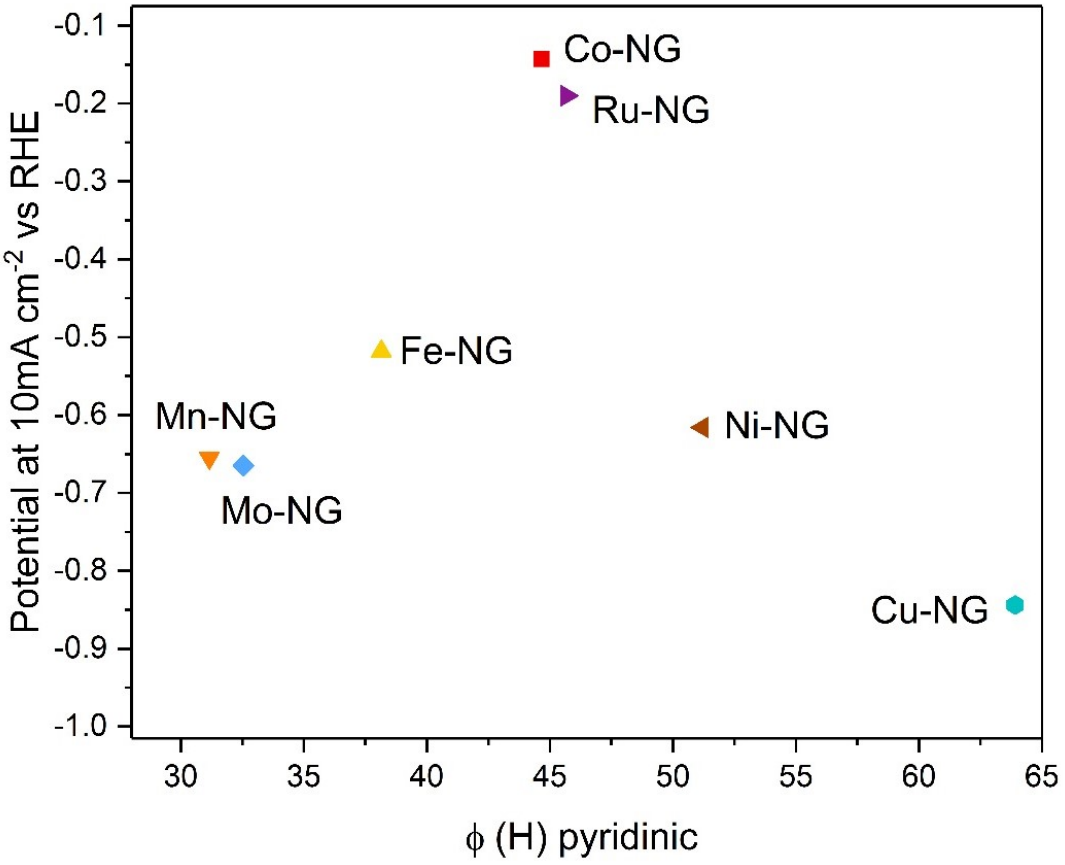


Figure 15: *Scatter plot of overpotential at 10mA cm^{-2} of M-NG catalysts vs phi factor*

In order to test the validity of φ, Xu et al. correlated some of their theoretical data with results on HER activity of metals on nitrogen-doped carbon published by Morozan et al.. The used experimental data[38,43] was obtained from catalysts containing significant amounts of metal nanoparticles, as well as metal carbides, nitrides and oxides, shown by TEM, XRD as well as XAS studies[43] and were in fact considered "almost free" of atomically dispersed metal species by the authors of the experimental paper themselves[43] rendering the comparison to the theoretical results invalid.

Hence, the data presented in this thesis constitute the first experimental validation of the φ factor as a predictor for HER activity of SACs using well-characterised atomically dispersed M-N_4 catalysts on N-doped carbon support.

4.5 Electrochemical Ammonia Synthesis

4.5.1 Experimental Methods

For details on the experimental methods, see Chapter 3 Section 2.2.

In a standard NRR experiment, the working electrode was held at -0.25V or -0.5V vs RHE for one to six hours while constantly bubbling N_2 gas. Two types of blank measurements were also carried out: first electrolyte was bubbled with N_2 in the cell without the catalyst present (referred to as blanks form here on) and secondly holding the catalyst at -0.25V or -0.5V vs RHE for one to six hours while constantly bubbling Ar gas (referred to as Ar blanks).

4.5.2 Ammonia Detection

Several different analytical techniques to quantify ammonia exist. We tested Nessler's method, an ion selective electrode (ISE) and the salicylate test, an adapted version of the Berthelot test. For details on the working principles and experimental protocols, see Chapter 3 Section 2.3.

The salicylate method to quantify ammonia in this chapter. Three solutions are prepared for the salicylate test: Solution A made up of 4g of sodium hydroxide, 5g of sodium citrate and 5g of salicylic acid in 100mL MQ water, solution B made up of 8mL sodium hypochlorite solution in 100mL MQ water and solution C consisting of 0.1g sodium ferricyanide dihydrate in 10mL MQ water. Initially the analysis was carried out in a well plate to enable rapid screening, later on cuvettes were used. Equal amounts of the analyte and solution A were mixed (100µL each/1mL each) followed by the addition of 50% of the analyte volume of solution B (50 µL/500 µL). Finally, 10% of the analyte volume of solution C were added (10 µL/100 µL). The samples were analysed using UV-Vis

spectrometer and quantified using the absorption at 650nm. Interferences and extraneous sources of ammonia are discussed in section 6.3.

4.5.3 Results and Discussion

Initially the salicylate method was performed in a well plate to enable rapid screening of catalysts. This was abandoned due to problems with cross contamination as well as errors introduced through varying path length in the wells caused by evaporation leading to poor calibration curves. Using cuvettes for the UV-Vis measurements increased the reliability of salicylate test calibrations drastically (Appendix Fig.A2).

In the first iteration of the NRR testing setup Nafion was used in the fabrication of the catalyst ink and a Nafion membrane was used to separate catholyte and anolyte. Using blank measurements of the cell and of solutions with a Nafion membrane dispersed in it, we found that Nafion can act as a sink, as well as a source of ammonia. These findings caused us to eliminate Nafion from our NRR setup. Similar behaviour has recently been reported by others, who deemed Nafion as inappropriate for use in NRR research.[44–46]

Furthermore, while doing further blank measurements the 3D printed cell itself was identified as a source of extraneous ammonia. We hypothesise that the material, Formlabs Clear Resin, can absorb small amounts of ammonia from air over time which is released when the cell comes into contact with the acidic electrolyte.

A second iteration of NRR setup consisting of a glass vial with a porous frit separating catholyte and anolyte was used for the remainder of the experiments. Blank electrolyte measurements in this setup usually contained much smaller amounts of ammonia (below 0.05ppm). An initial screen of the M-NG materials activity towards the NRR was conducted at potentials of -0.25V and -0.5V vs RHE in 0.1M HCl (Fig.16).

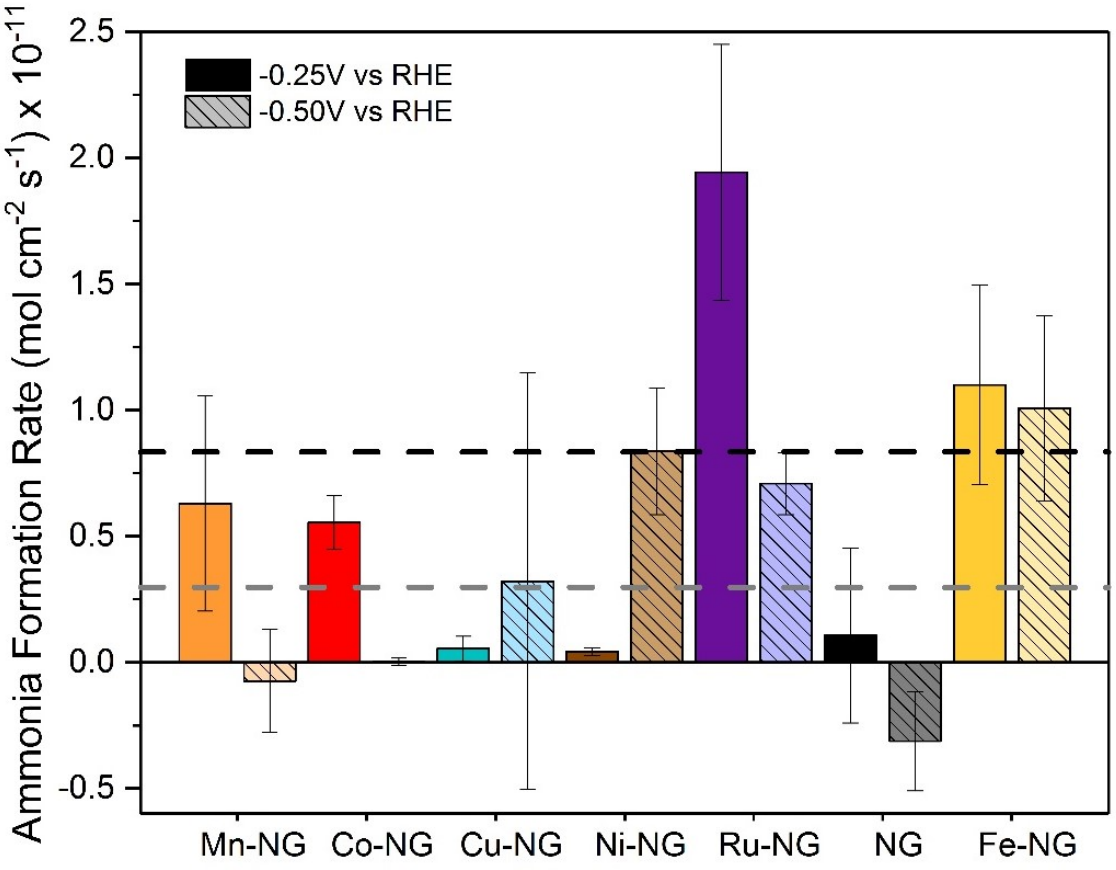


Figure 16: *Bar chart summarising the initial screening of M-NG catalysts for electrochemical ammonia synthesis in setup one in 0.1M HCl bubbled with N_2 without Nafion in the system. Measurements were carried out for around 1h. Grey dashed horizontal lines indicates rate corresponding to measuring 0.05ppm and black dashed horizontal line indicates rate for the highest measured blank (no catalyst present and no potential applied). Error bars show standard deviation of ammonia quantification using triplicate measurements. Colour code: Dark coloured bars correspond to measurements at -0.25V vs RHE and dashed faint coloured bars correspond to measurements at -0.5V vs RHE.*

Figure 16 shows that usually rates of around 10^{-11} to 10^{-12} mol cm^{-2} s^{-1} were measured for the M-NG catalysts. Results were not reproducible with large amounts of scatter in the data and sometimes negative NRR rates (this is due to contamination in the calibration samples or the blank measurements). Most results actually fall under the limit of detection of around 0.05ppm (grey dashed line) and all catalysts except for Ru-NG and Fe-NG exhibit rates lower than measured for the highest blank reading. Furthermore, sporadically significant amounts of ammonia were detected in Ar blank measurements

equalling or sometimes surpassing the amounts of ammonia detected under NRR conditions (shown for Fe-NG in Fig.17).

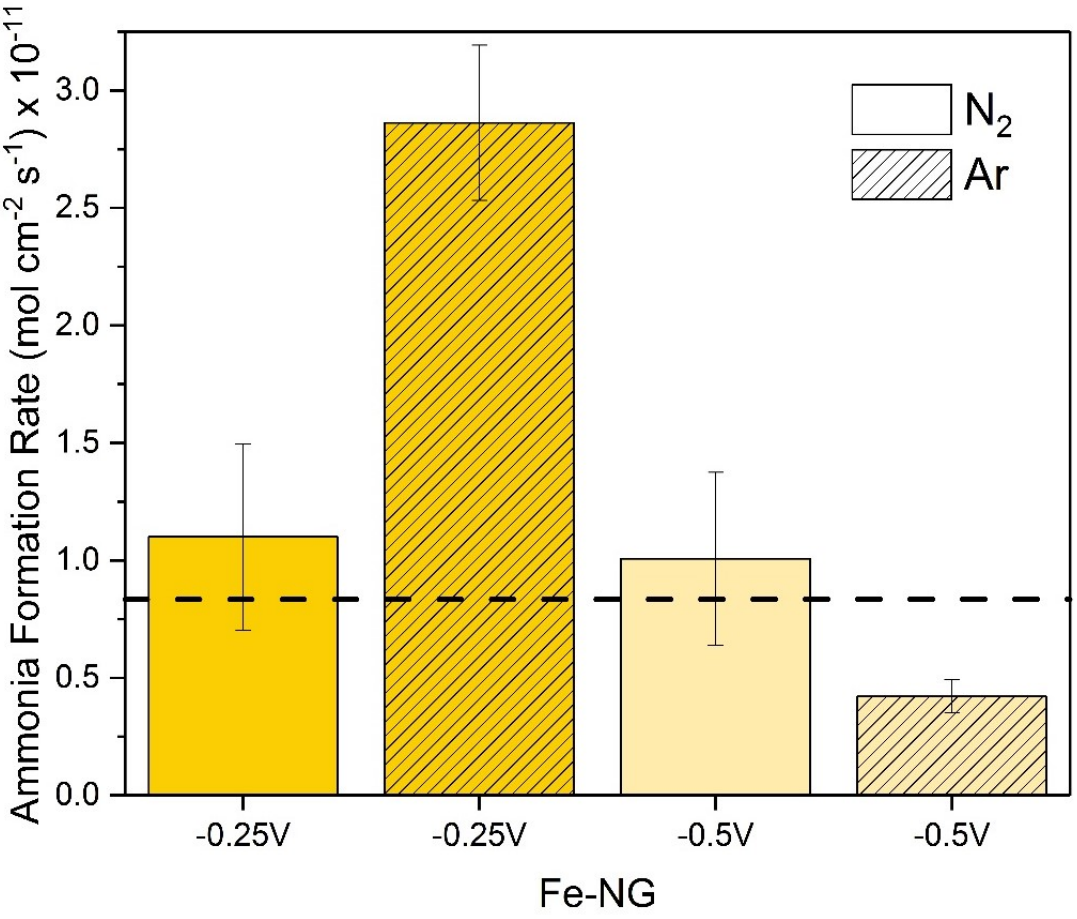


Figure 17: *Bar chart of Fe-NG catalyst NRR testing including Ar blanks in setup 1 in 0.1M HCl bubbled with N_2 without Nafion in the system. Measurements were carried out for around 1h. Black dashed horizontal line indicates rate for the highest measured blank (no catalyst present and no potential applied). Error bars show standard deviation of ammonia quantification using triplicate measurements. Colour code: Dark coloured bars correspond to measurements at -0.25V vs RHE and faint coloured bars correspond to measurements at -0.5V vs RHE.*

Overall, these preliminary results show that not all extraneous sources of ammonia were effectively controlled for leading to inconclusive data. One extraneous source that was observed is cleaning products. Large amounts of ammonia were detected in samples which run during weekly cleaning of the lab. Other possible sources of non-electrochemical ammonia or interference include lab air [45], organic amines from other

syntheses/experiments and even human breath[45]. Furthermore, ammonia was used in the preparation of the catalyst materials and although an acid leaching step was employed in the synthesis, as well as acid washing of the prepared electrodes, it cannot be excluded as an extraneous source beyond doubt.

Generally, using this data it cannot be ruled out that the as-prepared M-NG systems are active for the electrochemical nitrogen reduction reaction in 0.1M HCl but it can be shown that if active their NRR rate should be in the range of 10^{-12} to 10^{-11} mol cm^{-2} s^{-1} which is five or more orders of magnitude away from the US Department of Energy's target rate for electrochemical ammonia synthesis. Most literature on NRR in aqueous systems reports ammonia synthesis rates within that range, usually combined with low current efficiencies due to the competing HER reaction. Novel approaches that try to depress HER by limiting proton availability e.g. via using ionic liquids[47,48] or MOF coatings[49] have been proposed showing some promise in elevating the current efficiency but still exhibit only moderately low rates. Screening more catalysts, for example also the here presented M-NG systems, in such low proton concentration environments could lead to significant advancements not only in current efficiency but also in rate.

4.6 Conclusions

This chapter focused on the synthesis and characterisation of atomically dispersed transition metals on nitrogen-doped graphene. The activity of the as prepared M-NG systems towards the hydrogen evolution reaction and electrochemical nitrogen reduction reaction was explored.

A library of M-NG catalysts, including the novel materials Cu-NG, Mn-NG, and Mo-NG, was successfully synthesised using graphene oxide prepared via the improved

Hummers' method as a preformed carbon backbone which was annealed under ammonia together with metal chloride salts. The formed M-NG catalyst were acid-leached in concentrated HCl shown to remove unwanted metal species.

Using several characterisation techniques including XRD, TEM, XPS and STEM it was shown that the transition metals are indeed homogeneously atomically dispersed onto N-graphene support, most likely as M-N_4 centres. Single-atom catalysts of Co, Ru, Mn, Ni, Cu, Mo and Fe with similar morphology were successfully prepared. This illustrates the potential of the described backbone method to synthesise a wide-range of atomically dispersed metal catalysts while keeping other structural parameters constant.

The as-prepared M-NG catalysts were assessed for their HER activity in 0.5M H_2SO_4. All metal-doped systems showed higher activity, as determined by the overpotential at 10mA cm^{-2} and the Tafel slope, compared to the un-doped NG catalyst indicating that the dispersed M-N_4 centres are indeed the active site for HER. Ru-NG and especially Co-NG exhibited high activity with overpotentials of just 189mV and 116mV, respectively, at 10mA cm^{-2} and TOFs approaching those of the commercial Pt/C catalyst. Furthermore, Co-NG only exhibited a small drop in performance during an initial stability assessment at 10mA cm^{-2}.

Additionally, the HER activities were correlated to the recently proposed φ factor, a proxy for electron density on the metal centre. A volcano type relationship between the overpotential at 10mA cm^{-2} of the different M-NG catalysts and their φ factor was observed with Co-NG at the top. This is believed to be the first experimental substantiation of this design principle using well-characterised atomically dispersed catalysts.

After several iterations of experimental setup, electrochemical nitrogen reduction reaction testing in 0.1M HCl remained inconclusive due to low activity of the catalysts and extraneous sources of ammonia prohibiting the confident quantification of electrochemically produced ammonia in the described setups.

4.7 References

(1) Marcano, D. C.; Kosynkin, D. V.; Berlin, J. M.; Sinitskii, A.; Sun, Z.; Slesarev, A.; Alemany, L. B.; Lu, W.; Tour, J. M. Improved Synthesis of Graphene Oxide. *ACS Nano* **2010**, *4* (8), 4806–4814. https://doi.org/10.1021/nn1006368.

(2) Fei, H.; Dong, J.; Arellano-Jiménez, M. J.; Ye, G.; Dong Kim, N.; Samuel, E. L. G.; Peng, Z.; Zhu, Z.; Qin, F.; Bao, J.; et al. Atomic Cobalt on Nitrogen-Doped Graphene for Hydrogen Generation. *Nat. Commun.* **2015**, *6*, 8668. https://doi.org/10.1038/ncomms9668.

(3) Li, D.; Yu, C.; Wang, M.; Zhang, Y.; Pan, C. Synthesis of Nitrogen Doped Graphene from Graphene Oxide within an Ammonia Flame for High Performance Supercapacitors. *RSC Adv* **2014**, *4* (98), 55394–55399. https://doi.org/10.1039/C4RA10761F.

(4) Xing, Z.; Ju, Z.; Zhao, Y.; Wan, J.; Zhu, Y.; Qiang, Y.; Qian, Y. One-Pot Hydrothermal Synthesis of Nitrogen-Doped Graphene as High-Performance Anode Materials for Lithium Ion Batteries. *Sci. Rep.* **2016**, *6*, 26146. https://doi.org/10.1038/srep26146.

(5) Shao, Y.; Zhang, S.; Engelhard, M. H.; Li, G.; Shao, G.; Wang, Y.; Liu, J.; Aksay, I. A.; Lin, Y. Nitrogen-Doped Graphene and Its Electrochemical Applications. *J. Mater. Chem.* **2010**, *20* (35), 7491. https://doi.org/10.1039/c0jm00782j.

(6) Wang, H.; Maiyalagan, T.; Wang, X. Review on Recent Progress in Nitrogen-Doped Graphene: Synthesis, Characterization, and Its Potential Applications. *ACS Catal.* **2012**, *2* (5), 781–794. https://doi.org/10.1021/cs200652y.

(7) Fei, H.; Dong, J.; Feng, Y.; Allen, C. S.; Wan, C.; Volosskiy, B.; Li, M.; Zhao, Z.; Wang, Y.; Sun, H.; et al. General Synthesis and Definitive Structural Identification of MN_4C_4 Single-Atom Catalysts with Tunable Electrocatalytic Activities. *Nat. Catal.* **2018**, *1* (1), 63–72. https://doi.org/10.1038/s41929-017-0008-y.

(8) NIST XPS Database, Selected Element Search Result https://srdata.nist.gov/xps/EngElmSrchQuery.aspx?EType=PE&CSOpt=Retri_ex_dat&Elm=N (accessed Sep 10, 2019).

(9) Beamson, G.; Briggs, D. *High Resolution XPS of Organic Polymers: The Scienta ESCA300 Database*; Wiley, 1992.

(10) Biesinger, M. C. Advanced Analysis of Copper X-Ray Photoelectron Spectra: Advanced Analysis of Copper X-Ray Photoelectron Spectra. *Surf. Interface Anal.* **2017**, *49* (13), 1325–1334. https://doi.org/10.1002/sia.6239.

(11) Biesinger, M. C.; Lau, L. W. M.; Gerson, A. R.; Smart, R. S. C. Resolving Surface Chemical States in XPS Analysis of First Row Transition Metals, Oxides and Hydroxides: Sc, Ti, V, Cu and Zn. *Appl. Surf. Sci.* **2010**, *257* (3), 887–898. https://doi.org/10.1016/j.apsusc.2010.07.086.

(12) Biesinger, M. C.; Payne, B. P.; Lau, L. W. M.; Gerson, A.; Smart, R. S. C. X-Ray Photoelectron Spectroscopic Chemical State Quantification of Mixed Nickel Metal, Oxide and Hydroxide Systems. *Surf. Interface Anal.* **2009**, *41* (4), 324–332. https://doi.org/10.1002/sia.3026.

(13) C. Biesinger, M.; M. Lau, L. W.; R. Gerson, A.; C. Smart, R. S. The Role of the Auger Parameter in XPS Studies of Nickel Metal, Halides and Oxides. *Phys. Chem. Chem. Phys.* **2012**, *14* (7), 2434–2442. https://doi.org/10.1039/C2CP22419D.
(14) C. Biesinger, M.; M. Lau, L. W.; R. Gerson, A.; C. Smart, R. S. The Role of the Auger Parameter in XPS Studies of Nickel Metal, Halides and Oxides. *Phys. Chem. Chem. Phys.* **2012**, *14* (7), 2434–2442. https://doi.org/10.1039/C2CP22419D.
(15) Morgan, D. J. Resolving Ruthenium: XPS Studies of Common Ruthenium Materials. *Surf. Interface Anal.* **2015**, *47* (11), 1072–1079. https://doi.org/10.1002/sia.5852.
(16) Spevack, P. A.; McIntyre, N. S. Thermal Reduction of Molybdenum Trioxide. *J. Phys. Chem.* **1992**, *96* (22), 9029–9035. https://doi.org/10.1021/j100201a062.
(17) Clayton, C. R.; Lu, Y. C. Electrochemical and XPS Evidence of the Aqueous Formation of Mo2O5. *Surf. Interface Anal.* **1989**, *14* (1–2), 66–70. https://doi.org/10.1002/sia.740140114.
(18) Biesinger, M. C.; Payne, B. P.; Grosvenor, A. P.; Lau, L. W. M.; Gerson, A. R.; Smart, R. S. C. Resolving Surface Chemical States in XPS Analysis of First Row Transition Metals, Oxides and Hydroxides: Cr, Mn, Fe, Co and Ni. *Appl. Surf. Sci.* **2011**, *257* (7), 2717–2730. https://doi.org/10.1016/j.apsusc.2010.10.051.
(19) Banerjee, D.; Nesbitt, H. W. XPS Study of Dissolution of Birnessite by Humate with Constraints on Reaction Mechanism. *Geochim. Cosmochim. Acta* **2001**, *65* (11), 1703–1714. https://doi.org/10.1016/S0016-7037(01)00562-2.
(20) Bard, A. J. *Electrochemical Methods: Fundamentals and Applications*, Second edition.; Wiley: New York ; Chichester, 2001.
(21) Elbaz, L.; Korin, E.; Soifer, L.; Bettelheim, A. Electrocatalytic Oxygen Reduction by Co(III) Porphyrins Incorporated in Aerogel Carbon Electrodes. *J. Electroanal. Chem.* **2008**, *621* (1), 91–96. https://doi.org/10.1016/j.jelechem.2008.04.017.
(22) Gunasingham, H.; Fleet, B. Comparative Study of Glassy Carbon as an Electrode Material. *The Analyst* **1982**, *107* (1277), 896. https://doi.org/10.1039/an9820700896.
(23) Tavakkoli, M.; Holmberg, N.; Kronberg, R.; Jiang, H.; Sainio, J.; Kauppinen, E. I.; Kallio, T.; Laasonen, K. Electrochemical Activation of Single-Walled Carbon Nanotubes with Pseudo-Atomic-Scale Platinum for the Hydrogen Evolution Reaction. *ACS Catal.* **2017**, *7* (5), 3121–3130. https://doi.org/10.1021/acscatal.7b00199.
(24) Durst, J.; Siebel, A.; Simon, C.; Hasché, F.; Herranz, J.; Gasteiger, H. A. New Insights into the Electrochemical Hydrogen Oxidation and Evolution Reaction Mechanism. *Energy Env. Sci* **2014**, *7* (7), 2255–2260. https://doi.org/10.1039/C4EE00440J.
(25) Deng, J.; Ren, P.; Deng, D.; Yu, L.; Yang, F.; Bao, X. Highly Active and Durable Non-Precious-Metal Catalysts Encapsulated in Carbon Nanotubes for Hydrogen Evolution Reaction. *Energy Env. Sci* **2014**, *7* (6), 1919–1923. https://doi.org/10.1039/C4EE00370E.
(26) Mineral profiles | British Geological Survey | MineralsUK https://www.bgs.ac.uk/mineralsuk/statistics/mineralProfiles.html (accessed Jan 21, 2020).
(27) Strickland, K.; Miner, E.; Jia, Q.; Tylus, U.; Ramaswamy, N.; Liang, W.; Sougrati, M.-T.; Jaouen, F.; Mukerjee, S. Highly Active Oxygen Reduction Non-Platinum Group Metal Electrocatalyst without Direct Metal–Nitrogen Coordination. *Nat. Commun.* **2015**, *6* (1), 7343. https://doi.org/10.1038/ncomms8343.
(28) Jia, Q.; Ramaswamy, N.; Hafiz, H.; Tylus, U.; Strickland, K.; Wu, G.; Barbiellini, B.; Bansil, A.; Holby, E. F.; Zelenay, P.; et al. Experimental Observation of Redox-Induced Fe–N Switching Behavior as a Determinant Role for Oxygen Reduction Activity. *ACS Nano* **2015**, *9* (12), 12496–12505. https://doi.org/10.1021/acsnano.5b05984.
(29) Zitolo, A.; Ranjbar-Sahraie, N.; Mineva, T.; Li, J.; Jia, Q.; Stamatin, S.; Harrington, G. F.; Lyth, S. M.; Krtil, P.; Mukerjee, S.; et al. Identification of Catalytic Sites in Cobalt-

Nitrogen-Carbon Materials for the Oxygen Reduction Reaction. *Nat. Commun.* **2017**, *8* (1). https://doi.org/10.1038/s41467-017-01100-7.
(30) Sun, X.; Olivos-Suarez, A. I.; Osadchii, D.; Romero, M. J. V.; Kapteijn, F.; Gascon, J. Single Cobalt Sites in Mesoporous N-Doped Carbon Matrix for Selective Catalytic Hydrogenation of Nitroarenes. *J. Catal.* **2018**, *357*, 20–28. https://doi.org/10.1016/j.jcat.2017.10.030.
(31) Gao, Y.; Han, Z.; Hong, S.; Wu, T.; Li, X.; Qiu, J.; Sun, Z. ZIF-67 Derived Cobalt/Nitrogen-Doped Carbon Composites for Efficient Electrocatalytic N2 Reduction. *ACS Appl. Energy Mater.* **2019**, acsaem.9b01135. https://doi.org/10.1021/acsaem.9b01135.
(32) Aiyappa, H. B.; Thote, J.; Shinde, D. B.; Banerjee, R.; Kurungot, S. Cobalt-Modified Covalent Organic Framework as a Robust Water Oxidation Electrocatalyst. *Chem. Mater.* **2016**, *28* (12), 4375–4379. https://doi.org/10.1021/acs.chemmater.6b01370.
(33) Yan, Y.; He, T.; Zhao, B.; Qi, K.; Liu, H.; Xia, B. Y. Metal/Covalent–Organic Frameworks-Based Electrocatalysts for Water Splitting. *J. Mater. Chem. A* **2018**, *6* (33), 15905–15926. https://doi.org/10.1039/C8TA05985C.
(34) Wang, Z.-L.; Hao, X.-F.; Jiang, Z.; Sun, X.-P.; Xu, D.; Wang, J.; Zhong, H.-X.; Meng, F.-L.; Zhang, X.-B. C and N Hybrid Coordination Derived Co–C–N Complex as a Highly Efficient Electrocatalyst for Hydrogen Evolution Reaction. *J. Am. Chem. Soc.* **2015**, *137* (48), 15070–15073. https://doi.org/10.1021/jacs.5b09021.
(35) Zhang, M.; Wang, Y.-G.; Chen, W.; Dong, J.; Zheng, L.; Luo, J.; Wan, J.; Tian, S.; Cheong, W.-C.; Wang, D.; et al. Metal (Hydr)Oxides@Polymer Core–Shell Strategy to Metal Single-Atom Materials. *J. Am. Chem. Soc.* **2017**, *139* (32), 10976–10979. https://doi.org/10.1021/jacs.7b05372.
(36) Li, J.; Jia, Q.; Mukerjee, S.; Sougrati, M.-T.; Drazic, G.; Zitolo, A.; Jaouen, F. The Challenge of Achieving a High Density of Fe-Based Active Sites in a Highly Graphitic Carbon Matrix. *Catalysts* **2019**, *9* (2), 144. https://doi.org/10.3390/catal9020144.
(37) Zhu, C.; Fu, S.; Shi, Q.; Du, D.; Lin, Y. Single-Atom Electrocatalysts. *Angew. Chem. Int. Ed.* **2017**, *56* (45), 13944–13960. https://doi.org/10.1002/anie.201703864.
(38) Xu, H.; Cheng, D.; Cao, D.; Zeng, X. C. A Universal Principle for a Rational Design of Single-Atom Electrocatalysts. *Nat. Catal.* **2018**. https://doi.org/10.1038/s41929-018-0063-z.
(39) Parsons, R. The Rate of Electrolytic Hydrogen Evolution and the Heat of Adsorption of Hydrogen. *Trans. Faraday Soc.* **1958**, *54*, 1053. https://doi.org/10.1039/tf9585401053.
(40) Zhang, B.; Zhang, J.; Shi, J.; Tan, D.; Liu, L.; Zhang, F.; Lu, C.; Su, Z.; Tan, X.; Cheng, X.; et al. Manganese Acting as a High-Performance Heterogeneous Electrocatalyst in Carbon Dioxide Reduction. *Nat. Commun.* **2019**, *10* (1), 2980. https://doi.org/10.1038/s41467-019-10854-1.
(41) Benck, J. D.; Hellstern, T. R.; Kibsgaard, J.; Chakthranont, P.; Jaramillo, T. F. Catalyzing the Hydrogen Evolution Reaction (HER) with Molybdenum Sulfide Nanomaterials. *ACS Catal.* **2014**, *4* (11), 3957–3971. https://doi.org/10.1021/cs500923c.
(42) Yin, P.; Yao, T.; Wu, Y.; Zheng, L.; Lin, Y.; Liu, W.; Ju, H.; Zhu, J.; Hong, X.; Deng, Z.; et al. Single Cobalt Atoms with Precise N-Coordination as Superior Oxygen Reduction Reaction Catalysts. *Angew. Chem. Int. Ed.* **2016**, *55* (36), 10800–10805. https://doi.org/10.1002/anie.201604802.
(43) Morozan, A.; Goellner, V.; Nedellec, Y.; Hannauer, J.; Jaouen, F. Effect of the Transition Metal on Metal–Nitrogen–Carbon Catalysts for the Hydrogen Evolution Reaction. *J. Electrochem. Soc.* **2015**, *162* (9), H719–H726.
(44) Ren, Y.; Yu, C.; Tan, X.; Han, X.; Huang, H.; Huang, H.; Qiu, J. Is It Appropriate to Use the Nafion Membrane in Electrocatalytic N_2 Reduction? *Small Methods* **2019**, 1900474. https://doi.org/10.1002/smtd.201900474.

(45) Andersen, S. Z.; Čolić, V.; Yang, S.; Schwalbe, J. A.; Nielander, A. C.; McEnaney, J. M.; Enemark-Rasmussen, K.; Baker, J. G.; Singh, A. R.; Rohr, B. A.; et al. A Rigorous Electrochemical Ammonia Synthesis Protocol with Quantitative Isotope Measurements. *Nature* **2019**. https://doi.org/10.1038/s41586-019-1260-x.
(46) Nielander, A. C.; McEnaney, J. M.; Schwalbe, J. A.; Baker, J. G.; Blair, S. J.; Wang, L.; Pelton, J. G.; Andersen, S. Z.; Enemark-Rasmussen, K.; Čolić, V.; et al. A Versatile Method for Ammonia Detection in a Range of Relevant Electrolytes via Direct Nuclear Magnetic Resonance Techniques. *ACS Catal.* **2019**, 5797–5802. https://doi.org/10.1021/acscatal.9b00358.
(47) Suryanto, B. H. R.; Du, H.-L.; Wang, D.; Chen, J.; Simonov, A. N.; MacFarlane, D. R. Challenges and Prospects in the Catalysis of Electroreduction of Nitrogen to Ammonia. *Nat. Catal.* **2019**. https://doi.org/10.1038/s41929-019-0252-4.
(48) Zhou, F.; Azofra, L. M.; Ali, M.; Kar, M.; Simonov, A. N.; McDonnell-Worth, C.; Sun, C.; Zhang, X.; MacFarlane, D. R. Electro-Synthesis of Ammonia from Nitrogen at Ambient Temperature and Pressure in Ionic Liquids. *Energy Environ. Sci.* **2017**, *10* (12), 2516–2520. https://doi.org/10.1039/C7EE02716H.
(49) Yang, Y.; Wang, S.-Q.; Wen, H.; Ye, T.; Chen, J.; Li, C.-P.; Du, M. Nanoporous Gold Embedded ZIF Composite for Enhanced Electrochemical Nitrogen Fixation. *Angew. Chem.* **2019**, ange.201909770. https://doi.org/10.1002/ange.201909770.

5 Active Site Engineering – Tailoring and Probing of Metal Centre Environments in Cobalt-containing Single Atom Catalysts

5.1 Background and Objectives 129

5.2 Synthesis 130

5.3 Characterisation 131

5.3.1 XRD 131

5.3.2 XPS 132

5.3.3 TEM 142

5.3.4 STEM 142

5.4 Hydrogen Evolution Reaction 149

5.4.1 Experimental Methods 149

5.4.2 Results and Discussion 149

5.5 In-situ Infrared Spectroelectrochemistry 156

5.5.1 Background 156

5.5.2 Experimental Methods 158

5.5.3 Results and Discussion 159

5.6 In-situ X-ray Absorption Spectroscopy 168

5.6.1 Background 168

5.6.2 Experimental Methods 170

5.6.3 Results and Discussion 171

5.6.3.1 XANES 171

5.6.3.2 EXAFS 178

5.6.3.2.1 Wavelet Transform 178

5.7 XANES Modelling 181

5.7.1 Geometry Optimisation with Dmol3 181

5.7.2 Confirmation of Peak Assignment using FEFF9 184

5.7.3 The Effect of Coordination Sphere Composition and Geometry on XANES spectra assessed using CASTEP 186

5.8 Conclusions 191

5.9 References 193

5.1 Background and Objectives

Single atom catalysts (SACs) are often compared to homogeneous catalysts for which the ligand environment plays a pivotal role in their catalysis. In contrast to homogeneous systems, the exact elemental composition and spatial arrangement of the first coordination sphere is often only poorly understood in SACs. Recent experimental reports and computational studies have indicated that the environment of the metal can significantly affect HER activity of SACs[1,2] but only limited comparative studies exist. Interestingly, a recent report on a Mn-based SAC also hints at the importance of bonding geometry in HER.[3]

This chapter investigates the structure-activity relationship of atomically dispersed cobalt on 2D carbon supports for the acidic HER and explores the role of nitrogen doping in their synthesis and electrochemical performance. The synthesis of the most active HER catalyst, Co-NG, is adapted to obtain three different cobalt-containing single-atom catalysts (Co SACs) which are then tested for their HER activity. The characterisation techniques discussed in Chapter 4 are used again to confirm homogeneous atomic dispersion of cobalt on the carbon support and XPS is used to study the effect of acid leaching on the different Co SACs. Using two different in-situ characterisation techniques, IR spectroelectrochemistry and in-situ XAFS, the different catalysts are monitored during turn over. IR spectroelectrochemistry poisoning experiments are performed to look into the characteristics and relative amount of active sites on the Co SACs. In-situ XAFS during HER will provide insight into structural changes during operation and in combination with DFT–based XANES modelling is used to further clarify the different compositions of the Co-centres' first coordination shells.

Understanding factors that control HER activity is pivotal in rational design-based discovery of novel hydrogen evolution catalysts but also offers a pathway to increase selectivity in reactions where HER competes, such as nitrogen and carbon dioxide reduction. Parasitic hydrogen evolution is a major roadblock to commercialisation of these reactions as renewable energy storage and fuel production technologies.

5.2 Synthesis

Graphene oxide was synthesised using the improved Hummers' method (see Section 3.1). Using as-prepared GO, three different cobalt-containing single atom catalysts on carbon support (Co SACs) were synthesised, namely Co-NG, Co-NG/N and Co-G.

Co-NG was prepared in the same fashion as described in Chapter 3 Section 2. To synthesise Co-NG/N and Co-G, that preparation route was slightly altered as discussed below.

Co-NG/N: 50mg of graphene oxide were dispersed in 25mL MQ water and sonicated for 2h. 1.83mg of $Co(NO_3)_2 \cdot 6H_2O$ (6.3 μM) (Sigma-Aldrich, 10026-22-9) dissolved in 0.5mL MQ water were added to the suspension and further sonicated for 30min. The resulting mixture was freeze-dried to obtain a dark brown solid which was placed into a tube furnace and heated to 750°C at 10°C min^{-1} while flowing NH_3 at 150mL min^{-1}. The furnace was kept at 750°C for 1h and then cooled down under N_2 flow to obtain a black powder.

Co-G: 50mg of graphene oxide were dispersed in 25mL MQ water and sonicated for 2h. 1.5mg of $CoCl_2 \cdot 6H_2O$ (6.3 μM) (Sigma-Aldrich, 7791-13-1) dissolved in 0.5mL MQ water were added to the suspension and further sonicated for 30min. The resulting mixture was freeze-dried to obtain a dark brown solid which was placed into a tube

furnace and heated to 750°C at 10°C min^{-1} while flowing Ar at 150mL min^{-1}. The furnace was kept at 750°C for 1h and then cooled down under Ar flow to obtain a black powder

All three Co SAC materials were boiled in concentrated HCl at 60°C for 3h and subsequently collected using vacuum filtration. During the synthesis of Co-G a faint blue colour was observed in the supernatant during the acid leaching step which was absent in the other two syntheses. The filtrate was washed with MQ water until neutral washings were obtained and then dried to obtain black powders.

Table 1: *Overview of synthesis conditions used to prepare Co-NG, Co-NG/N and Co-G*

Sample	Metal Salt	Annealing Temperature (°C)	Gas Atmosphere
Co-NG	$CoCl_2 \cdot 6H_2O$	750	NH_3
Co-NG/N	$Co(NO_3)_2 \cdot 6H_2O$	750	NH_3
Co-G	$CoCl_2 \cdot 6H_2O$	750	Ar

5.3 Characterisation

5.3.1 XRD

X-ray diffraction patterns of the graphite, graphene oxide and M-NGs were obtained. Figure 1 confirms the synthesis of graphene oxide (black trace) from graphite (brown trace) exhibiting a main reflection at around 11° indicating a large increase in interlayer spacing which is in line with exfoliation and oxidation of the individual graphene planes during the improved Hummer's method[4].

Figure 1 shows that for NG, as well as for Co-NG and Co-NG/N only one broad main reflection can be observed at around 26.5° which can be identified as the (002) plane of N-graphene[5,6] similar to the patterns of other M-NG catalysts described in Section 3.4.1. Co-G exhibits a broad reflections at around 22.5° indicative of (002) plane of reduced graphene oxide[7,8]. No metal or metal oxide reflections were observed in any of the acid leached Co SAC samples.

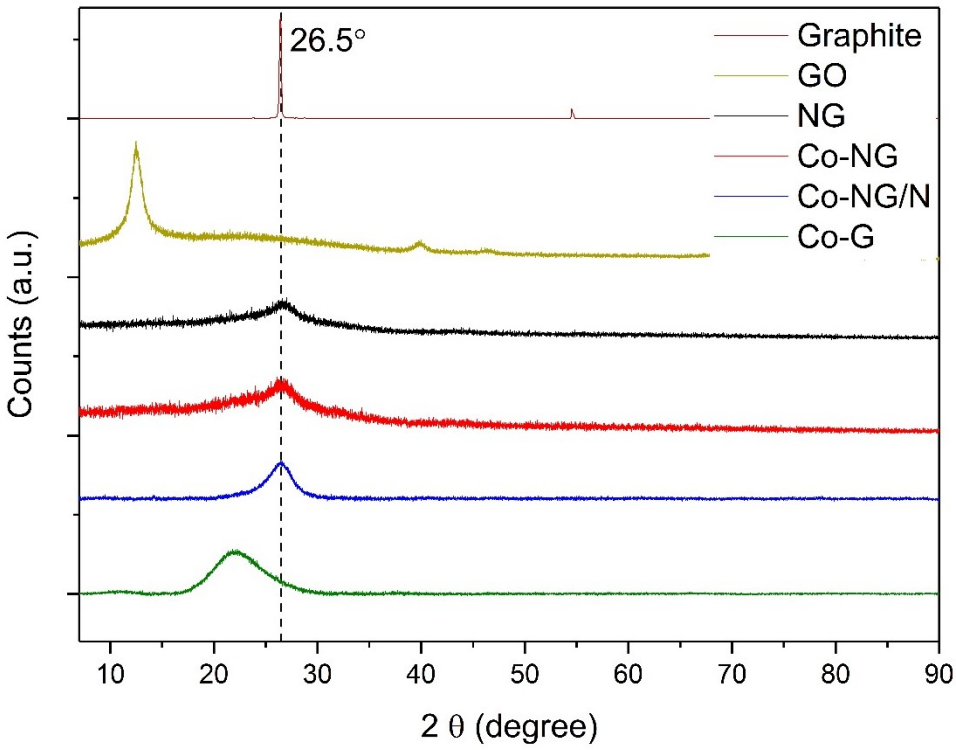


Figure 1: *X-ray diffraction patterns for Co-containing single-atom catalysts and precursors. Colour code: Co-G (olive), Co-NG/N (blue), Co-NG (red), NG (black), graphene oxide (golden), and graphite (brown).*

5.3.2 XPS

For details about the XPS acquisition procedure, refer to Chapter 3 Section 1.2.

XPS was used to establish the general elemental composition of the catalysts and confirm the reductive nitrogen doping for Co-NG and Co-NG/N. XPS spectra were acquired before and after the acid leaching step to investigate the effect on amount and type of

cobalt present in the final catalyst. As outlined in the Chapter 2 Section 3, while XPS is a near surface sensitive technique, the limited thickness of the M-NG systems (< 5nm) means that elemental compositions obtained using XPS are assumed to correspond to the bulk elemental composition.

The general elemental composition of the acid leached Co SACs varies slightly but carbon is the main component with around 90at% (Table 2) in all catalysts. Co-NG and Co-NG/N contain roughly the same amount of nitrogen as metal-free NG, between 6-7 at%. Interestingly, Co-G also contains small amounts of nitrogen although it was not annealed in ammonia. Cobalt was only detected in the survey scans of Co-NG and Co-Ng/N and quantified at 0.13 and 0.08at%, respectively. Small amounts of chlorine were shown to be present in Co-G and Co-NG, possibly as a result of the use of $CoCl_2 \cdot 6H_2O$ as a precursor in these samples or remnants of the acid leaching procedure in concentrated HCl.

Table 2: *Summary of composition of acid leached Co SACs in atomic % as determined by XPS*

Sample	Carbon (at%)	Nitrogen (at%)	Oxygen (at%)	Chlorine (at%)	Cobalt (at%)
NG	91.52	6.43	2.04	ND	ND
Co-NG	78.06	7.55	13.62	0.64	0.13
Co-NG/N	89.62	5.70	4.59	ND	0.08
Co-G	89.17	2.28	8.02	0.53	ND

ND: Not detected in survey (<<0.5at%)

Although not present in all of the survey scans, all Co SAC samples were shown to contain cobalt by high-resolution scans of the Co2p region (Figure 2). Co-NG and Co-NG/N show a fairly similar peak distribution in the Co2p region with the main $Co2p_{3/2}$ peak appearing at around 780eV with no detectable peak at 778eV showing that no metallic cobalt is present (Fig. 2.A and B).[1,9–11] A small satellite peak is observed at 786eV which suggests a mixture of Co(II) and Co(III) oxidation states in the samples (Fig. 2.A and B).[9–11] For Co-G the satellite feature is much more pronounced, indicating that cobalt is mostly +II oxidised (Fig. 2.C).[9–11] Additionally, the Co2p spectrum of Co-G and Co-NG/N appear more noisy than that of Co-NG suggesting lower Co loading on the surface for the first two in line with the survey observations.

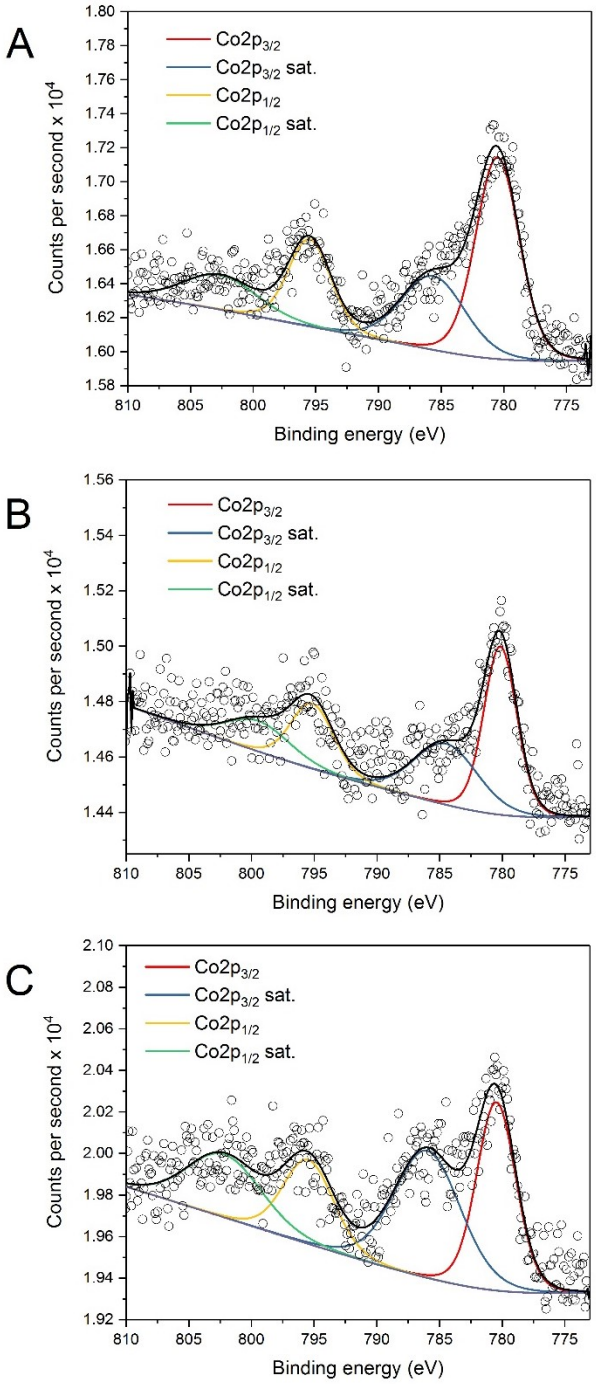


Figure 2: *High-resolution spectra of the Co2p region of Co-NG (A), Co-NG/N (B) and Co-G (C). Colour code: $Co2p_{3/2}$ (red), $Co2p_{3/2}$ satellite (blue), $Co2p_{1/2}$ (yellow), $Co2p_{1/2}$ satellite (green), total fit (black), and measured data (black circles).*

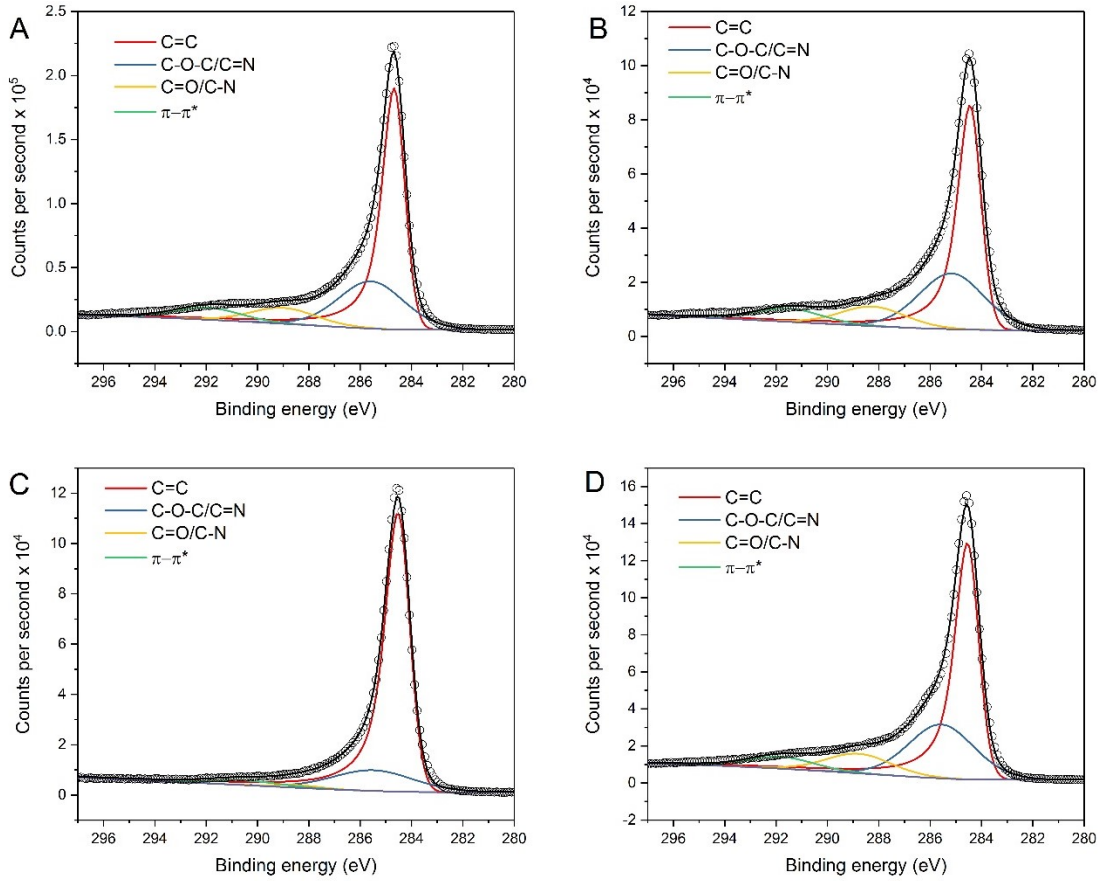


Figure 3: *High-resolution C1s spectra of NG (A), Co-NG (B), Co-NG/N (C) and Co-G (D). Colour code: Carbon double bond (red), ether or imine moiety (blue), keto or nitrile moiety (yellow), and π-π* satellite (green).*

The high-resolution C1s spectra of the Co SACs exhibit the typical broad asymmetric feature of sp^2 hybridised carbon at around 284.5eV (red traces), as well as a π- π* satellite at around 291eV (green traces) (Fig. 3). This shows reduction of graphene oxide occurred in all samples, despite a different annealing atmosphere for Co-G. Furthermore, carbon-oxygen/nitrogen functionalities are also resolved (blue and yellow traces) and shown to be similar in distribution to the metal-free NG C1s spectrum (Fig. 3.A), to other M-NG catalysts (Chapter 4 Section 4.2) and to literature reports on N-doped carbons.[5,7,12,13]

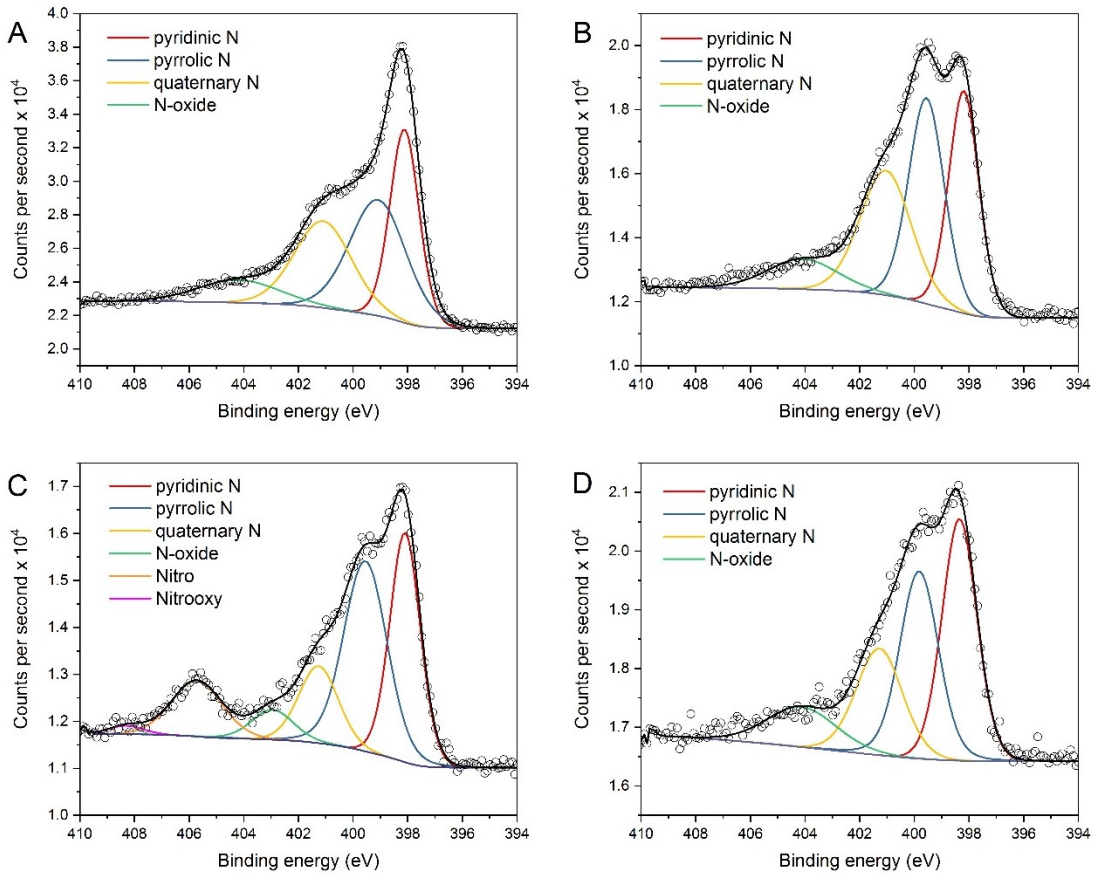


Figure 4: *High-resolution spectra of the N1s region of NG (A), Co-NG (B), Co-NG/N (C) and Co-G (D). Colour code: pyridinic N (red), pyrrolic N (blue), quaternary N (yellow), N-oxide (green), nitro moiety (orange), and nitrooxy moiety (pink).*

High-resolution scans of the N1s region of NG, Co-NG, Co-NG/N and Co-G (Fig.4.A-D) show that all Co SACs were nitrogen doped. This is surprising for Co-G since it was not annealed under ammonia flow but due to the low amount (2.23%, three times lower than in other samples) can possibly be explained by nitrogen impurities in the natural graphite starting material that either already are part of the lattice or will become so during the annealing procedure at 750°C in Ar. Generally in all Co SAC samples, as well as other M-NGs and NG, four types of nitrogen moieties are detected, namely pyridinic (red traces) at 398.0eV, pyrrolic (blue traces) at 399.5eV and quaternary nitrogen (yellow

traces) at 401.3eV, as well as small amounts of nitrogen-oxide groups (green traces) at around 404eV.

For Co-NG/N one further species is clearly observed at 405.7eV identified to be a nitro-species (-NO_2, orange trace) and potentially traces of a nitrooxy species at 408.3eV (–O-NO_2, pink trace).[14–16] These are believed to be remnants of cobalt nitrate hexahydrate used as the cobalt precursor for Co-NG/N. Usually cobalt nitrates decompose above temperatures of 185°C in unreactive atmospheres forming oxides.[17–19] Previous attempts to form atomically dispersed cobalt species on carbon supports using nitrate salts via the pyrolysis route have yielded carbon encapsulated cobalt nanoparticles only.[19] This was believed to be due to the decomposition of metal nitrates to oxides followed by subsequent reduction to metal nanoparticles before reaching temperatures high enough to facilitate atomic dispersion. [19–22] In the present catalyst system, synthesised via a carbon backbone method, nitro species persist despite being annealed at 750°C under reductive ammonia atmosphere. This is believed to be due to a strong interaction with the graphene oxide precursor preventing aggregation of cobalt nitrate species which would lead to decomposition into cobalt oxide. From XPS data alone it remains unclear if the nitro-species remain coordinated to cobalt or are attached to the carbon lattice.

The Co SACs contain significantly less pyridinic nitrogen compared to NG, most clearly seen for Co-NG where pyridinic N is only the second most abundant species after pyrrolic nitrogen. This seems to be an effect of the acid leaching step, as shown by Figure 5. Non-acid leached Co-NG (Fig. 5.A) shows similar nitrogen species distribution to NG which was also not subject to acid leaching (Fig.4.A) with roughly 40% of nitrogen being pyridinic in nature. After boiling in HCl the share of pyrdinic N drops to 30%, while

pyrrolic and quaternary N increase. Overall Co-NG loses roughly one atomic percent of nitrogen during acid leaching, mostly in the form of pyridinic N (Table 3).

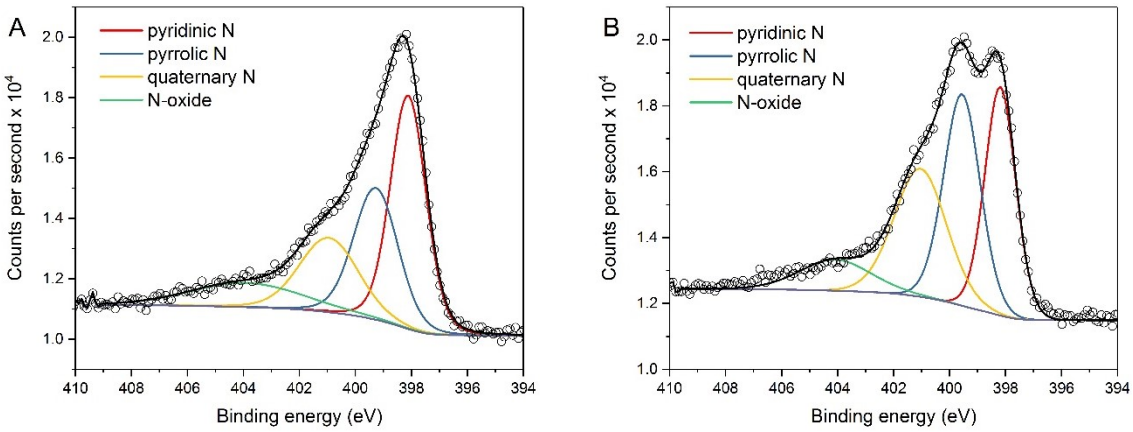


Figure 5: *High-resolution spectra of N1s region of Co-NG before (A) and after acid leaching (B). Colour code: pyridinic N (red), pyrrolic N (blue), quaternary N (yellow), and N-oxide (green). A smaller peak for pyridinic N is observed in comparison to other nitrogen species post acid leaching.*

Table 3: *Total nitrogen content and distribution of nitrogen species in Co-NG before and after acid leaching*

Nitrogen species	Pre acid leached Co-NG (%)	Acid leached Co-NG (%)
Pyridinic	39.2	29.8
Pyrrolic	27.5	32.6
Quaternary	20.6	28.3
N-oxide	12.7	9.3
Total N content in sample	8.41at%	7.55at%

Another effect of the acid leaching step is the reduction in cobalt loading which is illustrated in Table 4 and Figure 6 for Co-NG and Co-G. The cobalt content in Co-NG is reduced from 0.3at% to 0.13% and in Co-G from 0.18at% to below the limit of detection of the survey scan. A corresponding increase in noise can be observed for the high-resolution spectra for the acid washed samples of Co-NG and Co-G (see Fig.6.B and D). This is in line with the observation of a faint blue colour in the supernatant during acid leaching of Co-G suggesting that cobalt species from the sample dissolve and form cobalt chloride complexes in the concentrated HCl solution. Furthermore, Co-G exhibits a strong satellite feature at around 786eV (blue trace), before and after acid leaching (Fig.6.C-D), indicating that the oxidation state of cobalt is unaffected by the acid leaching step and Co(II) remains the predominant species. For Co-NG a smaller satellite feature (blue trace) is observed with the ratio to the main $Co2p_{3/2}$ peak (red trace) unchanged after acid leaching (Fig. 6.A-B). This is further evidence for the acid leaching step not affecting the oxidation state and indicates Co(III) to be the principal state of cobalt in Co-NG.

Table 4: *Cobalt content determined by XPS in Co-NG and Co-G before and after acid leaching step*

Sample	Cobalt content (at%)
Co-NG (before AL)	0.30%
Co-NG (after AL)	0.13%
Co-G (before AL)	0.18%
Co-G (after AL)	ND

AL: acid leaching, ND: Not detected in survey (<<0.5at%)

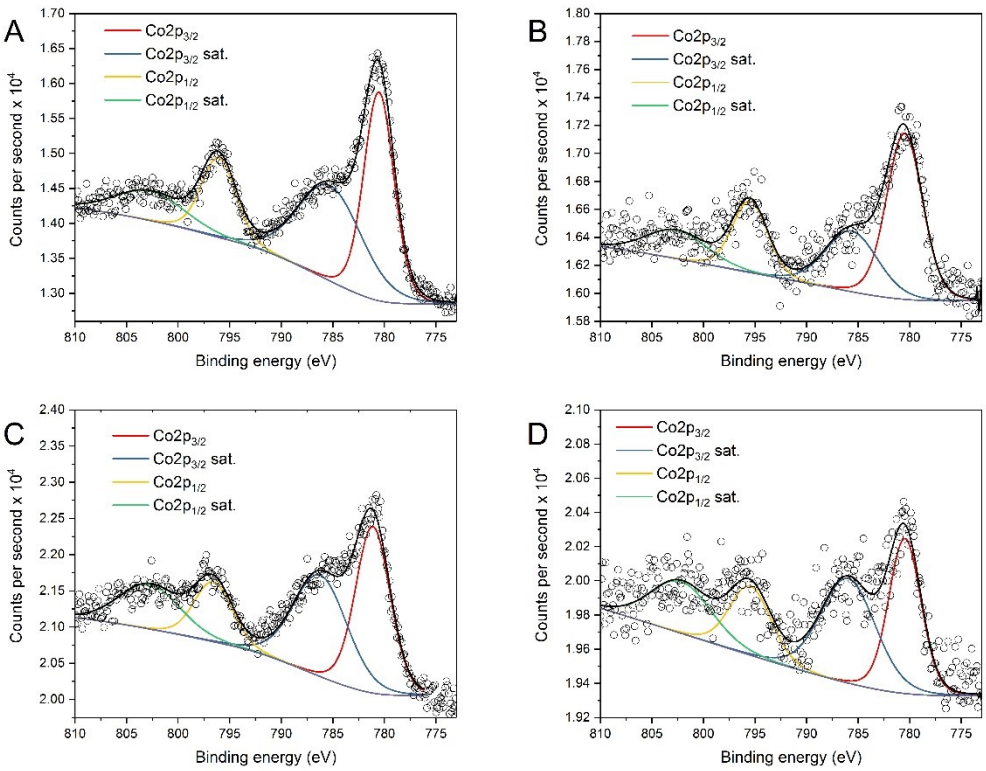


Figure 6: *High-resolution spectra of the Co2p region of Co-NG (A), Co-NG before acid leaching (B), Co-G (C), and Co-G before acid leaching. Colour code: $Co2p_{3/2}$ (red), $Co2p_{3/2}$ satellite (blue), $Co2p_{1/2}$ (yellow), $Co2p_{1/2}$ satellite (green), total fit (black), and measured data (black circles).*

5.3.3 TEM

Transmission electron microscopy was performed to investigate the morphology of the catalysts and check for the presence of nanoparticles. Figure 6 shows TEM micrographs for Co-NG and Co-NG/N.

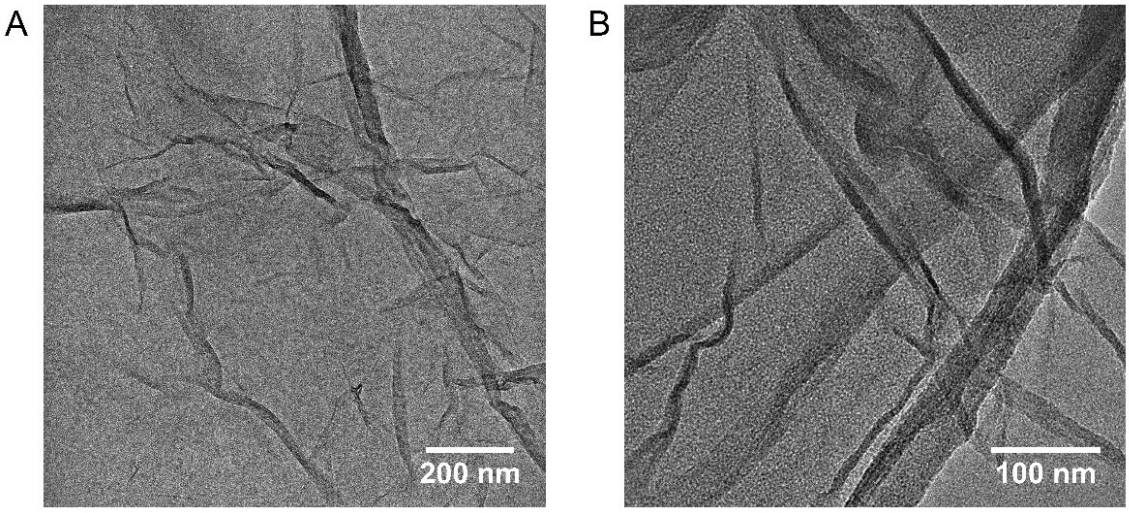


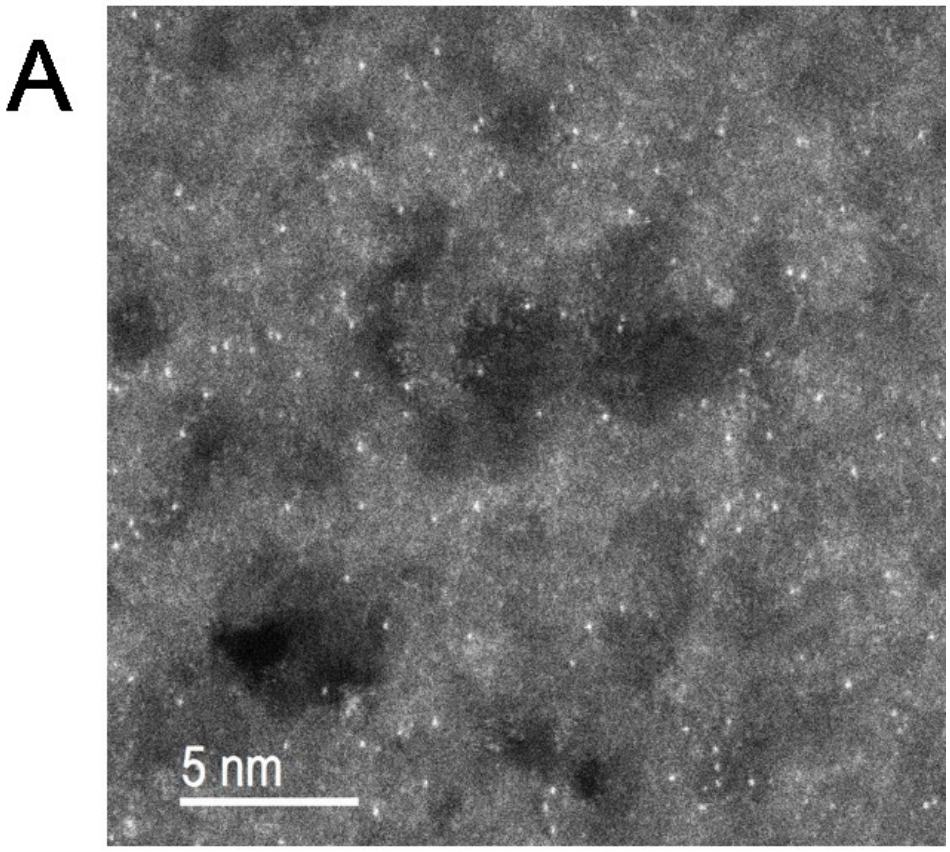
Figure 6: *Bright-field TEM image of Co-NG (A) and Co-NG/N (B)*

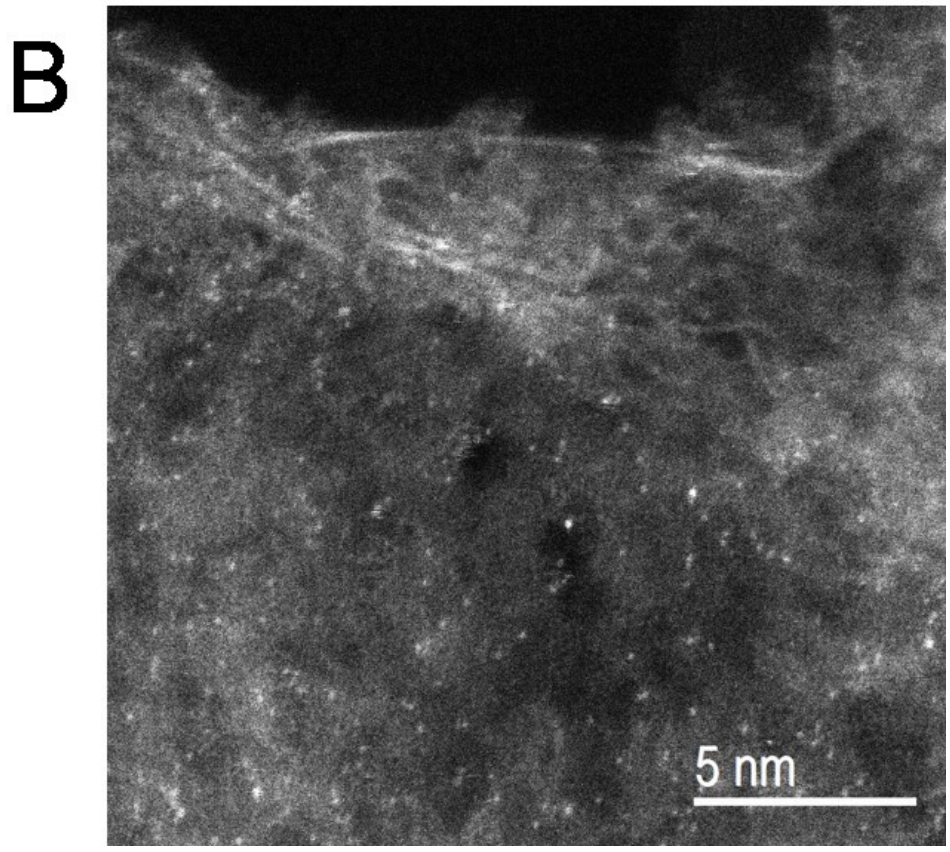
Similar to the previously described M-NG catalysts, all Co SACs exhibited a wrinkled graphene-like sheet morphology with no detectable nanoparticles. The N-graphene/ graphene sheets were found to measure roughly 50μm across.

5.3.4 STEM

To exclude the possibility of the formation of small metal clusters and confirm atomic dispersion of the metal onto the graphene-like supports, high resolution aberration corrected high-angle annular dark field scanning transmission electron microscopy (HAADF-STEM) was carried out. All samples were beam showered before high-resolution imaging was performed.

Figure 7 shows high-resolution HAADF-STEM images of all three Co SACs. A HAADF detector was used due to its increased Z ratio which allows facile distinction between Co (bright spots) and C/N/O (dark grey). Single bright spots of a diameter of below 0.3nm were found to be homogeneously dispersed on large sheets clearly showing that the cobalt indeed exists in single atom form on all three Co SACs. No nanoparticles or clusters were observed under normal imaging conditions in line with evidence from other characterisation techniques. Consecutive excessive beam showering did occasionally lead to severe damage to the graphene support creating large holes and lead to the artificial formation of nanoparticles on the remaining carbon islands.


A
5 nm


B
5 nm

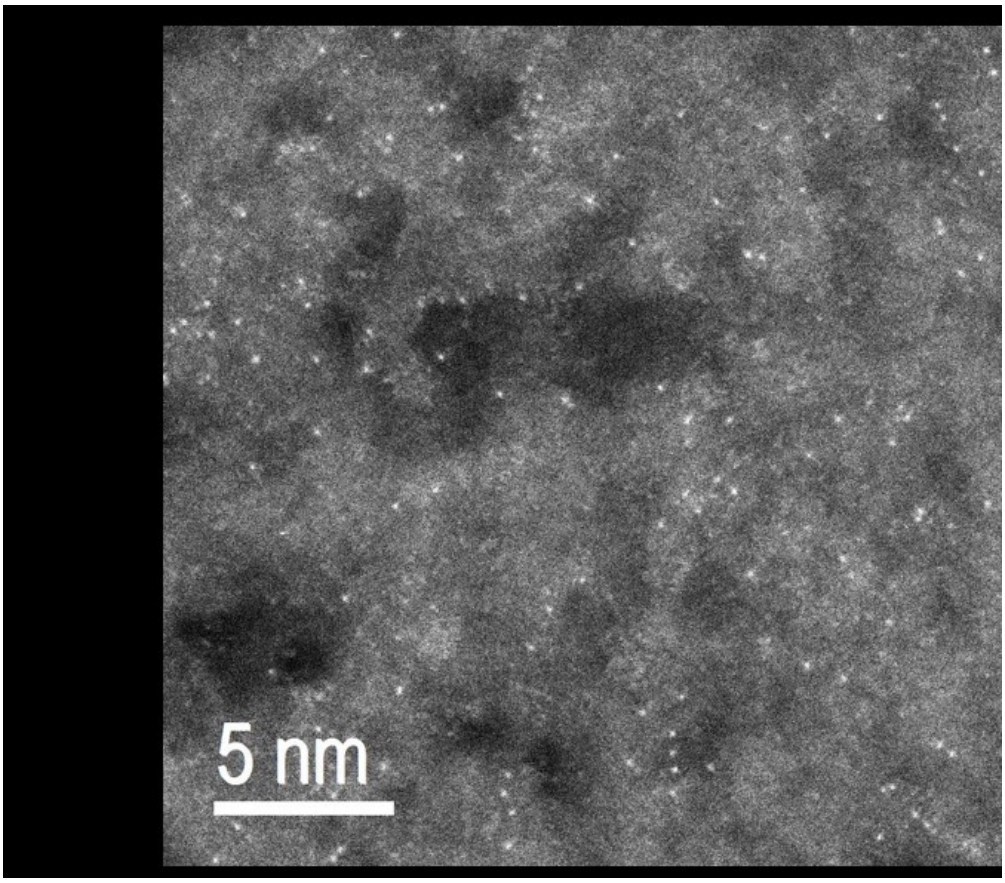
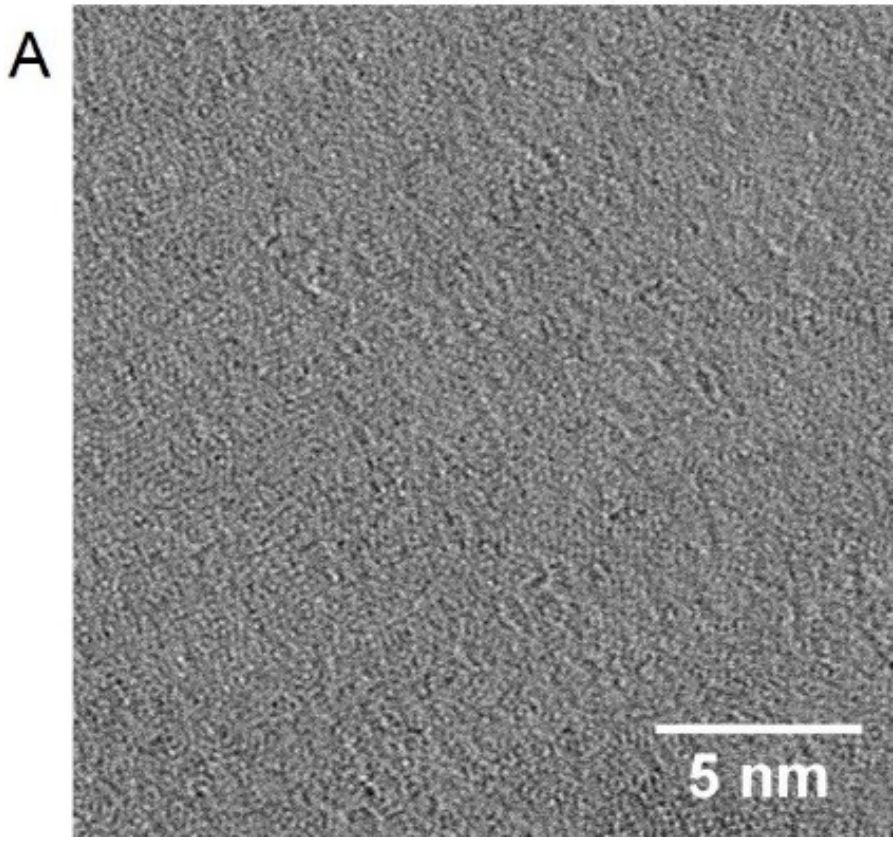
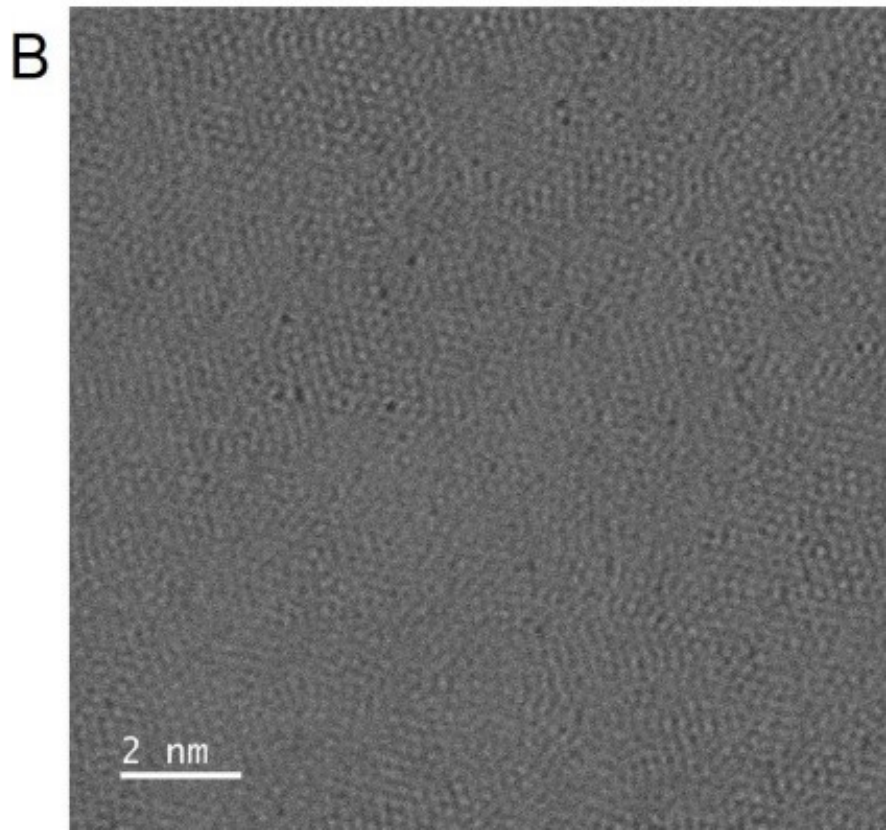


Figure 7: *HAADF images of Co-NG (A), Co-NG/N (B) and Co-G (C) obtained on a JEOL ARM200F*

Co-NG was further imaged on a JEOL ARM300F at higher magnifications. Bright-field images from that microscope can be found in Figure 8 showing large sheets with a honeycomb lattice clearly showing that the graphite-like structure is retained after exfoliation and subsequent annealing in Ar or NH_3. In Fig.8.B and Fig.8.C black dots can be observed disturbing the lattice indicating that Co is indeed incorporated into the lattice of Co-NG rather than sitting atop. Fig.8.C further more nicely illustrates how several layers of N-graphene, usually around two to five, stack up to form the catalyst.


A
5 nm


B
2 nm

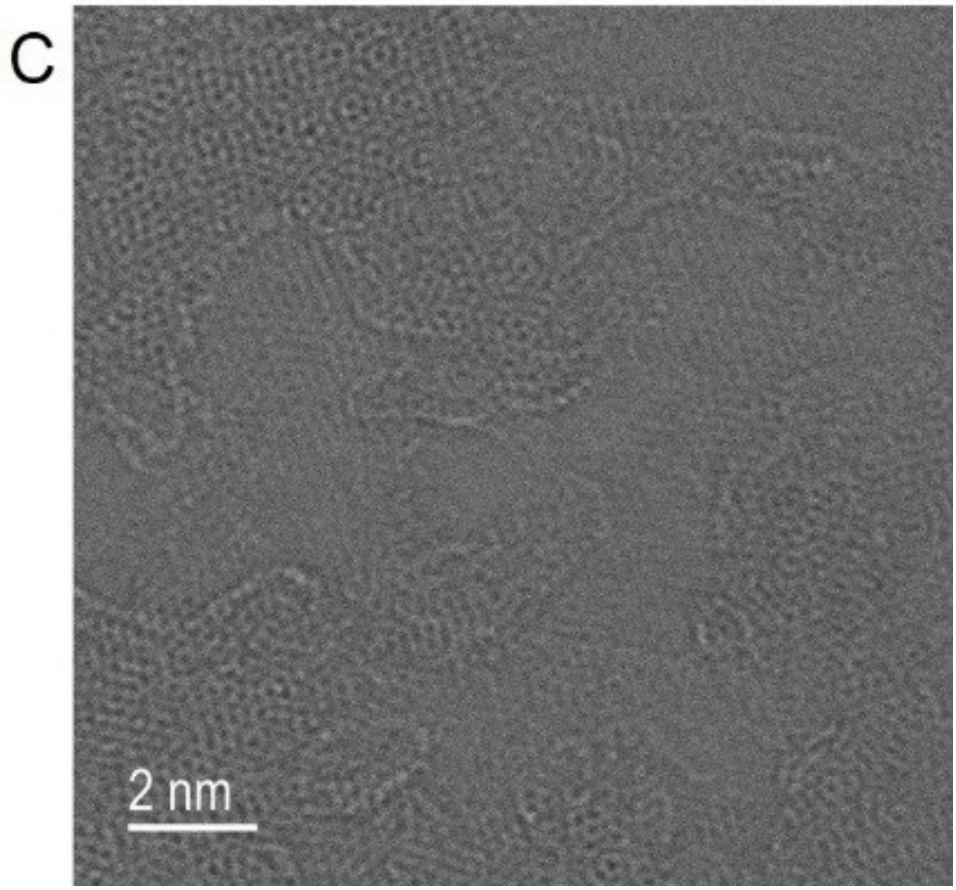


Figure 8: *Bright-field images of Co-NG at a magnification of 10M (A) and 10M (B and C) showing the honeycomb lattice of N-graphene and its layered structure obtained on a JEOL ARM300F*

Figure 9 includes further images of atomic cobalt species after further beam showering. The additional beam showering formed the holes observed in the centre of Fig.9.A and Fig.9.B but also exposed some atomically thin layers of N-graphene (very dark grey area around black holes). This enabled us to image single layers of N-graphene in HAADF mode, while simultaneously due to the high Z contrast clearly image atomically dispersed Co species too.

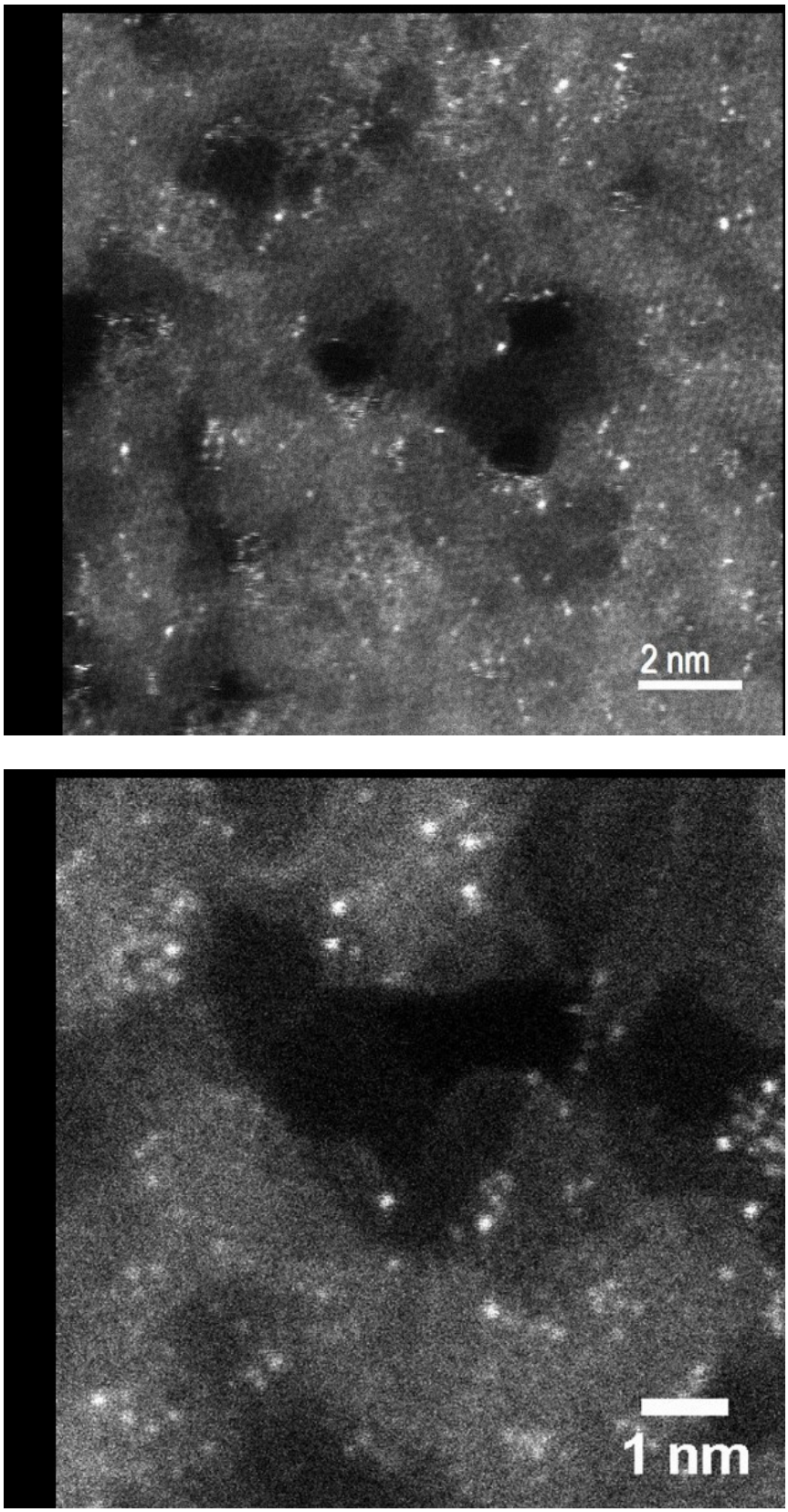


Figure 9: *Higher magnification HAADF images of Co-NG (A, B) obtained after beam showering on JEOL ARM300F*

5.4 Hydrogen Evolution Reaction

5.4.1 Experimental Methods

HER activity measurements were performed in the same way as for other M-NG catalysts and explained in Chapter 3.2.1. Briefly summarised, testing was carried out in a three electrode cell using Ar-sparged 0.5M H_2SO_4 as the electrolyte. The Co SACs were deposited onto the GC working electrode with a loading of around 0.27mg cm^{-2}. The catalysts were cycled between -0.5 and 1V vs RHE at 100mV s^{-1} ten times during which an increase in activity was observed similar to other M-NGs (Chapter 4 Section 5.2 and Chapter 4 Fig.7).

5.4.2 Results and Discussion

To compare the activity of the Co SAC catalysts LSVs from 0.2V to -1.2V vs RHE were recorded at a scan rate of 5mV s^{-1} (Fig. 10). Co-NG (red trace) is significantly more active than the other Co SACs with an overpotential at 10mA cm^{-2} of 116mV, compared to 372mV for Co-NG/N (blue trace) and 489mV for Co-G (green trace). Onset of hydrogen evolution is observed at significantly less negative potentials for Co-NG, illustrating the immense impact of synthetic conditions such as annealing atmosphere and metal precursor on HER performance.

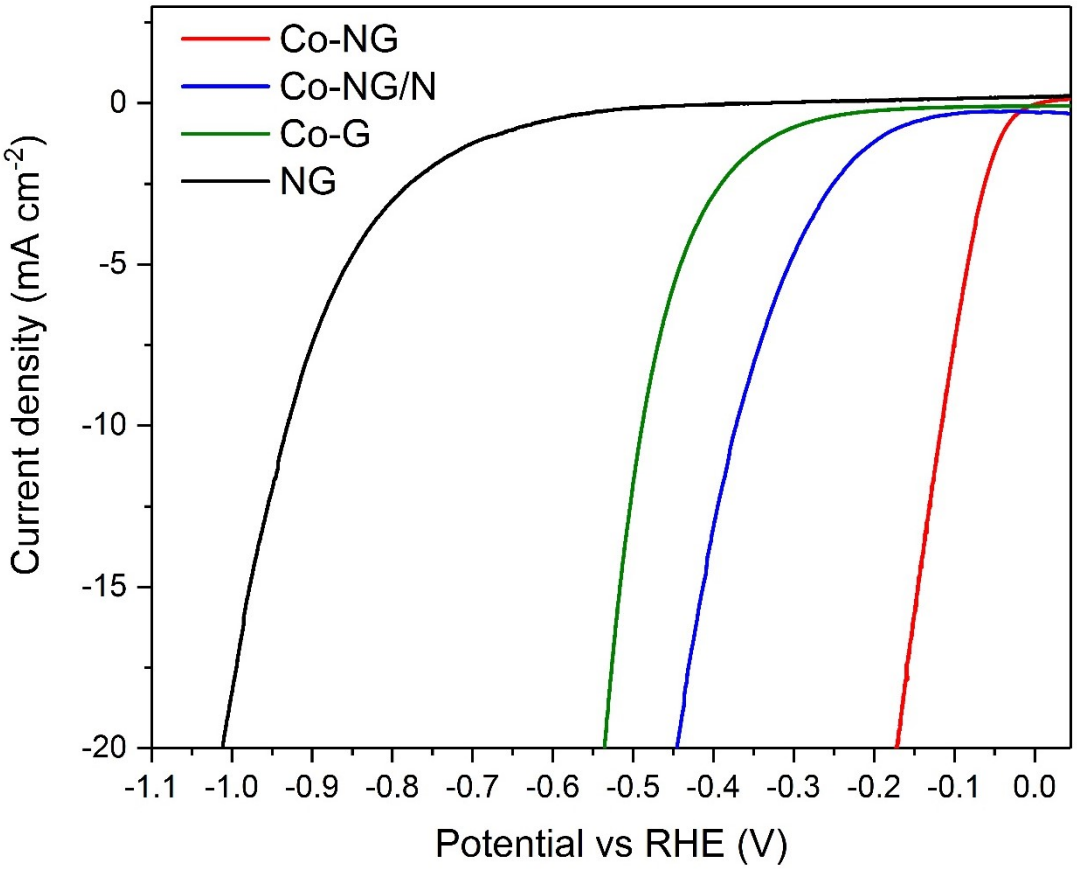


Figure 10: *LSVs of cobalt-containing single-atom catalysts Co-NG, Co-NG/N and Co-G in Ar-sparged 0.5M H_2SO_4 recorded at 5mV s^{-1} normalised to geometric surface area of the working electrode*

Tafel analysis was carried out to determine the Tafel slopes of all Co SACs (Figure 11). Co-NG exhibited the lowest Tafel slope at 51mV dec^{-1} indicating, as previously mentioned in Section 3.5.2 a Volmer-Heyrovsky mechanism to be at play with the capture of a solution proton by adsorbed hydrogen (the Heyrovsky step) being rate determining. Co-NG/N and Co-G display Tafel slopes in excess of 120mV dec^{-1}, with 160mV dec^{-1} and 171mV dec^{-1}, respectively, suggesting the initial proton adsorption (the Volmer step) to be the rate limiting step. Generally, the activity trend per geometric surface area of the electrode was found to be inversely proportional to the Tafel slope: Co-NG >> Co-NG/N > Co-G.

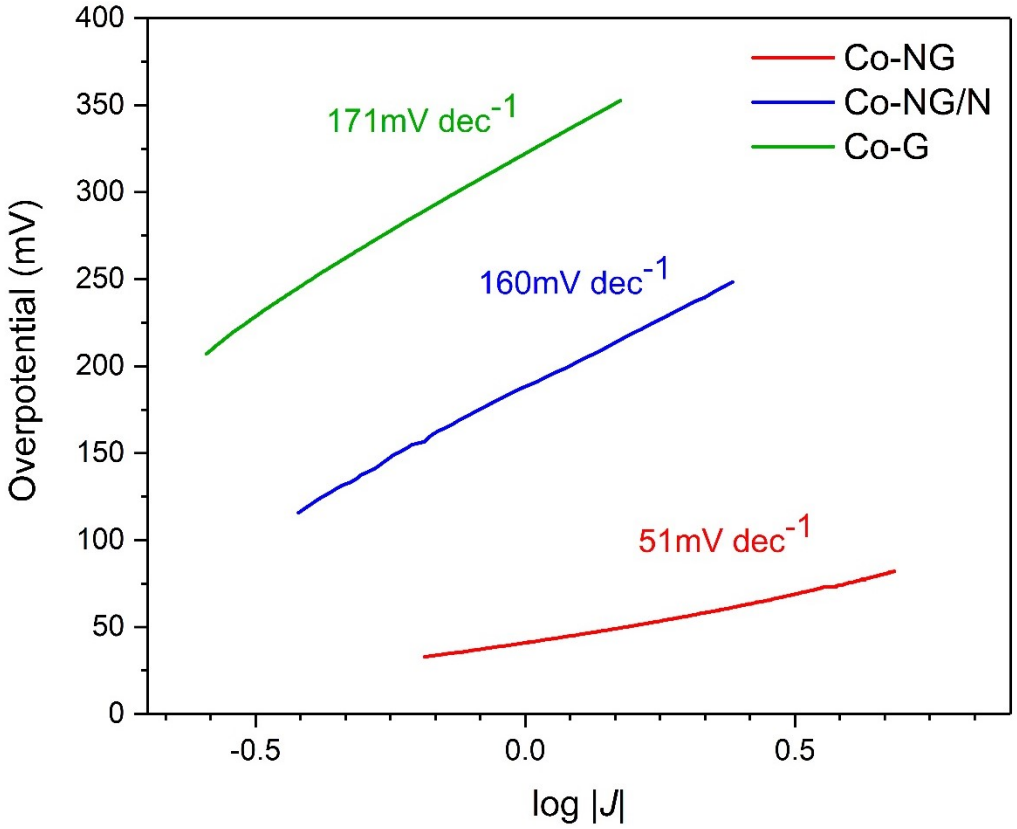


Figure 11: *Tafel plot of cobalt-containing single-atom catalysts Co-NG, Co-NG/N and Co-G*

Figure 12 shows the Tafel slopes for Co SACs over an extended range including 10mA cm^{-2} (equal to 1 on the logarithmic scale). Co-G (green trace) exhibits no change in Tafel slope over the range shown whereas Co-NG/N (blue trace) and Co-NG (red trace) display an increase in Tafel slopes at higher current densities.

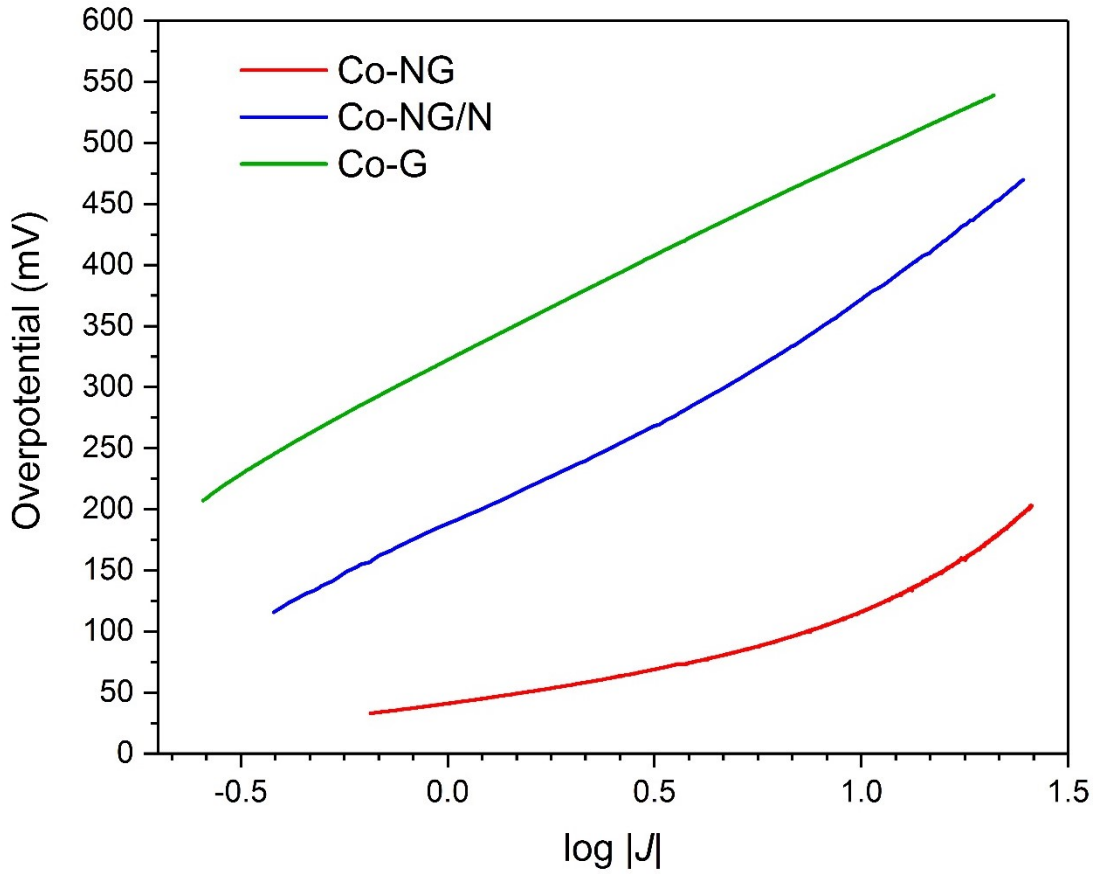


Figure 12: *Extended Tafel plot of cobalt-containing single-atom catalysts Co-NG, Co-NG/N and Co-G*

To investigate the impact of changing synthetic conditions on the surface of Co SACs, the electrochemically active surface area (ECSA) of the three catalysts was determined experimentally. ECSA was obtained by measuring the capacitive current in a non-Faradaic region at different scan rates (Fig. 13.A). By plotting the current density vs scan rate, the electrochemical double-layer capacitance (C_{dl}) can be determined by averaging the magnitude of the slopes for the positive and negative scans (Fig. 13.B). The ECSA can then be determined by dividing C_{dl} by the specific capacitance of a flat surface glassy carbon electrode with 1cm^2 of real surface area (C_s) for which we assume the value of 40μF cm^{-2}_{ECSA}[23–26]. We here assume the glassy carbon electrode to be atomically flat as well as double layer capacitance to be comparable between glassy carbon and graphene-like materials. The results of the ECSA measurements are summarised in Table 4.

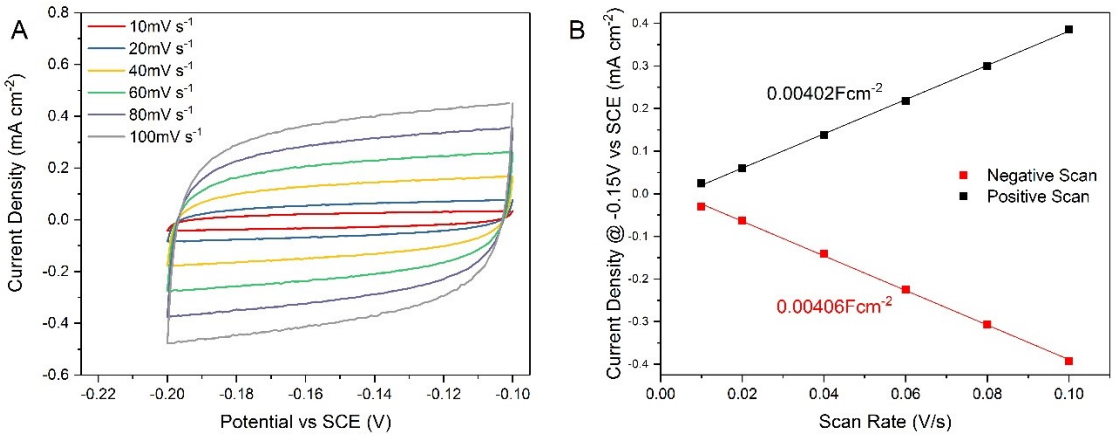


Figure 13: *ECSA measurement: CVs of Co-NG between -0.2 and -0.1 V vs SCE at different scan rates in Ar-sparged 0.5M H_2SO_4 (A) and the resulting geometrically normalised current densities of positive and negative scans plotted vs scan rate yielding the electrochemical double-layer capacitance as slope (B)*

Table 4: *Summary of electrochemical double-layer capacitance and ECSA for Co-NG, Co-NG/N and Co-G measured in 0.5M H_2SO_4*

Sample	C_{dl} (mF cm^{-2})	ECSA (cm_{ECSA}^2 cm^{-2})
Co-NG	4.04	101
Co-NG/N	3.76	94
Co-G	7.13	178

Both catalysts annealed under ammonia, Co-NG and Co-NG/N, have similar ECSA of around 100cm_{ECSA}^2 cm^{-2}. Co-G, annealed under Ar, exhibits a significantly higher ECSA of 178cm_{ECSA}^2 cm^{-2}. Annealing in a nonreactive atmosphere seems to increase the electrochemically active area. This could result from the different mechanism for reduction of the carbon backbone under the different annealing atmospheres. Experiments in unreactive atmospheres such as argon or vacuum have been shown to produce defective graphene structures where the simultaneous removal of carbon and

oxygen moieties as CO or CO_2 leaves behind defect sites which contribute to a higher ECSA.[27–29] An additional explanation for difference in ECSA between Co-NG, Co-NG/N and Co-G determined using the method above could be the difference in nitrogen content which could affect the capacitive behaviour of the material[26].

To account for the difference in ECSA the LSV curves in Fig. 14 are shown as normalised to electrochemically active, rather than geometric, surface area. The general trend is conserved although Co-G appears less active in comparison to the other Co SACs, with an overpotential (at -100μA cm^{-2}_{ECSA}) that is 1.5 and 5.5 times higher than overpotentials on Co-NG/N and Co-NG, respectively.

The ECSA is often used as an estimate for the number of active sites, especially in systems where the active centre is hard to probe or its exact nature remains elusive, based on the assumption that the number of active sites scales with catalyst surface area.[25] This has proven useful for some precious metal systems, in particular Pt nanoparticles[30], and non-precious molybdenum disulfide-based catalysts[25,31]. For such systems certain facets[23,30], edge sites[25,31] or defects in basal planes[25,31] are considered to be the active centres and it is reasonable to assume that such features should increase in number by nano-structuring or other means of enhancing the surface area. In the present case, the carbon backbone contributes significantly to the ECSA and it is not obvious why the number of active sites, i.e. cobalt centres, should scale with the surface area, especially considering that the same number of moles of cobalt was used to prepare the different Co SACs but Co-G shows a lower cobalt content in XPS compared to Co-NG despite its significantly higher ECSA.

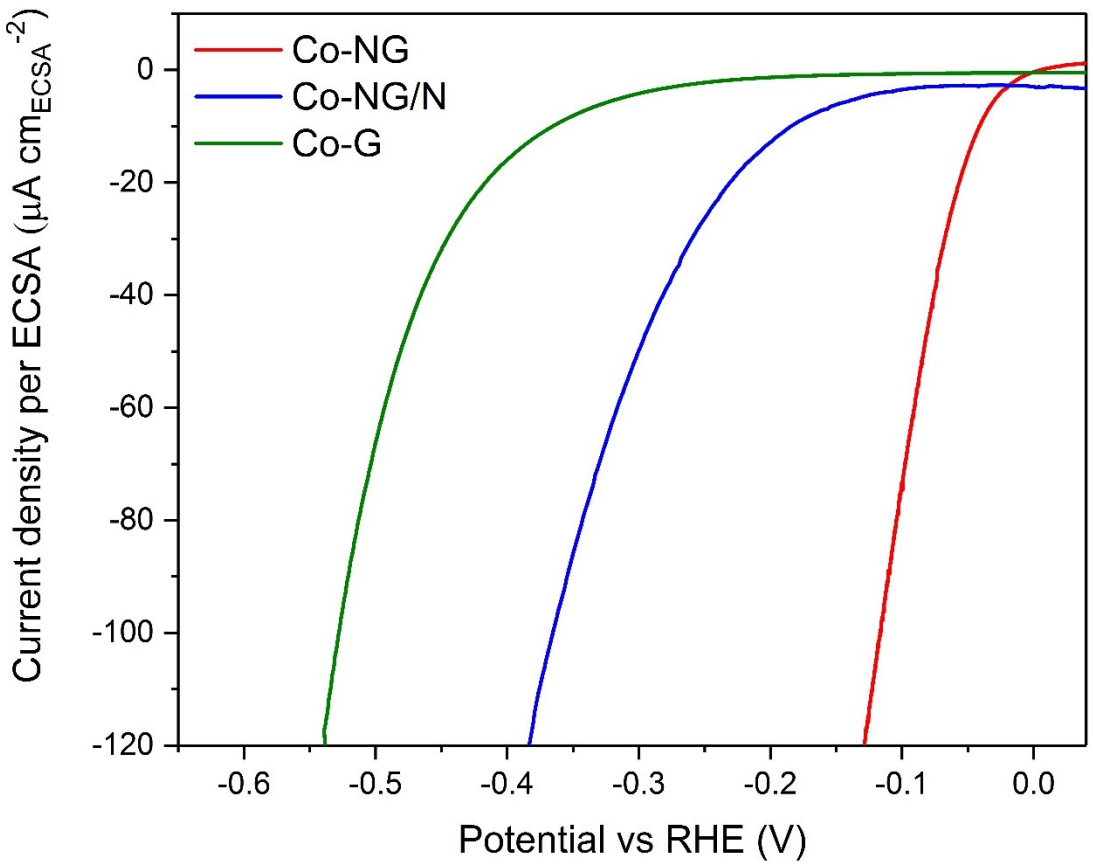


Figure 14: *LSVs of cobalt-containing single-atom catalysts Co-NG, Co-NG/N and Co-G in Ar-sparged 0.5M H_2SO_4 recorded at 5mV s^{-1} normalised to electrochemically active surface area of the electrocatalysts*

As such, the ECSA was not used as an estimate for the number of active sites and subsequent TOF calculations. For initial TOF calculations in this chapter, the active site density was approximated to be the same as for other M-NG catalysts (1.5 x 10^{-7} mol cm^{-2}, see Section 3.5.2 for calculation). Figure 15 shows the TOF plotted vs overpotential of the Co SACs which follow the order of Co-NG >> Co-NG/N > Co-G. A closer investigation into determining the active site densities of the Co SACs, at least qualitatively, is undertaken in Section 3.6.

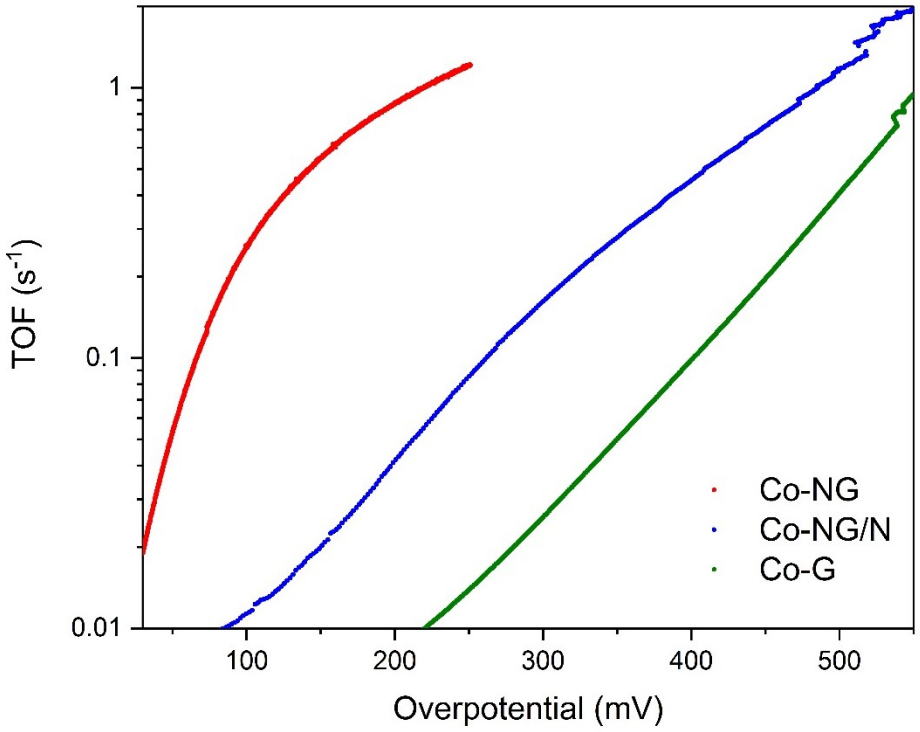


Figure 15: *Turn over frequency of Co-containing single-atom catalysts plotted against overpotential*

5.5 In-situ Infrared Spectroelectrochemistry

5.5.1 Background

As previously outlined, determining the active site density of single-atom transition metal catalysts has proven to be challenging. Traditionally consulted methods such as using ECSA as a proxy for active site density fall short for SACs and no defining electrochemical feature, such as H underpotential deposition for platinum catalysts[23,32] has been reported for SACs. Furthermore, ex-situ techniques to determine the amount of metal sites such as CO chemisorption were long believed to not be applicable to transition metal SACs since no CO absorption was observed. Recently, the group of Peter Strasser showed that it is indeed possible to probe M-N_x sites using pulsed CO chemisorption with TPD by working at low temperatures.[33,34] They were able to show that CO desorbs from M-N_x below room temperature already, explaining why previous CO chemisorption

experiments and also electrochemical CO stripping experiments failed.[33,34] CO chemisorption TPD can provide a good estimate of gas phase accessible metal sites and as such presents a significant advance from simply using the metal loading for active site density determination by excluding metal sites buried in the bulk from the equation. It further provides the energy of adsorption and as such can be used to differentiate between types of active sites. Assessing the active site density based on CO TPD still relies on the assumption that the probed metal sites are the actual active centres which might not always be the case. Furthermore, working at low temperatures and in the gas phase, the state of the active sites, as well as their exposure to the medium might be significantly different from electrochemical operating conditions.

A potential strategy to address these shortcomings could be to use a strongly adsorbing probe molecule which deactivates the catalyst (poisoning agent) to assess the active site density in-situ. Generally, atomically dispersed transition metal catalysts on carbon support have been shown to be quite resistant towards poisoning with many showing little response to commonly known electrocatalyst poisoning agents such as CH_3OH, CO or NH_3.[33,35–38] For Fe-N-C catalysts (based on atomically dispersed iron centres on nitrogen-doped carbon supports) which show high oxygen reduction reaction (ORR) activity, cyanide ions have been shown to be an effective poison,[37,38] although to date, no reports have shown successful use of CN^- as a probe for active site determination.[37] Recent studies proposed the use of nitrite ions as a poisoning agent coupled with reductive stripping experiments to determine active site density of Fe-N-C and Co-N-C systems used in ORR.[39,40] Unfortunately, the charge transferred in nitrite reduction was measured between 0.2V to -0.3V vs RHE, as such this approach is not applicable for highly active HER catalyst since hydrogen evolution current will mask the nitrite reduction.[39] Cobalt-

based systems, including catalysts previously reported as active in HER, can be poisoned by thiocyanate ions[19,41,42] though no attempts for active site density measurements using SCN^- have been reported.

In preliminary linear scanning voltammetry experiments it was shown that small amounts of KSCN significantly reduce HER activity of Co SACs (Fig.16). This effect was therefore investigated in further detail using IR spectroelectrochemistry. Using the CN-stretch of thiocyanate as a probe, the type and density of active centres on the Co-containing SACs are assessed, comparatively.

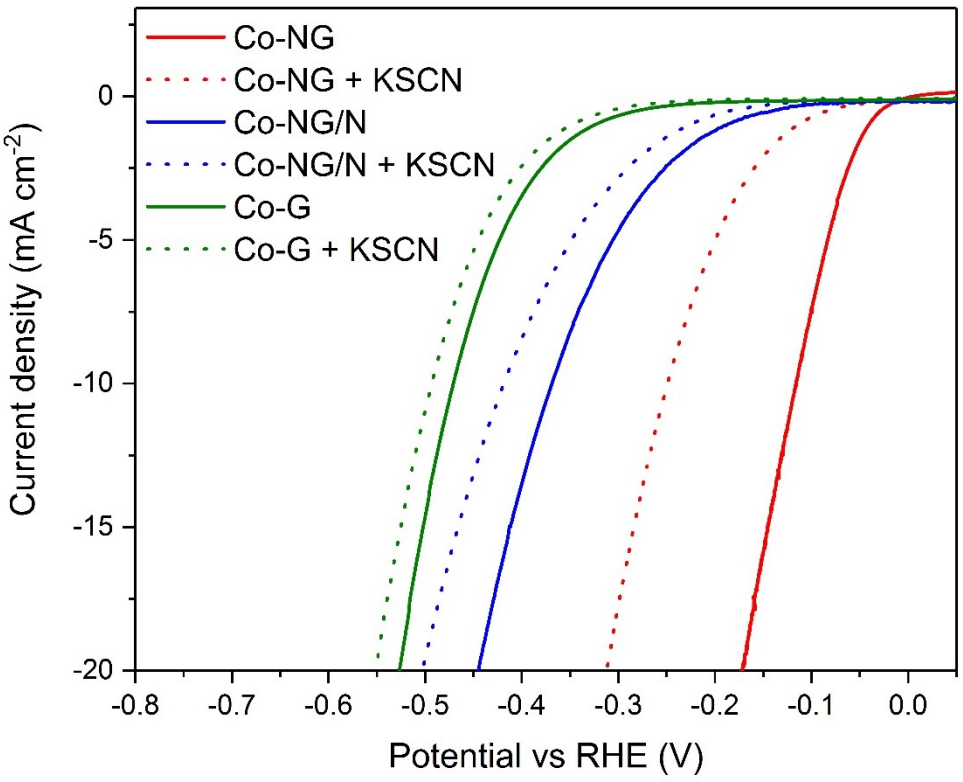


Figure 16: *Poisoning of Co SACs with potassium thiocyante. Dotted lines indicate presence of 27mM KSCN in 0.5M H_2SO_4.*

5.5.2 Experimental Methods

For details on the experimental methods, see Chapter 3 Section 2.4.

In summary, a spectroelectrochemical cell, designed to be operated under flow conditions and fitted with a trapezoidal Si ATR element, was used in the following experiments. The catalyst of interest was dropcasted directly onto the Si element with a loading of 0.016mg cm^{-2} and brought into electrical contact via a sheet of carbon paper connected to a glassy carbon rod. Ar-sparged 0.5M H_2SO_4 was used as the electrolyte.

Prior to electrochemical operation, several background IR spectra were collected. Once a background IR spectrum of the catalyst at OCP in 0.5M H_2SO_4 was acquired, the catalyst was cycled between -0.5V and 1V vs RHE for ten cycles and another background spectrum was acquired. Following that, 144µL of 0.3M KSCN in 0.5M H_2SO_4 solution were added leading to a KSCN concentration of 7mM in the electrolyte solution. Several IR spectra were obtained until no further increase in peak height for the C-N stretch was observed. Subsequently, chronoamperometry at following potentials was carried out for at least 420s each: 0.51V, 0.31V, 0.11V, -0.09V, -0.29V and -0.49V vs RHE. At each potential at least two IR spectra were recorded.

5.5.3 Results and Discussion

All catalysts exhibited similar activation behaviour upon cycling between -0.5V and 1V vs RHE compared to previous experiments in a glass cell showing that all Co SACs were in good contact with the working electrode, as well as with the electrolyte. Upon addition of KSCN solution to the electrolyte a feature between 2050 and 2060cm^{-1} started to develop. Difference spectra were used to highlight the changes on the surface of the catalyst in the presence of the more strongly IR absorbing solvent.

A difference spectrum of Co-NG at OCP in the presence of KSCN was generated by subtracting a spectrum of Co-NG at OCP in pure 0.5M H_2SO_4 (Fig.17). The broad feature

at around 3250cm^{-1} (OH stretch) can be explained by a change in hydration of the electrode over time, as well as the broad feature around 1650cm^{-1} and sharper features below 1300cm^{-1} which are associated with Nafion in the catalyst ink. [43]

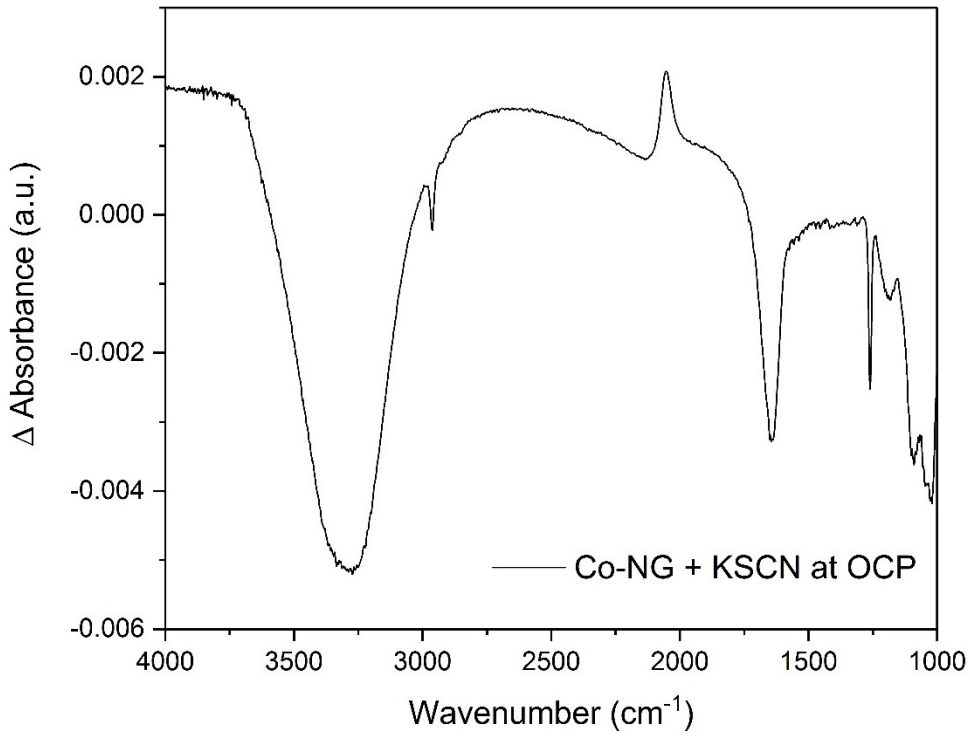


Figure 17: *Difference spectrum of Co-NG at OCP in the presence of 0.265µM of KSCN*

The feature between 2050 and 2060cm^{-1} in the Co SACs spectra can be identified as the C-N stretch of SCN^- when compared to the spectrum of free KSCN solution (Fig. 18), as well as other literature reports[44]. The CN stretching frequency of unbound SCN^- in 0.5M H_2SO_4 was found to be 2066cm^{-1} which is congruent with literature[44,45]. As previously described, SCN^- can bind via either S or N to metal complexes forming either thiocyanato or isothiocyanato complexes, respectively[44]. For all Co SACs the bound SCN^- species can be observed at around 2050 to 2065cm^{-1} which is typical for cobalt isothiocyanate complexes in contrast to M-SCN species which usually exhibit absorption bands above 2100cm^{-1}.[44] An additional explanation for the observed behaviour could be a possible

interaction between Nafion and SCN^- ions and further research is needed to account for potential influence of such an interaction on the shift in CN stretching frequency.

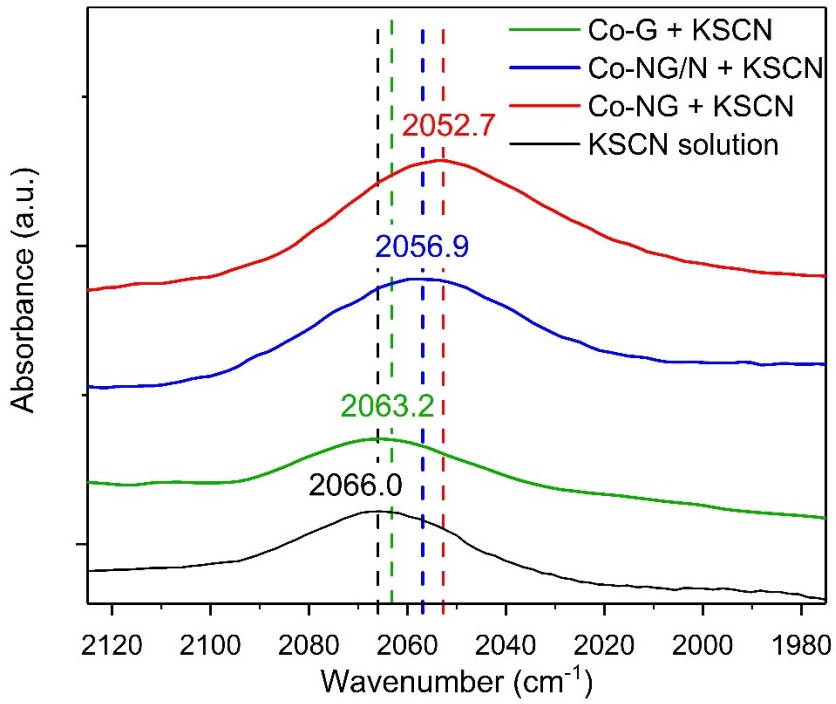


Figure 18: *Overlay of spectra of the C-N stretch region for SCN-poisoned Co-NG, Co-NG/N, Co-G and free KSCN solution*

After an initial induction period under OCP the CN stretching band reached a maximum height and remained stable, independent of applied potential, for all Co SACs (Fig. 19). This demonstrates that SCN^- effectively binds to the Co centres of the different catalysts even at potentials as low as -0.49V vs RHE where significant turn over is observed under pristine conditions (Fig.15). As such, these observations further establish SCN^- to be an effective poison for our Co SACs, as well as conclusively confirm atomically dispersed cobalt centres as the active site.

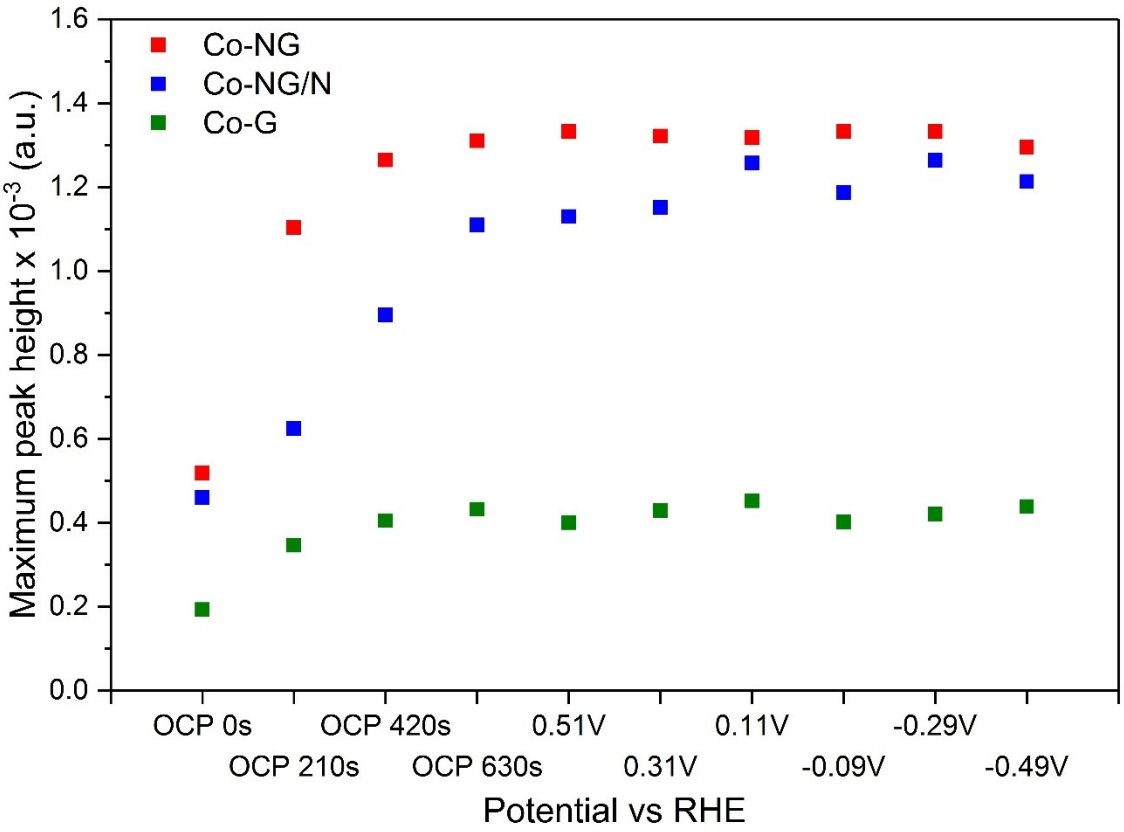


Figure 19: *Potential dependence of peak height of C-N stretch of SCN^- on Co-NG (red squares), Co-NG/N (blue traces), and Co-G (olive traces) in 0.5M H_2SO_4. The time stamp for the OCP measurements indicate the time when the IR spectra collection was started in relation to the injection of KSCN solution.*

Analysis of peak fitted spectra (Fig.20) further showed no potential dependence of the position of the CN-stretch peak maxima of Co-NG and Co-G (Fig.21A, C). Intriguingly, for Co-NG/N a linear dependence of the peak position with potential was observed yielding a subtle Stark shift of around $0.6 cm^{-1} V^{-1}$ (Fig.21.B). The underlying reason for the different response of the CN stretches in bound thiocyanate on Co SACs is subject to further investigation but clearly points towards structural differences of the active sites, indicating better electronic coupling to the electrode for Co-NG/N.

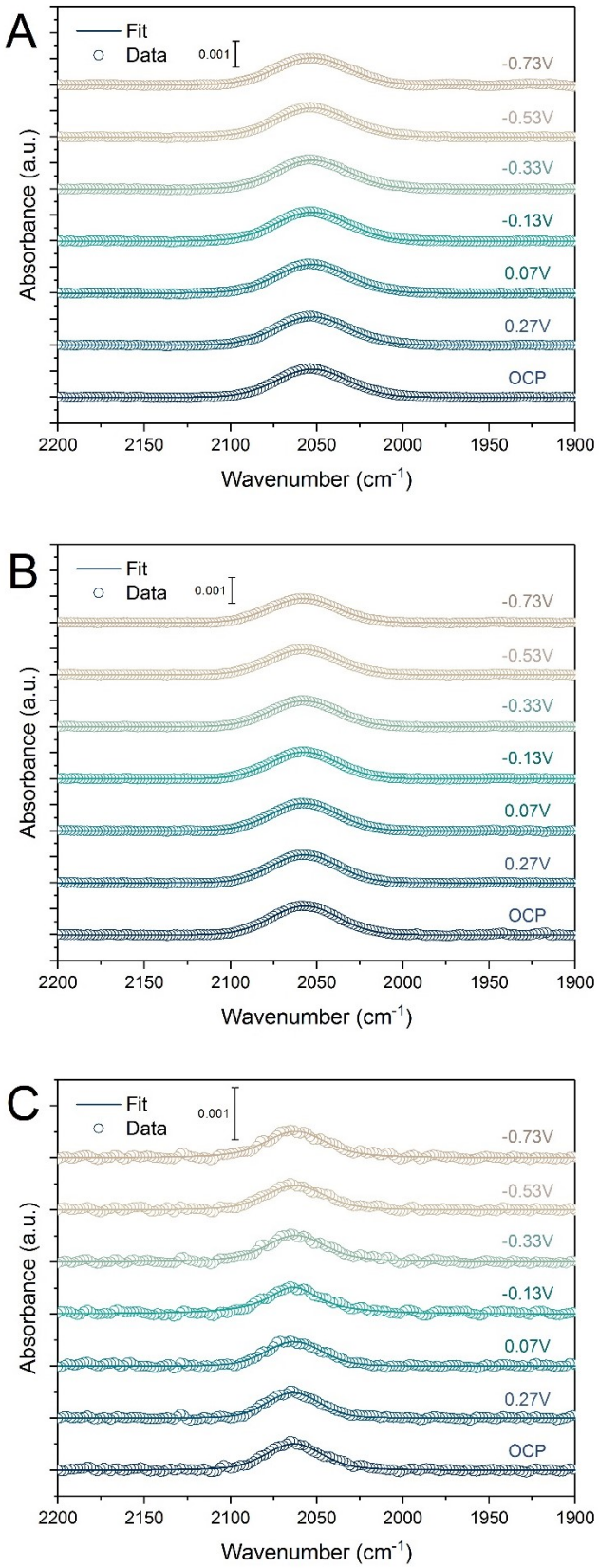

A
Fit
Data
0.001
-0.73V
-0.53V
-0.33V
-0.13V
0.07V
0.27V
OCP
Absorbance (a.u.)
2200
2150
2100
2050
2000
1950
1900
Wavenumber (cm-1)
B
Fit
Data
0.001
-0.73V
-0.53V
-0.33V
-0.13V
0.07V
0.27V
OCP
Absorbance (a.u.)
2200
2150
2100
2050
2000
1950
1900
Wavenumber (cm-1)
C
Fit
Data
0.001
-0.73V
-0.53V
-0.33V
-0.13V
0.07V
0.27V
OCP
Absorbance (a.u.)
2200
2150
2100
2050
2000
1950
1900
Wavenumber (cm-1)

Figure 20: *Fitted difference spectra of CN-stretch of SCN^- on Co-NG (A), Co-NG/N (B), and Co-G (C) at different potentials in 0.5M H_2SO_4. A baseline was fitted using asymmetric least squares smoothing and subtracted from the data. A Voigt profile was used to fit the peaks.*

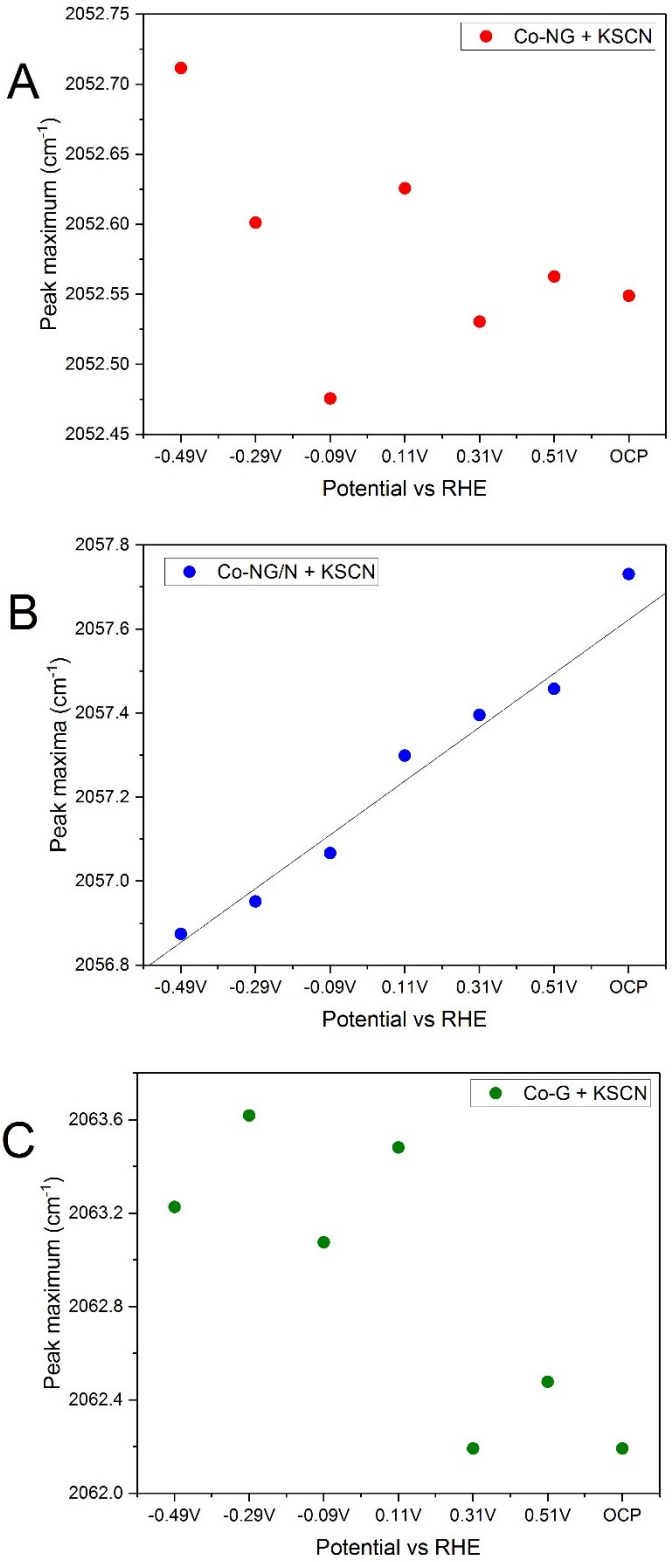


Figure 21: *Change in position of peak maximum of CN-stretch versus potential for SCN^- on Co-NG (A), Co-NG/N (B) and Co-G (C).*

It is interesting to note that the CN stretch occurs at different frequencies for all three Co SACs (Fig. 18) with the general trend being Co-G > Co-NG/N > Co-NG. A shift to lower wavenumbers in metal isothiocyanato complexes is said to occur due to weakening of the bond of interest and subsequent increase in bond length requiring lower energy radiation to be excited[44]. In our system the weakening of the CN-bond of the thiocyanate ion in the bound versus unbound state can possibly be explained by π backdonation, similar to variations in C-O stretching of carbon monoxide observed on electrocatalysts[46]. Upon binding of the thiocyanate ion to Co via N, given the overlap of adequate orbital, Co can donate electron density from its d orbitals into the π^* of CN leading its stretch to occur at a lower frequency. This hypothesis is supported by the observation of a positive Stark shift for Co-NG/N (Fig.21.B) for which at more negative potentials the CN stretch occurs at lower wavenumbers. This is consistent with increased π backdonation into the π^* orbital of the NCS ligand due to increased electron density on the cobalt.

The shift in peak maximum from Co-NG to Co-G correlates with the increase in overpotential needed to achieve a turn over frequency of $0.1s^{-1}$ (Fig. 21.B) indicating that the atomically dispersed Co-sites in the Co SACs have indeed different coordination environments affecting their HER activity.

We then used the peak area of the CN-stretches to comparatively determine the active site density. Co-NG and Co-NG/N exhibited very similar CN stretch peak areas at -0.49V vs RHE of 0.0542 and 0.0537, while it was more than two times smaller for Co-G with 0.0241. This is in line with the visible observation of cobalt dissolving off Co-G during the acid leaching step and the lower signal to noise ratio in its Co2p XPS spectrum (Fig. 2.C) compared to the other Co SACs. Assuming that the peak area scales with the number of active sites, we recalculated the turn over frequencies of the cobalt-containing single

atom catalysts by adjusting the previously estimated active site density (1.5 x 10^{-7} mol cm^{-2}, see Section 3.5.2) according to the ratio of peak areas of Co SACs setting Co-NG as one. The recalculated TOF plot in Figure 22.A shows Co-G to be significantly closer in activity to Co-NG and Co-NG/N and exhibiting similar turn over frequencies to Co-NG/N at higher overpotentials.

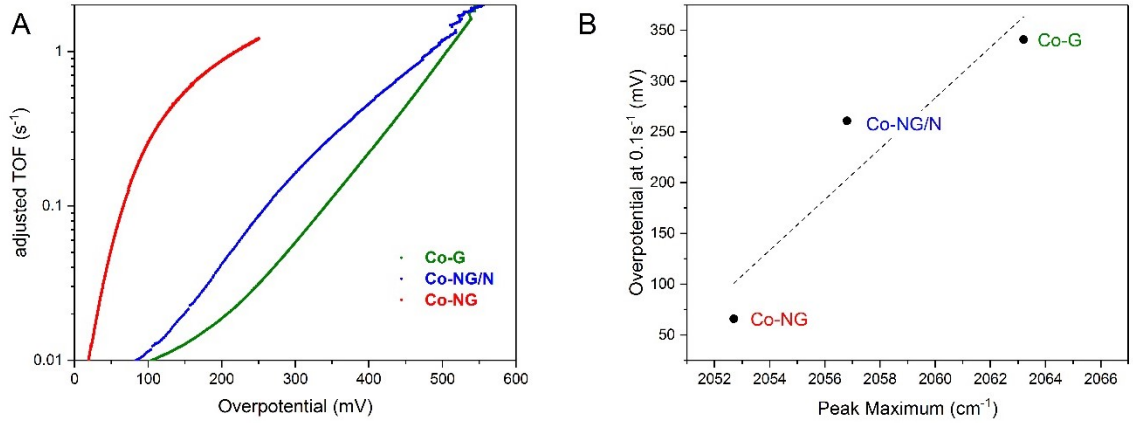


Figure 22: *Turn over frequencies of Co SACs normalised by C-N stretching peak area measured during SCN poisoning plotted against overpotential (A) and Overpotential at TOF of 0.1s^{-1} plotted vs peak maximum of CN stretch of adsorbed SCN^- (B). Dotted black line represents a linear fit for the three points and is provided to guide the eye.*

Overall, we show that by using SCN^- as a probe molecule in combination with IR spectroelectrochemistry that the three Co SACs have three distinct Co-based active centres. A decrease in wavenumber of the CN stretch, tentatively due to higher electron density around the cobalt, was found to correlate with lower overpotentials for HER. We qualitatively assess the active site density by comparing the peak area of the observed CN stretches showing Co-NG and Co-NG/N to contain the same amount and Co-G roughly half the amount of Co-centres.

We suggest that with further calibration and titration experiments, IR spectroelectrochemical thiocanate poisoning experiments could present a way to

investigate the active metal centres of SACs and quantitatively determine the number of active sites in-situ.

5.6 In-situ X-ray Absorption Spectroscopy

5.6.1 Background

In order to further investigate the bonding environment of Co in the cobalt-containing SACs and its effect on their HER activity in-situ X-ray absorption spectroscopy (XAS) studies were carried out.

As introduced in Section 2.4, XAS uses X-ray radiation to probe the electronic state, chemical bonding environment and local geometry of an element of interest (the absorber). High intensity X-ray radiation is used to excite core electrons of the absorber leading to element specific X-ray absorption and, due to electrons of higher orbitals dropping down to fill the core hole, emission of a photon. Measurements can therefore be made in either transmission mode or in fluorescence mode (measuring emitted photons). Fluorescence mode measurements make it possible to obtain XAS spectra for very dilute samples and are usually the mode of choice for investigating atomically dispersed metal on carbon supports. The structure of absorption spectra can be divided into two regions: the X-ray Absorption Near Edge Structure (XANES) and the Extended X-ray Absorption Fine Structure (EXAFS). XANES describes the area spectrum shortly before and after the edge. For transition metals next to the white line, the highest intensity edge feature, several other peaks are observed before (pre-edge) or in the edge (rising-edge). Such features are described as bound state transitions where a core electron is excited to an empty higher energy orbital instead of to the continuum, and as such require less energy and occur before the white line.[47] The position and intensity of bound state

transitions depends on the energy of the unoccupied, in the case of cobalt 4p, orbitals and in the case of multi-electron shakedown features also on the spatial orientation and energy of neighbouring occupied ligand orbitals (Fig. 23). As such XANES is sensitive to coordination environment and, importantly, bonding geometry of the absorber.

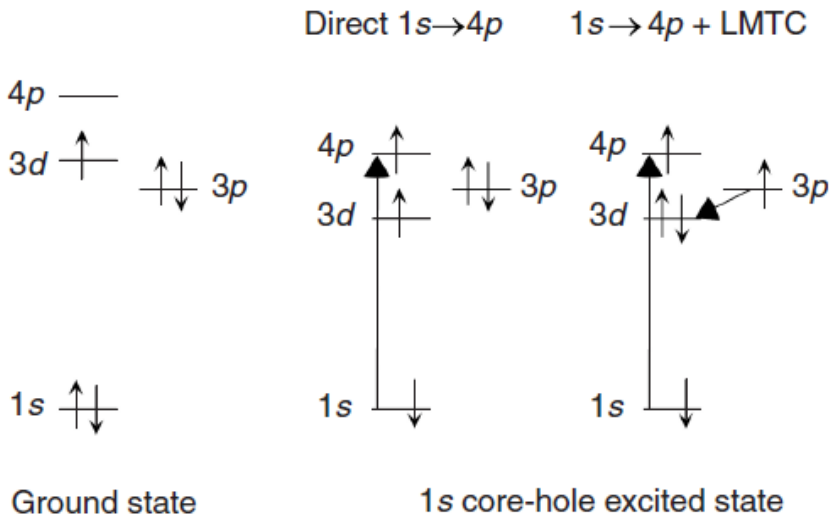


Figure 23: *Graphical representation of bound state transitions in first row transition metals. Left side shows energy levels in the ground state. The graphic in the middle illustrates the energy levels after 1s → 4p transition including the core hole. The right graphic illustrates a shakedown feature where an electron is transferred from a ligand orbital to the 3d of the metal. Reprinted from reference* [47] *with permission from Elsevier.*

The EXAFS region extends several 100eV past the white line absorption and is best understood as a scattering phenomenon of a photoelectron either constructively or destructively interfering with a second photoelectron from the absorber leading to an oscillating of its amplitude in the spectrum. By taking the Fourier transform of this region, it is possible to infer the distance and by modelling also the number of ligands in the first coordination shells. Furthermore, the wavelet transform technique is able to resolve the backscattering in energy space allowing identification of the ligands.[48]

In the following sections, in-situ XAS studies of all three Co SACs under HER conditions are presented. Analysis of XANES and EXAFS is carried out to identify the coordination environment and geometry of the atomic cobalt species to further the understanding of the active sites obtained by IR spectroelectrochemistry. Wavelet transform analysis is used to investigate the stability of atomic dispersion under operation.

5.6.2 Experimental Methods

For a detailed description of the experimental methods used in this section refer to Chapter 3 Section 2.5.

In summary, XAFS spectra of the Co K edge (7709eV) were obtained from 200eV before to 750eV after the edge. The measuring time of a XAS scan was about 3mins and usually five scans of the same condition were collected consecutively. All testing was carried out in a specially designed PTFE cell using a free-standing sheet of catalyst as working electrode. Five scans of a sample in the dry state were collected before moving on to in-situ measurements. Afterwards the cell was filled with 10mL of 0.5M H_2SO_4 and bubbled with Ar for 20min. Following that five XAS scans were collected at OCP. Subsequently, the catalyst was cycled between -0.8V and 0.8V vs RHE for ten cycles. After electrochemical activation, chronoamperometry experiments were carried out while collecting further XAS scans. The catalyst was stepped from 0.7V to -0.5V vs RHE in steps of 0.3V, holding the catalysts at each potential for 15min while collecting five XAS scans.

5.6.3 Results and Discussion

5.6.3.1 XANES

The Co K edge XANES spectra of all three Co SACs in static air after normalisation and background treatment are shown in Figure 24. Interestingly, all three Co SACs show a distinct profile with a stark difference between Co-NG (red trace) and Co-NG/N (blue trace), as well as Co-G (green trace), in several features. This is further evidence that in each Co SAC the cobalt centre is coordinated differently.

The position of the XANES edge is often used to determine the oxidation state of an absorber, however this is not possible here due to modulation of the edge by pre-edge and rising edge features. Five such features are observed around the Co K edge at 7709 (a), 7716 (b), 7724 (c), 7728 (d) and 7735eV (e) which are characteristic for the K edges of transition metals and described as bound state transitions where a core electron is excited to empty higher energy orbitals.[47] As such, these transitions are dependent on the electronic structure of the absorber and sensitive to bonding geometry. The pre-edge feature a) is assigned to be a 1s → 3d transition which is dipole selection rule forbidden but does occur due to p-d hybridisation[47,50]. This feature is especially pronounced for tetrahedral arrangements where stronger p-d mixing exists[47]. For the Co SACs only a small pre-edge feature is observed indicating Co to be in a more centrosymmetric environment such as octahedral or square-planar. Rising-edge feature b) is identified as 1s → $4p_z$ + a ligand-to-metal charge transfer (LMCT) often also referred to as a shakedown feature. LMCTs occur because the core hole formed in the initial X-ray absorption leads to the valence orbitals experiencing the effective nuclear charge of a Z+1 nucleus, decreasing the 3d orbital energy below that of the HOMO of the ligand.[47] Overall LMCT leads to a lower energy final state explaining why shakedown transitions

occur before their corresponding single electron bound state transition. The $1s \rightarrow 4p_z$ + LMCT is characteristic for transition metals in highly centrosymmetric environments such as square planar or linear arrangements.[1,47,50,51] Feature c) corresponds to a $1s \rightarrow 4p_z$ and is less pronounced in the Co SACs spectra. The remaining features d) and e) are described as $1s \rightarrow 4p_{xy}$ with and without LMCT, respectively.

Large differences between the catalysts are observed for features b), c) and d) (Fig.24). Co-NG (red trace) shows a pronounced rising-edge peak at 7716eV suggesting it is coordinated in a square planar fashion. Co-NG/N (blue trace) and especially Co-G (olive trace) exhibit only smaller shoulders for feature b) indicating that here centrosymmetry is distorted potentially by one or more additional axial ligands. Additionally, the ratio of peaks c)/d) to e) are significantly different across the Co SACs with Co-NG/N and Co-G showing a larger and downshifted peak for feature d) compared to Co-NG. This has previously shown to be related to increased amounts of oxygen in the first coordination shell, usually in the form of axially adsorbed O_2 or OH groups, as well as axial displacement of the metal.[51–53]

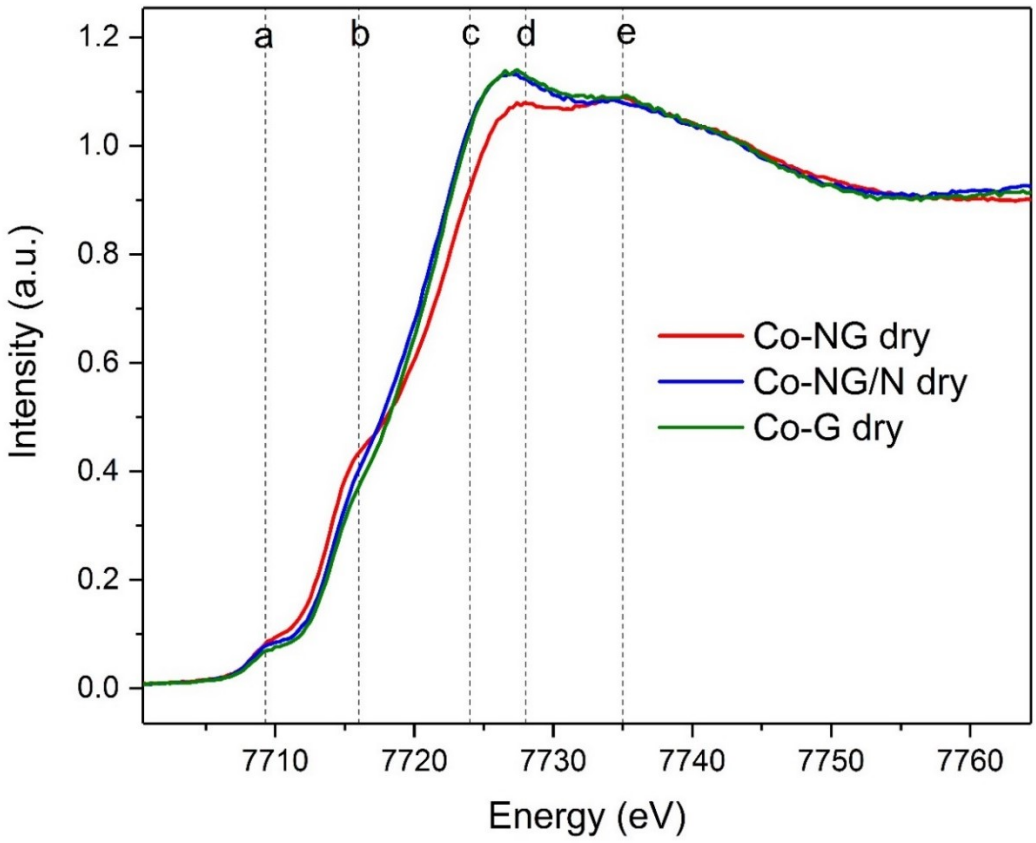


Figure 24: *Normalised Co K edge XANES spectra of Co-NG (red), Co-NG/N (blue) and Co-G (olive) in air measured in fluorescence mode.*

Table 5: *Features observed in XANES of cobalt-containing single atom catalysts, assignment based on reference*[50]*. LMCT is short for ligand-to-metal charge transfer.*

Feature	Energy (eV)	Assignment
a	7709	1s → 3d (p-d hybrid.)
b	7716	1s → $4p_z$ + LMCT
c	7724	1s → $4p_z$
d	7728	1s → $4p_{xy}$ + LMCT
e	7735	1s → $4p_{xy}$

XANES spectra of the catalyst in electrolyte and under electrochemical control are shown in Figure 25.

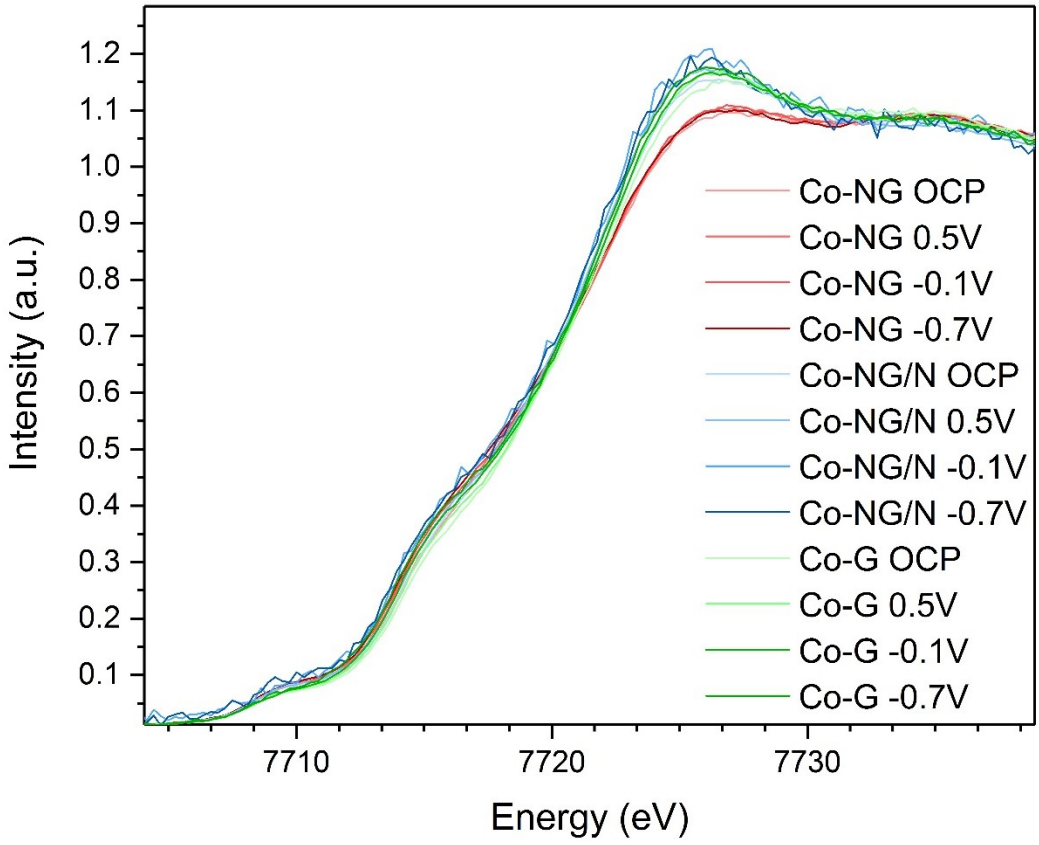


Figure 25: *Normalised Co K edge XANES spectra of Co-NG (red), Co-NG/N (blue) and Co-G (olive) in 0.5M H_2SO_4 measured in fluorescence mode. Colour code: Stronger colour indicates more negative potential.*

In order to highlight the changes the catalysts undergo in the electrolyte and during operation the Δμ-method was employed. Changes are emphasised by subtracting the XANES spectrum of the catalyst at OCP from all other spectra. Furthermore, employing difference spectra helps to distinguish between surface and buried sites since no change in XANES spectra is expected for metal centres that are not exposed to the electrolyte. Figure 26 illustrates the use of the method for the dry spectra of the Co SACs. Co-NG

undergoes drastic change when put in contact with electrolyte with a decrease in feature b) and an increase in feature c). This behaviour is also observed for Co-NG/N but to a much smaller degree and Co-G exhibits little change when exposed to 0.5M H_2SO_4. Loss of peak intensity of b) indicates a distortion of the square planar arrangement observed for Co-NG in air potentially due to the axial adsorption of a hydroxo or aquo ligand, which also explains an increase in feature c) under OCP conditions. Reduced magnitudes of aforementioned changes indicate that less of such binding events occur or that there is less change due to binding because the square planar arrangement is already distorted for Co-NG/N and Co-G in the dry state.

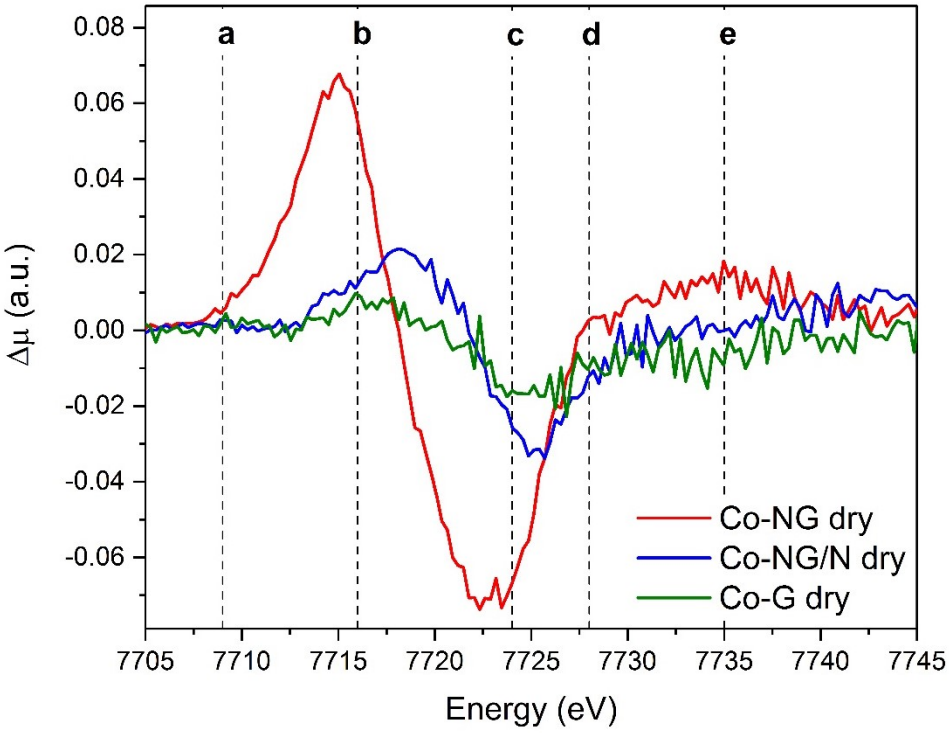


Figure 26: *Δμ-spectra of Co-NG (red), Co-NG/N (blue) and Co-G (green) obtained by subtracting XANES spectrum at OCP from the XANES spectrum of the dry catalyst.*

Figure 27 shows the Δμ-spectra for all Co SACs at various potentials again acquired by subtracting the XANES spectra of the catalysts at OCP. Co-NG experiences an increase in feature b) going from 0.7V to -0.5V vs RHE (Fig.27.A). Analogous trends are observed

for Co-NG/N (Fig.27.B) and Co-G (Fig.27.C). Compared to the catalysts at OCP both Co-NG/N and Co-G additionally show an increase in feature c) not observed for Co-NG. As previously mentioned such a feature in Δμ-spectra has previously been ascribed to axial displacement of a metal centre by Jia et al..[51] Potential axial displacement of the Co centre upon proton binding creating a large kinetic barrier could possibly explain why the Volmer step is rate determining for Co-NG/N and Co-G, as inferred from their Tafel slopes (Section 3.5.2).

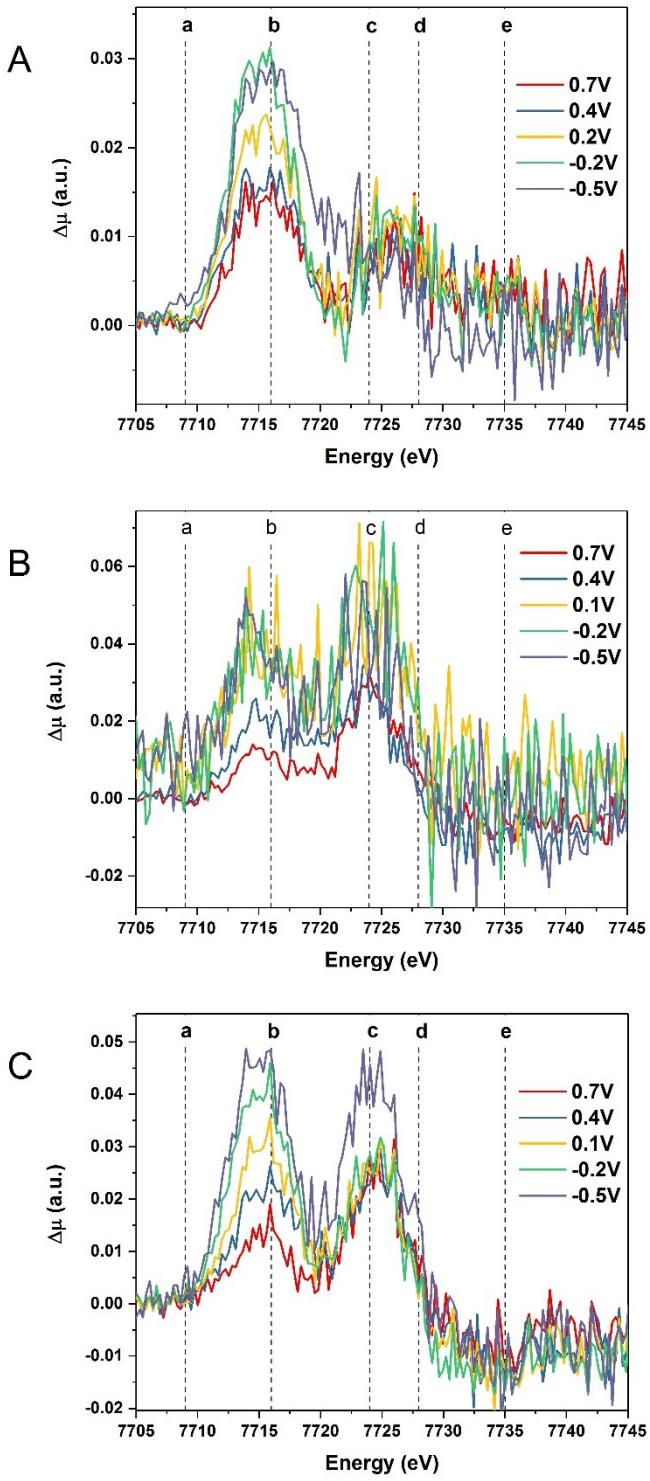


Figure 27: *Δμ-spectra of Co-NG (A), Co-NG/N (B) and Co-G (C) obtained in Ar-sparged 0.5M H_2SO_4 calculated by subtracting the XANES spectrum at OCP from the spectra outlined in the graphs. Colour code, all potentials vs RHE: 0.7V (red), 0.4V (blue), 0.1V (yellow), -0.2V (green), and -0.5V (purple).*

Overall the three Co SAC exhibit three distinct XANES spectra which undergo dynamic change under electrochemical conditions. The increase of feature b) under HER conditions observed for all catalysts illustrates the pivotal role of a square planar bonding arrangement for efficient hydrogen evolution. Normalised to the white line, feature b) is most prominent in Co-NG under all conditions with a general trend in peak height of Co-NG > Co-NG/N > Co-G which follows the trend for the HER activity of the Co SACs. By changing the metal salt or annealing atmosphere for Co-NG/N and Co-G, the coordination environment of the cobalt metal centres is significantly altered, possibly by the introduction of oxygen moieties. This leads to a distortion of the square planar bonding arrangement of the atomically dispersed cobalt atoms resulting in lower HER activity. It further seems to lead to an axial displacement of the active centres during HER offering an explanation for the increased Tafel slopes compared to Co-NG. These hypotheses are further investigated in the Section 7 using DFT calculations and XANES modelling approaches.

5.6.3.2 EXAFS

5.6.3.2.1 Wavelet Transform

Wavelet transform (WT) analysis was carried out to determine if there are contributions from Co-Co interactions to the XAS spectra of the Co SACs. As introduced in Section 2.4 wavelet transform enables the resolution of EXAFS backscattering in k- and R-space. As such, it enables the contributions from different atomic scatters with similar path lengths to be discriminated. Here the HAMA code was used to calculate 2D contour plots of the wavelet transform[54–56]. Morlet wavelets were used and their parameters, κ and σ, were varied depending on the range of interest. High κ values of around 7 were used to obtain overview WT plots of the whole spectrum (data not shown). In order to investigate

the first few coordination shells of the Co centre in the Co SACs, R_{max} was set to 3Å and a lower κ value of three was used to increase the resolution in k-space. Figure 28 shows WT contour plots for Co metal foil, Co-NG, Co-NG/N and Co-G, all in air and using the aforementioned fitting parameters. Co metal foil exhibits a maximum intensity at around 6.6Å^{-1} in k-space and around 2Å in R-space (not phase corrected) (Fig.28.A). This is in line with previous literature reports[1,52] and with a k-space value of 6.8Å^{-1} calculated by Fei et al. assuming a path length of 2Å[9]. All Co SAC catalysts also exhibit only one maximum but at a shorter path length (~1.3 Å) and R-values between 3.3 and 3.4Å^{-1} (Fig.28.B-D). No maximum at 6.6Å^{-1} is observed conclusively proving the absence of Co-Co interactions and as such Co nanoparticles or clusters.

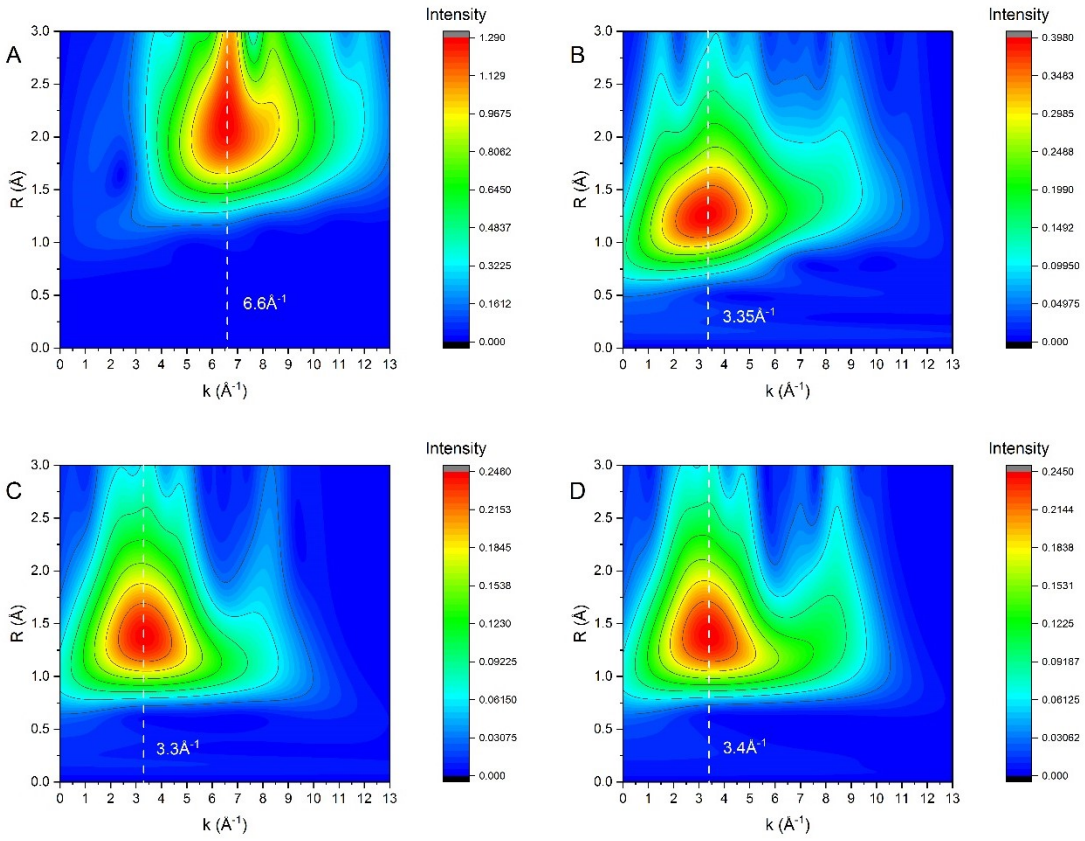


Figure 28: *Wavelet transform of EXAFS of Co metal foil (A), Co-NG (B), Co-NG/N (C), and Co-G (D), all measured in air. White dashed lines indicate k value for which intensity maxima is reached. The R axis is not phase corrected. Colour code: Warmer colours indicate higher intensity. All Co SACs exhibit only one*

maximum around 3.3Å^{-1} indicating Co is coordinated to C/N/O and no Co-Co interactions (6.3 Å^{-1}) are present. All wavelets were calculated from 0 to 3Å using k^2 weighting and Morlet parameters of κ=3 and σ=1.

WT analysis was also carried out for EXAFS spectra measured at -0.5V vs RHE (Fig. 29). For Co-NG and Co-G again only one maximum was observed (Fig.29.D and F) showing that the atomic dispersion of Co remains stable under HER conditions and no aggregation occurs. The EXAFS spectrum for Co-NG/N was found to be quite noisy due to significant bubble formation at the free-standing electrode leading to a lower quality WT plot (Fig.29.E). No maximum at 6.6Å^{-1} is observed for Co-NG/N at -0.5V vs RHE proving the absence of metallic cobalt aggregations but a second maximum at 10.5Å^{-1} with a path length of 2.75Å was found (Fig.29.E) the origin of which is yet to be determined.

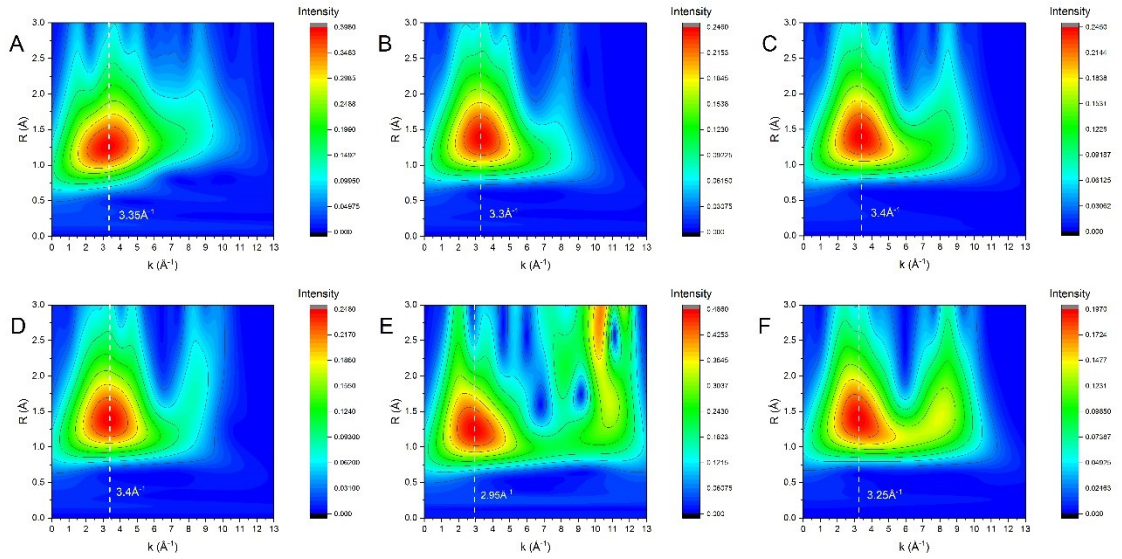


Figure 29: *Overview of wavelet transform of EXAFS of Co SACs in air and at -0.5V vs RHE in 0.5MH_2SO_4. Co-NG in air (A), Co-NG/N in air (B), Co-G in air (C), Co-NG at -0.5V (D), Co-NG/N at -0.5V (E), and Co-G at -0.5V (F).White dashed lines indicate k value for which intensity maxima is reached. The R axis is not phase corrected. Colour code: Warmer colours indicate higher intensity. No Co-Co interactions (6.3 Å^{-1}) are observed for any catalysts. All wavelets were calculated from 0 to 3Å using k^2 weighting and Morlet parameters of κ=3 and σ=1.*

WT analysis is only able to separate contributions to a scattering pathway to within Z±1 making it difficult to conclusively distinguish between scattering from carbon, nitrogen and oxygen. The measured maxima between 3.3 and 3.4 $Å^{-1}$ are close to the calculated values for Co-N, Co-C and Co-O interactions[9], as well as similar to experimental values for cobalt-carbon-nitrogen/oxygen bonds reported in literature[54,57,58].

In summary, WT analysis of Co SACs EXAFS spectra provides further evidence for the atomic dispersion of Co in the material and shows the stability of the single atom metal centres under HER conditions.

5.7 XANES Modelling

5.7.1 Geometry Optimisation with Dmol3

Geometry optimisation of potential active sites of the Co-X_4C_{10}-type were carried out in collaboration with Dr. Diego Gianolio and Dr. Matteo Aramini at Diamond Light Source, Harwell, UK. Dmol3 code within the Materials Studio suite was used to perform calculations with the GGA PBE functional[59]. A graphene-like lattice consisting of 36 carbon atoms was constructed where edge-sites are saturated with hydrogen. The lattice contains a central double vacancy which is filled by a cobalt centre connecting to the lattice by four carbon, nitrogen, or oxygen ligands or a combination thereof. This type of active site is referred to as M-X_4C_{10} arrangement with four ligands in the first and ten carbons in the second coordination shell of the atomically dispersed metal centre.[37,52] This configuration has previously been suggested as a model for atomically dispersed metals on carbon support synthesised via carbon backbone methods and is used as a starting point to determine the active site configuration in the Co SACs. [1,37,51–53]

Figure 30 shows geometry-optimised DFT structures for nine different active site configurations in planar view used as the basis for further calculations. In all structures an average C-C distance of around 1.42Å was found to agree well with the carbon bond length in graphene.[60] Co-X distances varied across structures and ligand type with Co-C bond length between 1.86 to 1.94Å, Co-N bond length between 1.86 to 1.92Å, and Co-O bond length between 1.92 to 1.94Å. Interestingly, all structures were found to be planar with the notable exception of Co-C_4 (Fig.30.B) which exhibits a curved distortion of the carbon lattice with an axial displacement of the Co out of the C_4 plane by around 0.4Å.

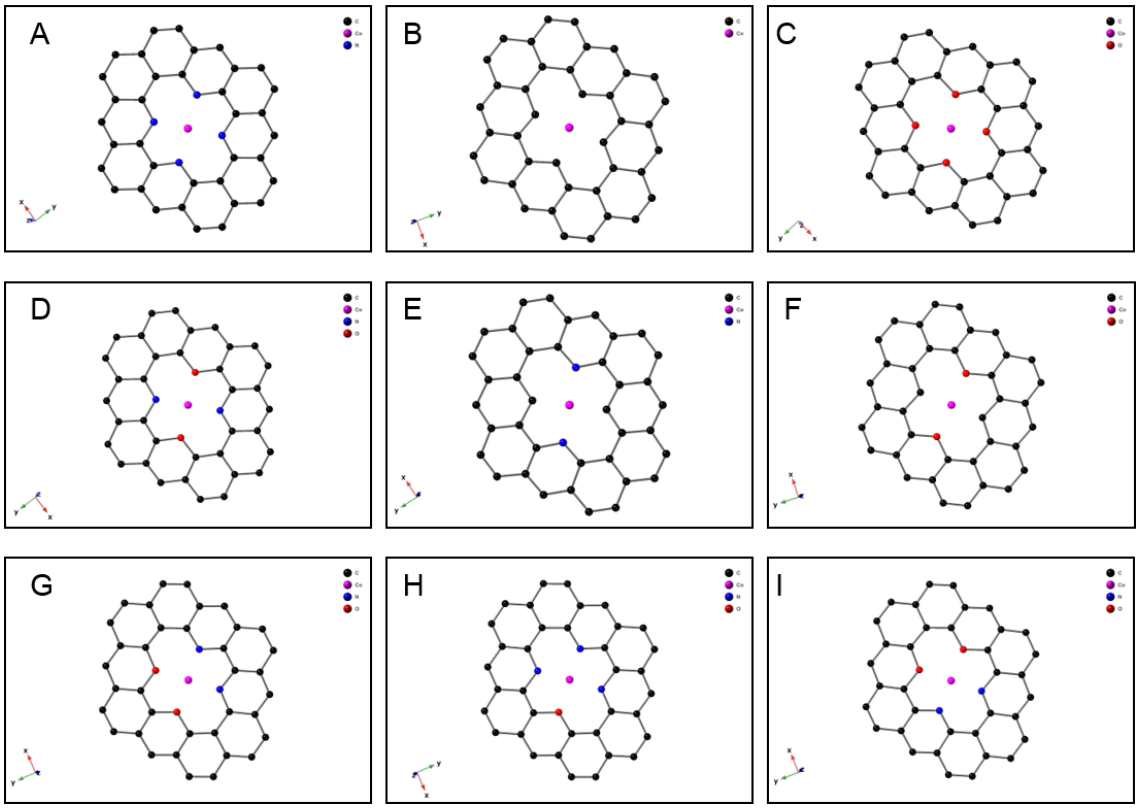


Figure 30: *Overview of geometry-optimised DFT structures based on the CoX_4C_{10} active site (X=N, O, C). Co-N_4 (A), Co-C_4 (B), Co-O_4 (C), Co-N_2O_2 across (D), Co-C_2N_2 across(E), Co-C_2O_2 (F), Co-C_2O_2 across (F), Co-N_2O_2 cis-connected via 2 carbons (G), Co-N_3O (H), and Co-N_2O_2 cis-connected via 3 carbons (I). Colour code: CPK with carbon (black), cobalt (pink), nitrogen (blue) and oxygen (red). Hydrogens terminating the 16 outwards facing carbons are not shown.*

These nine active sites were used to further calculate the structures with potential axial adsorbates attached. Adsorbates include: single O_2, two O_2, double-bonded O, OH, and H. Significant structural distortion to the square planar coordination environment of the Co centres was observed for all modelled active sites upon attachment of adsorbates, with the exception of Co-N_4. This is illustrated in Figure 31 for the attachment of double bonded oxygen to selected Co-X_4 configurations. Co-N_4=O only exhibits a small axial displacement of the Co from the N_4 plane of around 0.18Å compared to the free Co-N_4 site and the carbon lattice remains planar (Fig.31.A). For other coordination environments significantly larger Co displacements are observed (up to 1.4Å for Co-O_4. Fig.31.B). Furthermore, forming a Co=O bond leads to distortion of the carbon lattice as well as axial displacement of the cobalt centre in mixed element first coordination shell active sites (Fig.31.C-D).

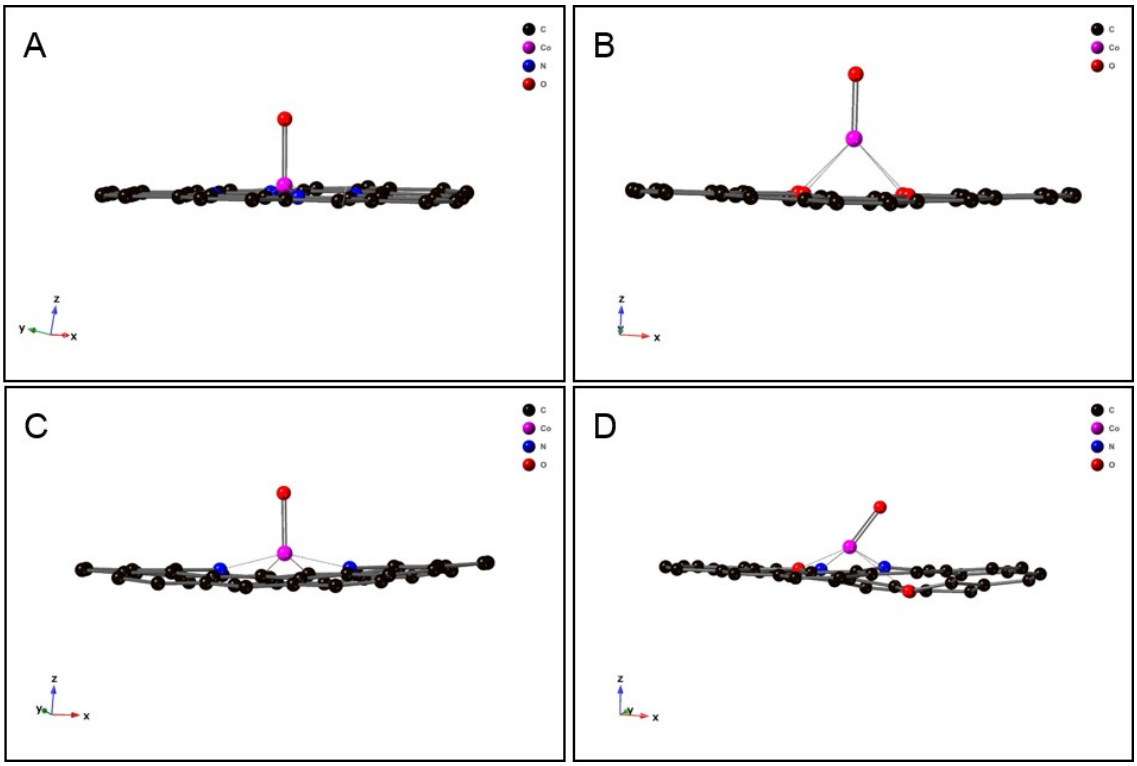


Figure 31: *Selected Co-X_4C_{10} sites (X=N, O, C) with doubly bonded oxygen axially attached to the cobalt. Co-N_4=O (A), Co-O_4=O (B), Co-C_2N_2=O across (C), Co-N_2O_2=O across (D). Colour code: CPK with carbon (black), cobalt (pink), nitrogen (blue) and oxygen (red). Hydrogens terminating the 16 outward facing carbons are not shown.*

DFT calculations show that change in elemental composition of the first coordination shell in CoX_4C_{10}-type active sites leads to significant structural changes from the initial square planar Co-X_4 centres upon adsorbate binding. The effect of such changes on X-ray absorption spectra will be simulated in the following section to help identify the active sites present in the three Co SACs.

5.7.2 Confirmation of Peak Assignment using FEFF9

Initial XANES simulation were performed with the FEFF9 code within the JFEFF suite.[61,62] FEFF9 is an ab-initio multiple scattering code based on the muffin-tin approximation.

In FEFF it is possible to simulate the XANES spectrum of a material under differently polarised X-ray radiation and as such carry out virtual polarisation experiments. Figure 32 illustrates this for Co-N_4-H simulating XANES spectra for z- and xy-polarised X-rays. Interestingly, feature b and c are only present under z-polarised X-ray radiation (red trace) whereas feature d and e only appear in the simulated xy-polarised spectrum (blue trace). This confirms our previous assignment of feature b and c as a 1s → $4p_z$ + LMCT and 1s → $4p_z$ transitions, respectively, and feature d and e as 1s → $4p_{xy}$ + LMCT and 1s → $4p_{xy}$ transitions, respectively. Feature a is not observed in the simulated XANES spectrum.

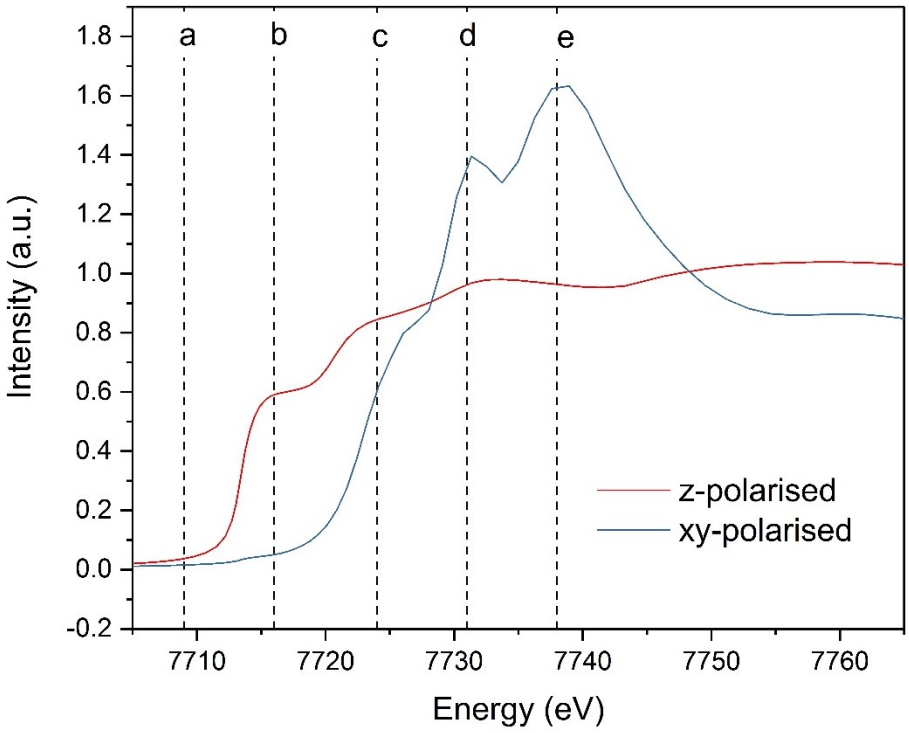


Figure 32: *Simulated polarised XANES spectra for Co-N_4-H. Dotted lines show five main features observed in the experimental XANES spectra of Co SACs. Feature d and e were slightly upshifted by 3eV. Colour code: z-polarisation (red) and xy-polarisation (blue).*

5.7.3 The Effect of Coordination Sphere Composition and Geometry on XANES spectra assessed using CASTEP

Feature b, the 1s → $4p_z$ + LMCT transition, is often described as a fingerprint feature for a square planar bonding arrangement of the cobalt. XANES modelling using the CASTEP code[63] as part of the MS suite confirmed this hypothesis showing strong peaks around 7716eV for all Co-X_4C_{10} model active sites with square planar coordination. Upon distortion of the square planar geometry by bonding of axial ligands, feature b, was significantly reduced in the resulting simulated XANES spectra. Figure 33 illustrates this for Co-N_4 (dark blue trace) which exhibits a strong feature b. When molecular oxygen is introduced as an axial ligand (light blue trace) coordination geometry changes to square pyramidal resulting in a significant decrease in feature b. Introduction of a second axial molecular oxygen ligand, trans to the first one, (olive trace) leads to a distorted octahedral coordination environment and a further reduction in feature b.

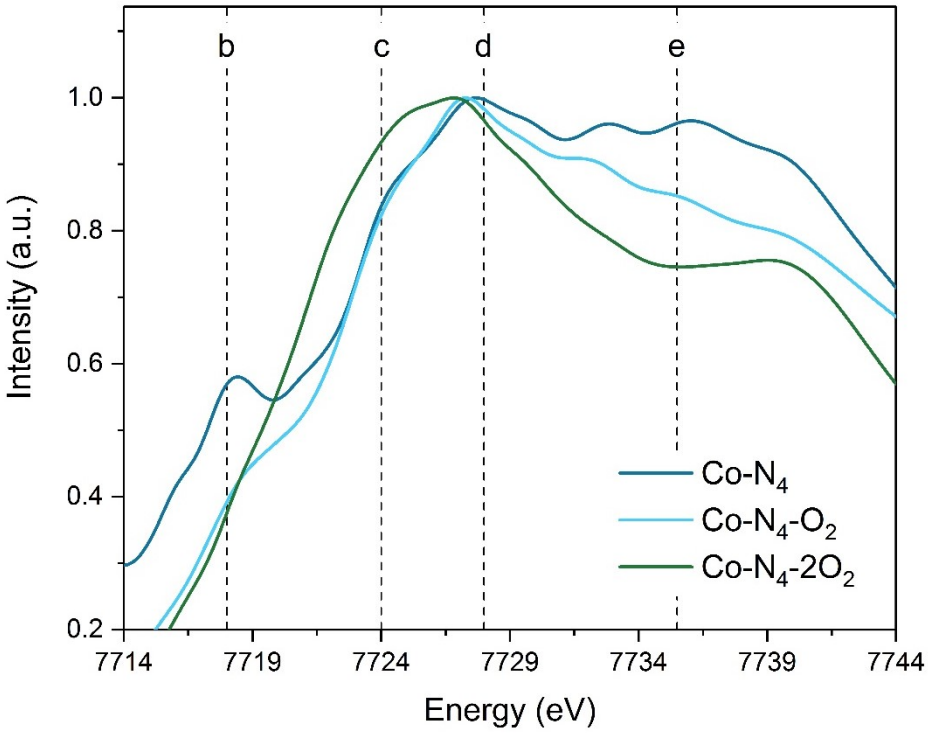


Figure 33: *Influence of coordination geometry on the 1s → 4p$_z$ + LMCT (feature b). Dotted lines show five main features observed in the experimental XANES spectra of Co SACs. Feature b was slightly upshifted by 2eV. Colour code: Co-N$_4$ (dark blue), Co-N$_4$-O$_2$ (light blue), and Co-N$_4$-2O$_2$ (green).*

The effect of increased presence of oxygen in the first coordination sphere is outlined for square planar active site configurations in Figure 34. More oxygen ligands around the Co absorber lead to an increase in the ratio of feature d to e (Fig.34.A). It further leads to a downshift of the main white line absorption from feature d (for Co-N$_4$, dark blue trace) towards feature c (for Co-O$_4$) (Fig.34.B). The same trend is observed when the oxygen ligand is in axial position rather than equatorial, which is shown in Figure 33 where the d to e ratio significantly increases upon binding of molecular oxygen and a downshift of the main white line is also observed.

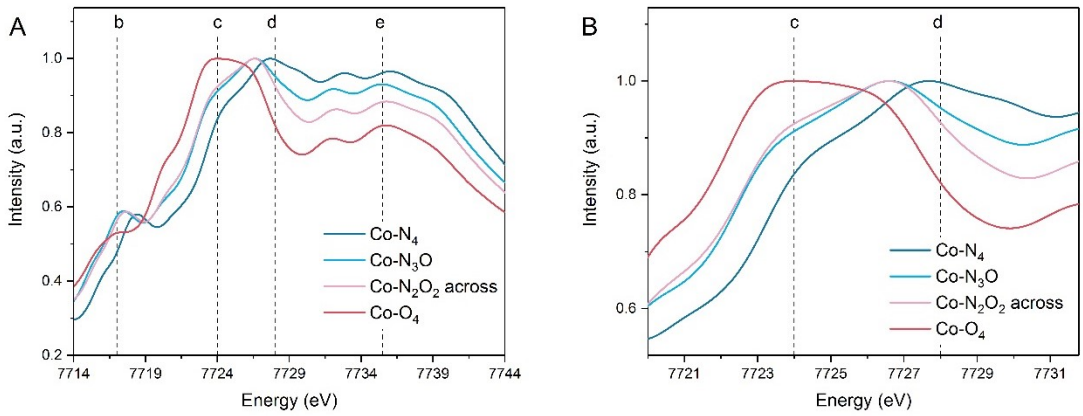


Figure 34: *Influence of oxygen in the first coordination shell on the XANES spectra of square planar Co-X_4C_{10} model active sites. Dotted lines show five main features observed in the experimental XANES spectra of Co SACs. Feature b was slightly upshifted by 2eV. Colour code: Co-N_4 (dark blue), Co-N_3O_1 (light blue), Co-N_2O_2 (light red), and Co-O_4.*

An increase in the ratio of d to e and downshift of the white line are observed in experimental spectra when comparing Co-G and Co-NG/N to the spectrum of Co-NG (Fig.24). Furthermore, Co-G and Co-NG/N exhibit significantly reduced intensity for feature b implying a distortion of square planarity caused by an axial ligand.

Based on these experimental observations and our theoretical investigation above, we propose a Co-N_4 active site for Co-NG. Figure 35 shows the CASTEP simulated XANES spectrum for the Co-N_4C_{10} site (dotted line) in comparison to the experimental XANES spectrum of Co-NG in air (red trace). All features observed in Co-NG are represented in the simulated spectrum of Co-N_4. Feature b is prominent in both spectra and the d/e feature ratio, as well as the position of the individual peaks is similar. The absolute intensities do not match which is likely due to inherent limitations of the CASTEP code.

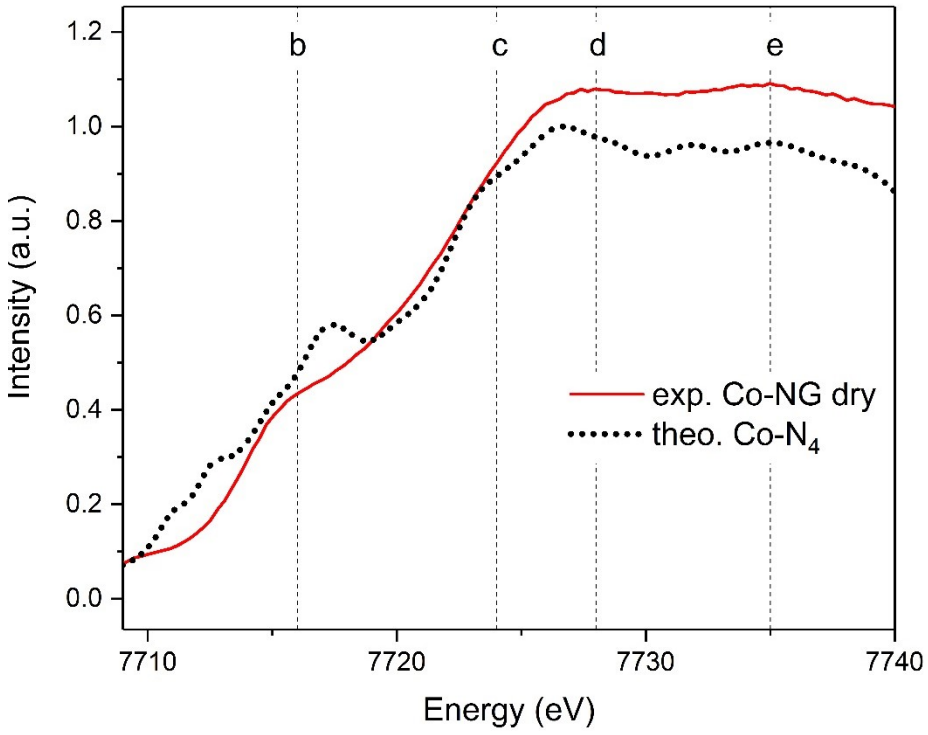


Figure 35: *Experimental XANES spectrum of Co-NG catalyst (red) and simulated XANES spectrum of Co-N_4C_{10} model active site (black dots). Vertical dotted lines show four of the five main features observed in the experimental XANES spectra of Co SACs.*

The downshifted white line features, less prominent feature b and increased d/e ratio for Co-NG/N and Co-G can possibly be explained by the presence of axial ligands and of oxygen in the first coordination shell. We propose active sites of Co-N_2C_2=O or Co-N_4=O type structure for Co-NG/N and Co-G where the axial oxo group is irreversibly attached during the synthesis procedures. Figure 36 provides a comparison between the experimental XANES spectra and CASTEP simulated Co-N_2C_2=O and Co-N_4=O. Co-N_2C_2=O captures all features exhibited in Co-NG/N and Co-G well. As Co-G and Co-NG/N exhibit quite similar XANES spectra, as well as Δμ-spectra, their active sites are believed to be structurally quite similar yet are believed to be distinct based on their HER performance and IR spectroelectrochemical data.

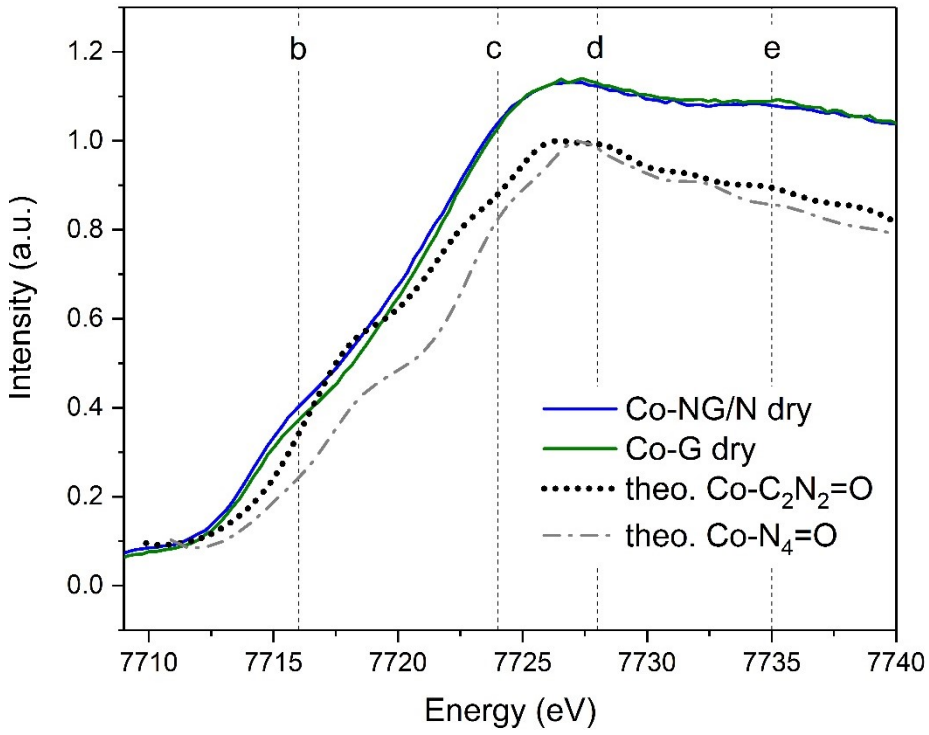


Figure 36: *Experimental XANES spectrum of Co-NG/N (blue) and Co-G (olive), as well as simulated XANES spectrum of Co-N_2C_2=O (black dotted) and Co-N_4=O (grey dash-dotted) model active sites. Vertical dotted lines show four of the five main features observed in the experimental XANES spectra of Co SACs.*

Figures 35 and 36 both show feature b to occur at higher energies in calculations compared to the experiments. As shown before, b is most likely dependent on charge-transfer, a phenomenon which is usually underestimated in DFT[64], yielding a higher energy final state in the CASTEP calculations.

To conclude, using DFT calculations we show that nitrogen as equatorial ligands in the first coordination shell is pivotal in maintaining a quasi-square planar arrangement, shown to be important for HER in Section 6.3.1, upon binding of different adsorbates. Furthermore, FEFF and CASTEP-based XANES simulations confirm feature b occurs indeed due to a 1s → $4p_z$ + LMCT transition and is indicative of a square planar arrangement. Additionally, insights from XANES modelling of different axial ligands

leads us to conclude that Co-NG/N and Co-G contain oxygen species around their active sites probably in the form of an axial oxo ligand. An active site of the type of Co-C_2N_2=O is suggested. The active centre for Co-NG is modelled as Co-N_4.

5.8 Conclusions

The work in this chapter focused on assessing the effect of the coordination environment of atomically dispersed cobalt centres on their HER activity and investigating the role of nitrogen doping in their synthesis and performance. To that end, two different strategies to alter the coordination environment of Co-NG were employed, changing the annealing atmosphere to argon and use of cobalt nitrate as a metal precursor, yielding Co-G and Co-NG/N, respectively. Co-NG, Co-NG/N and Co-G were shown to all consist of atomically dispersed Co on a graphene-like support via XRD, TEM, STEM and XPS.

The three Co SACs displayed significant difference in HER activity with the general trend Co-NG >> Co-NG/N > Co-G. Thiocyanate ions were found to poison Co SACs and were used as a probe in in-situ IR spectroelectrochemistry experiments. It was shown that SCN^- binds to the cobalt centres via nitrogen forming isothiocyanate complexes which remained stable even at potentials as low as -0.5V vs RHE. Hence, we conclusively determine cobalt as the active centre for hydrogen evolution in-situ. Interestingly, the CN-stretch occurred at different wavenumbers for all three Co SACs with the general trend Co-NG < Co-NG/N < Co-G inversely correlating to HER activity. Additionally, a minor Stark shift was only observed for Co-NG/N providing further evidence for each of the Co SACs having a distinct active site. Using the peak area of the CN-stretch, we were able to qualitatively assess the number of active sites of the catalysts showing Co-G to contain only half the amount of Co centres compared to Co-NG and Co-NG/N.

In-situ XAS studies of all three Co SACs were performed. WT analysis of the EXAFS region in air and under operation shows evidence for atomic dispersion of Co to remain stable for all Co SACs. Δμ-analysis of the XANES provided insight into to the geometry of the coordination environment and highlighted the importance of a quasi-square planar arrangement for efficient HER. The structure of the active sites was further clarified using DFT and XANES modelling suggesting Co-NG to contain Co-N_4 active sites, whereas Co-NG/N and Co-G are suggested to accommodate an axial oxo ligand and a mixed composition equatorial ligand sphere. This leads to greater distortion from the optimal coordination geometry and is hypothesised to cause the lower HER activity of Co-NG/N and Co-G. As such, these observations call into question the applicability of the φ factor for predicting HER activity of SACs with a mixed first coordination shell as it only accounts for electronegativity of the ligands and not their geometry.

Using cobalt nitrate as a precursor was previously shown to lead to cobalt nanoparticle formation instead of atomic dispersion on carbon supports.[19–22] Here we were able to form single atom cobalt centres from $Co(NO_3)_2 \bullet 6H_2O$ potentially due to stabilising effects of the preformed graphene oxide carbon backbone inhibiting aggregation of cobalt nitrate and subsequent decomposition and reduction to Co nanoparticles. The nitrate counterions are believed to either covalently attach to the carbon lattice or, when attached to a single Co centre, to decompose during the annealing step to form an oxo ligand, as suggested by the XANES modelling. Hence, we show that for the carbon backbone synthesis method, using nitrates as precursor provides a novel way to change the coordination environment of a metal centre in SACs.

Generally, the role of nitrogen doping in the synthesis and performance of SACs was found to be twofold. During the synthesis it stabilises atomically dispersed Co centres

leading to 2-fold increase in gravimetric active site density after acid leaching compared to samples without active nitrogen doping (Co-G). During turnover, nitrogen around the Co active site was shown by a combination of in-situ XANES and DFT modelling to play an important role in forming and maintaining a square planar coordination environment which is proposed as crucial for efficient HER by Δμ-analysis of in-situ XANES studies.

Overall, we report two strategies to tailor the active sites of SACs while maintaining atomic dispersion. Furthermore, we suggest thiocyanate poisoning experiments coupled with in-situ IR spectroelectrochemistry as a novel way to investigate the type and relative amount of active sites on SACs under HER conditions.

This provides further tools to control the HER activity of single-atom catalysts, which may improve selectivity in reactions where HER competes, such as nitrogen reduction or CO_2 reduction.

5.9 References

(1) Fei, H.; Dong, J.; Arellano-Jiménez, M. J.; Ye, G.; Dong Kim, N.; Samuel, E. L. G.; Peng, Z.; Zhu, Z.; Qin, F.; Bao, J.; et al. Atomic Cobalt on Nitrogen-Doped Graphene for Hydrogen Generation. *Nat. Commun.* **2015**, *6*, 8668. https://doi.org/10.1038/ncomms9668.

(2) Zhang, Y.; Li, W.; Lu, L.; Song, W.; Wang, C.; Zhou, L.; Liu, J.; Chen, Y.; Jin, H.; Zhang, Y. Tuning Active Sites on Cobalt/Nitrogen Doped Graphene for Electrocatalytic Hydrogen and Oxygen Evolution. *Electrochimica Acta* **2018**, *265*, 497–506. https://doi.org/10.1016/j.electacta.2018.01.203.

(3) Zhang, B.; Zhang, J.; Shi, J.; Tan, D.; Liu, L.; Zhang, F.; Lu, C.; Su, Z.; Tan, X.; Cheng, X.; et al. Manganese Acting as a High-Performance Heterogeneous Electrocatalyst in Carbon Dioxide Reduction. *Nat. Commun.* **2019**, *10* (1), 2980. https://doi.org/10.1038/s41467-019-10854-1.

(4) Marcano, D. C.; Kosynkin, D. V.; Berlin, J. M.; Sinitskii, A.; Sun, Z.; Slesarev, A.; Alemany, L. B.; Lu, W.; Tour, J. M. Improved Synthesis of Graphene Oxide. *ACS Nano* **2010**, *4* (8), 4806–4814. https://doi.org/10.1021/nn1006368.

(5) Li, D.; Yu, C.; Wang, M.; Zhang, Y.; Pan, C. Synthesis of Nitrogen Doped Graphene from Graphene Oxide within an Ammonia Flame for High Performance Supercapacitors. *RSC Adv* **2014**, *4* (98), 55394–55399. https://doi.org/10.1039/C4RA10761F.

(6) Xing, Z.; Ju, Z.; Zhao, Y.; Wan, J.; Zhu, Y.; Qiang, Y.; Qian, Y. One-Pot Hydrothermal Synthesis of Nitrogen-Doped Graphene as High-Performance Anode Materials for Lithium Ion Batteries. *Sci. Rep.* **2016**, *6*, 26146. https://doi.org/10.1038/srep26146.

(7) Park, S.; An, J.; Potts, J. R.; Velamakanni, A.; Murali, S.; Ruoff, R. S. Hydrazine-Reduction of Graphite- and Graphene Oxide. *Carbon* **2011**, *49* (9), 3019–3023. https://doi.org/10.1016/j.carbon.2011.02.071.
(8) Shen, J.; Hu, Y.; Shi, M.; Lu, X.; Qin, C.; Li, C.; Ye, M. Fast and Facile Preparation of Graphene Oxide and Reduced Graphene Oxide Nanoplatelets. *Chem. Mater.* **2009**, *21* (15), 3514–3520. https://doi.org/10.1021/cm901247t.
(9) Yang, J.; Liu, H.; Martens, W. N.; Frost, R. L. Synthesis and Characterization of Cobalt Hydroxide, Cobalt Oxyhydroxide, and Cobalt Oxide Nanodiscs. *J. Phys. Chem. C* **2010**, *114* (1), 111–119. https://doi.org/10.1021/jp908548f.
(10) Biesinger, M. C.; Payne, B. P.; Grosvenor, A. P.; Lau, L. W. M.; Gerson, A. R.; Smart, R. S. C. Resolving Surface Chemical States in XPS Analysis of First Row Transition Metals, Oxides and Hydroxides: Cr, Mn, Fe, Co and Ni. *Appl. Surf. Sci.* **2011**, *257* (7), 2717–2730. https://doi.org/10.1016/j.apsusc.2010.10.051.
(11) Behazin, M.; Biesinger, M. C.; Noël, J. J.; Wren, J. C. Comparative Study of Film Formation on High-Purity Co and Stellite-6: Probing the Roles of a Chromium Oxide Layer and Gamma-Radiation. *Corros. Sci.* **2012**, *63*, 40–50. https://doi.org/10.1016/j.corsci.2012.05.007.
(12) Shao, Y.; Zhang, S.; Engelhard, M. H.; Li, G.; Shao, G.; Wang, Y.; Liu, J.; Aksay, I. A.; Lin, Y. Nitrogen-Doped Graphene and Its Electrochemical Applications. *J. Mater. Chem.* **2010**, *20* (35), 7491. https://doi.org/10.1039/c0jm00782j.
(13) Wang, H.; Maiyalagan, T.; Wang, X. Review on Recent Progress in Nitrogen-Doped Graphene: Synthesis, Characterization, and Its Potential Applications. *ACS Catal.* **2012**, *2* (5), 781–794. https://doi.org/10.1021/cs200652y.
(14) Yang, G.; Hu, H.; Zhou, Y.; Hu, Y.; Huang, H.; Nie, F.; Shi, W. Synthesis of One-Molecule-Thick Single-Crystalline Nanosheets of Energetic Material for High-Sensitive Force Sensor. *Sci. Rep.* **2012**, *2* (1), 698. https://doi.org/10.1038/srep00698.
(15) Hueso, J. L.; Espinós, J. P.; Caballero, A.; Cotrino, J.; González-Elipe, A. R. XPS Investigation of the Reaction of Carbon with NO, O2, N2 and H2O Plasmas. *Carbon* **2007**, *45* (1), 89–96. https://doi.org/10.1016/j.carbon.2006.07.021.
(16) NIST XPS Database, Selected Element Search Result https://srdata.nist.gov/xps/EngElmSrchQuery.aspx?EType=PE&CSOpt=Retri_ex_dat&Elm=N (accessed Sep 10, 2019).
(17) Ehrhardt, C.; Gjikaj, M.; Brockner, W. Thermal Decomposition of Cobalt Nitrato Compounds: Preparation of Anhydrous Cobalt(II)Nitrate and Its Characterisation by Infrared and Raman Spectra. *Thermochim. Acta* **2005**, *432* (1), 36–40. https://doi.org/10.1016/j.tca.2005.04.010.
(18) Małecka, B.; Łącz, A.; Drożdż, E.; Małecki, A. Thermal Decomposition of D-Metal Nitrates Supported on Alumina. *J. Therm. Anal. Calorim.* **2015**, *119* (2), 1053–1061. https://doi.org/10.1007/s10973-014-4262-9.
(19) Wan, G.; Yang, C.; Zhao, W.; Li, Q.; Wang, N.; Li, T.; Zhou, H.; Chen, H.; Shi, J. Anion-Regulated Selective Generation of Cobalt Sites in Carbon: Toward Superior Bifunctional Electrocatalysis. *Adv. Mater.* **2017**, *29* (47), 1703436. https://doi.org/10.1002/adma.201703436.
(20) You, B.; Jiang, N.; Sheng, M.; Drisdell, W. S.; Yano, J.; Sun, Y. Bimetal–Organic Framework Self-Adjusted Synthesis of Support-Free Nonprecious Electrocatalysts for Efficient Oxygen Reduction. *ACS Catal.* **2015**, *5* (12), 7068–7076. https://doi.org/10.1021/acscatal.5b02325.
(21) Deng, J.; Ren, P.; Deng, D.; Bao, X. Enhanced Electron Penetration through an Ultrathin Graphene Layer for Highly Efficient Catalysis of the Hydrogen Evolution Reaction. *Angew. Chem. Int. Ed.* **2015**, *54* (7), 2100–2104. https://doi.org/10.1002/anie.201409524.

(22) Deng, J.; Ren, P.; Deng, D.; Yu, L.; Yang, F.; Bao, X. Highly Active and Durable Non-Precious-Metal Catalysts Encapsulated in Carbon Nanotubes for Hydrogen Evolution Reaction. *Energy Env. Sci* **2014**, *7* (6), 1919–1923. https://doi.org/10.1039/C4EE00370E.
(23) Bard, A. J. *Electrochemical Methods: Fundamentals and Applications*, Second edition.; Wiley: New York ; Chichester, 2001.
(24) Langhus, D. L. Analytical Electrochemistry, 2nd Edition (Wang, Joseph). *J. Chem. Educ.* **2001**, *78* (4), 457. https://doi.org/10.1021/ed078p457.2.
(25) Benck, J. D.; Hellstern, T. R.; Kibsgaard, J.; Chakthranont, P.; Jaramillo, T. F. Catalyzing the Hydrogen Evolution Reaction (HER) with Molybdenum Sulfide Nanomaterials. *ACS Catal.* **2014**, *4* (11), 3957–3971. https://doi.org/10.1021/cs500923c.
(26) Ji, H.; Zhao, X.; Qiao, Z.; Jung, J.; Zhu, Y.; Lu, Y.; Zhang, L. L.; MacDonald, A. H.; Ruoff, R. S. Capacitance of Carbon-Based Electrical Double-Layer Capacitors. Nat Commun 2014, 5 (1), 1–7. https://doi.org/10.1038/ncomms4317.
(27) Acik, M.; Lee, G.; Mattevi, C.; Pirkle, A.; Wallace, R. M.; Chhowalla, M.; Cho, K.; Chabal, Y. The Role of Oxygen during Thermal Reduction of Graphene Oxide Studied by Infrared Absorption Spectroscopy. *J. Phys. Chem. C* **2011**, *115* (40), 19761–19781. https://doi.org/10.1021/jp2052618.
(28) Larciprete, R.; Fabris, S.; Sun, T.; Lacovig, P.; Baraldi, A.; Lizzit, S. Dual Path Mechanism in the Thermal Reduction of Graphene Oxide. *J. Am. Chem. Soc.* **2011**, *133* (43), 17315–17321. https://doi.org/10.1021/ja205168x.
(29) Chen, W.; Yan, L.; Bangal, P. R. Preparation of Graphene by the Rapid and Mild Thermal Reduction of Graphene Oxide Induced by Microwaves. *Carbon* **2010**, *48* (4), 1146–1152. https://doi.org/10.1016/j.carbon.2009.11.037.
(30) Binninger, T.; Fabbri, E.; Kötz, R.; Schmidt, T. J. Determination of the Electrochemically Active Surface Area of Metal-Oxide Supported Platinum Catalyst. *J. Electrochem. Soc.* **2014**, *161* (3), H121–H128. https://doi.org/10.1149/2.055403jes.
(31) Kibsgaard, J.; Chen, Z.; Reinecke, B. N.; Jaramillo, T. F. Engineering the Surface Structure of MoS2 to Preferentially Expose Active Edge Sites for Electrocatalysis. *Nat. Mater.* **2012**, *11* (11), 963–969. https://doi.org/10.1038/nmat3439.
(32) Shao, M.; Odell, J. H.; Choi, S.-I.; Xia, Y. Electrochemical Surface Area Measurements of Platinum- and Palladium-Based Nanoparticles. *Electrochem. Commun.* **2013**, *31*, 46–48. https://doi.org/10.1016/j.elecom.2013.03.011.
(33) Sahraie, N. R.; Kramm, U. I.; Steinberg, J.; Zhang, Y.; Thomas, A.; Reier, T.; Paraknowitsch, J.-P.; Strasser, P. Quantifying the Density and Utilization of Active Sites in Non-Precious Metal Oxygen Electroreduction Catalysts. *Nat. Commun.* **2015**, *6*, 8618. https://doi.org/10.1038/ncomms9618.
(34) Leonard, N. D.; Wagner, S.; Luo, F.; Steinberg, J.; Ju, W.; Weidler, N.; Wang, H.; Kramm, U. I.; Strasser, P. Deconvolution of Utilization, Site Density, and Turnover Frequency of Fe–Nitrogen–Carbon Oxygen Reduction Reaction Catalysts Prepared with Secondary N-Precursors. *ACS Catal.* **2018**, *8* (3), 1640–1647. https://doi.org/10.1021/acscatal.7b02897.
(35) Ju, W.; Bagger, A.; Hao, G.-P.; Varela, A. S.; Sinev, I.; Bon, V.; Roldan Cuenya, B.; Kaskel, S.; Rossmeisl, J.; Strasser, P. Understanding Activity and Selectivity of Metal-Nitrogen-Doped Carbon Catalysts for Electrochemical Reduction of CO2. *Nat. Commun.* **2017**, *8* (1). https://doi.org/10.1038/s41467-017-01035-z.
(36) Liu, J.; Jiao, M.; Lu, L.; Barkholtz, H. M.; Li, Y.; Wang, Y.; Jiang, L.; Wu, Z.; Liu, D.; Zhuang, L.; et al. High Performance Platinum Single Atom Electrocatalyst for Oxygen Reduction Reaction. *Nat. Commun.* **2017**, *8*, 15938. https://doi.org/10.1038/ncomms15938.

(37) Li, J.; Jaouen, F. Structure and Activity of Metal-Centered Coordination Sites in Pyrolyzed Metal–Nitrogen–Carbon Catalysts for the Electrochemical Reduction of O2. *Curr. Opin. Electrochem.* **2018**, *9*, 198–206. https://doi.org/10.1016/j.coelec.2018.03.039.
(38) Sebastián, D.; Serov, A.; Artyushkova, K.; Atanassov, P.; Aricò, A. S.; Baglio, V. Performance, Methanol Tolerance and Stability of Fe-Aminobenzimidazole Derived Catalyst for Direct Methanol Fuel Cells. *J. Power Sources* **2016**, *319*, 235–246. https://doi.org/10.1016/j.jpowsour.2016.04.067.
(39) Malko, D.; Kucernak, A.; Lopes, T. In Situ Electrochemical Quantification of Active Sites in Fe–N/C Non-Precious Metal Catalysts. *Nat. Commun.* **2016**, *7* (1), 13285. https://doi.org/10.1038/ncomms13285.
(40) Chen, L.; Liu, X.; Zheng, L.; Li, Y.; Guo, X.; Wan, X.; Liu, Q.; Shang, J.; Shui, J. Insights into the Role of Active Site Density in the Fuel Cell Performance of Co-N-C Catalysts. *Appl. Catal. B Environ.* **2019**, *256*, 117849. https://doi.org/10.1016/j.apcatb.2019.117849.
(41) Liang, H.-W.; Brüller, S.; Dong, R.; Zhang, J.; Feng, X.; Müllen, K. Molecular Metal–Nx Centres in Porous Carbon for Electrocatalytic Hydrogen Evolution. *Nat. Commun.* **2015**, *6*, 7992. https://doi.org/10.1038/ncomms8992.
(42) Yang, J.; Cai, C.; Li, Y.; Gao, L.; Guo, H.; Wang, B.; Pu, B.; Niu, X. In-Situ Cobalt and Nitrogen Doped Mesoporous Graphitic Carbon Electrocatalyst via Directly Pyrolyzing Hyperbranched Cobalt Phthalocyanine for Hydrogen Evolution Reaction. *Electrochimica Acta* **2018**, *262*, 48–56. https://doi.org/10.1016/j.electacta.2018.01.014.
(43) Ludvigsson, M.; Lindgren, J.; Tegenfeldt, J. FTIR Study of Water in Cast Nafion Films. *Electrochimica Acta* **2000**, *45* (14), 2267–2271. https://doi.org/10.1016/S0013-4686(99)00438-7.
(44) Nakamoto, K. Infrared and Raman Spectra of Inorganic and Coordination Compounds. In *Handbook of Vibrational Spectroscopy*; American Cancer Society, 2006. https://doi.org/10.1002/0470027320.s4104.
(45) Bron, M.; Holze, R. The Adsorption of Thiocyanate Ions at Gold Electrodes from an Alkaline Electrolyte Solution: A Combined in Situ Infrared and Raman Spectroscopic Study. *Electrochimica Acta* **1999**, *45* (7), 1121–1126. https://doi.org/10.1016/S0013-4686(99)00302-3.
(46) McPherson, I. J.; Ash, P. A.; Jones, L.; Varambhia, A.; Jacobs, R. M. J.; Vincent, K. A. Electrochemical CO Oxidation at Platinum on Carbon Studied through Analysis of Anomalous in Situ IR Spectra. *J. Phys. Chem. C* **2017**, *121* (32), 17176–17187. https://doi.org/10.1021/acs.jpcc.7b02166.
(47) Penner-Hahn, J. E. 2.13 - X-Ray Absorption Spectroscopy. In *Comprehensive Coordination Chemistry II*; McCleverty, J. A., Meyer, T. J., Eds.; Pergamon: Oxford, 2003; pp 159–186. https://doi.org/10.1016/B0-08-043748-6/01063-X.
(48) van Bokhoven, J. A.; Lamberti, C. *X-Ray Absorption and X-Ray Emission Spectroscopy: Theory and Applications [Electronic Resource]*; Ebook central; Wiley: West Sussex, England, 2016.
(49) Genovese, C.; Schuster, M. E.; Gibson, E. K.; Gianolio, D.; Posligua, V.; Grau-Crespo, R.; Cibin, G.; Wells, P. P.; Garai, D.; Solokha, V.; et al. Operando Spectroscopy Study of the Carbon Dioxide Electro-Reduction by Iron Species on Nitrogen-Doped Carbon. *Nat. Commun.* **2018**, *9* (1). https://doi.org/10.1038/s41467-018-03138-7.
(50) Alves, M. C. M.; Dodelet, J. P.; Guay, D.; Ladouceur, M.; Tourillon, G. Origin of the Electrocatalytic Properties for Oxygen Reduction of Some Heat-Treated Polyacrylonitrile and Phthalocyanine Cobalt Compounds Adsorbed on Carbon Black as Probed by Electrochemistry and x-Ray Absorption Spectroscopy. *J. Phys. Chem.* **1992**, *96* (26), 10898–10905. https://doi.org/10.1021/j100205a054.

(51) Jia, Q.; Ramaswamy, N.; Hafiz, H.; Tylus, U.; Strickland, K.; Wu, G.; Barbiellini, B.; Bansil, A.; Holby, E. F.; Zelenay, P.; et al. Experimental Observation of Redox-Induced Fe–N Switching Behavior as a Determinant Role for Oxygen Reduction Activity. *ACS Nano* **2015**, *9* (12), 12496–12505. https://doi.org/10.1021/acsnano.5b05984.
(52) Fei, H.; Dong, J.; Feng, Y.; Allen, C. S.; Wan, C.; Volosskiy, B.; Li, M.; Zhao, Z.; Wang, Y.; Sun, H.; et al. General Synthesis and Definitive Structural Identification of MN4C4 Single-Atom Catalysts with Tunable Electrocatalytic Activities. *Nat. Catal.* **2018**, *1* (1), 63–72. https://doi.org/10.1038/s41929-017-0008-y.
(53) Jia, Q.; Liu, E.; Jiao, L.; Pann, S.; Mukerjee, S. X-Ray Absorption Spectroscopy Characterizations on PGM-Free Electrocatalysts: Justification, Advantages, and Limitations. *Adv. Mater.* **2018**, 1805157. https://doi.org/10.1002/adma.201805157.
(54) Timoshenko, J.; Kuzmin, A. Wavelet Data Analysis of EXAFS Spectra. *Comput. Phys. Commun.* **2009**, *180* (6), 920–925. https://doi.org/10.1016/j.cpc.2008.12.020.
(55) Funke, H.; Chukalina, M. Wavelet Analysis of EXAFS Data - First Studies. FZR Annu. Rep. 2001, 45.
(56) Funke, H.; Scheinost, A. C.; Chukalina, M. Wavelet Analysis of Extended X-Ray Absorption Fine Structure Data. *Phys. Rev. B* **2005**, *71* (9), 094110. https://doi.org/10.1103/PhysRevB.71.094110.
(57) Zhang, H.; Zhou, W.; Chen, T.; Guan, B. Y.; Li, Z.; Lou, X. W. (David). A Modular Strategy for Decorating Isolated Cobalt Atoms into Multichannel Carbon Matrix for Electrocatalytic Oxygen Reduction. *Energy Environ. Sci.* **2018**, *11* (8), 1980–1984. https://doi.org/10.1039/C8EE00901E.
(58) Han, Y.; Wang, Y.-G.; Chen, W.; Xu, R.; Zheng, L.; Zhang, J.; Luo, J.; Shen, R.-A.; Zhu, Y.; Cheong, W.-C.; et al. Hollow N-Doped Carbon Spheres with Isolated Cobalt Single Atomic Sites: Superior Electrocatalysts for Oxygen Reduction. *J. Am. Chem. Soc.* **2017**, *139* (48), 17269–17272. https://doi.org/10.1021/jacs.7b10194.
(59) Delley, B. From Molecules to Solids with the DMol3 Approach. *J. Chem. Phys.* **2000**, *113* (18), 7756–7764. https://doi.org/10.1063/1.1316015.
(60) Meyer, J. C.; Geim, A. K.; Katsnelson, M. I.; Novoselov, K. S.; Booth, T. J.; Roth, S. The Structure of Suspended Graphene Sheets. *Nature* **2007**, *446* (7131), 60–63. https://doi.org/10.1038/nature05545.
(61) J. Rehr, J.; J. Kas, J.; D. Vila, F.; P. Prange, M.; Jorissen, K. Parameter-Free Calculations of X-Ray Spectra with FEFF9. *Phys. Chem. Chem. Phys.* **2010**, *12* (21), 5503–5513. https://doi.org/10.1039/B926434E.
(62) Rehr, J. J.; Kas, J. J.; Prange, M. P.; Sorini, A. P.; Takimoto, Y.; Vila, F. Ab Initio Theory and Calculations of X-Ray Spectra. *Comptes Rendus Phys.* **2009**, *10* (6), 548–559. https://doi.org/10.1016/j.crhy.2008.08.004.
(63) Clark, S. J.; Segall, M. D.; Pickard, C. J.; Hasnip, P. J.; Probert, M. I. J.; Refson, K.; Payne, M. C. First Principles Methods Using CASTEP. *Z. Für Krist. - Cryst. Mater.* **2005**, *220* (5/6). https://doi.org/10.1524/zkri.220.5.567.65075.
(64) Kümmel, S. Charge-Transfer Excitations: A Challenge for Time-Dependent Density Functional Theory That Has Been Met. *Adv. Energy Mater.* **2017**, *7* (16), 1700440. https://doi.org/10.1002/aenm.201700440.

6 Cobalt Molybdenum Nitride for Electrochemical Nitrogen Reduction in Molten Salts

6.1 Background and Objectives 199

6.2 Synthesis 200

6.2.1 Powder 200

6.3 Characterisation 201

6.3.1 XRD 201

6.3.2 TPR 202

6.3.3 XPS 205

6.3.4 TEM 212

6.4 Thermal Ammonia Synthesis 213

6.4.1 Experimental Methods 213

6.4.2 Results and Discussion 213

6.5 Nitrogen Reduction Reaction Testing 214

6.5.1 Experimental Methods 214

6.5.2 Results and Discussion 217

6.6 Conclusions 229

6.7 References 231

6.1 Background and Objectives

Several metal nitride catalyst have shown significant activity for thermal ammonia synthesis and ammonia production via chemical looping.[1,2] Interstitial metal nitrides, especially Cs-promoted Co_3Mo_3N, rank among the best performing ammonia synthesis catalysts and show improved activities compared to the commercial Haber-Bosch Fe-catalyst under mild conditions.[1–4] Recent reports of the Hargreaves group in collaboration with the Catlow group propose a Mars-van Krevelen-type mechanism for Co_3Mo_3N where lattice nitrogen participates in the reaction.[5–7] Furthermore, the Hargreaves group found the lattice nitrogen to be mobile within Co_3Mo_3N.[8,9] It was shown that when treated in 3:1 H_2/Ar at 400°C lattice nitrogen of Co_3Mo_3N is lost in form of NH_3 and N_2 while the more reduced η-12 Co_6Mo_6N phase is formed.[9,9,10] This phase consists of the same cubic metal lattice as Co_3Mo_3N with a slightly smaller lattice parameter (10.88 vs. 11.02Å)[8] but half of the interstitial nitrogen is lost and the other half migrates within the structure from the 16c Wyckoff site to the 8a Wyckoff site.[8,11] In the Wyckoff notation the number stands for the multiplicity, i.e. the number of symmetry-related positions in the unit cell and the letter is a label which is applied successively from the lowest to highest site symmetry. This clearly shows that all lattice nitrogen within the structure is mobile. Furthermore, Co_6Mo_6N can be transformed back into Co_3Mo_3N by treatment in 3:1 H_2/N_2 at 400°C.[9] Strikingly, this transformation occurs in pure N_2 atmosphere as well, with partial recovery of the η-6 phase at 500°C and full regeneration being observed at 700°C.[9] As such, Co_6Mo_6N is able to effectively activate and reductively split dinitrogen in the absence of any external reducing agents such as H_2.

In the following sections it will be investigated if similar behaviour can be observed by making Co_3Mo_3N part of an electrochemical cell and using an applied potential, rather

than H_2, to induce reduction and release of N^{3-} ions. As outlined earlier, LiCl/KCl eutectics are able to stabilise N^{3-} in solution, and may therefore facilitate the reduction. Subsequent reaction of the N^{3-} with H_2 or another source of protons to form NH_3, and of Co_6Mo_6N or similar reduced cobalt molybdenum phases with N_2 to reform Co_3Mo_3N, would then constitute an (electro)catalytic cycle for the production of NH_3 via a Mars-van Krevelen type mechanism.

6.2 Synthesis

6.2.1 Powder

A synthesis method by Markel et al. developed for the synthesis of high surface area Mo_2N[12] was adapted for the synthesis of Co_3Mo_3N. Figure 1 provides a pictorial overview of the synthesis procedure.

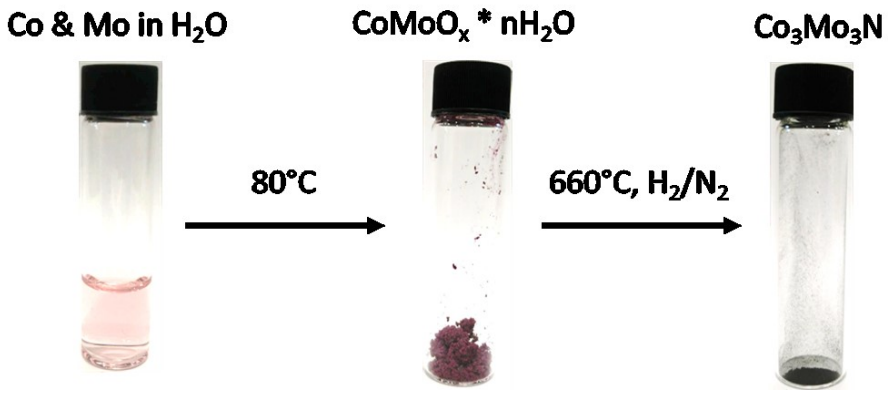


Figure 1: *Overview of steps in the synthesis of cobalt molybdenum nitride.*

Cobalt molybdenum nitride was synthesised by dissolving equimolar amounts of $Co(NO_3)_2 \cdot 6H_2O$ (1.82g) (Sigma-Aldrich, 10026-22-9) and $(NH_4)_6Mo_7O_{24} \cdot 4H_2O$ (1.11g) (Sigma-Aldrich, 12054-85-2) in 50mL Milli-Q water. The solvent was evaporated under constant stirring and the resulting purple solid was dried at 80°C for several hours yielding a dark red powder. Around 1g of the resulting oxide precursor was

placed inside a quartz furnace boat and transferred into a furnace tube. The sample was nitrided in 100mL min^{-1} 5.5:1 H_2/N_2 heating to 660°C with a ramp rate of 0.6°C min^{-1} in a split tube furnace connected to a paraffin bubbler. The sample was held at 660°C for 2h and then cooled down to room temperature at 5°C min^{-1} under 100mL min^{-1} N_2 flow. After reaching room temperature, the sample was passivated by stopping the N_2 flow, disconnecting the bubbler and letting air diffuse into the tube for 24h.

The synthesis of Co_3Mo_3N supported on carbon felt via electrodeposition of a CoMo precursor was also attempted and is outlined in Supporting Information 1 in the Appendix including XRD (Fig.A3) and XPS (Fig.A4) characterisation.

6.3 Characterisation

6.3.1 XRD

X-ray diffraction patterns of the synthesised Co_3Mo_3N powder and its precursors were obtained to confirm its successful synthesis. Figure 2 shows XRD patterns for CoMo precursor after drying (black trace) which exhibits a rather amorphous diffraction pattern with one main reflection at around 26°. Upon calcination in air at 400°C the crystalline anhydrous β-$CoMoO_4$ phase is formed (grey trace, JCPDS: 021-0868) confirming that the dried amorphous phase contains equimolar amounts of cobalt and molybdenum. Note that the amorphous phase was used as a precursor directly without a calcination step during Co_3Mo_3N synthesis. The red trace confirms the successful synthesis of the η-6 cobalt molybdenum nitride phase (JCPDS: 01-89-7953). Small impurities of metallic Mo are observed at around 40.7° ((110) peak, JCPDS: 00-001-1207).

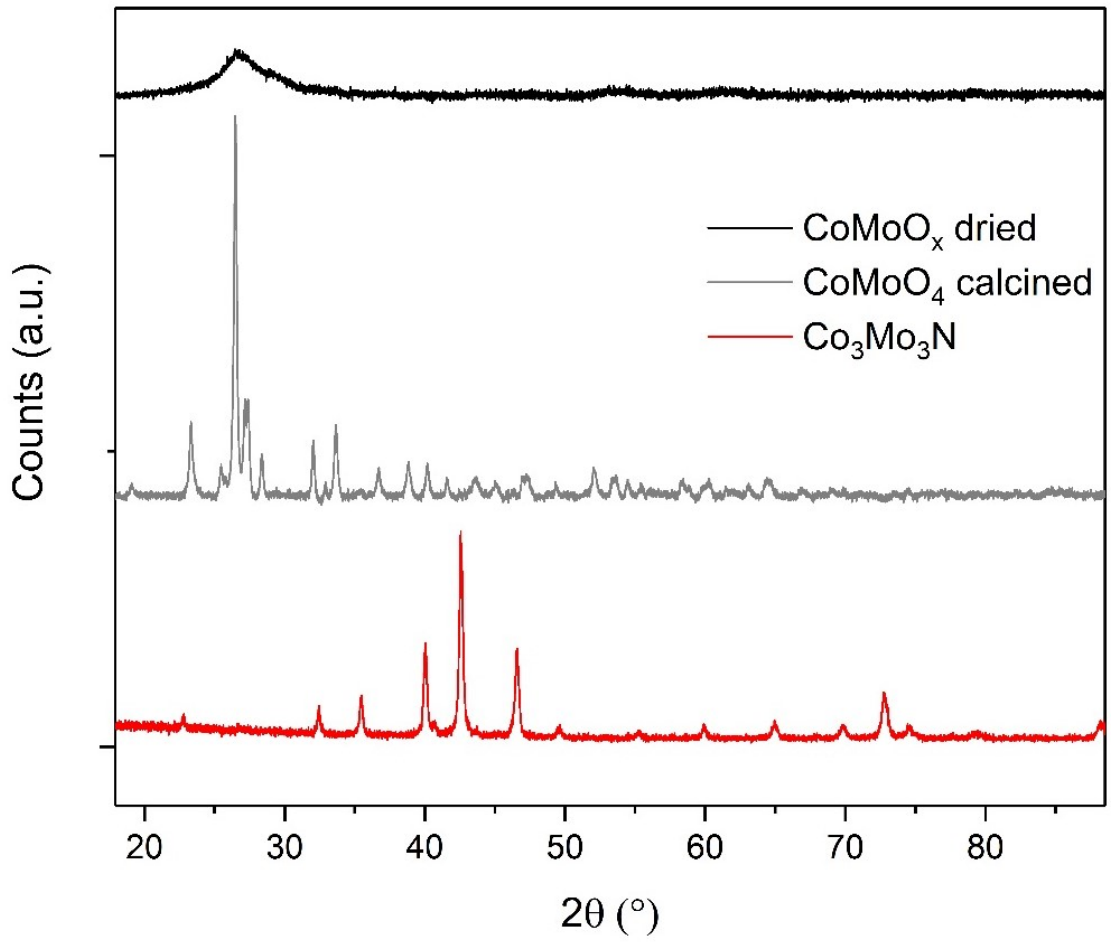


Figure 2: *XRD patterns of Co_3Mo_3N and precursors. Colour code: dried $CoMoO_x$ phase (black), calcined $CoMoO_4$ (grey), and Co_3Mo_3N (red).*

6.3.2 TPR

To investigate the reactivity of the lattice nitrogen in Co_3Mo_3N, temperature-programmed reduction of a Co_3Mo_3N powder sample was carried out under pure H_2 flow heating to 800°C at 10°C min^{-1}. Figure 3.A compares the XRD patterns of as-prepared Co_3Mo_3N (black trace) and of the sample post TPR procedure (red trace). All main η-6 Co_3Mo_3N phase reflections are conserved but shifted towards higher 2θ values. This is in line with previous reports on the formation of the nitrogen-deficient η-12 Co_6Mo_6N phase which has a smaller unit cell volume compared to the η-6 phase.[8,9,11,13] Furthermore, from the TCD signal curve shown in Figure 3.B significant evolution of gas can be observed

starting at 655°C, consistent with the loss of N_2 and NH_3. This is congruent with studies by Mckay et al. showing ammonia formation when Co_3Mo_3N samples are treated in H_2/Ar mixtures at 400°C after 30 minutes of stabilisation.[8,10] They observed a further increase in rate of ammonia formation when the sample was heated to 600°C and 700°C in line with our observation. [10] The initial decrease in TCD signal observed for temperatures up to 200°C can be assigned to loss of adsorbed water and ammonia from the catalyst.

From the observations above it can be inferred that it is indeed possible to form the Co_6Mo_6N phase from Co_3Mo_3N, as previously reported in literature[8–11] and that as such the lattice nitrogen within Co_3Mo_3N is mobile.

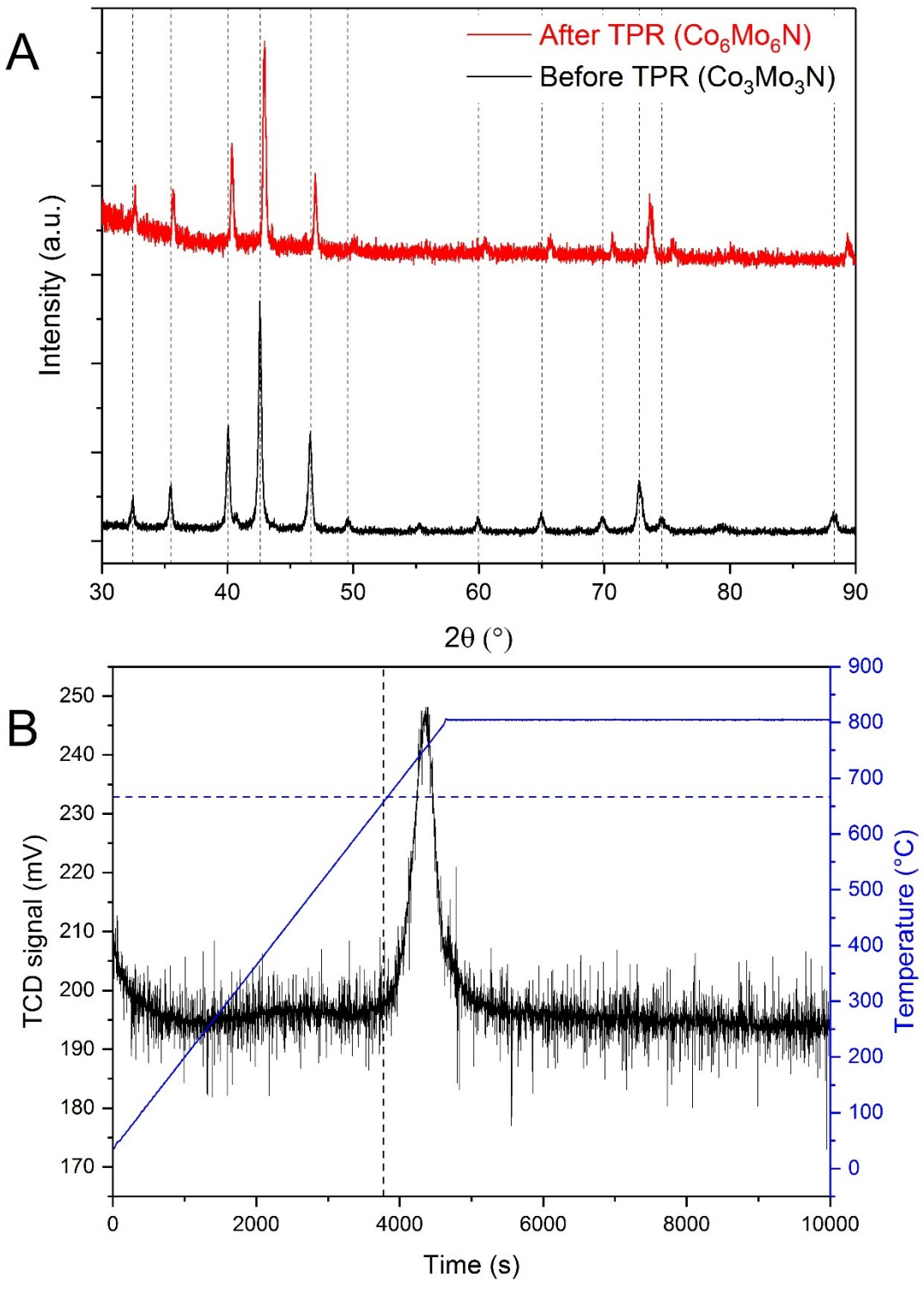


Figure 3: *Temperature programmed reduction of Co_3Mo_3N. (A) shows XRD pattern of catalyst before (black) and after (red) TPR under H_2 flow up to 800°C. (B) plots the TCD signal (black) and temperature (blue) vs time for Co_3Mo_3N. Dashed lines indicate onset of signal in TCD.*

6.3.3 XPS

For details about the XPS acquisition and peak fitting procedure, refer to Chapter 3 Section 1.2.

XPS was carried out to investigate the elemental composition of the cobalt molybdenum nitride materials, as well as investigate the structure of the surface versus the bulk using Ar sputtering experiments.

Figure 4 shows the Co2p region of Co_3Mo_3N before (A) and after Ar sputtering (B). Ar sputtering is used to remove the top layer of material, which is believed to be an oxide layer formed during the passivation procedure, and expose the underlying bulk structure. Overall both spectra show the presence of Co(0), Co(II), Co(II) satellite and Co(III) features at peak positions coherent with values reported in literature.[14,15] Fig.4.B shows a clear increase of peaks around 778eV and 793eV (red traces) compared to the spectrum of passivated Co_3Mo_3N. The peaks are assigned as $Co2p_{3/2}$ and $Co2p_{1/2}$ of Co^0, respectively. The peak splitting of around 15eV, as well as the position of the $Co2p_{3/2}$ peak, agree nicely with the reported values for metallic cobalt of 14.99eV and 778.1eV.[14,15] Furthermore, a small decrease in peak height is observed for peaks attributed to $Co2p_{3/2}$ and $Co2p_{1/2}$ of Co(III) at around 783eV and 298eV, respectively.

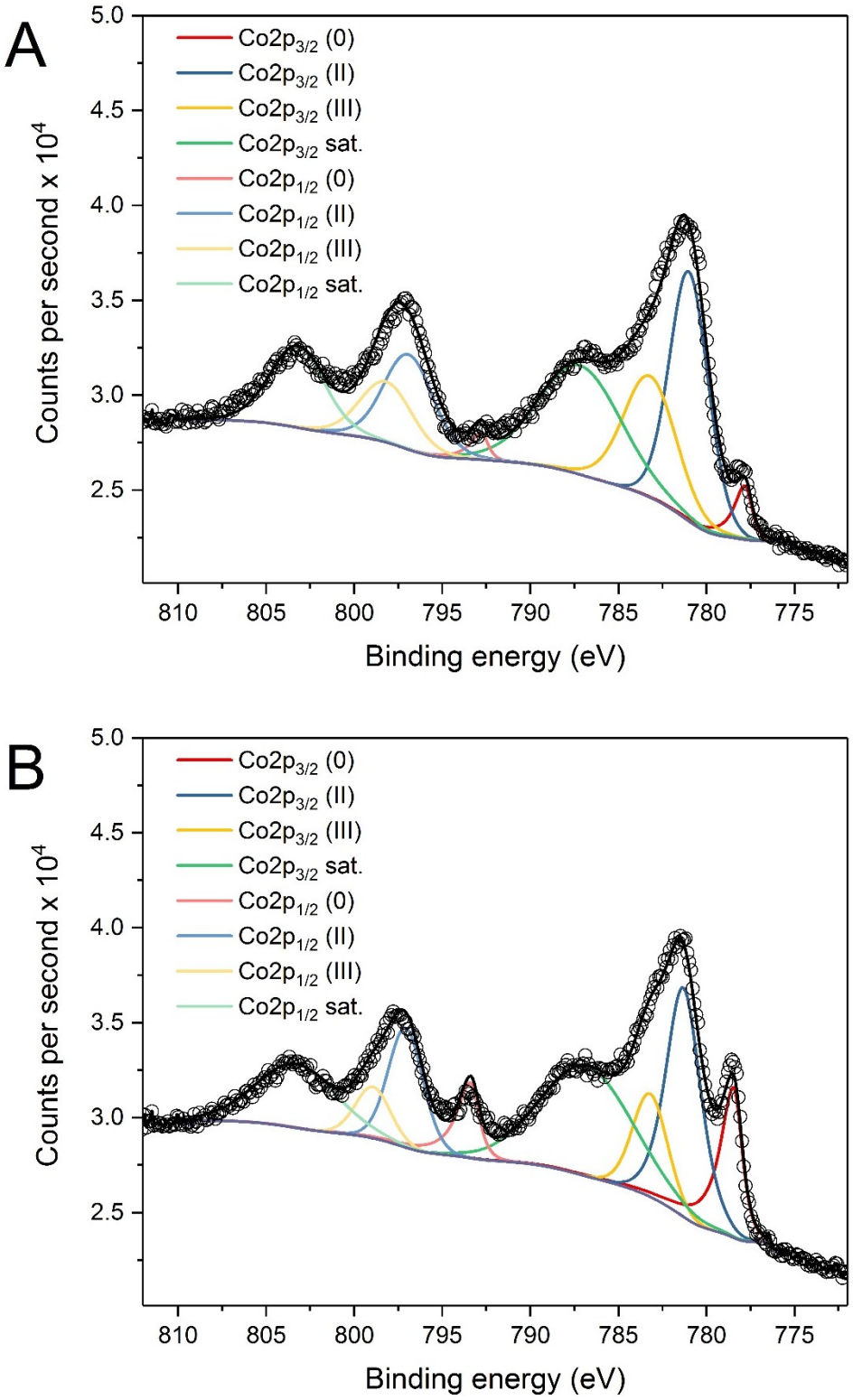


Figure 4: *High-resolution Co2p spectra of Co_3Mo_3N before (A) and after removal of top oxide layer with Ar sputtering (B). Colour code: metallic $Co2p_{3/2}$ (red), +II $Co2p_{3/2}$ (blue), +III $Co2p_{3/2}$ (yellow),+II $Co2p_{3/2}$ satellite (green). The black line, purple line and empty black circles, respectively represent the overall fit, background, and data points. Faint coloured traces represent corresponding $Co2p_{1/2}$ peaks.*

Figure 5 shows the Mo3d region of Co_3Mo_3N before (A) and after Ar sputtering (B). In both cases a complex spectrum is observed similar to previously reported Mo3d regions of molybdenum containing metal nitride catalysts.[13,16,17] Peaks for Mo(0), Mo(IV), Mo(V), as well as Mo(VI) were found to fit the spectra with peak positions in accordance with a literature and with spin-orbit splittings close to the reported value of 3.15eV.[15,18]

Similar to the Co2p case, an increase in height of peaks at 227.5eV and 230.8eV assigned as the $3d_{5/2}$ and $3d_{1/2}$ contributions of metallic Mo is observed for the Ar sputtered sample (Fig.5.B). Concomitantly, increased contribution of the $3d_{5/2}$ and $3d_{1/2}$ peaks of Mo(IV) (blue trace) are observed at 229.9eV and 232.9eV, respectively, is observed while in contrast to the passivated Co_3Mo_3N sample no Mo(VI) is detected.

High-resolution spectra of the N1s region are shown in Figure 6. Unfortunately, it overlaps with the Mo3p region significantly impairing the quantification of nitrogen in Mo-containing nitrides using XPS, worsened by the fact that the relative sensitivity factor of Mo3p is considerably higher than for N1s (8.66 versus 1.8). A small peak at around 398eV can nevertheless be found in the spectra (yellow trace), corresponding to N^{3-},[15,19,20] which slightly increases after Ar sputtering (Fig.6.B). Additionally, post Ar sputtering the peaks identified as Mo(0)[21] at 395.1eV and 412.5eV (red traces) become more prominent. Peaks for Mo(IV) and Mo(VI) were not resolved in the Mo3p region but based on the Mo3d region it is likely that small of amounts of such species exist in the bulk and the oxide surface layer, respectively.

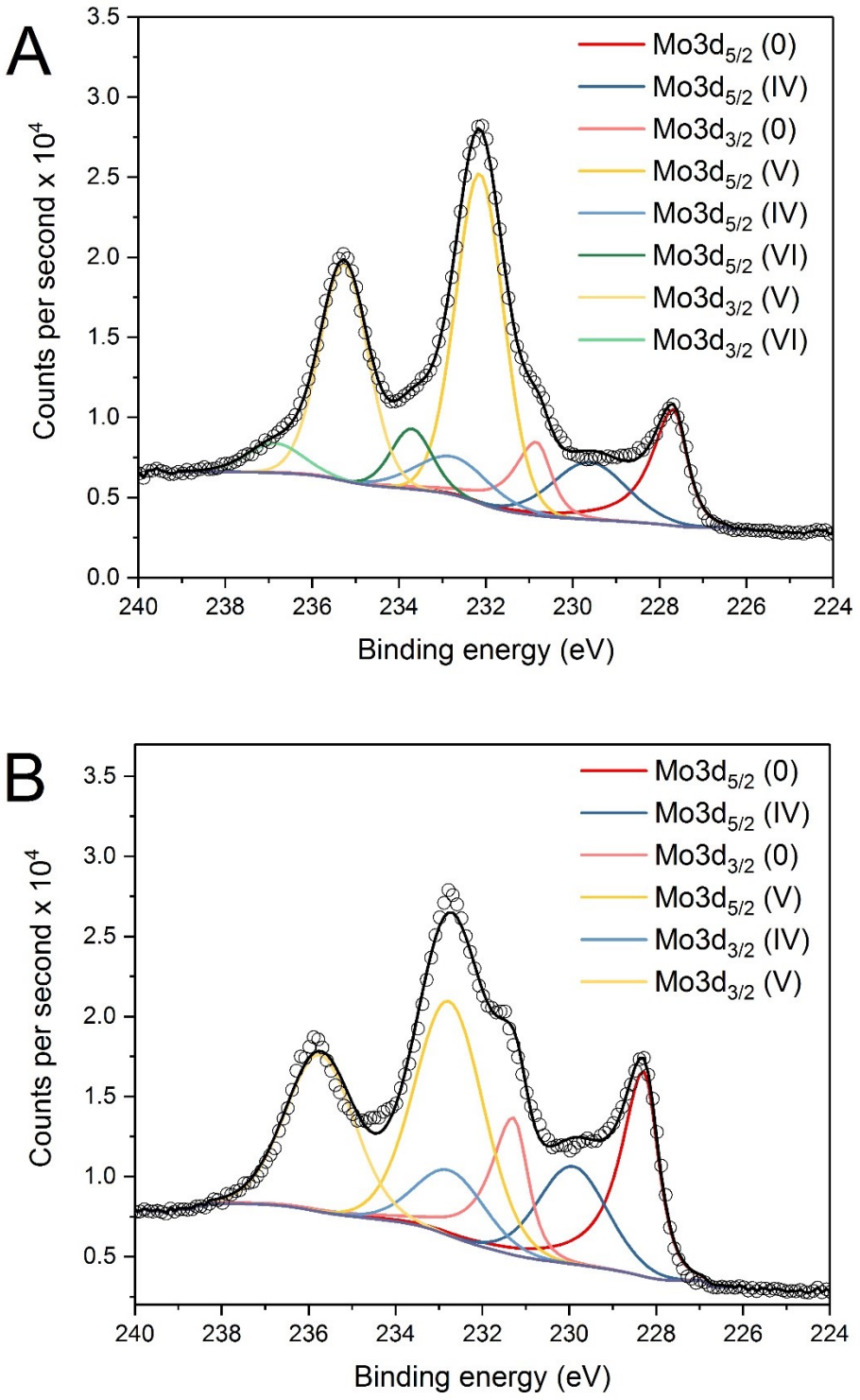


Figure 5: *High-resolution Mo3d spectra of Co_3Mo_3N before (A) and after removal of top oxide layer with Ar sputtering (B). Colour code: metallic $Mo3d_{5/2}$ (red), +IV $Mo3d_{5/2}$ (blue), +V $Mo3d_{5/2}$ (yellow),+VI $Mo3d_{5/2}$ (green). The black line, purple line and empty black circles, respectively represent the overall fit, background, and data points. Faint coloured traces represent corresponding $Mo3d_{3/2}$ peaks.*

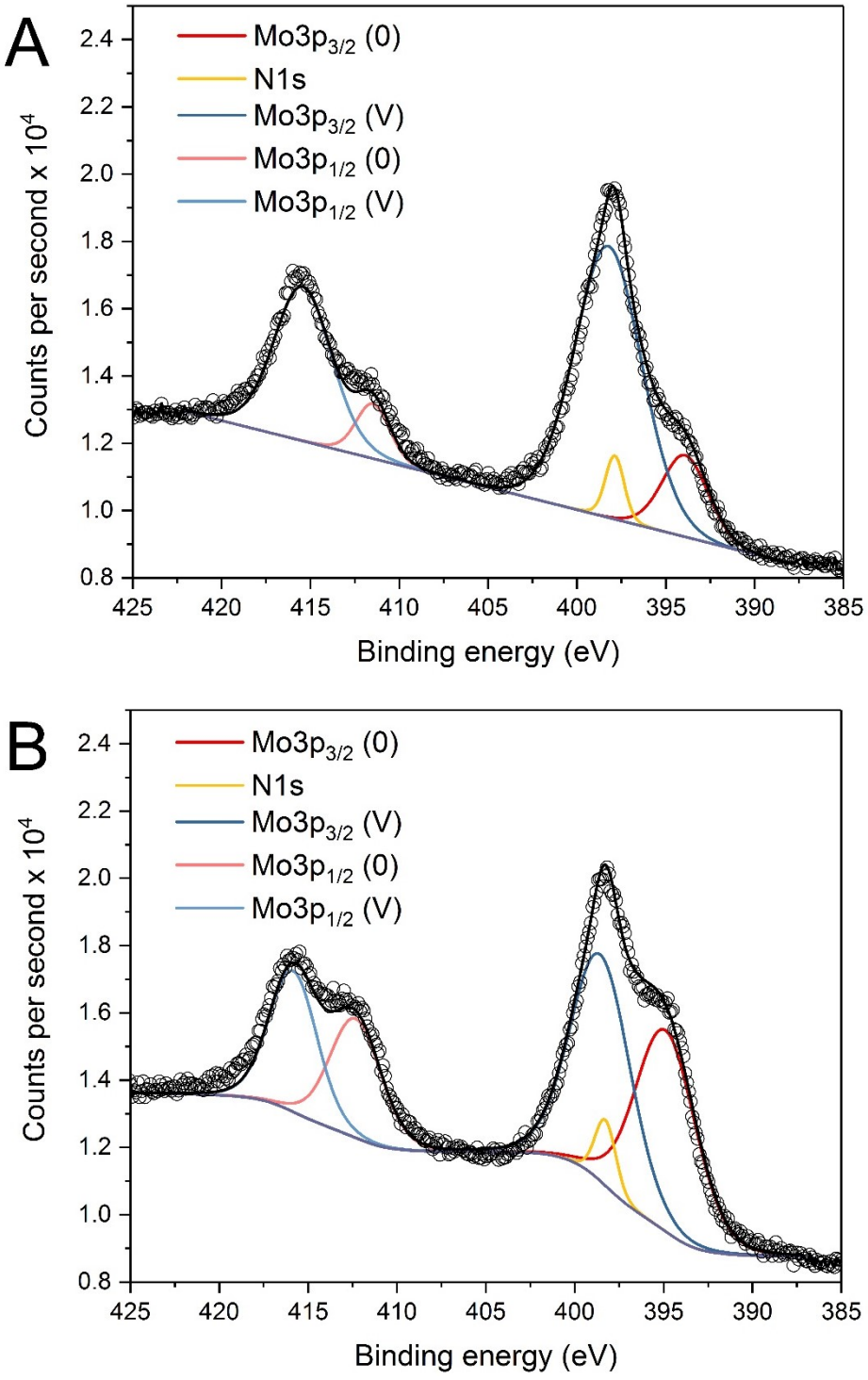


Figure 6: *High-resolution Mo3p/N1s spectra of Co_3Mo_3N before (A) and after removal of top oxide layer with Ar sputtering (B). Colour code: metallic $Mo3p_{3/2}$ (red), +V $Mo3p_{3/2}$ (blue), and N1s (yellow). The black line, purple line and empty black circles, respectively represent the overall fit, background, and data points. Faint coloured traces represent corresponding $Mo3p_{1/2}$ peaks.*

Figure 7 further shows the O1s region before (A) and after Ar sputtering (B). Generally, two peaks are needed to obtain a good fit at around 230.6eV and 232.0eV, corresponding to O^{2-} (red trace) and metal hydroxide or carbon-oxygen species (blue trace).[14,22,23] After Ar sputtering a reduction of peak area for the M-OH/C-O peak is observed (Fig.7.B) compared to the spectrum of passivated Co_3Mo_3N (Fig.7.A). This is possibly explained by the removal of hydroxyl groups terminating the oxide surface layer formed during the passivation procedure, as well as a reduction in adventitious carbon containing C-O moieties adsorbed to the surface post Ar sputtering. Further evidence for this explanation is provided by the overall elemental composition shown in Table 1. The carbon content is reduced from roughly 15 to 10at% and the oxygen content drops from 47.4 to 45.7at% following Ar sputtering.

Overall, the presented XPS data are in agreement with the formation of only a thin oxide layer upon passivation. Upon removal of this layer using Ar sputtering, more reduced metal states are observed for Co and Mo. The observed cobalt to molybdenum ratio is close to the expected value of one, and their overall contribution to the elemental composition increases slightly after Ar sputtering from 18.3 to 20.3at%, and 19.1 to 23.5at%, respectively (Table 1). Additionally, indications of an increase in nitrogen content post Ar sputtering are found in the Mo3p/N1s region showing that the η-6 phase observed in XRD indeed corresponds to Co_3Mo_3N. Although a decrease in oxygen content was found, large amounts of oxide remain present in the catalyst even after sputtering which indicates that the formed Co_3Mo_3N phase also contains O in the bulk forming an oxynitride phase. This is a common phenomenon for transition metal nitrides produced via nitridation of metal oxide precursors[2,24] and was expected to occur.

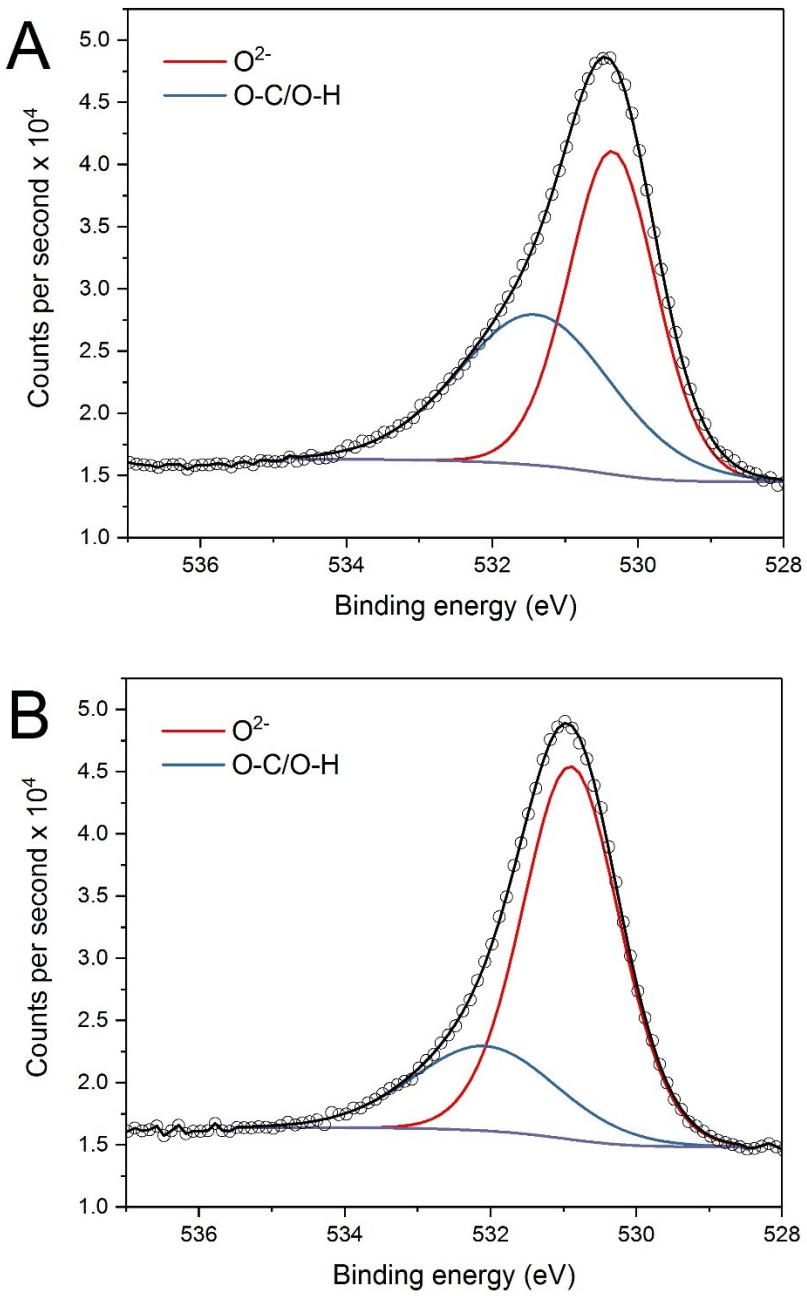


Figure 7: *High-resolution O1s spectra of Co_3Mo_3N before (A) and after removal of top oxide layer with Ar sputtering (B). The black line, purple line and empty black circles, respectively represent the overall fit, background, and data points. Colour code: metal oxide (red) and C-O/metal hydroxide (blue).*

Table 1: *Overview of elemental composition of Co_3Mo_3N powder and Co_xMo_yN/CF deduced from XPS survey scans. Nitrogen content not shown due to the overlap of the N1s and Mo3p region prohibiting its unambiguous quantification using XPS survey scans.*

Element	Oxide surface of Co_3Mo_3N	Bulk Co_3Mo_3N
Co (at%)	18.3	20.3
Mo (at%)	19.1	23.5
O (at%)	47.4	45.7
C (at%)	15.2	10.5

In summary, the presented XPS studies show that only a thin oxide layer is formed on top of the bulk material due to the passivation procedure for Co_3Mo_3N. The underlying bulk material was found to consist of more reduced Co and Mo species but still contains significant amounts of oxygen suggesting that instead of a pure nitride phase, an oxynitride phase is formed. The Co to Mo ratio was found to be close to the expected value of one for Co_3Mo_3N.

6.3.4 TEM

Transmission electron micrographs of as-prepared passivated Co_3Mo_3N were collected. Figure 8 shows representative micrographs in which the typical merged-particle morphology of Co_3Mo_3N is observed with individual cuboid particles of around 20-50nm forming a larger structure. Such morphology was also reported for Co_3Mo_3N prepared via annealing in ammonia atmosphere[16], as well as via the decomposition pathway using HMT[25].

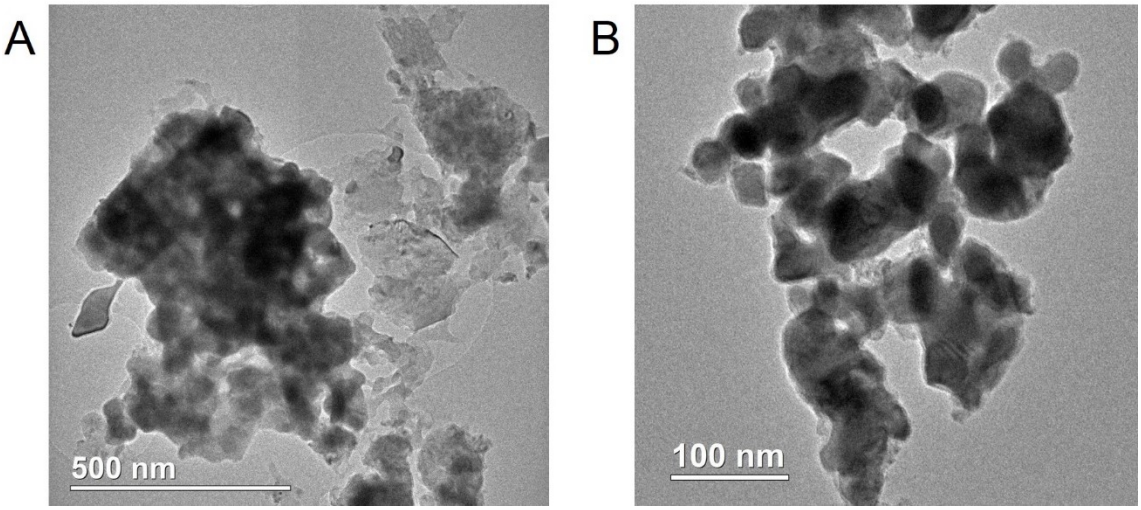


Figure 8: *Bright-field TEM micrograph of Co_3Mo_3N powder at 40000X magnification.*

6.4 Thermal Ammonia Synthesis

In order to further assess the ability of Co_3Mo_3N to activate nitrogen and to compare it to other reported Co_3Mo_3N catalysts, the as-prepared catalyst was tested for its activity in thermal ammonia synthesis.

6.4.1 Experimental Methods

100mg of as-prepared Co_3Mo_3N were packed into a fixed bed reactor. The catalyst was activated at 500°C and atmospheric pressure flowing 3:1 H_2/N_2 at 50mL min^{-1}. Activity testing was carried out for 1h at 470°C and 50bar pressure while flowing 3:1 H_2/N_2 at 50mL min^{-1}. Ammonia was trapped in 1M H_2SO_4 and quantified by titration of the acid solution.

6.4.2 Results and Discussion

An ammonia synthesis rate of 6363µmol $g_{cat.}^{-1}h^{-1}$ was measured at 50bar and 470°C which compares well with reported rates of other unpromoted Co_3Mo_3N catalysts (Table 2).

This demonstrates the ability of the as-prepared cobalt molybdenum nitride catalyst to effectively activate nitrogen at temperatures similar to those employed in the molten salt reactor (450°C).

Table 2: *Comparison of ammonia synthesis rate of Co_3Mo_3N catalysts from this work and literature reports.*

Material	Temperature (°C)	Pressure (bar)	Rate ($\mu mol\ g_{cat.}^{-1} h^{-1}$)	Reference
Co_3Mo_3N	470	50	6363	this work
Co_3Mo_3N from $CoMoO_4 \cdot xH_2O$	400	31	4500	Ref.[1]
Co_3Mo_3N from $CoMoO_4$	400	100	5357	Ref.[26]
5wt% Cs/Co_3Mo_3N	400	100	46427	Ref.[26]

6.5 Nitrogen Reduction Reaction Testing

6.5.1 Experimental Methods

For details on the setup, salt preparation and use of the molten salt reactor see Chapter 3 Section 3.

Figure 9 gives a pictorial overview of the conditions used to investigate the stability of Co_3Mo_3N in molten Li-K-Cl at 450°C, as well as its nitrogen reduction ability. Pellets of Co_3Mo_3N were prepared by pressing around 250mg of passivated Co_3Mo_3N powder into 13mm diameter pellets using a bench top press. As-prepared pellets were found to be

conductive and held in electrical contact with carbon felt inside a 1.2cm diameter alumina tube.

Initially the stability of Co_3Mo_3N was assessed by submerging a pellet as the working electrode held between carbon felt sheets at open-circuit potential (OCP) for ~ 3h while flowing Ar (Condition 1, Table 3). After the open-circuit measurement the working electrode was removed from the melt and small amounts of molten chloride were extracted from the reactor by suction into a quartz sampling tube showing the melt to be bright blue in the liquid state. This was tentatively ascribed to cobalt dissolving out of the Co_3Mo_3N pellet to form blue cobalt chloride complexes in the molten chloride salts.

Similar experiments were repeated while applying a potential to Co_3Mo_3N. Pellets were submerged under potential control while flowing either Ar (Condition 2, Table 3) or N_2 (Condition 3, Table 3) at 20mL min^{-1} over the catalyst and held at 0.35V vs Li^+/Li. After the chronoamperometry the working electrodes were removed from the melt and small amounts of molten chloride were extracted showing the melt to be clear and colourless under both, Ar and N_2 flow. The same experiment was repeated using only carbon felt as the working electrode under N_2 flow.

The amount of nitride lost from the cobalt molybdenum nitride pellets or formed by reducing dinitrogen was measured in the form of ammonia trapped in the acid bubbler on the outgoing gas stream and ammonia formed by dissolving frozen Li-K-Cl eutectic post experiment in 10mM H_2SO_4. Ammonia detected in the acid bubbler is believed to stem from reactions of N^{3-} with residual water in the melt or could be due to Co_3Mo_3N losing chemisorbed NH_x species formed during synthesis from N_2 and H_2, when exposed to the melt. The catalyst pellets were subjected to characterisation using XRD and XPS before

and after exposure to the melt to investigate the behaviour of Co_3Mo_3N in molten Li-K-Cl eutectics.

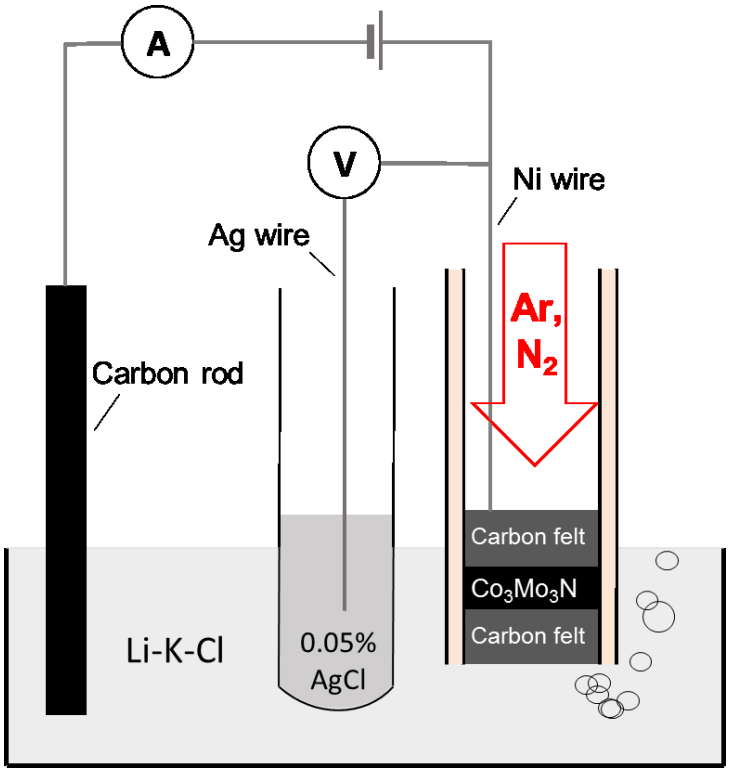


Figure 9: *Pictorial overview of electrochemical testing of Co_3Mo_3N in Li-K-Cl eutectic at 450°C. A carbon rod was used as counter electrode while a Ag/AgCl electrode consisting of a silver wire in a closed Pyrex tube containing 0.05mol% AgCl in Li-K-Cl eutectic was employed as the reference electrode. The working electrode was prepared by fixing a Co_3Mo_3N pellet between sheets of carbon felt connected to the potentiostat by a nickel wire. Argon or dinitrogen were flown over the working electrode at 20mL min^{-1}.*

Table 3: *Overview of electrochemical conditions used to test stability and NRR activity of Co_3Mo_3N at 450°C. Gases were flown at 20mL min^{-1} over the working electrode while 350mL min^{-1} Ar were supplied via the purge line.*

Testing Condition	Gas flown	Applied Potential
1	Ar	OCP
2	Ar	0.35V vs Li^+/Li
3	N_2	0.35V vs Li^+/Li

6.5.2 Results and Discussion

Figure 10 shows XPS spectra of the Co2p region of as-prepared Co_3Mo_3N catalyst (A) and of Co_3Mo_3N after exposure to the melt under different conditions (B-D). In all spectra only contributions from Co(II) are detected in form of $2p_{3/2}$ and $2p_{1/2}$ peaks of Co(II) and its satellite. Hence, no change in oxidation state is observed for Co post melt exposure, indicating that all catalysts are covered with a surface oxide layer. Notably, the Co2p spectrum of Co_3Mo_3N exposed to the melt under open-circuit conditions (Fig.10.B) is significantly noisier compared to the other spectra, implying smaller amounts of cobalt to be present.

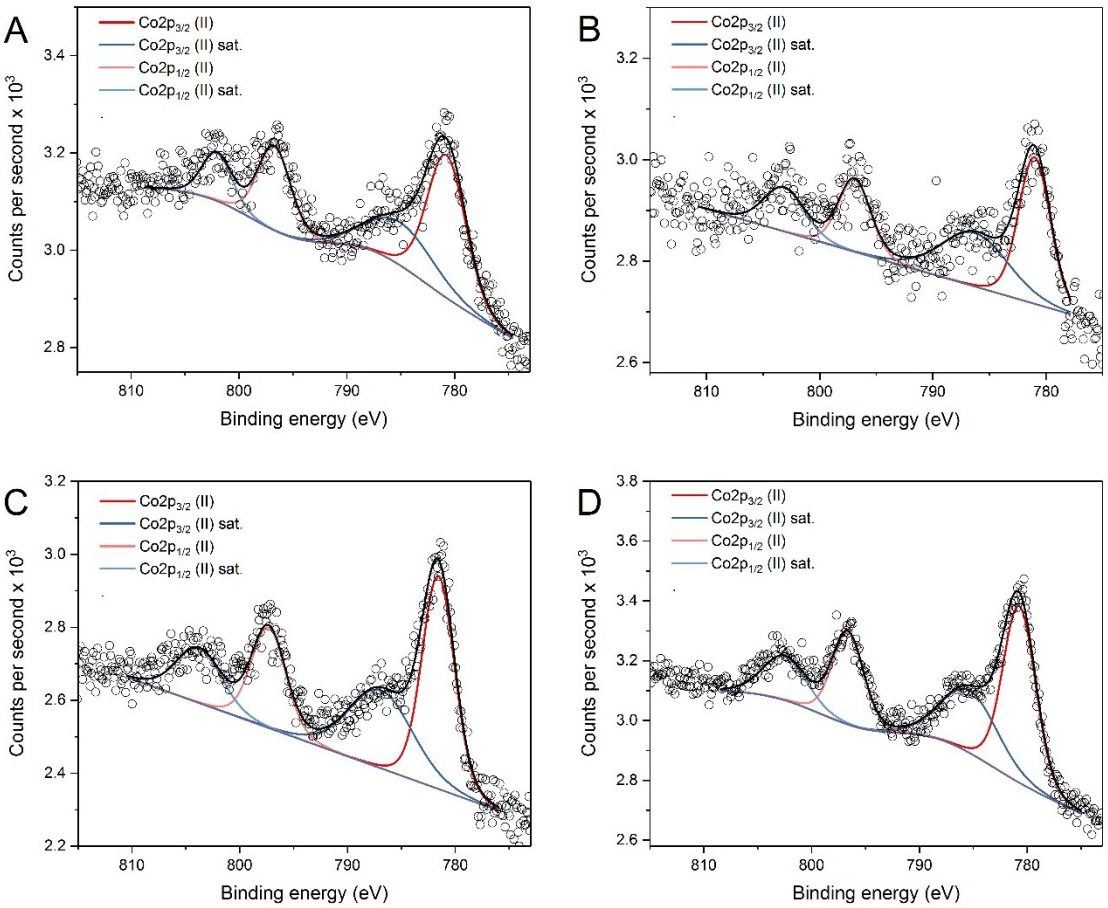


Figure 10: *XPS spectra of Co2p region of Co_3Mo_3N as-prepared (A), at OCP (B), at 0.35V vs Li^+/Li under Ar flow (C), and at 0.35V vs Li^+/Li under N_2 flow (D). Colour code: +II $Co2p_{3/2}$ (red), and +II $Co2p_{3/2}$ satellite (blue). The black line, purple line and empty black circles, respectively represent the overall fit, background, and data points. Faint coloured traces represent corresponding $Co2p_{1/2}$ peaks.*

Figure 11 shows XPS spectra of the Mo3d region of as-prepared Co_3Mo_3N catalyst (A) and of Co_3Mo_3N after exposure to the melt under different conditions (B-D). For as-prepared Co_3Mo_3N contributions from Mo(0) and Mo(V) were detected, with their $2p_{3/2}$ peaks being centred at 228.3 and 232.3eV (Fig.11.A), respectively, which is congruent with literature values of molybdenum in these oxidation states.[15,18] As shown in high resolution XPS spectra in Fig.5, Mo(IV) and Mo(V) species might be present as well in the Co_3Mo_3N catalysts, although most likely in low concentration since they could not be conclusively accounted for in lower resolution Mo3d spectra. Strikingly, the Mo3d

regions of all Co_3Mo_3N catalysts that were exposed to the melt (Fig.12.B-D) markedly changed compared to the as–synthesised catalyst (Fig.11.A). Only Mo(V) is detected with no visible contributions from more reduced molybdenum species. This is likely explained by the lack of passivation procedure after exposure to the melt. It is hypothesised that phases containing more reduced Mo are formed during reaction in the melt which upon sudden exposure to air when removed from the reactor oxidise rapidly and form a thicker oxide surface layer compared to the layer formed during the 24h long passivation procedure employed during the synthesis of Co_3Mo_3N.

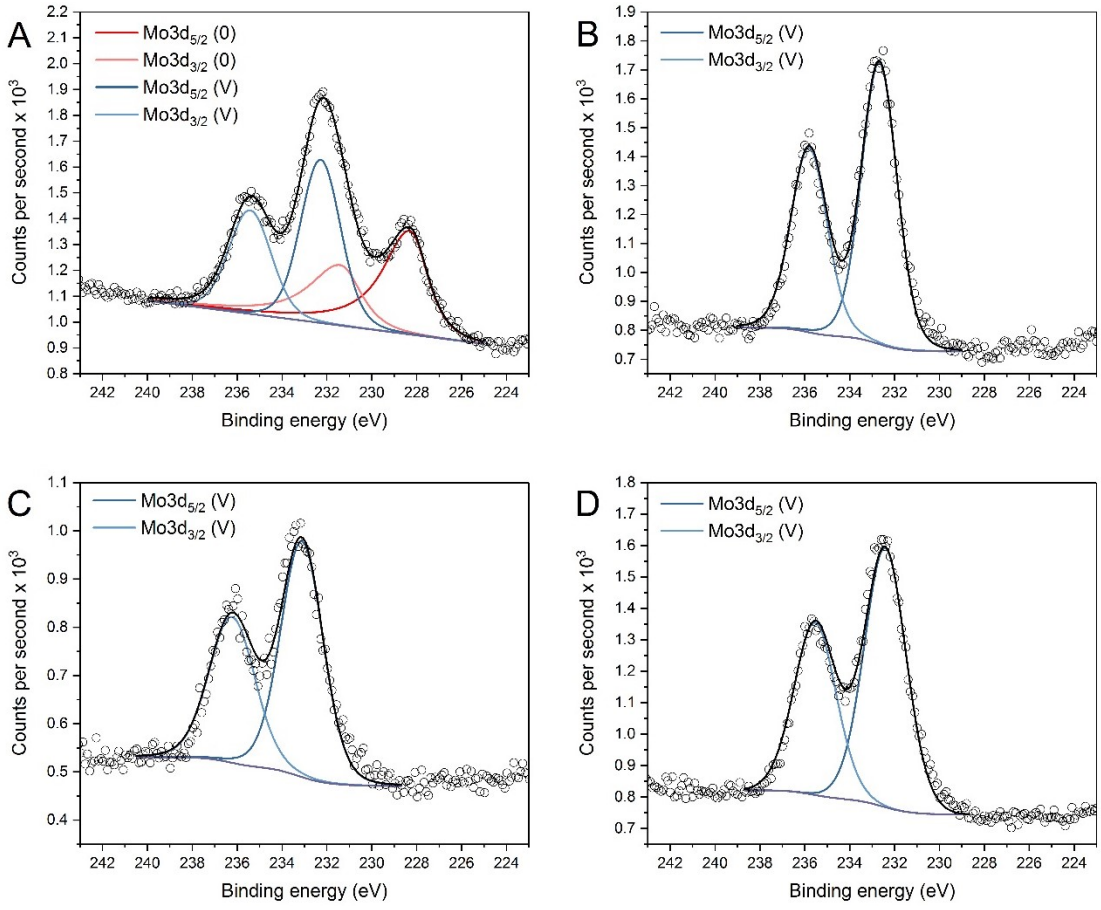


Figure 11: *XPS spectra of Mo3d region of Co_3Mo_3N as-prepared (A), at OCP (B), at 0.35V vs Li^+/Li under Ar flow (C), and at 0.35V vs Li^+/Li under N_2 flow (D). Colour code: metallic $Mo3d_{5/2}$ (red), and +V $Mo3d_{5/2}$ (blue). The black line, purple line and empty black circles, respectively represent the overall fit, background, and data points. Faint coloured traces represent corresponding $Mo3d_{3/2}$ peaks.*

The ratio of cobalt-to-molybdenum was determined using XPS survey scans and is summarised for all catalysts in Table 4. For as-prepared Co_3Mo_3N and cobalt molybdenum nitride exposed to the melt under potential control the ratio is close the expected value of one to one indicating that no change in metal composition occurs under potential control. For the sample which was held at OCP a Co/Mo ratio of 1:3 is observed clearly showing the loss of cobalt from the catalyst during the measurement which is in agreement with its Co2p spectrum and with the blue appearance of the melt post experiment.

Table 4: *Overview of cobalt to molybdenum ratio of Co_3Mo_3N under different conditions.*

Sample	Co/Mo ratio
As-prepared Co_3Mo_3N	1 : 1.4
Co_3Mo_3N at OCP	1 : 3.0
Co_3Mo_3N at 0.35V under Ar	1 : 0.95
Co_3Mo_3N at 0.35V under N_2	1 : 1.22

To investigate the structural integrity of Co_3Mo_3N, XRD patterns of the spent catalysts were obtained and are summarised in Figure 12. The as-prepared Co_3Mo_3N sample (red trace) was shown to be the η-6 Co_3Mo_3N phase (JPCDS: 01-89-7953) containing minor impurities of metallic Co (JPCDS: 00-015-0806), metallic Mo (JPCDS: 01-089-5023), and β- or γ-Mo_2N (JPCDS: 00-025-1368 and 00-025-1366). When exposed to the melt at OCP (blue trace) the η-6 Co_3Mo_3N phase is almost completely lost while Mo_2N, Co, and Mo are still detected. Reflections of the Li-K-Cl eutectic crystallising in the sylvite

structure (for pure KCl, JCPDS: 00-004-0587) are also found at around 28.5 and 40.5°. Similarly, the η-6 cobalt molybdenum nitride phase largely disappears when Co_3Mo_3N is held at 0.35V vs Li^+/Li (yellow trace). Again, impurities of Mo_2N, Co, and Mo are still detected. Under N_2 flow and application of 0.35V vs Li^+/Li (green trace), the η-6 Co_3Mo_3N phase was found to remain stable with no obvious changes to peak positions or intensities. This clearly indicates that Co_3Mo_3N can indeed be stabilised in Li-K-Cl at 450°C but only under simultaneously applied potential and dinitrogen flow.

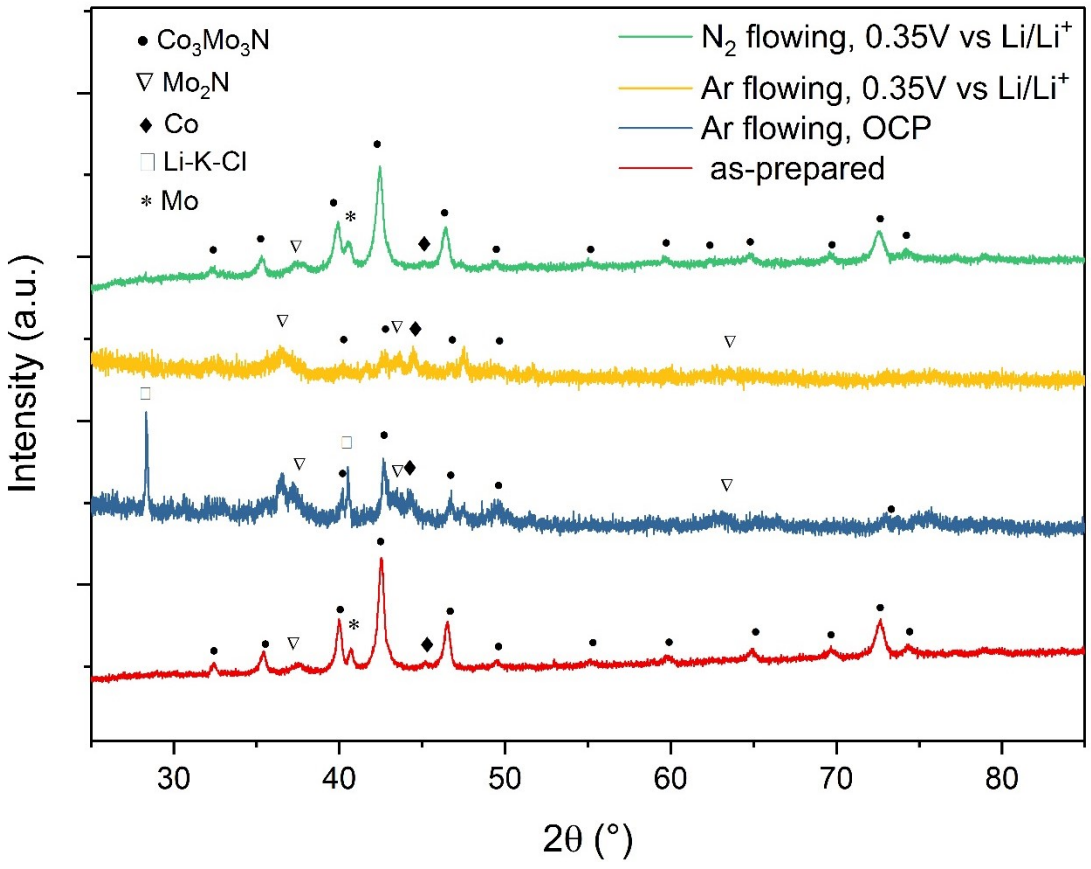


Figure 12: *XRD patterns of Co_3Mo_3N pellets before and after exposure to Li-K-Cl melt under different conditions. Colour code: as-prepared Co_3Mo_3N (red), Co_3Mo_3N after melt at OCP and Ar flow (blue), Co_3Mo_3N after melt at 0.35 vs Li^+/Li and Ar flow (yellow), and Co_3Mo_3N after melt at 0.35 vs Li^+/Li and N_2 flow (green). Reflections of the Co_3Mo_3N phase (•), as well as impurities/ reaction products including Mo_2N (▼), Mo (*), Co (◊), and Li-K-Cl (•) are labelled using symbols.*

The amount of N^{3-} formed was measured by integrating amounts of ammonia detected in the acid trap and dissolved melt post reaction and is summarised in Figure 13. Less than 0.1μmol was detected in a blank experiment using only carbon felt as the working electrode while applying 0.35V vs Li^+/Li for 1000s seconds under N_2 flow. For both, Co_3Mo_3N at OCP and at 0.35V vs Li^+/Li under Ar flow around 3.5μmol of ammonia were detected. Since no N_2 was supplied the measured reduced nitrogen is believed to originate from lattice N^{3-} dissolving into the melt which also explains the loss of the η-6 Co_3Mo_3N phase observed in XRD.

When N_2 is flowed over Co_3Mo_3N at 0.35V vs Li^+/Li for 1000s, a total of 6.18μmol of ammonia was detected. Although this is less than the amount of N^{3-} present in the amount of Co_3Mo_3N added, it is significant since compared to testing at open-circuit and under Ar flow no catalyst degradation was observed in post-mortem XPS or XRD analysis, indicating that the measured reduced nitrogen does not originate from catalyst decomposition. Another possible sources is adsorbed NH_x species on the catalyst surface formed during the synthesis. A contribution from such species to the measured reduced nitrogen cannot be completely ruled out but is believed to be minimal due to the vacuum treatment at 150°C of the catalysts before melt exposure.

As such, the detected ammonia for Co_3Mo_3N at 0.35V under N_2 flow is attributed to the reduction of dinitrogen to nitride ions. The measured amount corresponds to a NRR rate of 5.40×10^{-9}mol cm^{-2} s^{-1} for Co_3Mo_3N at a current efficiency of ~1%. This is among the highest nitrogen reduction rates recorded in literature.[28,29] It is important to keep in mind that the above measurements correspond only to the nitrogen reduction half reaction, with protonation occurring ex-situ on dissolving the melt in 10mM sulphuric acid. A continuous synthesis process must incorporate this step into the cycle (vide infra), as most

of the similar reports of ammonia synthesis have done. Nevertheless, this shows that Co_3Mo_3N has the potential to be a very active catalyst for NRR in molten salt systems. The current densities for CF and Co_3Mo_3N at 0.35V vs Li^+/Li and under N_2 are shown in Figure 14. High current densities of above 200mA cm^{-2} are initially recorded for CF and even higher ones for Co_3Mo_3N, although both level off after around two minutes. It is important to note that the Co_3Mo_3N pellet is held in place by CF meaning a large proportion of the current observed for Co_3Mo_3N could be due to contributions from the carbon felt. Also note that no reduced nitrogen was detected after CF testing meaning potentially higher current efficiencies, as well as higher rates due to increased surface area, could be achieved for Co_3Mo_3N catalysts when directly deposited onto a gas electrode support. Further long-term activity tests and isotope labelling experiments are suggested to determine the rate of dinitrogen reduction more accurately.

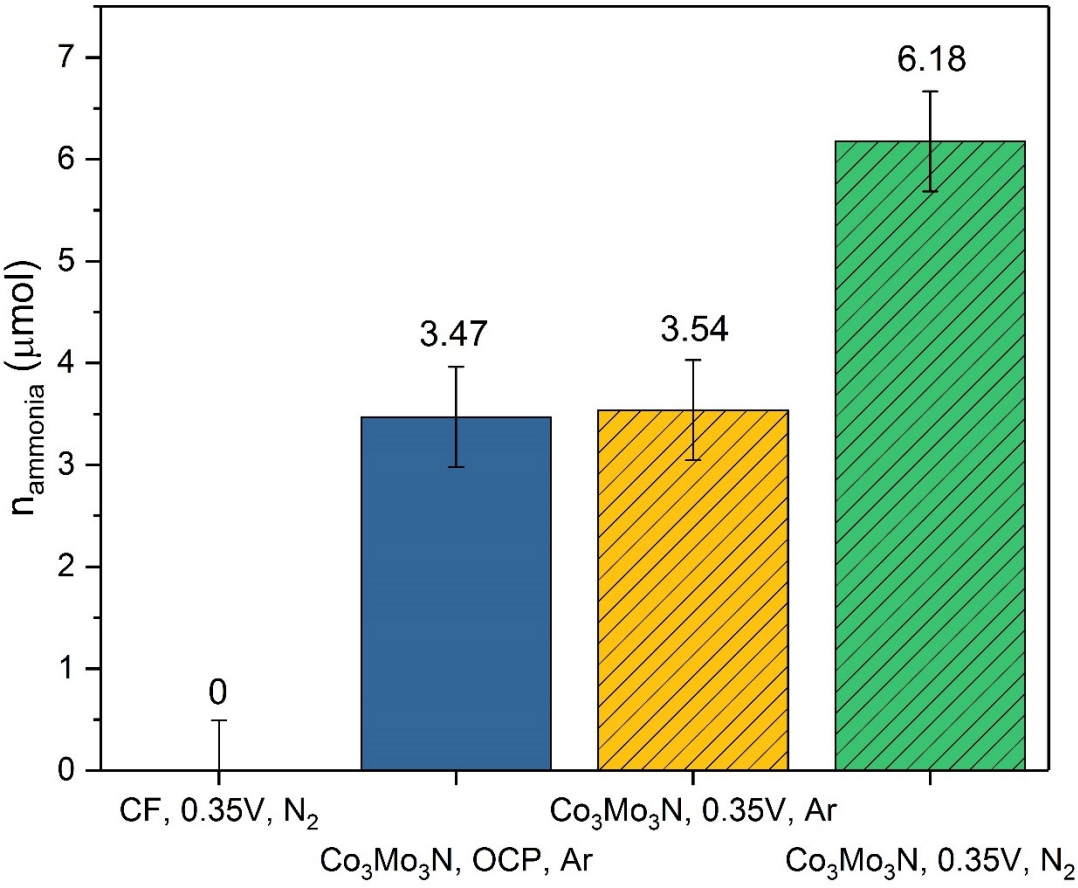


Figure 13: *Bar chart of total amounts of ammonia detected during experiments in molten Li-K-Cl at 450°C. Striped bars indicate application of 0.35V vs Li^+/Li to the working electrode during the experiment. Number of moles detected in post-reactor acid trap and in the melt were combined, a total of three measurements, to obtain the total amount of ammonia. Error bars correspond to a typical measurement error of 0.05ppm in each of the three ammonia measurements.*

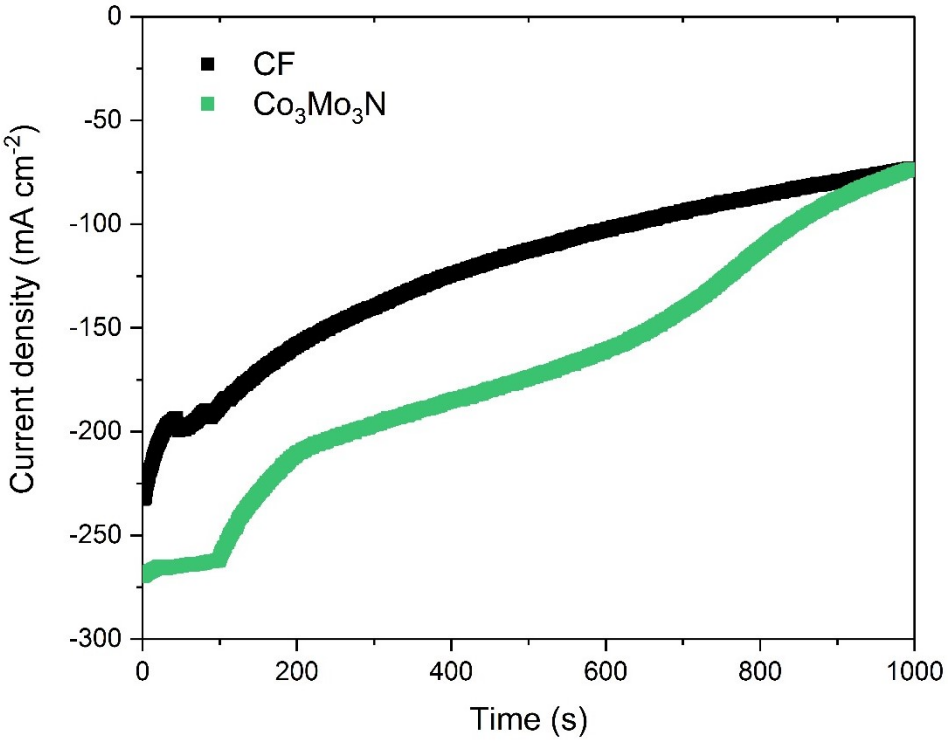


Figure 14: Current densities recorded for CF (black trace) and Co_3Mo_3N with CF (green) at 0.35V vs Li^+/Li under N_2 flow in molten Li-K-Cl eutectic at 450°C.

Based on the observations above, tentative reaction mechanisms under the different testing conditions are postulated below. Under open-circuit conditions concomitant dissolution of cobalt and nitride are observed. This is attributed to the high affinity of lithium towards nitrogen leading to a displacement of the cobalt ions from the Co_3Mo_3N lattice. The formed Li_3N is highly soluble in the melt and as such will dissolve leaving mostly amorphous cobalt-deficient CoMo phase and Mo_2N behind (Eq. 1). Co_3Mo_3N has previously been reported as a stable anode material in Li-O_2 batteries at room temperature using 1M $Li[(CF_3SO_2)_2N]$ in tetraethylene glycol dimethyl ether as electrolyte.[30] In the present system the concentration of Li^+ is significantly higher (close to 18M) which is believed to enable the decomposition of Co_3Mo_3N aided by the elevated temperature (450°C), as well as the high concentration of Cl^- ions which are considered to facilitate the dissolution of cobalt.

[redacted] (1)

Upon application of 0.35V vs Li^+/Li, Co_3Mo_3N is believed to fully reduced to the metallic state while expelling N^{3-} into the melt, facilitated by lithium ions (Eq.2). Similar behaviour has been observed for thin film anodes of Co_3N,[31] Fe_3N,[31] Zn_3N_2,[32] Sn_3N_4,[33] and InN [33] during the discharge process in lithium ion batteries. In these systems the metal is reduced to the metallic state forming small particles inside a concomitantly forming Li_3N matrix. Similar reactions occur for transition metal oxide anodes, such as CoO, where the formed metal particles are often below 5nm and as such undetectable in powder XRD.[34,35] It is believed that the current system undergoes a similar reaction where instead of forming a matrix, Li_3N dissolves in the molten chloride eutectic. No crystalline metallic cobalt, molybdenum or alloy thereof is observed in XRD post-reaction which can possibly be explained by the formation of small nanoparticulate or amorphous CoMo structures akin to those formed in CoO Li battery anodes[34].

[redacted] (2)

With applied potential and under N_2 flow the Co_3Mo_3N phase was found to be stable in the melt while simultaneously high amounts of nitride were detected. It is hypothesised that Co_3Mo_3N is first reduced to a more metallic state as shown in Eq.2 which then chemically reacts with dinitrogen to regenerate the initial η-6 cobalt molybdenum nitride phase (Eq.3). It is possible that this mechanism operates via an intermediate phase such as the η-12 Co_6Mo_6N phase and is not actually fully reduced to the metal state. As previously mentioned the η-12 Co_6Mo_6N phase is able to reduce N_2 in absence of any external reducing agent, such as H_2, to reform the η-6 phase.[9–11] Effectively, this closes

the catalytic cycle where cobalt molybdenum nitride is constantly alternating between nitrogen-rich and deficient phases while overall N_2 is reduced to N^{3-}.

$$3CoMo + ½\ N_2 \rightarrow Co_3Mo_3N \tag{3}$$

Such a mechanism can be described as Mars-van Krevelen-type (MvK) for which the lattice anion participates in the reaction and is constantly replenished by an external, usually gaseous, source.[2,36] A MvK mechanism has recently also been proposed to be at play during thermal ammonia synthesis over Co_3Mo_3N by theory[5–7,37], as well as experiments, using isotope labelling and insights from ammonia synthesis experiments over isostructural cobalt molybdenum carbides.[5,8,11,38] In the proposed reaction scheme for Co_3Mo_3N, gaseous dinitrogen binds head-on to a surface nitrogen vacancy (Fig.16). Following the initial activation, the nitrogen away from the surface is suggested to be hydrogenated first (distal pathway) and eventually leave in form of ammonia. The nitrogen vacancy, the initial active site, is then regenerated by further hydrogenation of the remaining bound N_{ad} leading to the formation of a second molecule of ammonia. As such, this mechanism is an associative mechanism, meaning dinitrogen is hydrogenated prior to N-N bond dissociation which is similar to the mechanism at play in the room temperature ammonia synthesis in nitrogenase enzymes.[39] Commonly used industrial catalysts for thermal ammonia synthesis, like Ru-based and Fe-based systems, are believed to operate via dissociative mechanisms where the initial adsorption leads to bond scission and the formation of two N_{ad} species.[40–42] We were recently able to show that by doping a ruthenium based catalyst with Li it is possible to switch to an associative mechanism, eliminate hydrogen poisoning and significantly increase the ammonia synthesis rate under mild conditions.[43] Calculations show that in this case Li^+ can stabilise

the NNH intermediate, as well as enable further backdonation from Ru, leading to a lower activation barrier for an associative pathway favouring it over an dissociative mechanism.[43] Similarly to this, LiH has been shown to facilitate nitrogen hydrogenation in LiH-Mn ammonia synthesis catalysts.[44] Here, Mn is suggested to activate nitrogen to N_{ad} which is then transferred to LiH forming imide and amide species and eventually evolving ammonia.[44] The authors suggest this leads to a breaking of the scaling relations which limit many thermal ammonia synthesis catalysts, by providing two distinct surfaces for nitrogen adsorption and ammonia desorption.[44] Lithium doping has also been shown to increase activity of manganese nitride catalysts for chemical looping ammonia synthesis.[45]

The reports discussed above indicate that lithium can play a special role in dinitrogen activation by stabilising key intermediates, as well as activate lattice nitrogen in metal nitride catalysts. Based on this literature and on observations made here, it is postulated that in the molten salt system presented in this thesis Li^+ can dissolve the lattice nitrogen of Co_3Mo_3N, as well as stabilise adsorbed N-N species on the reduced state of Co_3Mo_3N helping to fill nitrogen vacancies formed by expulsion of N^{3-} into the melt.

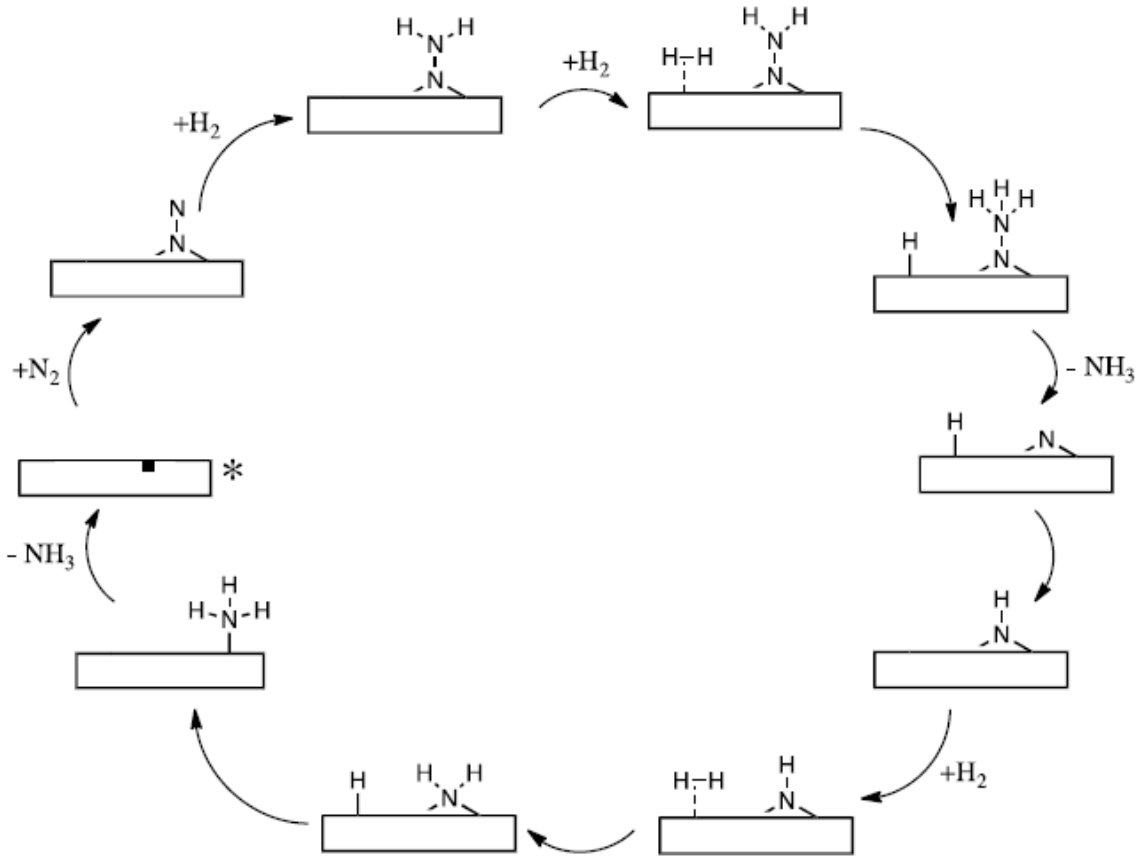


Figure 15: *Simplified reaction scheme for Eley-Rideal/Mars-van Krevelen type associative mechanism. Reaction starting point is marked with an asterisk. Reproduced from reference* [7] *– published by the Royal Society of Chemistry.*

6.6 Conclusions

The work in this chapter focused on investigating Co_3Mo_3N as an electrocatalyst for the direct electrochemical reduction of N_2 to N^{3-} in a molten Li-K-Cl eutectic. Previously only metallic nickel had been reported as an electrocatalyst for the NRR in Li-K-Cl.

The η-6 phase of cobalt molybdenum nitride was successfully synthesised and characterised using XRD, XPS and TEM. A passivation procedure was carried out post synthesis to prevent oxidation in air shown to create a thin protective surface oxide layer by XPS. Furthermore, a TPR study showed it is indeed possible to transform the

Co_3Mo_3N phase into Co_6Mo_6N by treatment in H_2 clearly demonstrating the mobility of lattice nitrogen in the prepared material.

Initial stability testing of Co_3Mo_3N in the melt at open-circuit potential was shown to lead to dissolution of cobalt and nitride from the material, as well as loss of the cobalt nitride phase. Under potential control and Ar flow the cobalt-to-molybdenum ratio was kept stable but nitride dissolution and decomposition of the η-6 phase still occurred. Under applied potential and N_2 flow large amounts of nitride were detected in the melt while no decomposition of Co_3Mo_3N was observed in XPS or XRD indicating catalytic electrochemical reduction of dinitrogen to nitride ions. A nitrogen reduction rate of 5.40×10^{-9} mol cm^{-2} s^{-1} at a current efficiency of 1% was measured for the Co_3Mo_3N catalyst comparing favourably with most electrochemical ammonia synthesis catalysts.

Based on experimental evidence and previous literature reports a MvK-type mechanism is suggested for the reaction in which Li^+ ions facilitate the activation of dinitrogen, as well as enable participation of the lattice nitrogen of Co_3Mo_3N.

In order to further investigate the mechanism and accurately quantify the nitrogen reduction rate, isotope labelling studies as well as long-term catalyst stability tests are suggested. Also it should be noted that presented measurements here are N_2 half cell experiments and further research into the nitrogen redox chemistry in molten chlorides is needed to establish a continuous ammonia synthesis cell. Potential solutions towards this goal include the use of high temperature proton conducting membranes or bipolar membranes (e.g. Pd), as recently suggested in literature[46].

6.7 References

(1) Kojima, R.; Aika, K. Cobalt Molybdenum Bimetallic Nitride Catalysts for Ammonia Synthesis. *Chemistry Letters* **2000**, No. 5, 514–515.

(2) Alexander, A.-M.; Hargreaves, J. S. J. Alternative Catalytic Materials: Carbides, Nitrides, Phosphides and Amorphous Boron Alloys. *Chemical Society Reviews* **2010**, *39* (11), 4388. https://doi.org/10.1039/b916787k.

(3) Kojima, R.; Aika, K. Molybdenum Nitride and Carbide Catalysts for Ammonia Synthesis. *Applied Catalysis A: General* **2001**, *219* (1), 141–147. https://doi.org/10.1016/S0926-860X(01)00676-7.

(4) Kojima, R.; Aika, K. Rhenium Containing Binary Catalysts for Ammonia Synthesis. *Applied Catalysis A: General* **2001**, *209* (1), 317–325. https://doi.org/10.1016/S0926-860X(00)00764-X.

(5) Zeinalipour-Yazdi, C. D.; Hargreaves, J. S. J.; Catlow, C. R. A. DFT-D3 Study of Molecular N $_2$ and H $_2$ Activation on Co $_3$ Mo $_3$ N Surfaces. *The Journal of Physical Chemistry C* **2016**. https://doi.org/10.1021/acs.jpcc.6b04748.

(6) Zeinalipour-Yazdi, C. D.; Hargreaves, J. S. J.; Catlow, C. R. A. Nitrogen Activation in a Mars - Van Krevelen Mechanism for Ammonia Synthesis on Co $_3$ Mo $_3$ N. *The Journal of Physical Chemistry C* **2015**, 151005212740001. https://doi.org/10.1021/acs.jpcc.5b06811.

(7) Zeinalipour-Yazdi, C. D.; Hargreaves, J.; Laassiri, S.; Catlow, R. C. A. The Integration of Experiment and Computational Modelling in Heterogeneously Catalysed Ammonia Synthesis over Metal Nitrides. *Physical Chemistry Chemical Physics* **2018**. https://doi.org/10.1039/C8CP04216K.

(8) Hunter, S. M.; Mckay, D.; Smith, R. I.; Hargreaves, J. S. J.; Gregory, D. H. Topotactic Nitrogen Transfer: Structural Transformation in Cobalt Molybdenum Nitrides. *Chemistry of Materials* **2010**, *22* (9), 2898–2907. https://doi.org/10.1021/cm100208a.

(9) Gregory, D. H.; Hargreaves, J. S. J.; Hunter, S. M. On the Regeneration of Co3Mo3N from Co6Mo6N with N2. *Catalysis Letters* **2011**, *141* (1), 22–26. https://doi.org/10.1007/s10562-010-0464-3.

(10) Mckay, D.; Gregory, D. H.; Hargreaves, J. S. J.; Hunter, S. M.; Sun, X. Towards Nitrogen Transfer Catalysis: Reactive Lattice Nitrogen in Cobalt Molybdenum Nitride. *Chem. Commun.* **2007**, No. 29, 3051. https://doi.org/10.1039/b707913c.

(11) Hunter, S. M.; Gregory, D. H.; Hargreaves, J. S. J.; Richard, M.; Duprez, D.; Bion, N. A Study of ^{15} N/ ^{14} N Isotopic Exchange over Cobalt Molybdenum Nitrides. *ACS Catalysis* **2013**, *3* (8), 1719–1725. https://doi.org/10.1021/cs400336z.

(12) Wise, R. S.; Markel, E. J. Synthesis of High Surface Area Molybdenum Nitride in Mixtures of Nitrogen and Hydrogen. *Journal of Catalysis* **1994**, *145* (2), 344–355. https://doi.org/10.1006/jcat.1994.1043.

(13) Mckay, D. Catalysis over Molybdenum Containing Nitride Materials, University of Glasgow, 2008.

(14) Biesinger, M. C.; Payne, B. P.; Grosvenor, A. P.; Lau, L. W. M.; Gerson, A. R.; Smart, R. S. C. Resolving Surface Chemical States in XPS Analysis of First Row Transition Metals, Oxides and Hydroxides: Cr, Mn, Fe, Co and Ni. *Applied Surface Science* **2011**, *257* (7), 2717–2730. https://doi.org/10.1016/j.apsusc.2010.10.051.

(15) NIST XPS Database, Selected Element Search Result https://srdata.nist.gov/xps/EngElmSrchQuery.aspx?EType=PE&CSOpt=Retri_ex_dat&Elm=N (accessed Sep 10, 2019).

(16) Fu, X.; Su, H.; Yin, W.; Huang, Y.; Gu, X. Bimetallic Molybdenum Nitride Co $_3$ Mo $_3$ N: A New Promising Catalyst for CO $_2$ Reforming of Methane. *Catal. Sci. Technol.* **2017**, *7* (8), 1671–1678. https://doi.org/10.1039/C6CY02428A.

(17) Podila, S.; Zaman, S. F.; Driss, H.; Al-Zahrani, A. A.; Daous, M. A.; Petrov, L. A. High Performance of Bulk Mo2N and Co3Mo3N Catalysts for Hydrogen Production from Ammonia: Role of Citric Acid to Mo Molar Ratio in Preparation of High Surface Area Nitride Catalysts. *International Journal of Hydrogen Energy* **2017**, *42* (12), 8006–8020. https://doi.org/10.1016/j.ijhydene.2017.01.044.
(18) Spevack, P. A.; McIntyre, N. S. Thermal Reduction of Molybdenum Trioxide. *J. Phys. Chem.* **1992**, *96* (22), 9029–9035. https://doi.org/10.1021/j100201a062.
(19) Jaeger, D.; Patscheider, J. A Complete and Self-Consistent Evaluation of XPS Spectra of TiN. *Journal of Electron Spectroscopy and Related Phenomena* **2012**, *185* (11), 523–534. https://doi.org/10.1016/j.elspec.2012.10.011.
(20) Sanjinés, R.; Wiemer, C.; Almeida, J.; Lévy, F. Valence Band Photoemission Study of the Ti-Mo-N System. *Thin Solid Films* **1996**, *290–291*, 334–338. https://doi.org/10.1016/S0040-6090(96)09082-7.
(21) Wang, L.; Kirk, E.; Wäckerlin, C.; Schneider, C. W.; Hojeij, M.; Gobrecht, J.; Ekinci, Y. Nearly Amorphous Mo-N Gratings for Ultimate Resolution in Extreme Ultraviolet Interference Lithography. *Nanotechnology* **2014**, *25* (23), 235305. https://doi.org/10.1088/0957-4484/25/23/235305.
(22) Biesinger, M. C.; Lau, L. W. M.; Gerson, A. R.; Smart, R. S. C. Resolving Surface Chemical States in XPS Analysis of First Row Transition Metals, Oxides and Hydroxides: Sc, Ti, V, Cu and Zn. *Applied Surface Science* **2010**, *257* (3), 887–898. https://doi.org/10.1016/j.apsusc.2010.07.086.
(23) Beamson, G.; Briggs, D. *High Resolution XPS of Organic Polymers: The Scienta ESCA300 Database*; Wiley, 1992.
(24) Oyama, S. T.; Congress of Pacific Rim Chemical Societies Honolulu, H. *The Chemistry of Transition Metal Carbides and Nitrides*; Blackie Academic & Professional: London, 1996.
(25) Srifa, A.; Okura, K.; Okanishi, T.; Muroyama, H.; Matsui, T.; Eguchi, K. Hydrogen Production by Ammonia Decomposition over Cs-Modified Co3Mo3N Catalysts. *Applied Catalysis B: Environmental* **2017**, *218*, 1–8. https://doi.org/10.1016/j.apcatb.2017.06.034.
(26) Jacobsen, C. J. H. Novel Class of Ammonia Synthesis Catalysts. *Chem. Commun.* **2000**, No. 12, 1057–1058. https://doi.org/10.1039/b002930k.
(27) McPherson, I. J.; Sudmeier, T.; Fellowes, J. P.; Wilkinson, I.; Hughes, T.; Tsang, E. S. C. The Feasibility of Electrochemical Ammonia Synthesis in Molten LiCl-KCl Eutectics. *Angewandte Chemie International Edition* **2019**. https://doi.org/10.1002/anie.201909831.
(28) McPherson, I.J.; Sudmeier, T.; Fellowes, J.; Tsang, S. C. E. Materials for Electrochemical Ammonia Synthesis. *Dalton Transactions* **2019**, *48* (5), 1562–1568. https://doi.org/10.1039/C8DT04019B.
(29) Giddey, S.; Badwal, S. P. S.; Kulkarni, A. Review of Electrochemical Ammonia Production Technologies and Materials. *International Journal of Hydrogen Energy* **2013**, *38* (34), 14576–14594. https://doi.org/10.1016/j.ijhydene.2013.09.054.
(30) Zhang, K.; Zhang, L.; Chen, X.; He, X.; Wang, X.; Dong, S.; Han, P.; Zhang, C.; Wang, S.; Gu, L.; et al. Mesoporous Cobalt Molybdenum Nitride: A Highly Active Bifunctional Electrocatalyst and Its Application in Lithium–O $_2$ Batteries. *The Journal of Physical Chemistry C* **2013**, *117* (2), 858–865. https://doi.org/10.1021/jp310571y.
(31) Fu, Z.-W.; Wang, Y.; Yue, X.-L.; Zhao, S.-L.; Qin, Q.-Z. Electrochemical Reactions of Lithium with Transition Metal Nitride Electrodes. *The Journal of Physical Chemistry B* **2004**, *108* (7), 2236–2244. https://doi.org/10.1021/jp030530s.

(32) Pereira, N.; Klein, L. C.; Amatucci, G. G. The Electrochemistry of Zn[Sub 3]N[Sub 2] and LiZnN. *Journal of The Electrochemical Society* **2002**, *149* (3), A262. https://doi.org/10.1149/1.1446079.
(33) Nazri, G.; Thackeray, M.; Ohzuku, T. *Intercalation Compounds for Battery Materials: Proceedings of the International Symposium*; The Electrochemical Society, 2000.
(34) Poizot, P.; Laruelle, S.; Grugeon, S.; Dupont, L.; Tarascon, J.-M. Nano-Sized Transition-Metal Oxides as Negative-Electrode Materials for Lithium-Ion Batteries. *Nature* **2000**, *407* (6803), 496–499. https://doi.org/10.1038/35035045.
(35) Obrovac, M. N.; Dunlap, R. A.; Sanderson, R. J.; Dahn, J. R. The Electrochemical Displacement Reaction of Lithium with Metal Oxides. *J. Electrochem. Soc.* **2001**, *148* (6), A576–A588. https://doi.org/10.1149/1.1370962.
(36) Doornkamp, C.; Ponec, V. The Universal Character of the Mars and Van Krevelen Mechanism. *Journal of Molecular Catalysis A: Chemical* **2000**, *162* (1), 19–32. https://doi.org/10.1016/S1381-1169(00)00319-8.
(37) Zeinalipour-Yazdi, C. D.; Hargreaves, J. S. J.; Catlow, C. R. A. Low-T Mechanisms of Ammonia Synthesis on Co_3Mo_3N. *J. Phys. Chem. C* **2018**, *122* (11), 6078–6082. https://doi.org/10.1021/acs.jpcc.7b12364.
(38) AlShibane, I.; Daisley, A.; Hargreaves, J. S. J.; Hector, A. L.; Laassiri, S.; Rico, J. L.; Smith, R. I. The Role of Composition for Cobalt Molybdenum Carbide in Ammonia Synthesis. *ACS Sustainable Chem. Eng.* **2017**, *5* (10), 9214–9222. https://doi.org/10.1021/acssuschemeng.7b02168.
(39) Hoffman, B. M.; Lukoyanov, D.; Yang, Z.-Y.; Dean, D. R.; Seefeldt, L. C. Mechanism of Nitrogen Fixation by Nitrogenase: The Next Stage. *Chemical Reviews* **2014**, *114* (8), 4041–4062. https://doi.org/10.1021/cr400641x.
(40) Ertl, G. Primary Steps in Catalytic Synthesis of Ammonia. *Journal of Vacuum Science & Technology A: Vacuum, Surfaces, and Films* **1983**, *1* (2), 1247–1253. https://doi.org/10.1116/1.572299.
(41) Ertl, G. *Handbook of Heterogeneous Catalysis.*, 2nd, completely rev. and enl. ed. / edited by Gerhard Ertl ... [et al.]. ed.; Wiley-VCH: Weinheim, 2008.
(42) Jacobsen, C. J. H.; Dahl, S.; Hansen, P. L.; Törnqvist, E.; Jensen, L.; Topsøe, H.; Prip, D. V.; Møenshaug, P. B.; Chorkendorff, I. Structure Sensitivity of Supported Ruthenium Catalysts for Ammonia Synthesis. *Journal of Molecular Catalysis A: Chemical* **2000**, *163* (1), 19–26. https://doi.org/10.1016/S1381-1169(00)00396-4.
(43) Zheng, J.; Liao, F.; Wu, S.; Jones, G.; Chen, T.; Fellowes, J.; Sudmeier, T.; MacPherson, I.; Wilkinson, I.; Tsang, E. S. C. Efficient Non-Dissociative Activation of Dinitrogen to Ammonia over Li Promoted Ru Nanoparticles at Low Pressure. *Angewandte Chemie International Edition 0* (ja). https://doi.org/10.1002/anie.201907171.
(44) Wang, P.; Chang, F.; Gao, W.; Guo, J.; Wu, G.; He, T.; Chen, P. Breaking Scaling Relations to Achieve Low-Temperature Ammonia Synthesis through LiH-Mediated Nitrogen Transfer and Hydrogenation. *Nature Chemistry* **2016**. https://doi.org/10.1038/nchem.2595.
(45) Laassiri, S.; Zeinalipour-Yazdi, C. D.; Catlow, C. R. A.; Hargreaves, J. S. J. The Potential of Manganese Nitride Based Materials as Nitrogen Transfer Reagents for Nitrogen Chemical Looping. *Applied Catalysis B: Environmental* **2018**, *223*, 60–66. https://doi.org/10.1016/j.apcatb.2017.04.073.
(46) Ito, Y.; Nishikiori, T.; Tsujimura, H. Advances toward Industrialization of Novel Molten Salt Electrochemical Processes. *Faraday Discuss.* **2016**, *190*, 307–326. https://doi.org/10.1039/C5FD00237K.

7 Conclusions and Outlook

7.1 Conclusions 236

7.2 Outlook 238

7.3 References 240

7.1 Conclusions

This thesis explored two different cell geometries and catalyst classes, single-atom catalysts in 0.1M HCl and Co_3Mo_3N in Li-K-Cl, for the nitrogen reduction reaction. The SACs were further extensively tested for their hydrogen evolution performance.

A library of M-NG catalysts, including the novel materials Cu-NG, Mn-NG, and Mo-NG, was successfully synthesised via a carbon backbone method and the atomic dispersion of the metals was demonstrated while other structural parameters were kept similar across catalysts. All metal-doped systems showed higher activity, as determined by overpotential at 10mA cm^{-2} and Tafel slope, compared to the un-doped NG catalyst indicating that the dispersed M-N_4 centres are indeed the active site for HER. Ru-NG and especially Co-NG exhibited high activity with overpotentials of just 189mV and 143mV, respectively, at 10mA cm^{-2} and TOFs approaching those of the commercial Pt/C catalyst.

In comparing the activity across catalysts this thesis has shown for the first time that the HER activity of SACs can be systematically tailored by varying the metal dopant in accordance with the φ factor, a descriptor suggested by computation. Additionally it was demonstrated that HER activity can be further tuned by changing the coordination environment of the metal. Two synthesis methods, annealing under argon and use of nitrate metal precursors, were demonstrated to form atomically dispersed Co-G and Co-NG/N with significantly lower activities towards HER compared to Co-NG.

In-situ IR spectroelectrochemistry thiocyanate poisoning experiments suggested that all three Co SACs have a distinct cobalt active sites identified by different C-N stretch frequencies of the adsorbed SCN. A decrease in C-N stretching frequency was correlated with increased HER activity potentially indicating that higher electron density on the

cobalt leads to a lower activation barrier for electrocatalytic hydrogen evolution. Additionally, the peak area of the C-N stretch was used to qualitatively assess the active site density showing Co-G to contain only half as many Co centres as Co-NG and Co-NG/N.

In-situ XANES investigations showed that a square-planar active site arrangement is highly correlated with increased HER activity. In combination with DFT-based XANES modelling using the CASTEP code it is suggested that using nitrate salts and annealing under Ar does lead to distinct atomic active sites which include oxygen in the first coordination sphere leading to a persistent geometrical distortion from the square planar $Co\text{-}N_4$ active site observed for Co-NG. This likely is the reason for the attenuated HER activity of Co-NG/N and Co-G. This has some implications for the φ factor which only takes the electron negativity of the active site ligands into consideration but does not contain a geometrical component. Adding such an additional component might be necessary to accurately predict the activity of SACs with non-square planar active site arrangements.

M-NG systems were tested for their activity in the electrochemical nitrogen reduction reaction testing in 0.1M HCl remained inconclusive due to low activity of the catalysts and extraneous sources of ammonia prohibiting the confident quantification of electrochemically produced ammonia in the described setups.

Overall the first part of this thesis provides some further tools to tune the HER activity of single-atom catalysts, which is hoped to provide guidance in the discovery of novel hydrogen evolution catalysts. Additionally, the aforementioned strategies may be used to

improve selectivity in reactions where HER competes, such as nitrogen reduction and CO_2 reduction.

In the second part of this thesis Co_3Mo_3N was identified as potential electrocatalysts for the nitrogen reduction reaction in molten chloride eutectics. In these systems N_2 is directly reduced to N^{3-} which is stabilised in the lithium-containing melt. Under applied potential and N_2 flow large amounts of N^{3-} were detected in the melt while no decomposition of Co_3Mo_3N was observed in XPS or XRD indicating catalytic electrochemical reduction of dinitrogen to nitride ions.

Based on experimental evidence and previous literature reports a Mars-van Krevelen-type mechanism is suggested for the reaction in which Li^+ ions facilitate the activation of dinitrogen, as well as enable participation of the lattice nitrogen of Co_3Mo_3N. This potentially provides an interesting parallel to the positive effect of lithium promotion on ruthenium-based thermal ammonia synthesis catalysts.

In order to further investigate the mechanism and accurately quantify the nitrogen reduction rate, isotope labelling studies as well as long-term catalyst stability tests are suggested. Also it should be noted that presented measurements here are N_2 half cell experiments and further research into the nitrogen redox chemistry in molten chlorides is needed to establish a continuous ammonia synthesis cell.

7.2 Outlook

The work on SACs in this thesis provides some insights into the structural factors determining HER activity which are hoped to provide inspiration for the rational designed based search for non-PGM hydrogen evolution catalysts. Additionally, they may be useful in limiting HER in reactions such nitrogen and CO_2 reduction.

Generally, competing HER remains the principle challenge in aqueous electrolyte-based electrochemical ammonia synthesis and next to catalyst engineering additional strategies to limit proton or electron availability are needed to tackle this challenge. A potential solution could be the use of low temperature ionic liquid electrolytes with low water contents and increased nitrogen solubility, recently reported for NRR applications.[1,2] NRR testing of the here presented M-NG and Co SAC systems in low temperature ionic liquid systems is suggested.

Nitrogen reduction in molten Li-K-Cl systems is theoretically not limited by HER since N_2 can be directly reduced to N^{3-} in the absence of protons. In order to move from a batch process to the continuous production of NH_3, a hydrogen source has to be introduced at some point of the process. We recently reported on the existence of several chemical reactions of H_2 with N^{3-} in the melt which complicate the search for the right melt conditions enabling continuous NH_3 evolution.[3] Potential solutions to this could be the use of a bipolar membrane as suggested by Ito et al.[4], a proton-conducting membrane, e.g. yttrium-doped barium zirconates, or porous membranes.

Moreover, further screening for cathode materials should be carried out potentially first in N_2 half cell experiments. The here reported activity of Co_3Mo_3N provides an exciting avenue for further research due to the existence of the isostructural Co_3Mo_3C and Fe_3Mo_3N phases. Testing of the carbide phase could provide insights into the effect of nitrogen in the lattice. Fe_3Mo_3N also exhibits lattice nitrogen mobility[5] albeit to a lesser degree and forms solid solutions with Co_3Mo_3N[5,6] which opens up the possibility to investigate the impact of lattice nitrogen mobility and elemental composition on NRR activity. Additionally, Ni_2Mo_3N was also shown to exhibit slight lattice nitrogen

mobility[7] and is known to form quaternary nitride solid solution with Co[5,8] which could be a possible way to investigate the effect of crystal structure on NRR activity.

In order to increase the rate of Co_3Mo_3N higher surface area catalysts are needed, optimally directly support on a gas electrode. First steps in that direction are shown in the Appendix using a novel electrodeposition method to precipitate CoMo precursor onto carbon felt followed by nitridation.

7.3 References

(1) Kang, C. S. M.; Zhang, X.; MacFarlane, D. R. High Nitrogen Gas Solubility and Physicochemical Properties of [C4mpyr][EFAP]–Fluorinated Solvent Mixtures. *J. Phys. Chem. C* **2019**, acs.jpcc.9b06000. https://doi.org/10.1021/acs.jpcc.9b06000.

(2) Zhou, F.; Azofra, L. M.; Ali, M.; Kar, M.; Simonov, A. N.; McDonnell-Worth, C.; Sun, C.; Zhang, X.; MacFarlane, D. R. Electro-Synthesis of Ammonia from Nitrogen at Ambient Temperature and Pressure in Ionic Liquids. *Energy Environ. Sci.* **2017**, *10* (12), 2516–2520. https://doi.org/10.1039/C7EE02716H.

(3) McPherson, I. J.; Sudmeier, T.; Fellowes, J. P.; Wilkinson, I.; Hughes, T.; Tsang, E. S. C. The Feasibility of Electrochemical Ammonia Synthesis in Molten LiCl-KCl Eutectics. *Angew. Chem. Int. Ed.* **2019**. https://doi.org/10.1002/anie.201909831.

(4) Okabe, T. H.; Kuzmina, O.; Sudmeier, T.; Liu, K.; Xu, L.; Yue, X.; Doherty, A.; Jiao, S.; Xu, Q.; Madden, P.; et al. Developments for Nuclear Reactors and Spent Fuels Processing: General Discussion. *Faraday Discuss.* **2016**, *190*, 399–419. https://doi.org/10.1039/C6FD90031C.

(5) Hunter, S. M. Molybdenum Nitrides: Structural and Reactivity Studies, University of Glasgow, 2012.

(6) Prior, T. J.; Battle, P. D. Superparamagnetism and Metal-Site Ordering in Quaternary Nitrides with the η-Carbide Structure. *J Mater Chem* **2004**, *14* (20), 3001–3007. https://doi.org/10.1039/B408040H.

(7) Hargreaves, J. S. J.; Mckay, D. A Comparison of the Reactivity of Lattice Nitrogen in Co3Mo3N and Ni2Mo3N Catalysts. *J. Mol. Catal. Chem.* **2009**, *305* (1–2), 125–129. https://doi.org/10.1016/j.molcata.2008.08.006.

(8) Prior, T. J.; Battle, P. D. Facile Synthesis of Interstitial Metal Nitrides with the Filled β-Manganese Structure. *J. Solid State Chem.* **2003**, *172* (1), 138–147. https://doi.org/10.1016/S0022-4596(02)00171-8.

8 Appendix

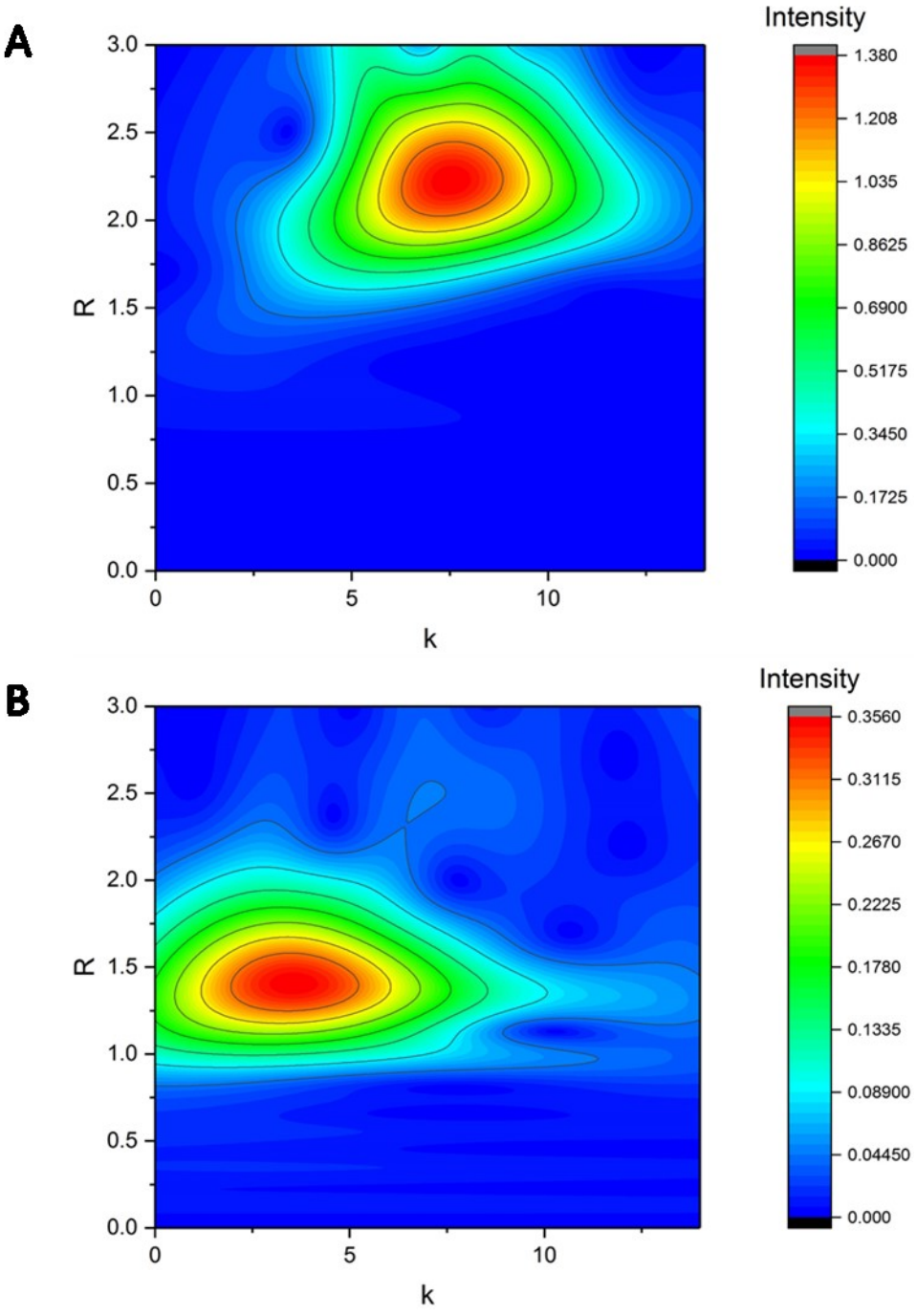


Figure A1: *Wavelet transform of EXAFS of Fe metal foil (A), and Fe-NG (B) all measured in air. The R axis is not phase corrected. Colour code: Warmer colours indicate higher intensity. Only one energy maximum is found for Fe-NG(B) at around 3-4 k and 1.4R which is significantly lower than the maximum observed for Fe metal conclusively showing that no iron-iron interactions are present in Fe-NG and as such Fe is atomically dispersed.*

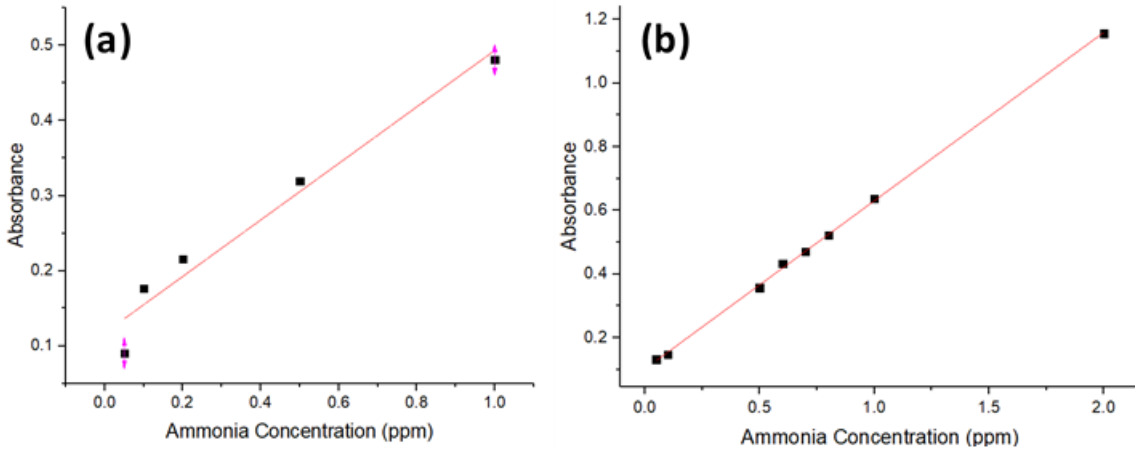


Figure A2: *Comparison of calibration curves for ammonia detection with the salicylate method using a well-plate (A) and using cuvettes (B).*

Supporting Information 1: *Preliminary Experimental Method for Electrodeposition of CoMo Precursor onto Carbon Felt and subsequent Nitridation*

Electrodeposition of CoMo-containing metal alloys or mixed-metal oxides onto carbon felt was explored. Electrodeposition of molybdenum, especially from aqueous solutions, is highly challenging due to its oxophilicity and stability of oxides in water making the complete reduction nearly impossible. [1–3] Metals such as Mo are labelled reluctant metals and can be electroplated more easily using a process called induced codeposition in the presence of a second metal, for Mo usually Fe, Co or Ni. Several different explanations for the mechanism of induced codeposition are laid out in literature including the formation of M-Mo- species (M=Fe, Co, Ni) in solution that are coreduced, the reduction of formed molybdenum oxide phases by H_2 evolved from metallic M, as well as solution species of M favouring the formation of MoO_2 deposits which can subsequently form an adsorbed M-MoO_2 intermediate. [1,4–7] Further additives such as complexing agents have been shown to have an effect on the composition of the deposit by changing the surface

concentration, usually of the inducing species, inhibiting build up of electrochemically inactive clusters and are believed to facilitate the formation of adsorbed M-MoO_2 species.[1,4,8,9] In situ surface Raman studies have provided some evidence for the formation of such an adsorbed species when using citrate in the electrodeposition of NiMo alloys ([(Ni-Citrate)$^-$-MoO_2]).[6,10]

We used a bath containing a combination of hexamethylenetetramine and ammonia and Co/Mo in a 1:10 molar ratio for the electrodepositon of the Co_3Mo_3N. The bath was made up of 5.50g of sodium molybdate dihydrate (0.23mol), 0.66g of cobalt nitrate hexahydrate (0.023mol), as well as 2.10g of hexamethylenetetramine (0.15mol) with 35% ammonia solution and concentrated nitric acid being used to adjust the pH.

Upon addition of solids to MQ water a cloudy purple solution with a pH of 8.2 was obtained. The solution was first acidified using concentrated HNO_3 to a pH of ~6 leading to pink solution containing white precipitate before 35% ammonia solution was used to adjust the pH to 9.5 leading to a clear dark maroon coloured solution. The initial acidification step was need to achieve complete dissolution.The carbon felt support was activated by immersion in concentrated HNO_3 for 12h followed by three consecutive wash cycles with MQ water, ethanol and acetone. Electrodeposition was performed at room temperature in a two electrode cell using the carbon felt support as working electrode, a Pt mesh counter electrode and the respective bath as electrolyte. Galvanostatic conditions were chosen to carry out the deposition meaning constant current density of 100mA cm^{-2} was applied across the cell for 900s. The as-plated felts appeared dark black with an oily lustre. The plated felts were dried over night at 80°C before being calcined in air at 400°C for 1h resulting in the colour of the felts changing to purple. The nitridation was performed by heating the samples to 700°C under 3:1 H_2/N_2

at a ramp rate of 0.6°C/min in a split tube furnace connected to a paraffin bubbler. Samples were held at 700°C for 2h before cooling to room temperature under N_2 flow. The surface of the samples was passivate by disconnecting the bubbler and letting air diffuse into the furnace tube over 24h. Dark gray/ silver felts were obtained.

X-ray diffraction patterns of the synthesised Co_xMo_yN/CF and its precursors were also obtained. Figure A3 compares the reflection patterns of untreated CF (blue trace), CF after CoMo electrodeposition (black trace), calcined $CoMoO_x$/CF composite (grey trace), and the final nitrided Co_xMo_xN/CF material (red trace). The untreated carbon felt exhibits the typical reflections for the (002) plane at around 26° and (100) at around 44° (JCPDS: 01-075-1621).[11] After electrodeposition only one broad reflection at around 26° is observed, similar to the $CoMoO_x$ phase (black trace, Chapter 6, Fig.2) indicating that a an amorphous phase is deposited onto the CF. Upon calcination of the CoMo/CF sample, three small peaks at around 23.1°, 25.1° and 26.5° are observed, superimposed onto the amorphous reflection which preliminarily assigned as the three main reflections of $CoMoO_4$ (grey trace, Chapter 6, Fig.2). After nitridation in H_2/N_2 a crystalline pattern is observed for Co_xMo_yN/CF including all main reflections of the η-6 Co_3Mo_3N phase (JPCDS: 01-89-7953) although significantly upshifted by around 1.6°. The peak at around 41.2° is suspected to be a composite peak of the Co_3Mo_3N reflection and of the (110) plane of metallic molybdenum.

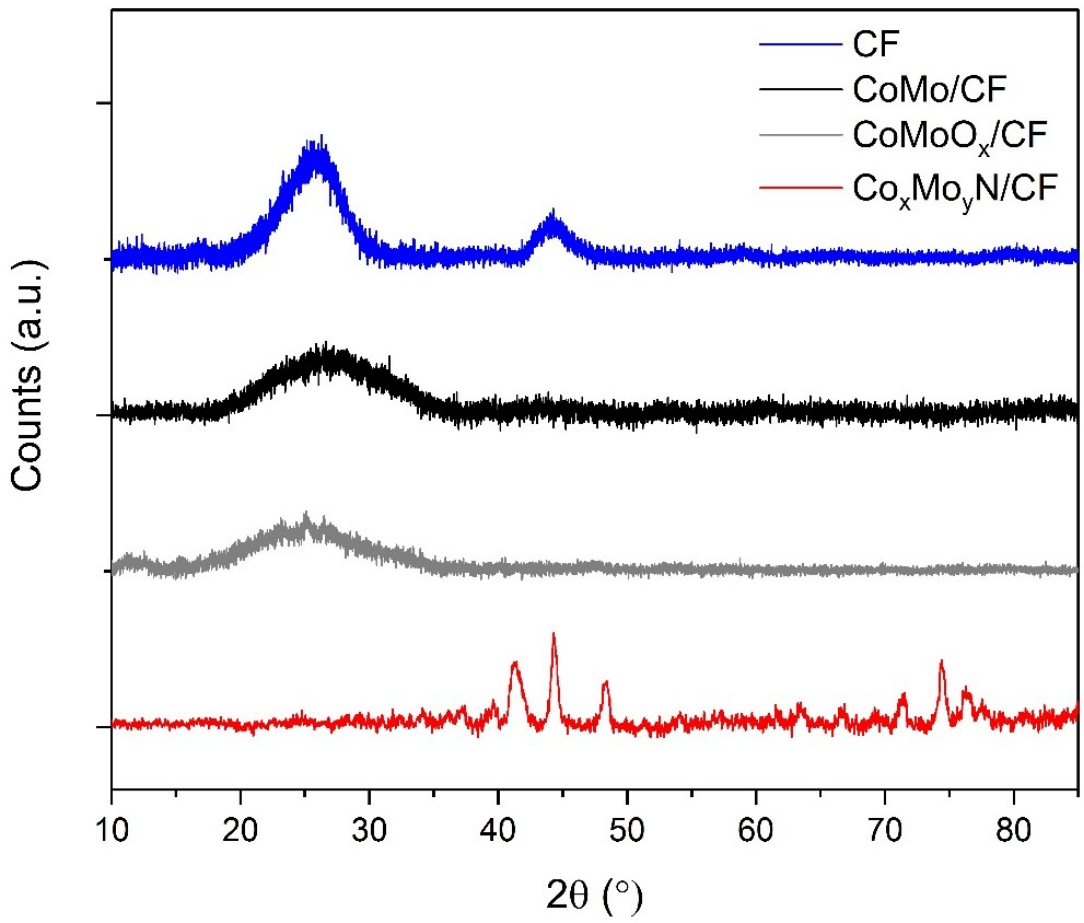


Figure A3: *XRD patterns of Co_xMo_yN/CF and precursors. Colour code: CF (blue), dried CoMo/CF phase (black), calcined $CoMoO_x$/CF phase (grey), and Co_xMo_yN/CF (red).*

Co_xMo_yN/CF was also characterised using XPS with its Co2p, Mo3d, N1s/Mo3p, and O1s regions shown in Figure A4. The elemental composition was determined from survey scans showing the main component to be carbon (77.0at%) followed by oxygen (16.1at%). Co and Mo make up around 2.1 and 4.8at%, respectively, meaning that the cobalt to molybdenum ratio is significantly lower compared to Co_3Mo_3N powder. This in agreement with the observation of a second, spatially separated, phase in XRD next to the distorted Co_3Mo_3N phase, potentially consisting of molybdenum nitride. Analogously to Co_3Mo_3N, nitrogen cannot be quantified precisely using XPS survey scan due to the overlap of the N1s and Mo3p regions.

Due to its low Co content, the spectrum of the Co2p is quite noisy but shows the existence of cobalt in metallic, as well as +II oxidation state (Fig.A4.A). Co might also be present as +III ion which could not be shown unambiguously due to the low signal-to-noise ratio. The spectrum of the Mo3d region of Co_xMo_yN/CF (Fig.A4.B) is similar to the one of Ar-sputtered Co_3Mo_3N (Chapter 6, Fig.4.B) potentially indicating that a thinner oxide layer is formed for Co_xMo_yN/CF upon passivation. Generally, Mo(0) and Mo(V) species are observed with $3d_{5/2}$ peaks at 228.3eV and 232eV, respectively. Mo(IV) and Mo(V) species might be present as well, although most likely in low concentration since they could not be conclusively accounted for in the Mo3d region. Figure A4.C show the XPS spectrum of the N1s/Mo3p region of Co_xMo_yN/CF. Contributions from Mo(0) $3p_{3/2}$ (red trace), Mo(V) $3p_{3/2}$ (blue trace) and N1s (yellow trace) can be accounted for at peak positions of 394.1eV, 398.0eV, and 397.5eV, respectively, in agreement with literature values.[12–14] Similar to Co_3Mo_3N (Chapter 6, Fig.7.B), significant amounts of metal oxide (red trace) can be detected in the O1s region of Co_xMo_yN/CF at around 530.5eV (Fig.A4.D). Additionally, oxygen bound to aromatic carbon/ chemisorbed water is observed at 533.8eV (C-O/OH, blue trace). This is most likely a contribution from the carbon felt support as carbon-oxygen functionalities are a well-known component of processed carbon materials.[15,16]

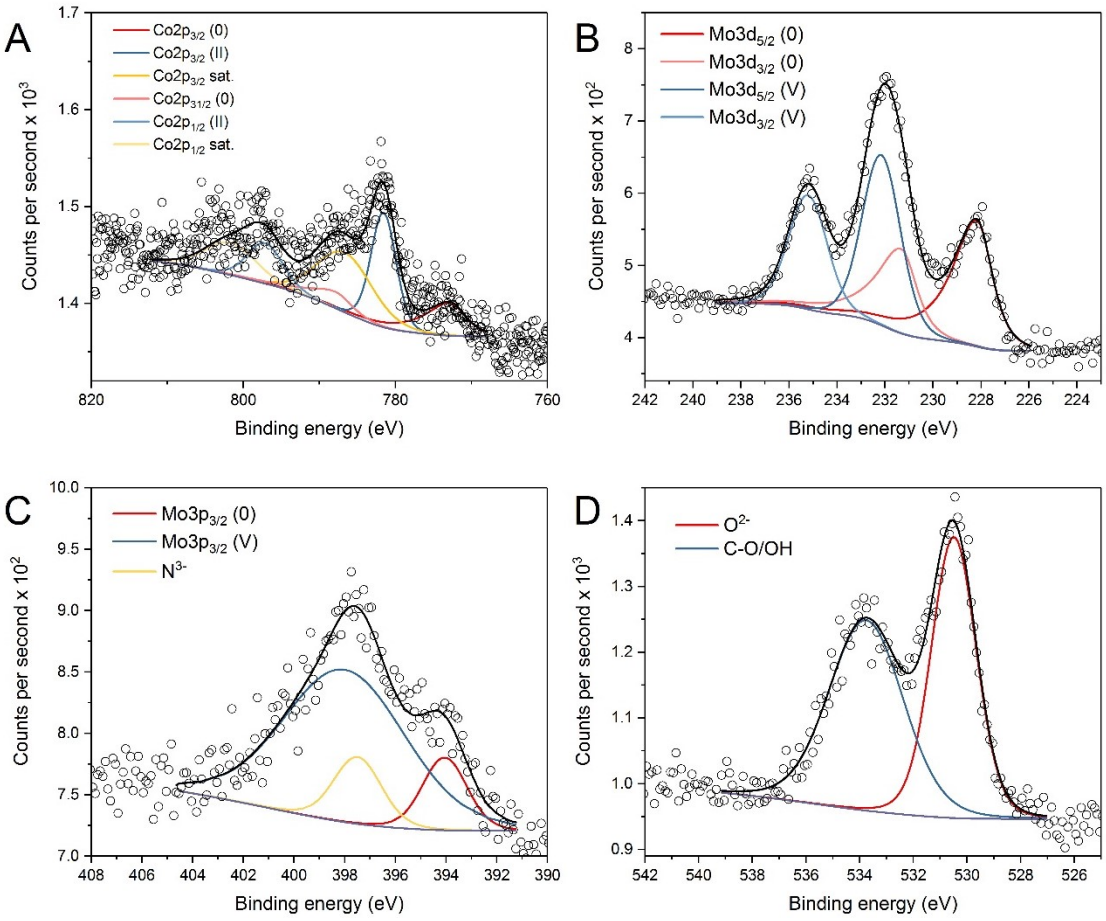


Figure A4: *XPS spectra of Co_xMo_yN/CF. Co2p region (A), Mo3d (B), N1s/Mo3p (C), and O1s (D). The black line, purple line and empty black circles, respectively represent the overall fit, background, and data points. Faint coloured traces represent corresponding $Co2p_{1/2}$ (A), $Mo3d_{3/2}$ (B) and $Mo3p_{1/2}$ peaks (C), respectively.*

8.1 References

(1) Brenner, A. *Electrodeposition of Alloys: Principles and Practice*; Elsevier, 2013.

(2) Morley, T. J.; Penner, L.; Schaffer, P.; Ruth, T. J.; Bénard, F.; Asselin, E. The Deposition of Smooth Metallic Molybdenum from Aqueous Electrolytes Containing Molybdate Ions. *Electrochemistry Communications* **2012**, *15* (1), 78–80. https://doi.org/10.1016/j.elecom.2011.11.026.

(3) Manazoğlu, M.; Hapçı, G.; Orhan, G. Electrochemical Deposition and Characterization of Ni-Mo Alloys as Cathode for Alkaline Water Electrolysis. *Journal of Materials Engineering and Performance* **2016**, *25* (1), 130–137. https://doi.org/10.1007/s11665-015-1849-7.

(4) Subramania, A.; Sathiyapriya, A.; Muralidharan, V. Electrocatalytic Cobalt–Molybdenum Alloy Deposits. *International Journal of Hydrogen Energy* **2007**, *32* (14), 2843–2847. https://doi.org/10.1016/j.ijhydene.2006.12.027.

(5) Podlaha, E. J.; Landolt, D.; Ecublens, M.-C. I. An Experimental Investigation of Ni-Mo Alloys. *J. Electrochem. Soc.* **1996**, *143*, 8.

(6) Podlaha, E. J.; Landolrt, D. Ill. Molybdenum Alloys with Nickel, Cobalt, and Iron. *J. Electrochem. Soc.* **1997**, *144* (5), 9.
(7) Xu, C.; Zhou, J.; Zeng, M.; Fu, X.; Liu, X.; Li, J. Electrodeposition Mechanism and Characterization of Ni–Mo Alloy and Its Electrocatalytic Performance for Hydrogen Evolution. *International Journal of Hydrogen Energy* **2016**, *41* (31), 13341–13349. https://doi.org/10.1016/j.ijhydene.2016.06.205.
(8) Beltowska-Lehman, E.; Indyka, P. Kinetics of Ni–Mo Electrodeposition from Ni-Rich Citrate Baths. *Thin Solid Films* **2012**, *520* (6), 2046–2051. https://doi.org/10.1016/j.tsf.2011.10.024.
(9) Jović, B. M.; Jović, V. D.; Maksimović, V. M.; Pavlović, M. G. Characterization of Electrodeposited Powders of the System Ni–Mo–O. *Electrochimica Acta* **2008**, *53* (14), 4796–4804. https://doi.org/10.1016/j.electacta.2008.02.004.
(10) Zeng, Y.; Li, Z.; Ma, M.; Zhou, S. In Situ Surface Raman Study of the Induced Codeposition Mechanism of Ni–Mo Alloys. *Electrochemistry Communications* **2000**, *2* (1), 36–38. https://doi.org/10.1016/S1388-2481(99)00137-X.
(11) Li, Z. Q.; Lu, C. J.; Xia, Z. P.; Zhou, Y.; Luo, Z. X-Ray Diffraction Patterns of Graphite and Turbostratic Carbon. *Carbon* **2007**, *45* (8), 1686–1695. https://doi.org/10.1016/j.carbon.2007.03.038.
(12) Jaeger, D.; Patscheider, J. A Complete and Self-Consistent Evaluation of XPS Spectra of TiN. *Journal of Electron Spectroscopy and Related Phenomena* **2012**, *185* (11), 523–534. https://doi.org/10.1016/j.elspec.2012.10.011.
(13) Sanjinés, R.; Wiemer, C.; Almeida, J.; Lévy, F. Valence Band Photoemission Study of the Ti□Mo□N System. *Thin Solid Films* **1996**, *290–291*, 334–338. https://doi.org/10.1016/S0040-6090(96)09082-7.
(14) Wang, L.; Kirk, E.; Wäckerlin, C.; Schneider, C. W.; Hojeij, M.; Gobrecht, J.; Ekinci, Y. Nearly Amorphous Mo-N Gratings for Ultimate Resolution in Extreme Ultraviolet Interference Lithography. *Nanotechnology* **2014**, *25* (23), 235305. https://doi.org/10.1088/0957-4484/25/23/235305.
(15) Beamson, G.; Briggs, D. *High Resolution XPS of Organic Polymers: The Scienta ESCA300 Database*; Wiley, 1992.
(16) Ganguly, A.; Sharma, S.; Papakonstantinou, P.; Hamilton, J. Probing the Thermal Deoxygenation of Graphene Oxide Using High-Resolution In Situ X-Ray-Based Spectroscopies. *J. Phys. Chem. C* **2011**, *115* (34), 17009–17019. https://doi.org/10.1021/jp203741y.